Structural, electronic and magnetic properties of ferromagnetic perovskites: a comparative study.

A thesis submitted to the

University of Dublin

in application for the degree of

Doctor of Philosophy

by

Rhian-Mari Thomas

Department of Pure and Applied Physics

Trinity College

Dublin2

November 1999

I fy rhieni, â diolch

Dyfal donc a dyrr y garreg....

Declaration

This thesis is submitted by the undersigned for examination for the degree of Doctor in Philosophy to the University of Dublin. It has not been submitted as an exercise to any other university.

Apart from the advice and assistance mentioned in the acknowledgements, this thesis is my own work.

I agree that this thesis may be freely lent or copied.

Rhian-Mari Thomas
November 1999

TABLE OF CONTENTS

ACKNOWLEDGEMENTS

During the course of this degree I have benefited from the knowledge, advice and assistance of many people. My utmost thanks go to my supervisor, Professsor J. M. D. Coey for providing me with both the opportunity and the means to carry out this work. His compendious knowledge of, and unremitting enthusiasm for magnetism has been truly inspiring.

I wish to thank Laurent Ranno for his unfailing support, and assistance with the XMCD measurements. Thanks to Vassil Skumryev for helping with the ac-susceptibility measurements and high field measurements in Grenoble; to Joe McCauley for his continuing battle with the pulsed field; to Steffen Wirth for manning the high fields at Tallahassee; to Colin Reed for the SEM measurements and David Doff for X-ray fluorescence and taming the XRD. Sincerest thanks are also owed to Jackie Armstrong, Fred Ott, Janko Versluijs, Amanda Barry, Mazhar Bari, and Paul Smith for their general assistance and encouragement throughout.

Thankyou to the ever-changing motley crew that is Group D; to the departmental secretarial and technical staff and to the usual suspects who loiter in and around the Pavillion Bar.

Finally, I acknowledge the great debt I owe to my family and friends. Special thanks go to my sister and best friend, Catrin, for her non-stop encouragment, contagious laughter and understanding during the past year.

ABSTRACT

During the course of this research work, the physical properties of twelve mixed-valence manganites have been investigated and compared. Upon embarking on this project, the prospect of incorporating these newly re-discovered "colossal magnetoresistance" materials in future device applications, provided the impetus for determining which principal factors govern their ferromagnetic ordering temperatures, T_C, and thus optimising this value through judicious chemical substitution.

The original sample set for this investigation comprised sixteen polycrystalline, ceramic manganites, $(A_{1-x}A'_x)MnO_3$, (A = La^{3+}, Nd^{3+}, Pr^{3+}, Sm^{3+}; A' = Ca^{2+}, Sr^{2+}, Ba^{2+}, Pb^{2+}), where x = 0.3. This doping fraction yields the strongest ferromagnets from the palette of magnetic structures which constitute the colourful phase diagram. The samples were prepared using a standard solid state reaction method. A sol-gel synthesis route was also explored. X-ray diffraction established the crystal structure and phase purity of the samples, whilst X-ray fluorescence confirmed the nominal stoichiometry of all compounds, with the exception of the Pb^{2+} substituted compounds, which were deemed lead deficient; $(La_{0.7}Pb_{0.15})MnO_3$, $(Pr_{0.7}Pb_{0.07})MnO_3$, $(Nd_{0.7}Pb_{0.10})MnO_3$ and $(Sm_{0.7}Pb_{0.02})MnO_3$ were subsequently omitted from further studies.

The transport properties of the twelve remaining manganites were examined through measuring their resistivity as a function of temperature, $\rho(T)$, in the range 15 K to 300 K. Two distinct behaviours emerged: four of the compounds studied showed an activated conduction mechanism down to lowest temperatures, whereas the remainder exhibited a transition from an activated conduction mechanism to a "metallic" state as the temperature was lowered. For all twelve samples the data in the activated conduction regime varied as $T^{-\frac{1}{4}}$, thus supporting a variable-range hopping (VRH) model of current transport. Based on these experimental observations a new theory of electron localisation was formulated, which introduced random, spin-dependent potential fluctuations of magnetic origin into Mott's VRH theory. Values of the density of states, deduced from specific heat capacity measurements - $N(E_F) \sim 3 \times 10^{28} m^{-3} eV^{-1}$ for $(La_{0.7}Sr_{0.3})MnO_3$ - were incorporated into the model, yielding physically plausible room temperature localisation and hopping lengths. This magnetic localisation theory has since been superseded by theories of small magnetopolaron formation due to the dynamic Jahn-Teller effect, and the VRH behaviour is currently attributed to extrinsic effects such as electron tunneling through grain boundaries The merits of these various models are discussed with reference to the measured data.

Analysis of the samples' magnetic structure forms the bulk of this research work. The variation of low field (80 A/m) ac-susceptibility in the temperature range 5K to 300K represents the first such systematic study of the manganese perovskites. The measured data elicits the ordering temperatures of the com-

pounds which were found to correlate with their crystal structures. The enhanced Curie constants measured for all twelve samples can be attributed to short-range ferromagnetic correlations in the paramagnetic phase, providing new experimental evidence for cluster formation above T_C.

The magnetisation measurements conducted at 4.2K in a steady applied field ranging up to 23T, provided a wealth of information about the varying magnetic ground states of the twelve oxides under study. Whereas the negligible high field slope measured for $(La_{0.7}Sr_{0.3})MnO_3$ confirms the strong ferromagnetic nature of this compound, the ground state of $(Pr_{0.7}Ca_{0.3})MnO_3$ does not appear to be ferromagnetic, and is presumed to be charge-ordered. Moreover, although the first transition shown by the latter compound at 5T has been widely observed (in pulsed field measurements) a further first-order magnetisation process exhibited at 6T has never been previously reported. A subsequent calculation of the crystal field interaction at the rare-earth site convincingly attributes this second transformation to level crossing transition of the lowest lying Pr^{3+} crystal field levels. The magnetisation of this intriguing compound and that of $(Nd_{0.7}Ca_{0.3})MnO_3$ - also believed to be partly charge-ordered - was further investigated by a 25T pulsed field measurement at 4.2K and 77K. The relaxation and hysteresis observed for both samples is quantitatively discussed. This study of the manganites' magnetic propeties coucludes with a discussion of the rare-earth and manganese sublattice coupling n the Nd containing compounds, with reference to the X-ray magnetic circular dichroism spectra measured for these three samples.

The influence of oxygen stoichiometry on the physical properties of the end-member, $LaMnO_3$ is considered in the penultimate chapter of this work. Resistivity, ac-suscetibility and magnetisation data measured for $LaMnO_3$ and $(LaMn)_{0.95}O_3$ polycrystalline, ceramic samples are presented and discussed.

This study confirms that the maximum ferromagnetic ordering temperature obtainable through chemical substitution or varying the oxygen stoichiometry of the manganites is achieved for $(La_{0.7}Sr_{0.3})MnO_3$. The measured Curie temperature of this manganese perovskite, $T_C \sim 370$ K, is exceeded by that of Sr_2FeMoO_6 - a "double perovskite". A preliminary study of the crystal structure, transport and magnetic properties of this compound, in addition to those of Ca_2FeMoO_6 and Ba_2FeMoO_6, comprise the final chapter of this thesis, which in view of the stated objective represents both a conclusion and introduction.

Chapter 1
Introduction

The discovery of high-temperature superconductivity in copper-based oxides earned Bednorz and Müller the 1987 Nobel Prize for Physics. This "important breakthrough in the discovery of superconductivity in ceramic materials" prompted a surge of scientific interest in the properties of such transition metal oxides.

During the mid 1990's, the expertise honed through the preparation and characterisation of superconducting cuprate ceramics and thin-films was applied to the structurally related manganese oxides. The consequent discovery of a negative magnetoresistance effect of unprecedented magnitude [1] raised expectations of a new generation of magnetic devices and sensors, and captivated the global condensed matter research community [2] [3] [4] [5]. The mixed-valence manganese perovskites, although not superconducting, exhibit a colourful spectrum of crystallographic, electronic and magnetic phases. Their chemical flexibility offers a laboratory within which, the fine balance of interactions which together determine the electronic ground states, can be systematically studied.

However, unlike the brain-child of Bednorz and Müller, the manganites are not a new discovery. On the contrary, their properties have inspired scientific research for the past 50 years [6]. This first chapter serves to introduce the physics, accumulated to date, which pertains to this study of the mixed-valence manganese perovskites; a more detailed treatment of the relevant theory is presented where applicable in subsequent chapters.

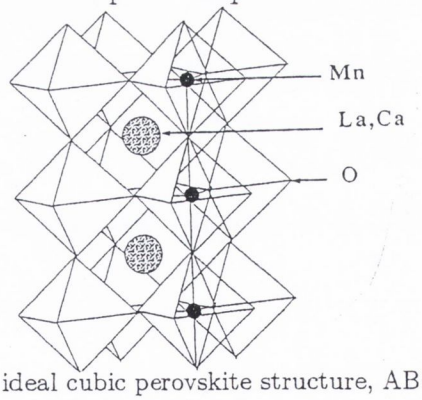

Figure 1.1 The ideal cubic perovskite structure, ABO_3.

$LaMnO_3$ is an insulating antiferromagnet with a Néel temperature $T_N \approx 130K$ and an orthorhombic crystal structure related to the ideal cubic crystal structure of perovskite, $CaTiO_3$, shown in figure 1.1. Within this ABO_3 structure, the B-site Mn^{3+} ($3d^4$) ion is surrounded by an octahedral arrangement of equidistant oxygen ions. The d-electrons are subject to a variety of interactions; of foremost importance is the crystal field splitting, Δ_{cf} between the lower-lying t_{2g} triplet and two higher lying states, which form an e_g doublet if the crystal field has perfect cubic symmetry. Indeed, measurements of the crystal structure, by both Ellemaans *et al.* [7] and Urushibara *et al.*

[8], confirm that the Mn-O bond lengths are unequal, reflecting a tetragonal elongation of the octahedron which alternates throughout the basal plane in a "chequerboard" arrangement.

The driving force for the lattice distortion is the *Jahn-Teller effect* of the Mn^{3+} ion [9], with a $3d^4$ electronic configuration, where the degenerate $eg^{\uparrow}$ orbitals are half-filled. The Jahn-Teller effect lifts the degeneracy of the $e_g^{\uparrow}$ orbitals, stabilizing a lower d_{z^2} orbital relative to a $d_{x^2-y^2}$ orbital, and resulting in an energy gain δ_{JT}, if the e_g orbital is preferentially occupied [figure 1.2]. Conversely, the preferential occupancy of one orbital will induce a lattice distortion.

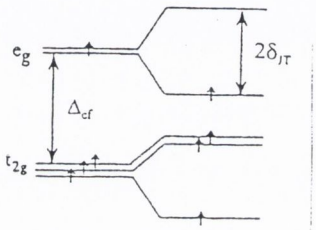

Figure 1.2 The occupancy of one electron energy levels for Mn^{3+}.

The Jahn-Teller distortion crucially determines the physical properties of stoichiometric $LaMnO_3$. In its absence, band structure calculations have repeatedly predicted a ferromagnetic metallic ground state for the compound [10] [11] [12] [13]. This finding directly contradicts experiment, which reveals $LaMnO_3$ to be an "A-type antiferromagnet", where the magnetic moments at Mn sites are ferromagnetically coupled in planes with alternating spin orientations [figure 1.4]. Furthermore, the material is insulating with a small activation energy $\sim$ 0.1 eV! The LSDA (local spin-density approximation) band calculations of Satpathy *et al.* [14] investigate the introduction of different distortions into the oxygen octahdera. Their studies indicate that the displacement of the basal-plane oxygen atoms by a minimum of $\approx$ 0.1 Å, in accordance with a Jahn-Teller-like distortion, results in an indirect gap of order 0.1 eV between the split e_g bands, which are both, W $\sim$ 1 eV wide [figure 1.3]. They also show that such distortions favour planar antiferromagnetic rather than ferromagnetic order.

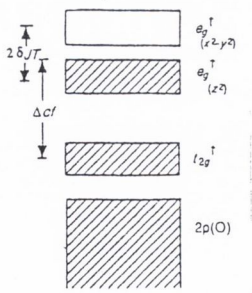

Figure 1.3 Schematic energy band structure of $LaMnO_3$.

Further support for these assertions is provided by Millis [15]. His theoretical considerations of the electron-phonon coupling arising from the Jahn-Teller

distortion are in agreement with the energy levels deduced from previous optical absorption measurements of $LaMnO_3$ [16]. The principal conclusion of [15] is that the electron-phonon interaction is dominant. Other authors regard the electron-electron interaction as pivotal in determining the properties of the compound [17] [18]. This latter, strong on-site Coulomb interaction is reponsible for the high spin state, and exchange stability of the $3d^{\uparrow}$ and $3d^{\downarrow}$ orbitals implicated in figures 1.2 and 1.3. This on-site Mott-Hubbard interaction, $U_{dd} \approx 4$ eV, was introduced into the LSDA calculations of Satpathy *et al.* [14]. A more modest value of U, which mainly involves t_{2g} electrons was used in the band calculations of Solovyev *et al.* [13] who thereby resolve the discrepancies between LSDA predictions and experiment.

In the laboratory, the end-member has displayed a plethora of crystal, electronic and magnetic structures, all of which can be ascribed to deviations from ideal stoichiometry. Preparation conditions often result in a strongly oxygenated compound with a formula which is occasionally written, $(LaMn)O_{3+\delta}$. However, since additional oxygen is accommodated within the close-packed ABO_3 structure as vacancies on the A and B-sites, this is a misleading representation, as discussed in 2.1.4. For $\delta > 0.05$, the material becomes ferromagnetic and metallic - the result of a Mn^{3+}-Mn^{4+} mixed-valence state [chapter 5].

Similarly, mixed-valence is readily achieved in the manganites through the substitution of a divalent (or monovalent) cation for La^{3+}, typically Sr^{2+}, Ca^{2+}, Ba^{2+} or Pb^{2+}. The formula for the mixed-valence manganites with divalent cation doping may be written

$$(A^{3+}_{1-x}A'^{2+}_{x})(Mn^{3+}_{1-x}Mn^{4+}_{x})O_3 \qquad (1)$$

where A^{3+} may be a rare-earth ion other than La^{3+}, such as Pr^{3+}, Nd^{3+}, Sm^{3+} and $0 \leq x \leq 1$. The compounds crystallize in distorted variants of the ideal ABO_3 structure [section 2.3.2]. However, they all share the basic feature of a network of Mn ions, six-fold coordinated by oxygen, which lifts the five-fold degeneracy of the d-shell electronic energy levels, as previously discussed. For $(A_{1-x}A'_x)MnO_3$, the number of d-electrons is (4-x). The strong on-site Hund coupling, J_H, requires that all d-electrons on a given Mn ion be of the same spin. Consequently, of the (4-x) electrons at a Mn site, three occupy the lowest t_{2g} levels, forming a localised core spin, $S = \frac{3}{2}$, whereas the remaining (1-x) electron enters a linear combination of e_g levels and 2p orbitals of adjacent oxygen ions; a σ^* antibonding band is formed by the direct overlap of e_g orbitals with the 2p(O) orbitals, $[e_g(Mn) - 2p_\sigma(O) - e_g(Mn)]$. The delocalised (1-x) e_g electron in the partly-filled σ^* band hops between Mn sites, subject to the constraint that its spin is parallel to that of the localised core at each site. This arrangement strictly requires $J_H \sim \infty$, otherwise three alternative higher energy configurations become admissable: the e_g spin may be coupled antiparallel to the t_{2g} core spin; the t_{2g} electrons may be arranged in a non-maximal spin state or the additional (1-x) electron may enter the t_{2g} levels. Recent optical data [19] imply that the former antiparallel configuration is ~ 3 eV higher than the e_g-t_{2g} parallel spin configuration. Despite the absence

of direct experimental evidence the energies of the two latter scenarios are expected to be yet higher [15]. Thus, the Hund energy, while far from infinite, is at least comparable to the σ^* bandwidth.

This is the essence of the *double exchange mechanism*, proposed by Zener in 1952 [20] to explain the observed simultaneous occurrence of ferromagnetism and metallicity in the manganites, both as a function of x and temperature [21] [22]. The large on-site Hund coupling dictates that the delocalised electron retains its spin as it moves between Mn sites and therefore, the hopping amplitude depends on the relative orientation of the core spins on the sites involved. As a result, electron transfer is modulated by a spin-dependent overlap factor which is maximal when adjacent core spins are parallel and minimal when antiparallel. Thus, double exchange is always ferromagnetic, and the e_g "Zener" electrons are both conduction electrons and mediators of the ferromagnetic exchange; if the t_{2g} core spins are not parallel electron transfer is impeded and the mobility decreases.

The direct connection between ferromagnetic alignment and conductivity in the mixed-valence manganites was unequivocally established by Wollan and Koehler [1] in 1955, in a rigorous study of the transport, and crystallographic and magnetic structures of $(La_{1-x}Ca_x)MnO_3$ $0 \leq x \leq 1$. Neutron and x-ray diffraction measurements of the polycrystalline ceramics revealed a variety of magnetic structures, illustrated in figure 1.4 as a function of Mn^{4+} content. Members of the series are predominantly antiferromagnetic, however for x $\sim$0.3 the compounds exhibit ferromagnetism with a moment almost equal to the spin-only value, $M_s = Ng\mu_B < S >$ where N is the number of Mn ions per formula unit, g is the gyromagnetic ratio of 2 and $< S >$ represents the average spin of the constituent Mn^{3+} (S=2) and Mn^{4+} (S=$\frac{3}{2}$). The resistivity measurements correlated with these results, showing a maximum conductivity for the ferromagnetic samples.

The spectrum of deduced magnetic phases illustrated in the following figure [figure 1.4], result from competing indirect exchange mechanisms between the different manganese ions, as first outlined by Goodenough [24]. Through consideration of the possible Mn-O-Mn bonding arrangements through which the magnetic coupling is mediated, he concluded that whereas Zener's double-exchange between heterovalent (Mn^{3+}, Mn^{4+}) neighbours is ferromagnetic, Mn^{4+}-Mn^{4+} and Mn^{3+}-Mn^{3+} ions are coupled via antiferromagnetic superexchange between the localised t_{2g} spins [t_{2g}(Mn)-2$p_\pi(O)$-t_{2g}(Mn)]. Furthermore, in accordance with the second Goodenough-Kanamori rule for asymmetric d^3-d^3 overlap [25], the Mn^{3+}-Mn^{3+} interaction is ferromagnetic. The model provided a qualitative account of the phase diagram above, and furthermore, confirmed that a doping fraction of x = 0.31 corresponds to the composition for which the double-exchange mechanism is optimised, through "considering the problem of calculating the fraction of randomly distributed Mn^{4+} ions which gives the largest number of Mn^{3+} ions with one and only one Mn^{4+} neighbour in a random matrix of Mn^{4+} and Mn^{3+} ions"

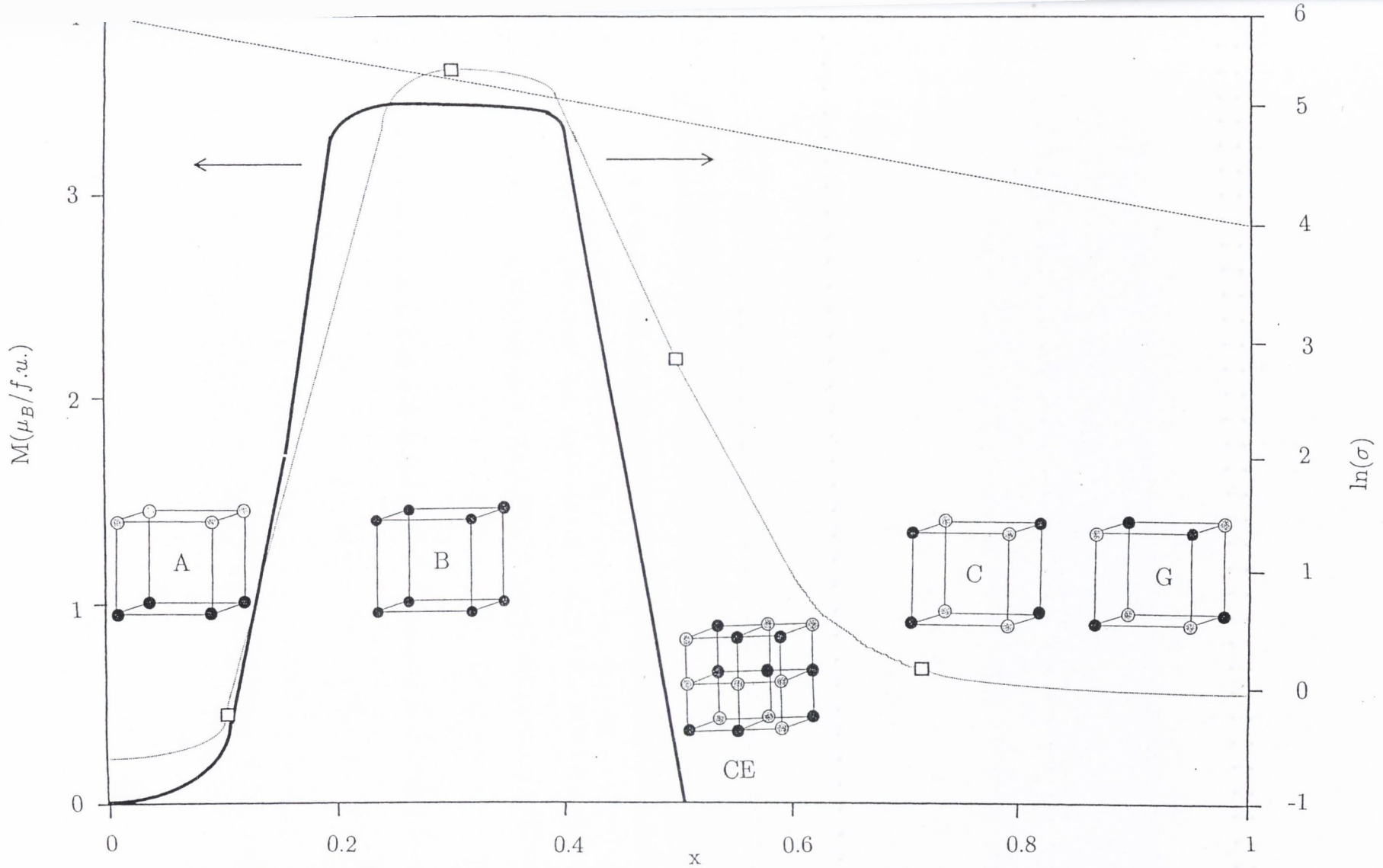

Figure 1.4 The magnetic ground state structures and ferromagnetic moments for the $(La_{1-x}Ca_x)MnO_3$ series, with reference to the electrical conductivity measured at 80K and the theoretical spin only moment (adapted from [2]).

Further interactions play an important role in determining the low-temperature magnetic arrangements of the doped manganites. Most notably, strong interatomic d-d correlations, V, may become comparable with the e_g electron bandwidth, W, for particular occupancies of the d band [11], resulting in the localisation of itinerant electrons on certain Mn ions, which form an ordered superlattice of Mn^{3+} and Mn^{4+}; a *charge-ordered state*. Figure 1.5 illustrates the idealised charge-ordered arrangement of Mn^{3+} and Mn^{4+} ions present in equal numbers; the Mn^{3+} species is characterised by the tetragonally elongated octahedron indicative of the Jahn-Teller polarisation of the e_g electron levels, whereas Mn^{4+} is located within the regular octahedron. The structural distortion associated with this cooperative arrangement of $Mn^{3+}$and Mn^{4+} leads to the doubling of the crystallographic cell evidenced by superlattice peaks in diffraction patterns [26]. Since both ferromagnetism and charge-order are mediated by the same e_g conduction electrons, charge-ordering (also known as Wigner crystallisation) impedes the formation of the metallic state. The underlying competition between metallicity and charge-order is influenced through bandfilling, with the strongest tendency to charge-ordering shown at low temperature when the doping ratio, x, is a rational fraction such as $\frac{1}{8}$, $\frac{1}{2}$ or $\frac{3}{4}$ [27] [28] [29] [30].

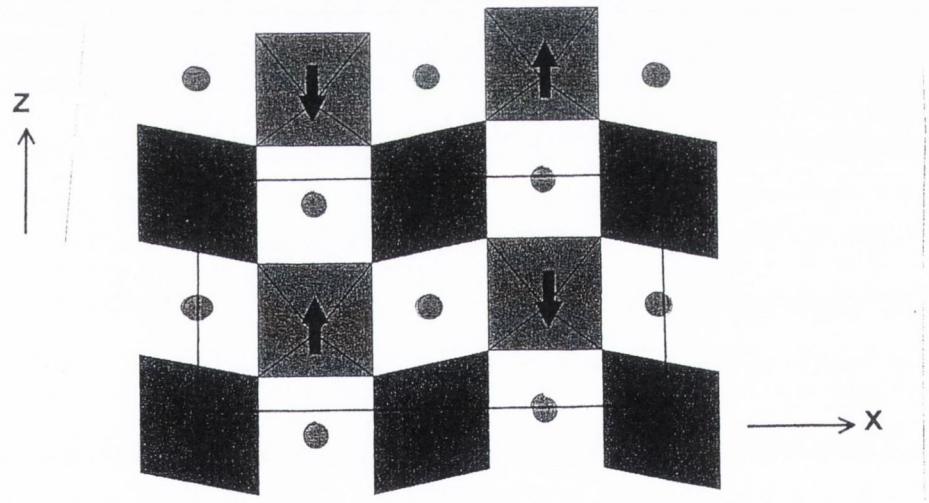

Figure 1.5 Schematic representation of the 1:1 (Mn^{3+}=Mn^{4+}) charge-ordered and antiferromagnetic spin-ordered state.

Besides varying the number of charge carriers entering the σ^* conduction band, the variation of doping ratio, x, through cation substitution (or the introduction of cation vacancies) serves to alter the interatomic distances and bond angles [31] [32]. Due to the sensitive dependence of the conduction bandwidth, W on the Mn-O-Mn bond angle, [section 4.2.4] the sizes of the substituted cations further influence the manganites' observed behaviour [chapter 4]. Thus, the physical properties of the manganese perovskites are determined by both the doping ratio and the lattice distortion; the combined effects of *bandfilling* and *bandwidth* within the double-exchange framework.

The full consequences of double-exchange have been studied in detail by many authors [33] [34] [35] [36] [37] [38]. The theory successfully predicts that the transition of an optimally doped manganite from the paramagnetic to the ferromagnetic state should be accompanied by a metal to insulator transition (compounds which prove an exception to this rule are discussed in section 3.5). However, the increase in kinetic energy of the carriers on passing from an uncorrelated spin state to the fully polarised ferromagnetic state upon application of a magnetic field or cooling through the magnetic ordering temperature, T_C, is a mere 30% and it appears that the double exchange mechanism as the sole governing interaction, is insufficient to account for the physics of the mixed-valence manganites. This modest magnetoresistance is at odds with the colossal effect recorded by Jin for a $(La_{0.67}Ca_{0.33})MnO_3$ thin film ($R(0)/R(6T) = 10\,000$ at 110K; figure 3.1) The additional interactions which may be invoked to account for the discrepancy are discussed in Chapter 3.

This brief introduction forms the basis for discussing the results presented in the following chapters: the preparation and structural characterisation of $(A_{0.7}A'_{0.3})MnO_3$, A = La^{3+}, Pr^{3+}, Nd^{3+}, Sm^{3+}, A = Ca^{2+}, Sr^{2+}, Ba^{2+}, Pb^{2+} in chapter 2; the transport properties of this materials' matrix [chapter 3] and their magnetic properties [chapter 4]. In chapters 5 and 6, studies of related compounds, $LaMnO_3$ and the double perovskites respectively, complement the main body of research work presented.

[1] S. Jin, T. H. Tiefel, M. McCormack, R. A. Fastnacht, R. Ramesh and L. H. Chen, Science, **264**, 413, (1994).

[2] J. M. D. Coey, M. Viret and S. von Molnár, Advances in Physics, **48**, 167, (1999).

[3] A. Ramirez, Journal of Physics: Condensed Matter, **9**, 8171, (1997).

[4] Y. Tokura, preprint

[5] J. Fontcuberta, Physics World, February 1999.

[6] G. Jonker and J. van Santen, Physica, **16**, 337, (1950).

[7] J. B. A. Ellemaans, B. van Laar, K. J. R. van der Veer and B. O. Loopstra, Journal of Solid State Chemistry, **3**, 238, (1971).

[8] A. Urushibara, Y. Moritomo, T. Arima, A. Asamitsu, G. Kido and Y. Tokura, Physical Review B **51**, 14103, (1995).

[9] H. A. Jahn and E. Teller, Proceedings of the Royal Society **A 161**, 220, (1937).

[10] D. Sarma, N. Shanthi, S. Barman, N. Hamada, H. Sawada and K. Terakura, Physical Review Letters, **75**, 109, (1995).

[11] W. E. Pickett and D. J. Singh, Europhysics Letters, **32**, 759, (1995).

[12] W. E. Pickett and D. J. Singh, Physical Review B **53**, 1146, (1996).

[13] I. Solovyev, N. Hamada and K. Terakura, Physical Review Letters, **76**, 4825, (1996).

[14] S. Satpathy, Z. S. Popovic and F. R. Vukajlovic, Physical Review Letters, **76**, 295, (1996).

[15] A. J. Millis, Philosophical Transactions of the Royal Society, London, **356**, 1473, (1998).

[16] T. Arima and Y. Tokura, Journal of the Physical Society of Japan, **64**, 2488, (1995).

[17] C. M. Varma, Physical Review B **54**, 7328, (1996).

[18] N. Nagaosa, S. Murakami and H. C. Lee, Physical Review B **57**, 6767, (1998).

[19] M. Quijada, J. Cerne, J. R. Simpson, H. D. Drew, K. H. Ahn, A. J. Millis, G. C. Xiong, R. Ramesh, C. Kwon, M. Rajeswari and T. Venkatesan, Physical Review B **58**, 16093, (1998).

[20] C. Zener, Physical Review, **82**, 403, (1952).

[21] G. Jonker and J. van Santen, Physica, **16**, 337, (1950)

[22] J. H. van Santen and G. H. Jonker, Physica, **16**, 599, (1950).

[23] E. O. Wollan and W. C. Koehler, Physical Review, 100, 545, (1955).

[24] J. B. Goodenough, Physical Review 100, 564, (1955).

[25] J. B. Goodenough, *Magnetism and the Chemical Bond*, (Wiley Interscience, New York), 1996.

[26] Z. Jirak, S. Krupicka, Z. Simsa, M. Dlouha and S. Vratislav, Journal of Magnetism and Magnetic Materials, **53**, 153, (1985).

[27] Y. Yamada, O. Hino, S. Nohodo, R. Kanao, T. Inami and S. Katano, Physical Review Letters, **77**, 904, (1996).

[28] Y. Tomioka, A. Asamitsu, H. Kuwahara, Y. Moritomo and Y. Tokura, Physical Review B **53**, R1689, (1996).

[29] S. Mori, C. H. Chen and S. W. Cheong, Nature, **392**, 473, (1998).

[30] S. Mori, C. H. Chen and S. W. Cheong, Physical Review Letters, **81**, 3972, (1998)

[31] H. Y. Hwang, S. W. cheong, P. G. Radaelli, M. Marezio and B. Batlogg, Physical Review Letters, **75**, 914, (1995).

[32] J. L. Garcia-Munoz, J. Fontcuberta, B. Martinez, A. Seffar, S. Pinol and X. Obradors, Physical Review B **55**, R668, (1997).

[33] P. W. Anderson and H. Hasegawa, Physical Review, 100, 675, (1955).

[34] P. G. de Gennes, Physical Review 118, 141, (1960).

[35] K. Kubo and A. Ohata, Journal of the Physical Society of Japan, 33, 21, (1972).
[36] N. Furukawa, Journal of the Physical Society of Japan, 63, 3214, (1994).
[37] H. Röder, J. Zang, A. R. Bishop, Physical Review Letters, 76, 13 569, (1996).
[38] A. J. Millis, P. B. Littlewood, B. I. Shraiman, Physical Review Letters, 75; 5144, (1995).

Chapter 2
Materials' Preparation and Structural Characterization

The original sample matrix, which formed the basis of this study, consisted of sixteen polycrystalline compounds: $(A_{0.7}A'_{0.3})MnO_3$ where A = La^{3+}, Pr^{3+}, Nd^{3+}, Sm^{3+} and A' = Sr^{2+}, Ca^{2+}, Ba^{2+}, Pb^{2+}. Their synthesis and the techniques subsequently used to verify their structure and quality are described.

2.1 Materials' Preparation

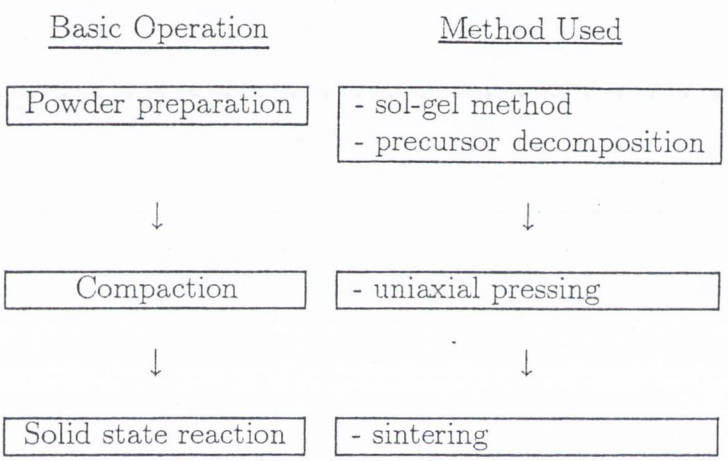

Figure 2.1 The three basic operations in the preparation of ceramic manganites

The sixteen polycrystalline mangnaites intended for study, were prepared using the standard ceramic technique [1] represented schematically in Figure 2.1. The basis of this reaction method is the interdiffusion of the reactant metal oxide powders. This necessitates the use of fine-grained powders which provide a high contact surface area for the initiation of the solid state reaction and promote a more efficient completion of the reaction by presenting shorter diffusion paths. Two different techniques were employed in order to prepare the prerequisite fine oxides - a wet chemical, citrate gel technique and a second method which involved the thermal decomposition of precursors. The reactant powders were well mixed and compacted by dry-pressing in stainless steel dies. The resulting pellets were calcined in air and then repeatedly ground, compacted and sintered until a uniform, single phase was achieved, as determined by X-ray diffraction [section 2.3].

Despite the attractive simplicity of this recipe, an inherent problem of the standard ceramic method is the realisation of nominal oxygen stoichiometry. The influence of the preparative conditions chosen on the composition, stoichiometry and defect structure of the samples is discussed.

2.1.1 Powder preparation

Successful ceramics fabrication demands high quality reactant powders. The ideal powder is highly pure and stoichiometric, consisting of spheroidal, small-sized (submicron) particles with a narrow size distribution [1], believed to facilitate homogeneous dispersion and lead to highly dense (i.e. less porous) powder compacts [2]. The resulting densely packed particles minimize pore volume, thus promoting pore elimination, and present a high contact surface area which facilitates the solid state reaction. furthermore, . To this end, two powder preparation methods were investigated and developed: a citrate gel "sol-gel" process and a "precursor decomposition" powder preparation method.

2.1.1.1 (i) Sol-gel method

Broadly defined as a process involving the transition of a colloidal suspension of solid particles in a liquid, known as a "sol" into an amorphous, two-component "gel" of semi-solid nature, the "sol-gel" method is a versatile technique for producing fine ceramic powders and glass materials. This process of homogeneous powder preparation was first popularized within the ceramics community in the 1950s by Roy [3] and its applications have subsequently evolved to include methods of producing thin film coatings, ceramic fibres, microporous inorganic membranes, monolithic ceramics and glasses, and highly porous aerogel materials [4].

A typical sol-gel route starts with the preparation of a sol from inorganic metal salts or more commonly, metal alkoxides. Following hydrolysis and addition of a suitable catalyst, these precursors polymerize in a condensation reaction, thus forming the sol. Subsequent processing yields the semi-solid gel phase. The precise processing route determines the nature of the ceramic end-product. For the purpose of producing monodisperse, small-sized powder particles, the basic principle of the procedure requires the dispersion of an aqueous sol in a hydrophobic organic liquid so that the sol forms small spherical droplets which subsequently gel upon heating. An overview of some possible processes is presented schematically in Figure 2.2 whereas a comprehensive, coherent review of sol-gel science is offered by Brinker and Scherrer [5] [1].

[1] *metal alkoxides are metal-organic compounds which have an organic ligand attached to a metal or metalloid atom

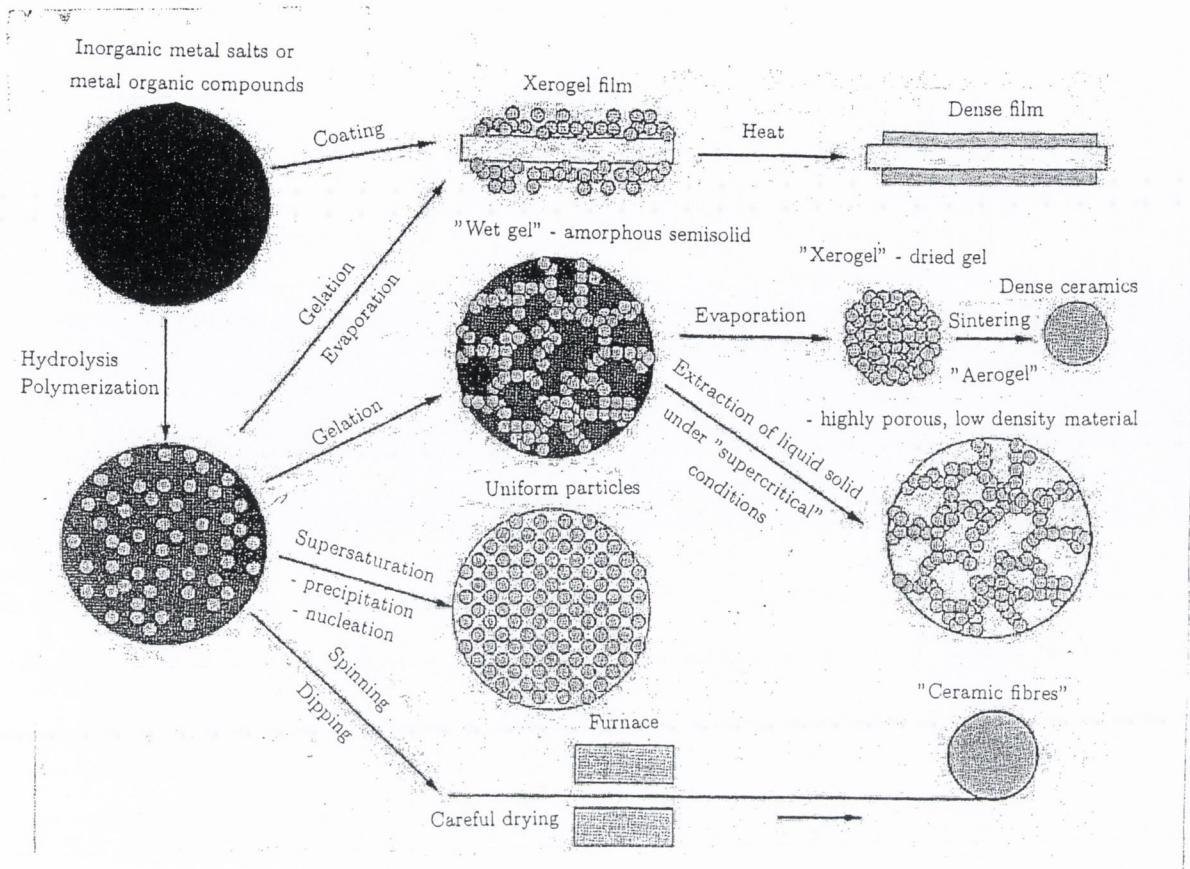

Figure 2.2 General overview of possible sol-gel processing routes.

The preparation of ceramic materials by the sol-gel technique has not been widely favored by the manganite community. It is a complex science, the fundamental principles of which incorporate disparate aspects of physics (e.g. fractal geometry and percolation theory), chemistry (mechanisms of hydrolysis and condensation) and ceramic science (sintering and structural relaxation). It is a messy process, often involving noxious chemicals and by-products. Of the few reported cases in the literature, the earliest example is given by Jonker in 1950 [6] whereby solutions of metal nitrates were dissolved in a solution of ammonia, with the addition of ammonium carbonate and hydrogen peroxide as chelating agents (see figure 2.3). Upon heating, the strongly basic solution served to hydrolyze the complexes formed between the metal cations and chelating agents, yielding metal oxides.

The method adopted during the course of this research was based on a citrate gel method originally patented by Pechini [7] for making multi-component powders containing oxides of titanium, niobium or zirconium. The process was subsequently developed to make stoichiometric powders of barium titanate, yttrium-doped zirconia and La_2NiO_4[8] before its successful deployment in the preparation of manganites by Ibarra [9] and Hervieu [10].

Stoichiometric amounts of the appropriate metal carbonates were dissolved in concentrated nitric acid resulting in a light yellow solution of metal nitrates. Ethylene glycol, a polyhydroxy alcohol, and a chelating agent, citric acid, were

added to the solution in the ratio 4g acid to 1ml alcohol and 1g metal nitrates, resulting in a yellow coloured sol. Metal complexes were formed in a complicated chelation reaction which involved the coordination of organic ligands to the metal cations, via loose bonds formed by the lone pairs of the oxygen anion. This is illustrated schematically in Figure 2.3 below. Heating the sol to $400°C$ evaporated any excess acidic solvent and water by-product, and promoted the decomposition of the chelated metal complexes, yielding a yellow-brown gel. Further heating to $600°C$ caused the thermal decomposition of the amorphous gel leading to the crystallization of a highly-porous, homogeneous oxide powder, which was later compacted and sintered.

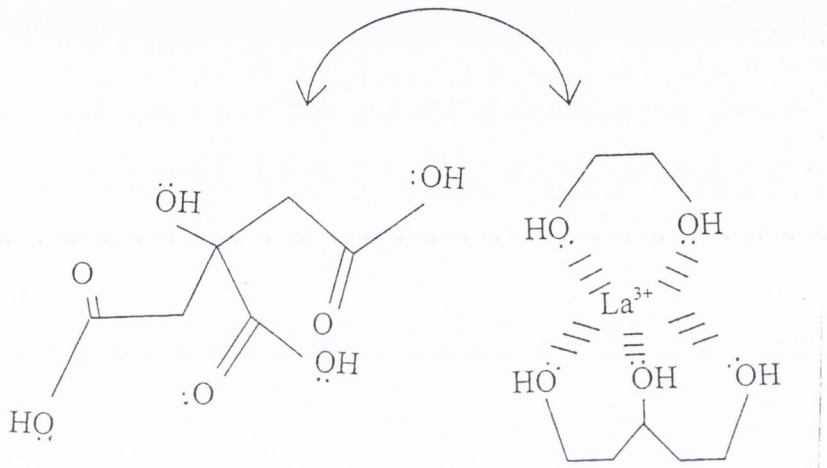

Figure 2.3 Chelation - the coordination of a central metal cation between the organic ligands of a single molecule.

The citrate gel technique described, was used to prepare three of the sixteen samples, $(La_{0.7}Sr_{0.3})MnO_3$, $(Sm_{0.7}Sr_{0.3})MnO_3$ and $(Nd_{0.7}Sr_{0.3})MnO_3$. Subsequent X-ray diffraction (see section 2.3) determined that of these, only the Nd compound had been successfully produced as a single-phase. The failure of the process for the preceeding samples was ascribed to the loss of material which occurred during the initial heating stage. Further characterisation of this Nd compound through scanning electron microscopy (see subsection 2.2.2), compared unfavourably with the samples produced through the "precursor decomposition" method (see next subsection) These results, combined with the hazardous nature of the gaseous by-products and general practical inconvenience of this method influenced the decision to continue sample preparation using the alternative technique outlined below.

2.1.1.2 (ii) Precursor decomposition

This method of powder preparation involves precursor materials in which reactants are present in the required stoichiometry; upon initial heating- calcining - thermal decomposition occurs, yielding finely-divided, reactive metal oxides. The precursors used, as listed in Table 2.1, were mixed in the correct ratios in a pestle and mortar and calcined at $900°C$. The purity of all the reagents used was greater that 99.99% in each case. With the exception of lanthanum

oxalate, hydrophilic compounds were avoided due to possible ambiguity regarding their H_2O content.

CATION	PRECURSOR	
	Name	Chemical formula
La^{3+}	lanthanum oxalate	$La_2(C_2O_4)_3.9H_2O$
Pr^{3+}	praesodynimum sesquioxide	Pr_6O_{11}
Nd^{3+}	neodymium sesquioxide	Nd_2O_3
Sm^{3+}	samarium sesquioxide	Sm_2O_3
Sr^{2+}	strontium carbonate	$SrCO_3$
Ca^{2+}	calcium carbonate	$CaCO_3$
Ba^{2+}	barium carbonate	$BaCO_3$
Pb^{2+}	lead (II) oxide	PbO
$Mn^{3+/4+}$	mangnanese (II) carbonate	$MnCO_3$

Table 2.1 The metal cations and the precursor compounds from which they were derived.

2.1.2 Compaction

Prior to sintering, the powder is compacted into a "green-body" to achieve a high-density particle packing and thus, a high contact surface area and small porosity. During the subsequent sintering procedure, these aspects facilitate the elimination of pores through the diffusion of the material. The simplest compaction technique is uniaxial pressing. Using this method, hardened stainless steel dies and a hydraulic bench-top press, uniaxial pressures up to a maximum of 1 GPa were applied to the dry powder, to produce compacts of diameter 5mm, 8mm and 13mm. A pressure sensor consisting of a strain gauge with a 4 - 20 mA output was connected to the oil output of the "Buehler" sample press and the pressure recorded using a meter with inbuilt power supply and zero balance configuration. An inherent problem of this technique is that the friction between the powder and the die walls produces an inhomogeneous flow of particles, resulting in local variations in pressure and density within the compact. Although the addition of a few drops of alcohol prior of pressing eased particle flow, the separation of top layers of the pellets after pressing - "capping"- was observed on numerous occasions; evidence of pressure density gradients. To eradicate the problem, the die's walls were sprayed with a "Buehler"silicon-based lubricant, which evaporated on heating, leaving no discernible residue.

2.1.3 Sintering

Sintering, in this context, requires heating a compacted powder greenbody for a given time at a sufficiently high temperature to promote diffusion, without exceeding the melting point of the constituent components. The ideal end-product is a fully dense material, resulting from the elimination of porosity. Several sintering mechanisms are possible, depending on the phases present.

During the solid-state sintering method used, the materials were in the solid phase throughout the process.

Solid-state sintering is a process of densification, driven by the reduction in the surface free energy of the powder. This energy is partially transformed into the interfacial energy of the grain boundaries in the resulting polycrystalline aggregate. The role of surfaces and interfaces is not only pivotal in determining the macroscopic driving force, but also the microscopic diffusion mechanism. Although the microstructure continuously evolves during sintering, the process has been conceptually divided into three stages, as described diagrammatically in Figure 2.4 below.

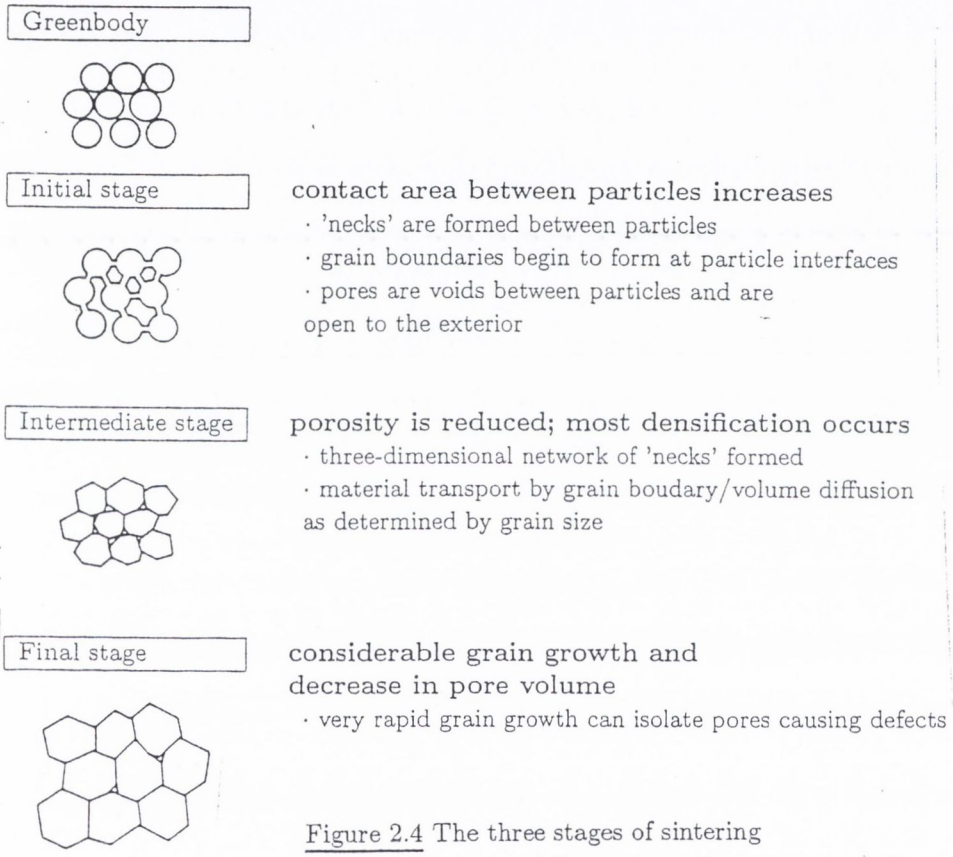

Figure 2.4 The three stages of sintering

With the exception of the Pb^{2+}containing compounds, the manganite ceramics were all sintered repeatedly at $1200°C$ in unsealed MgO vessels. Due to the high volatility of lead ($T_{melting}$ of $PbO = 888°C$) the $(La_{0.7}Pb_{0.3})MnO_3$, $(Pr_{0.7}Pb_{0.3})MnO_3$, $(Nd_{0.7}Pb_{0.3})MnO_3$ and $(Sm_{0.7}Pb_{0.3})MnO_3$ greenbodies were sealed in platinum foil prior to calcination at $600°C$ and during subsequent repeated sintering at $1200°C$. The manual re-grinding of the compacts in a pestle and mortar, followed by compaction and sintering was repeated until a single phase, as determined by X-ray diffraction (2.3) was achieved for each compound.

2.1.4 Non-stoichiometry and sublattice vacancies

The conditions used during the preparation of manganese oxides determine the composition, stoichiometry and defect structures of the samples produced. Not surprisingly therefore, this has been the topic of intense study [11] [12] [13] with a particular focus on the extended homogeneity range and physical properties exhibited by the end-member $LaMnO_{3+\delta}$ [14], as discussed in chapter 6. However, the influence of preparation conditions on the full range of substituted manganites, is illustrated by the forest of transition temperatures compiled from the literature for $(La_{1-x}Ca_x)MnO_{3+\delta}$ and $(La_{1-x}Sr_x)MnO_{3+\delta}$ where $0 \leq x \leq 1$ [15].

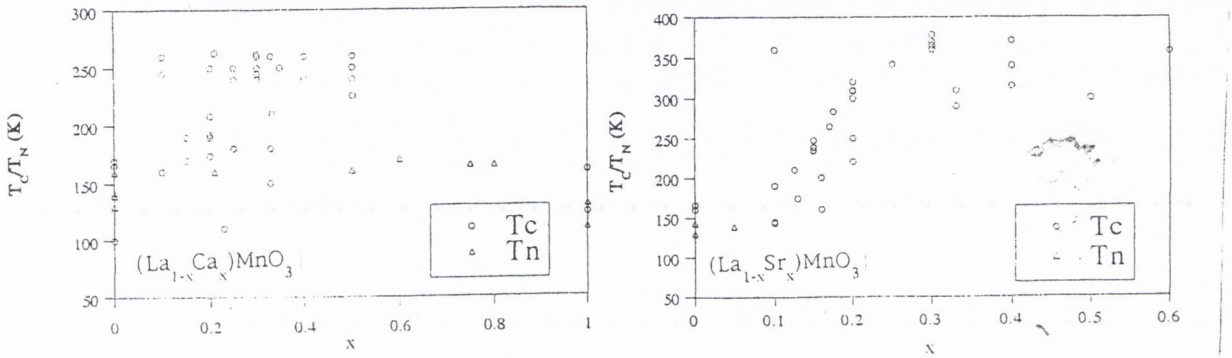

Figure 2.5 Data compiled from published literature for $(La_{1-x}Ca_x)MnO_{3+\delta}$ and $(La_{1-x}Sr_x)MnO_{3+\delta}$ polycrystalline ceramics, thin films and single crystals.

The authoritative work of Kuo [12] established a phase diagram for the equilibrium oxygen content of both $LaMnO_{3+\delta}$ and $(La_{1-x}Sr_x)MnO_{3+\delta}$ as a function of sintering temperature and oxygen pressure. It concludes that when fired at $1200°C$, $LaMnO_3$ forms stoichiometrically for an oxygen pressure of 10^{-5} Pa$<P_{O_2}<1$ Pa. Since the oxygen partial pressure in the ambient atmosphere at this temperature is 2 x 10^4 Pa, the oxide produced is slightly oxygen-rich; δ =0.06. However, the subsititution of lanthanum by a divalent cation shifts the equilibrium to higher oxygen pressures. Therefore, sintering the compounds with composition $x = 0.3$ in air at $1200°C$ is likely to yield fully-oxygenated material with only a slight tendency towards over-oxygenation.

Here it should be noted that despite the conventional reference to the "oxygen-excess" of the nominal compositions, structural studies of neutron diffraction data have established that instead of incorporating oxygen interstitials into the close-packed perovskite structure, the defects take the form of Mn and/or A-site cation vacancies. [11] [16] [17]. Thus, the formula of the over-oxygenated end-member is more accurately written $(LaMn)_{1-\delta}O_3$. These studies concluded that the defect chemistry of this compound was best described by randomly distributed La and Mn vacancies, present in equal amounts, so that the crystallographic formula could be written as

$$(La^{3+}_{1-\delta}\square_\delta)(Mn^{3+}_{1-7\delta}Mn^{4+}_{6\delta}\square_\delta)O_3 \qquad (1)$$

However, recent investigations using neutron diffraction, thermal analysis and chemical titration [13], have shown definitively that the proportion of $Mn^{3+/4+}$ vacancies is substantially higher than those on the A-site, especially when samples are sintered under more oxidizing conditions (i.e. lower temperatures and higher oxygen pressures). The presence of unwanted Mn vacancies is a possible reason why the measured saturation magnetization of the x=0.3 polycrystalline mangnanites rarely attains the full, theoretical spin-only value expected [18].

The sintering temperature determines the microstructure of the samples, which has been shown to have a striking effect on the resistance and magnetoresistance [19]. The grain sizes of polycrystalline samples sintered at higher temperatures ($1700°C$) are smaller that those fired at more moderate temperatures ($1300°C$), presenting more grain boundaries which contribute significantly to the "extrinsic" transport properties [20]; as discussed in the following chapter.

2.2 Materials' Characterization

The principal experimental tool used to verify the structure and purity of the polycrystalline powders was X-ray diffraction. [Section 2.3] X-ray flourescence (XRF) was used to establish whether the nominal stoichiometry was achieved within the bulk. The micrographs obtained from scanning electron microscopy are also included to provide an indication of the distribution of grain sizes. Both these procedures are briefly outlined and the results presented below.

2.2.1 X-ray Fluorescence (XRF)

X-ray fluorescence is a powerful spectrochemical technique for elemental analysis. Primary radiation from a X-ray tube excites atoms in the analysed specimen, resulting in the emission of lower energy "fluorescent" radiation, characteristic of the chemical elements present. The conventional spectrometer configuration [21] for the computation of intensities in $\theta - 2\theta$ geometry is illustrated in figure 2.6.

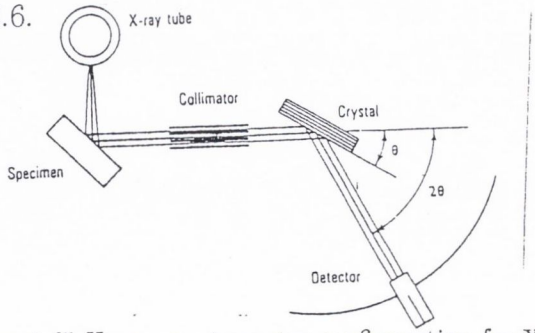

Figure 2.6 The "flat crystal" X-ray spectrometer configuration for X-ray fluorescence.

Quantitative analysis of measured XRF intensities proceeds via many different routes which can be broadly described as either "mathematical" or "comparative". The former method attempts to calculate the problematic interele-

mental effects inherent to the XRF technique[2] from first physical principles [22]. In contrast, the comparative method compensates for these effects, most commonly through comparison with the line spectra measured for external standards. For the analysis of powder oxide samples, the latter method is most appropriate, as the reliability of the theoretical calculations depend on the availability of information pertaining to particle size distribution and the distribution of elements within the particles.

Suitable samples are required to be representative of the material with a flat, smooth, homogeneous surface and to be sufficiently thick as to represent an "infintely thick" specimen to the X-rays. To these ends, 100mg of each sample studied was "wet ground" in isopropyl alcohol to increase grinding efficiency and homogenization, and mixed with a cellulose binder in a ratio 1:9. The well-mixed powders were poured into a 30 mm diameter nitrided steel die and compacted in a hydraulic press at $\sim$ 130 MPa (10 tons inch^{-2}). The external sample, for comparison, comprised unsintered precursors mixed in the correct stoichiometric ratios, and was similarly prepared.

The Link systems 860 spectrometer used was fitted with a silver anode X-ray tube and a Si(Li) detector. The accelerating voltage was 35 kV and fluorescent radiation was detected from a spot size of roughly 15 mm diameter. The preparation technique used ensured that this was not a surface measurement and that the signal from a large number of grains was representative of the bulk sample. The exposure time for each sample was normalised with respect to 200 000 counts measured for the Mn Kα peak. The superposition of different spectral lines with this peak (e.g. Nd Lα,Nd Lβ) meant that direct comparisons could only be made between the samples and their controls.

With the exception of the Pb containing samples, the nominal stoichiometry of all samples was confirmed within the resolution and error margin of the spectrometer. In figure 2.7 the spectra obtained for three representative compounds, $(Pr_{0.7}Ca_{0.3})MnO_3$, $(Nd_{0.7}Ba_{0.3})MnO_3$, $(Sm_{0.7}Sr_{0.3})MnO_3$, and their control samples are shown. The sample and control peaks are seen to virtually superimpose; the slight discrepancy reflects differences in the distribution of the sample grains within the cellulose matrix and is not attributable to non-stoichiometry.

The spectra of the lead containing samples [figure 2.7 (d)-(g)] indicate that these compounds are severly Pb deficient despite the precautions taken to prevent the evaporation of Pb during calcination and sintering. A comparison of peak heights serves as a first approximation of the samples' stoichiometry, giving: $(La_{0.7}Pb_{0.15})MnO_3$, $(Pr_{0.7}Pb_{0.07})MnO_3$, $(Nd_{0.7}Pb_{0.10})MnO_3$ and $(Sm_{0.7}Pb_{0.02})MnO_3$. Discussion of these four samples is omitted from subsequent chapters.

[2] Interelement effects can be a major source of error in the quantitative analyisis of a multicomponent sample. Since the relative fluorescence intensity R_i of an element i at concentration C_i, depends on the total composition of the specimen $R_i = f(C_i, C_j, C_k, ...C_n)$, this can lead to the enhancement of certain intensities when the radiation from another element of the specimen excites the analyte, i. More complex interelement effects, known as "third element effects" result from the combined, non-additive absoprtion-enhancement of two or more elements $(j, k...)$ on the analyte, i.

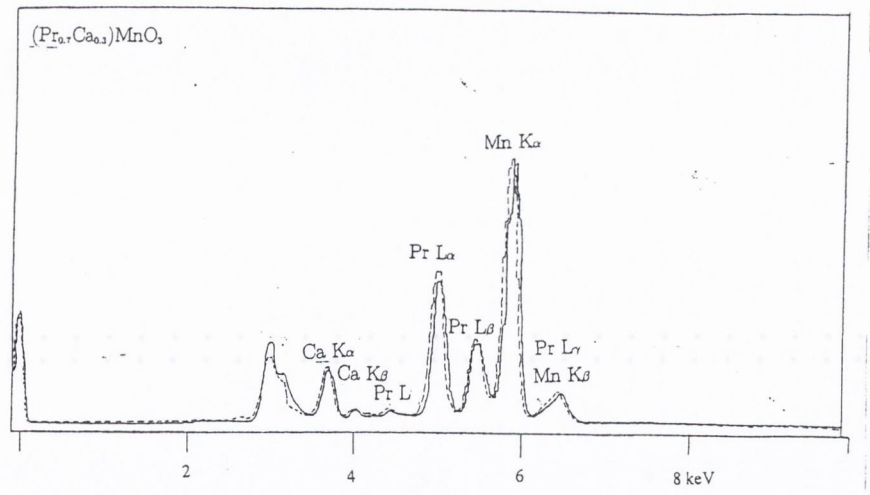
(Pr0.7Ca0.3)MnO3
Mn Kα
Pr Lα
Pr Lβ
Pr Lγ
Mn Kβ
Ca Kα
Ca Kβ
Pr L
2
4
6
8 keV

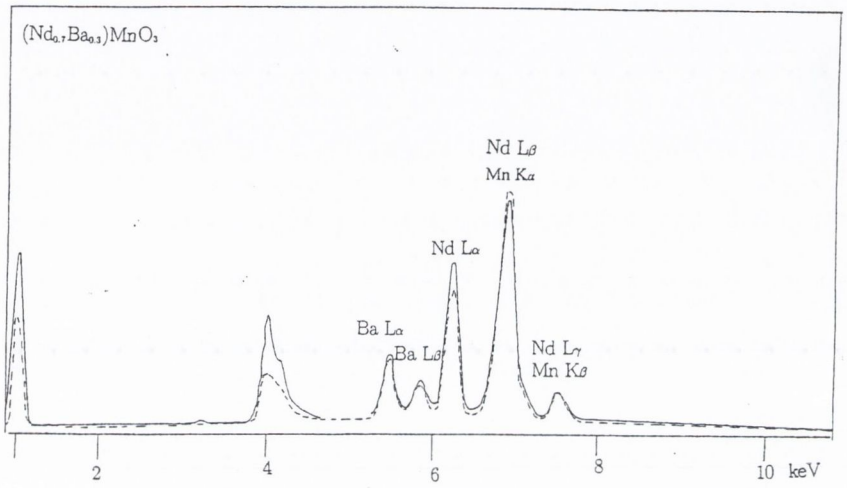
(Nd0.7Ba0.3)MnO3
Nd Lβ
Mn Kα
Nd Lα
Ba Lα
Ba Lβ
Nd Lγ
Mn Kβ
2
4
6
8
10 keV

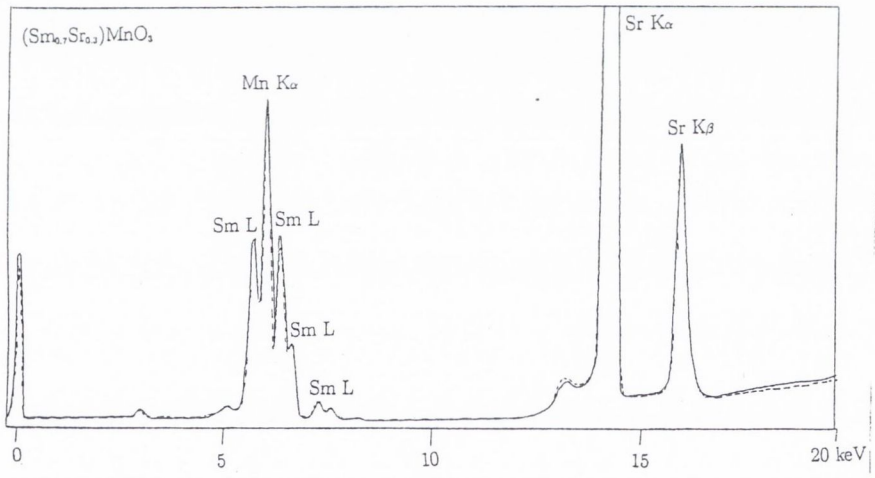
(Sm0.7Sr0.3)MnO3
Sr Kα
Mn Kα
Sr Kβ
Sm L
Sm L
Sm L
Sm L
0
5
10
15
20 keV

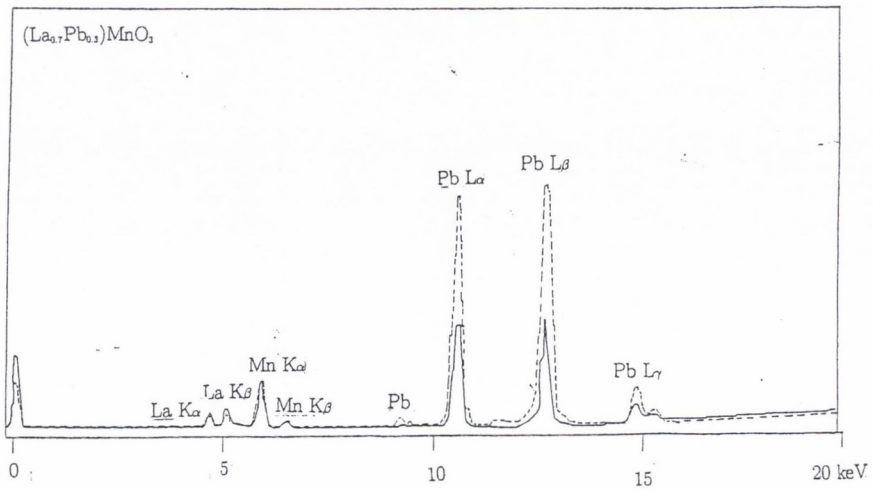
(La0.7Pb0.3)MnO3
Pb Lα
Pb Lβ
Mn Kα
La Kβ
La Kα
Mn Kβ
Pb
Pb Lγ
0
5
10
15
20 keV

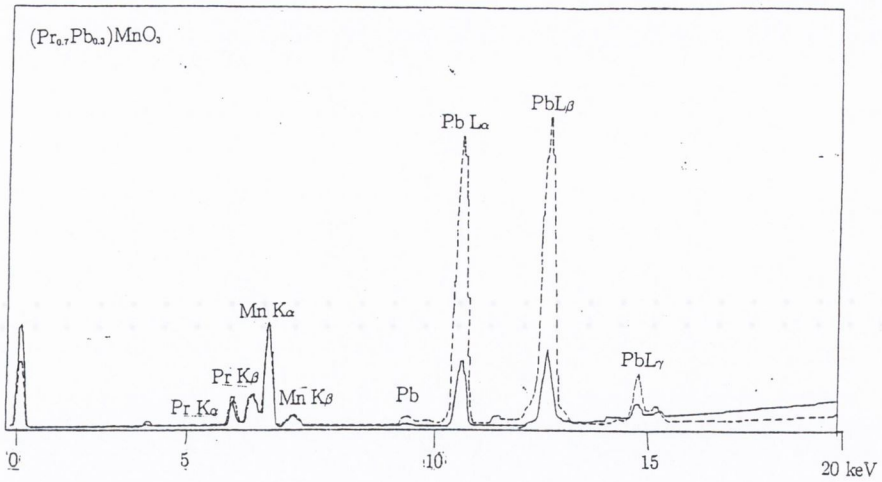

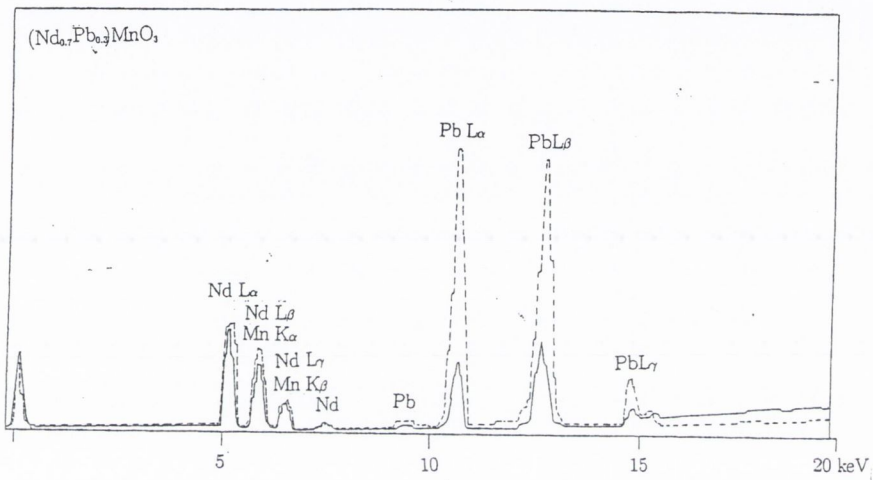

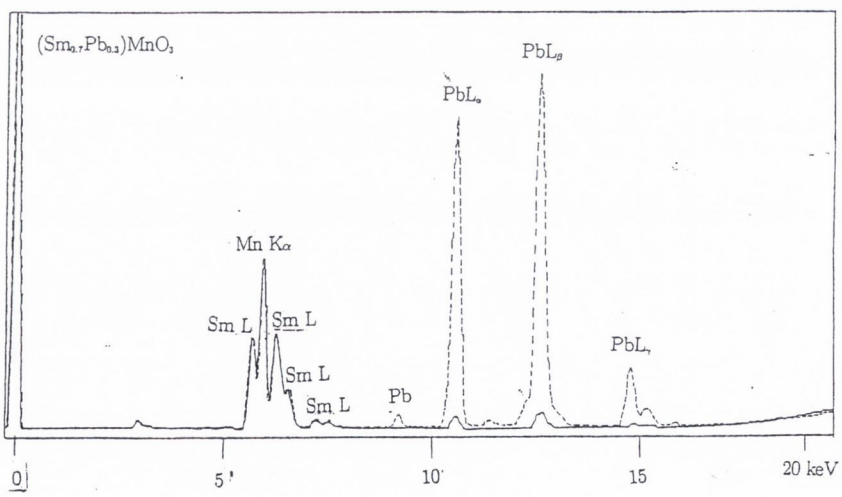

Figure 2.7 X-ray flourescence spectra for (a) $(Pr_{0.7}Ca_{0.3})MnO_3$, (b) $(Nd_{0.7}Ba_{0.3})MnO_3$, (c) $(Sm_{0.7}Sr_{0.3})MnO_3$, (d) $(La_{0.7}Pb_{0.3})MnO_3$, (e) $(Pr_{0.7}Pb_{0.3})MnO_3$, (f) $(Nd_{0.7}Pb_{0.3})MnO_3$ and (g) $(Sm_{0.7}Pb_{0.3})MnO_3$.

2.2.2 Scanning Electron Microscopy (SEM)

Scanning electron microscopy is widely used to image both microstructure and topography with an ultimate resolution of 15 Å for an high-performance instrument operating at 15 keV. A finely focussed beam of electrons is scanned across a sample surface while a detector records the number of low energy secondary electrons or backscattered electrons emitted from the surface. The morphology of the polycrystalline samples was studied using a Hitachi Field Emission S-4300 SEM incorporating a cold cathode field emission source. This electron source is typically three times brighter than conventional tungsten or thermally assisted field emission sources, enabling a resolution of 0.5 μm at an accelerating voltage of 20 kV to be achieved. The ceramic samples were sufficiently conducting at room temperature to be imaged through the detection of the backscattered electrons by a "Centaurus" scintillator. The system was fully PC controlled, with the resulting digital micrograph images produced with 1200 dpi resolution.

2.2.2.1 Results and discussion

SEM micrographs of $(La_{0.7}Ca_{0.3})MnO_3$, $(Pr_{0.7}Ca_{0.3})MnO_3$,$(Nd_{0.7}Sr_{0.3})MnO_3$ (sol-gel), $(Nd_{0.7}Ba_{0.3})MnO_3$, $(Sm_{0.7}Sr_{0.3})MnO_3$ and $(Sm_{0.7}Ba_{0.3})MnO_3$ at 500x and 2000x magnification are shown in figure 2.8 (a) - (f) below. The grain size distribution and apparent homogeneity of the samples' surface show considerable variation between the different samples; $(Sm_{0.7}Sr_{0.3})MnO_3$ exhibits the highest local homogeneity [figure (e)], whereas the $(Nd_{0.7}Sr_{0.3})MnO_3$ sample produced using the sol-gel technique is disappointingly inhomogeneous, with clusters of typical dimension 5-10 μm clearly discernible in figure (c).

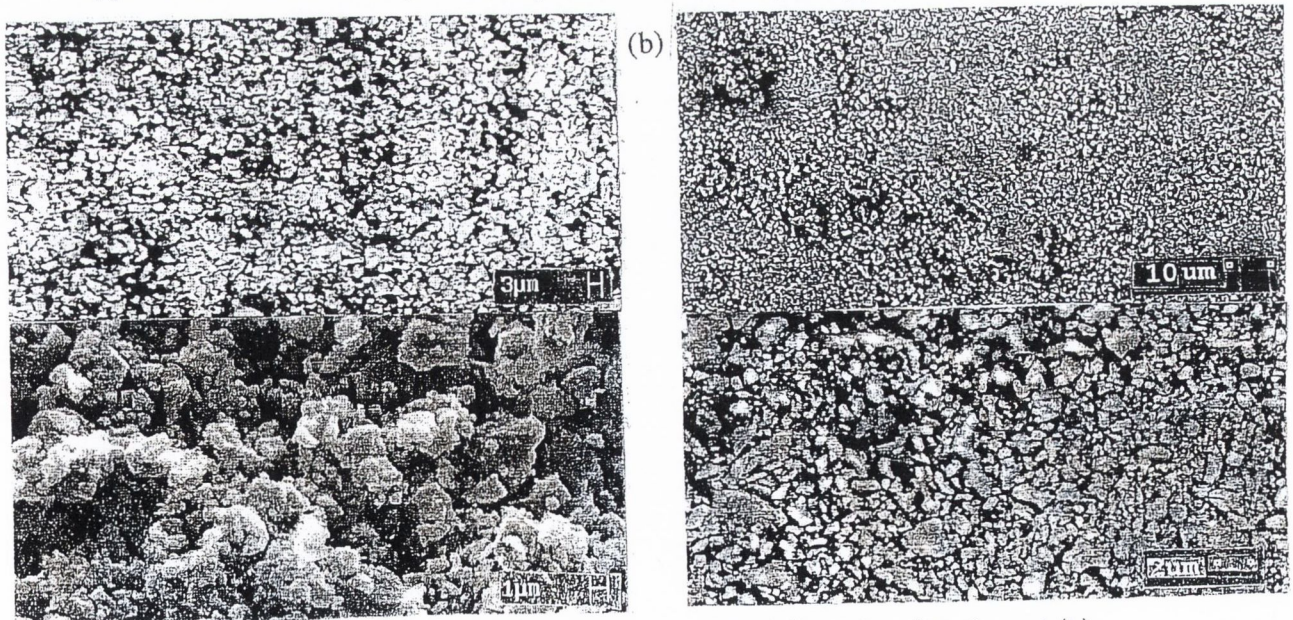

Figure 2.8 Scanning electron microscopy images of (a) $(La_{0.7}Ca_{0.3})MnO_3$ and (b) $(Pr_{0.7}Ca_{0.3})MnO_3$.

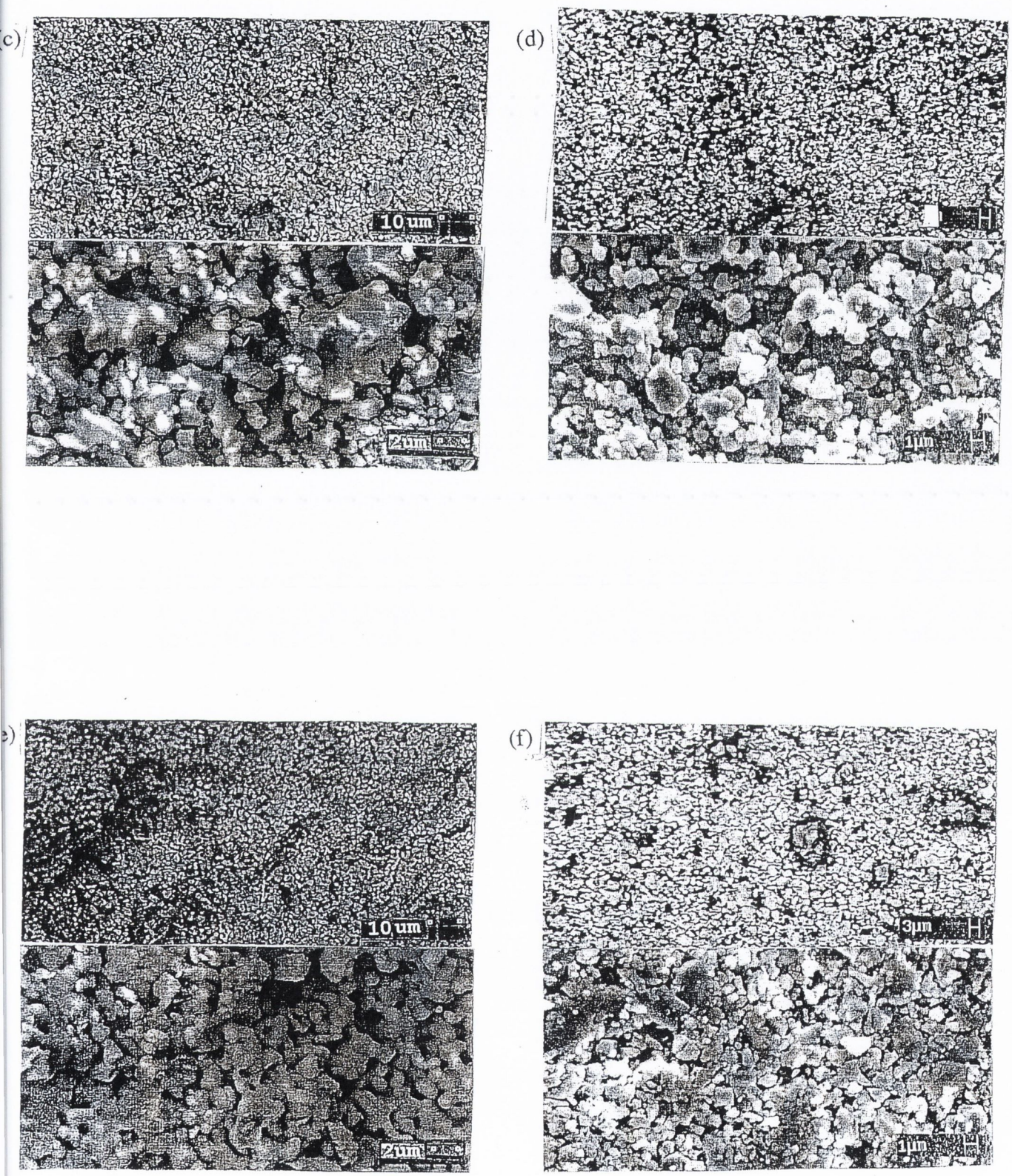

Figure 2.8 Scanning electron microscopy images of (c) $(Nd_{0.7}Sr_{0.3})MnO_3$ (sol-gel) (d) $(Nd_{0.7}Ba_{0.3})MnO_3$ (e) $(Sm_{0.7}Sr_{0.3})MnO_3$, and (f) $(Sm_{0.7}Ba_{0.3})MnO_3$.

2.3 Structural Characterization

2.3.1 X-ray diffraction

2.3.1.1 Experimental arrangement

The standard laboratory method for the determination of crystallographic structure is X-ray diffraction. The X-ray diffractometer used was a Siemens D500 with copper K_α radiation ($\lambda = 1.542$ Å) mounted with a graphite monochromator. Powder samples were mounted on glass slides using double-sided adhesive tape and measured in the $\theta - 2\theta$ geometry. The beam path of the diffractometer for this operating mode is shown in figure 2.9. All samples were measured in the range $2\theta = 20° - 70°$ by using the step scanning technique with a step size of 0.05° and a measurement time of 2 seconds/step. Control and data storage was performed by a "Microvax" system, using standard Siemens software packages. Bragg reflections were indexed using the "Index2" programme and the lattice parameters were refined by profile fitting these principal lattice reflections using a "Celref" least-squares refinement programme.

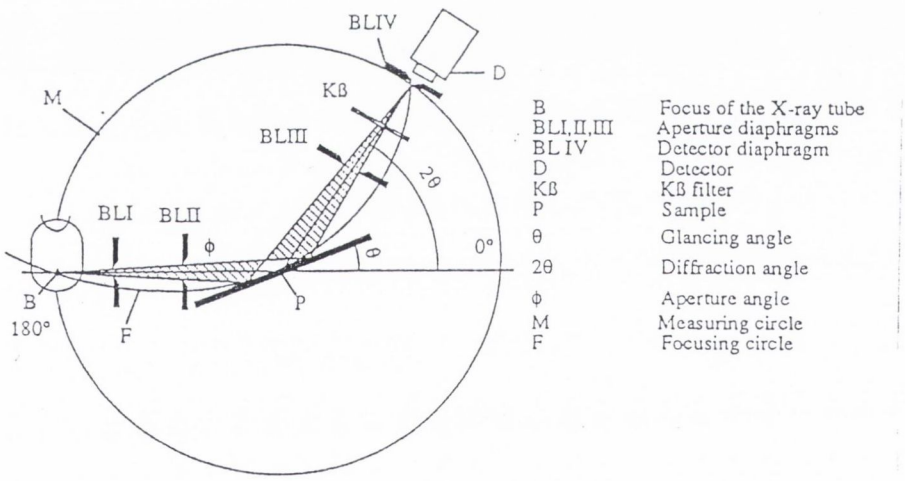

Figure 2.9 Schematic diagram of X-ray beam path for operation in $2\theta - \theta$ geometry.

2.3.1.2 Results

The powder X-ray diffraction spectra of all sixteen samples are presented in the following figure 2.10.

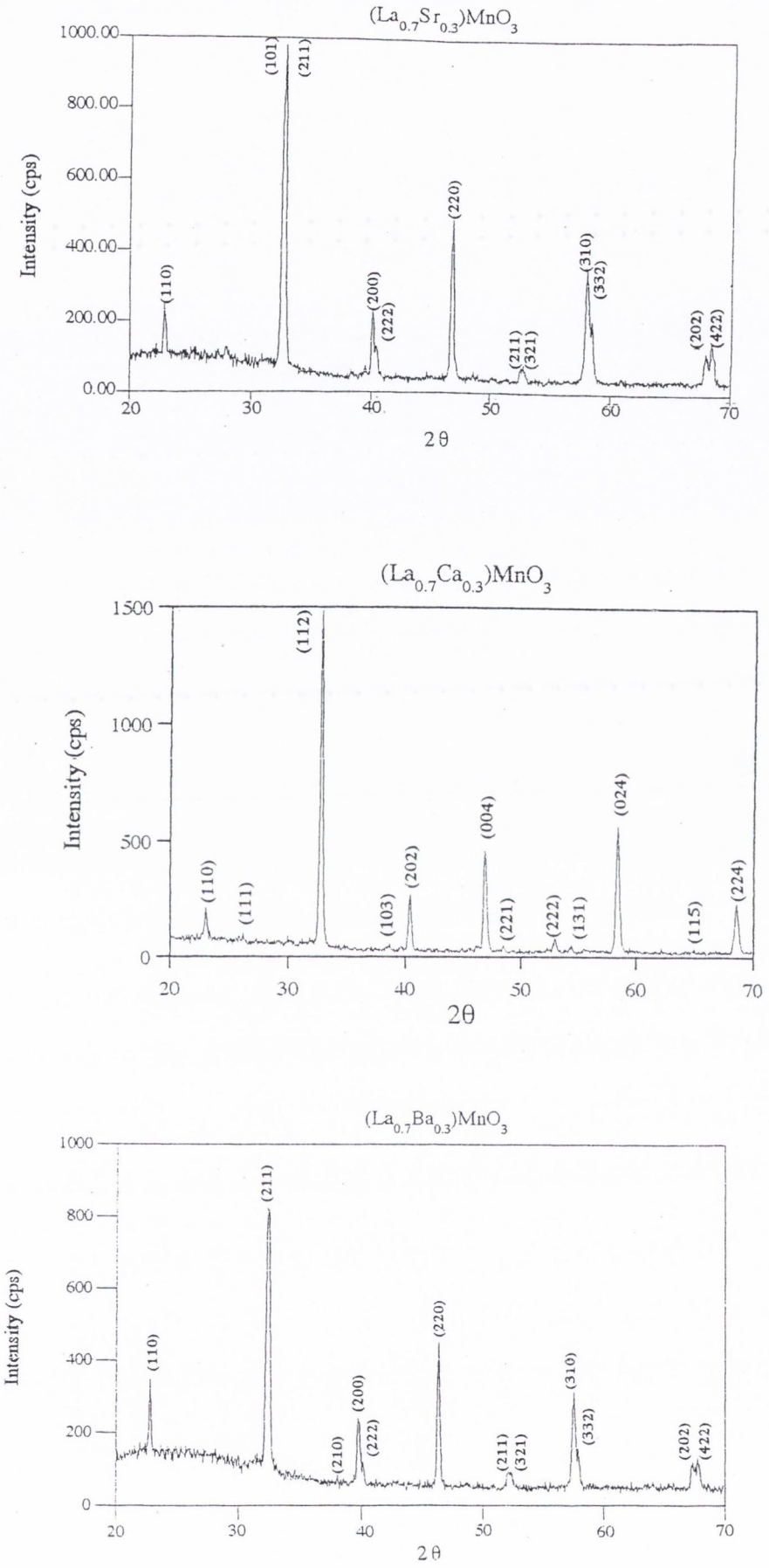

Figure 2.10 The X-ray diffraction spectra of $(La_{0.7}A_{0.3})MnO_3$, A = Sr, Ca, Ba.

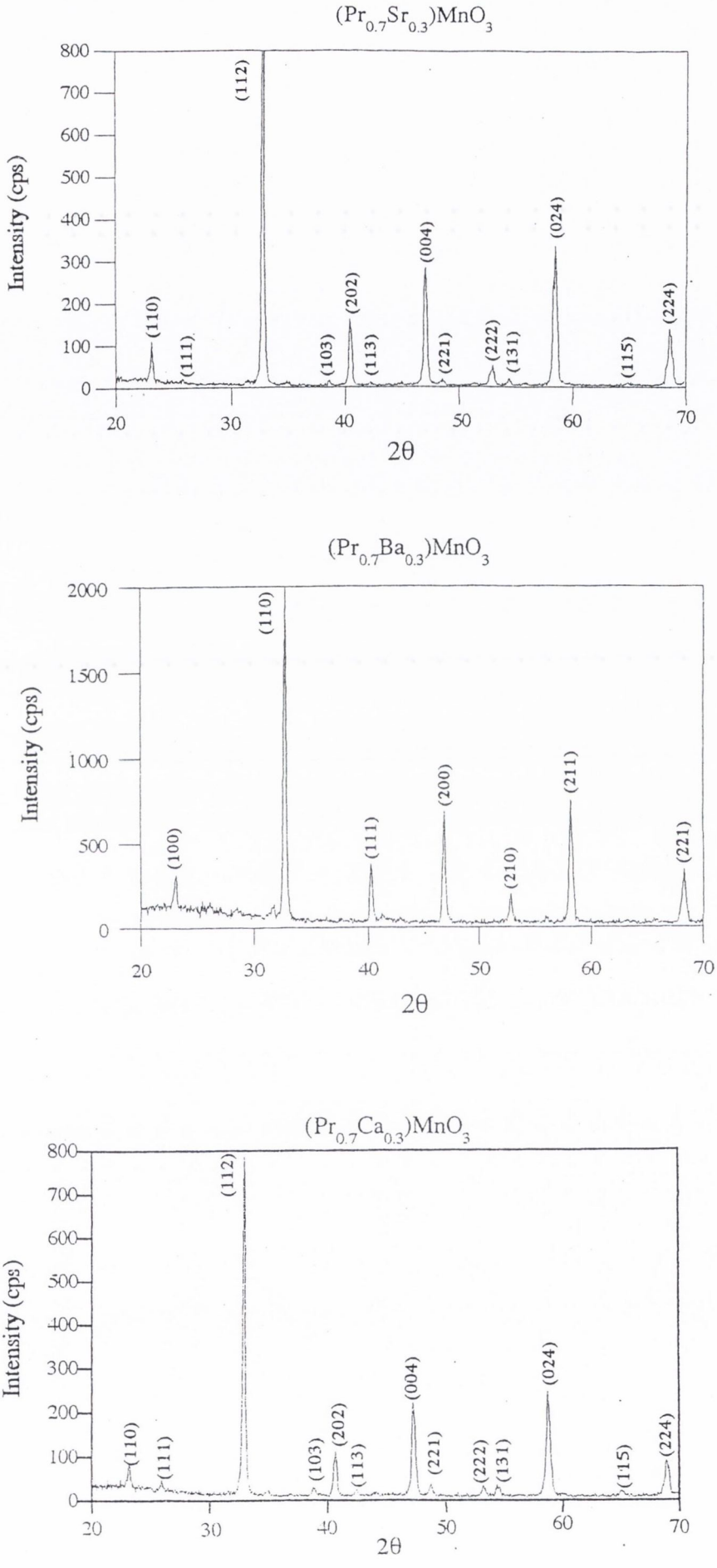

Figure 2.10 The X-ray diffraction spectra of $(Pr_{0.7}A_{0.3})MnO_3$, A = Sr, Ca, Ba.

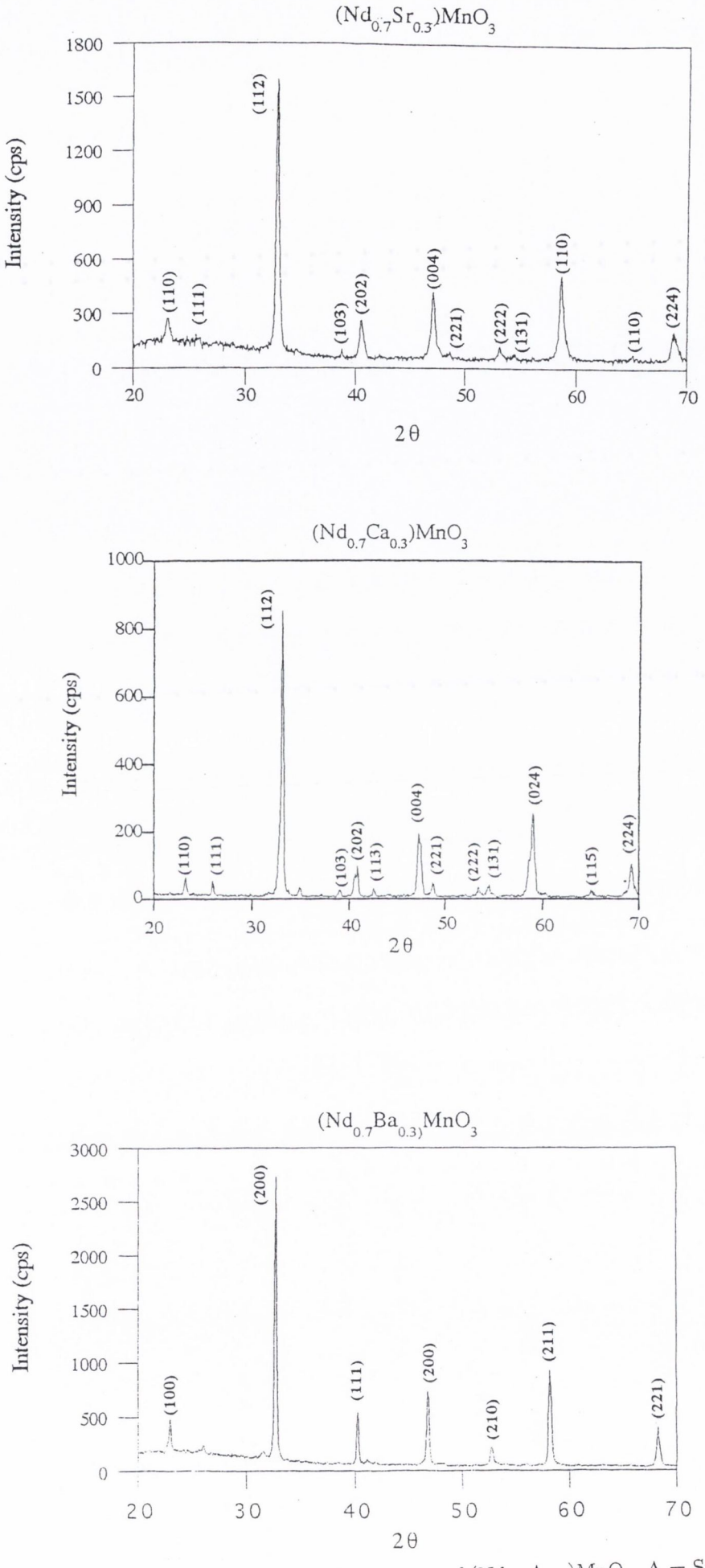

Figure 2.10 The X-ray diffraction spectra of $(Nd_{0.7}A_{0.3})MnO_3$, A = Sr, Ca, Ba.

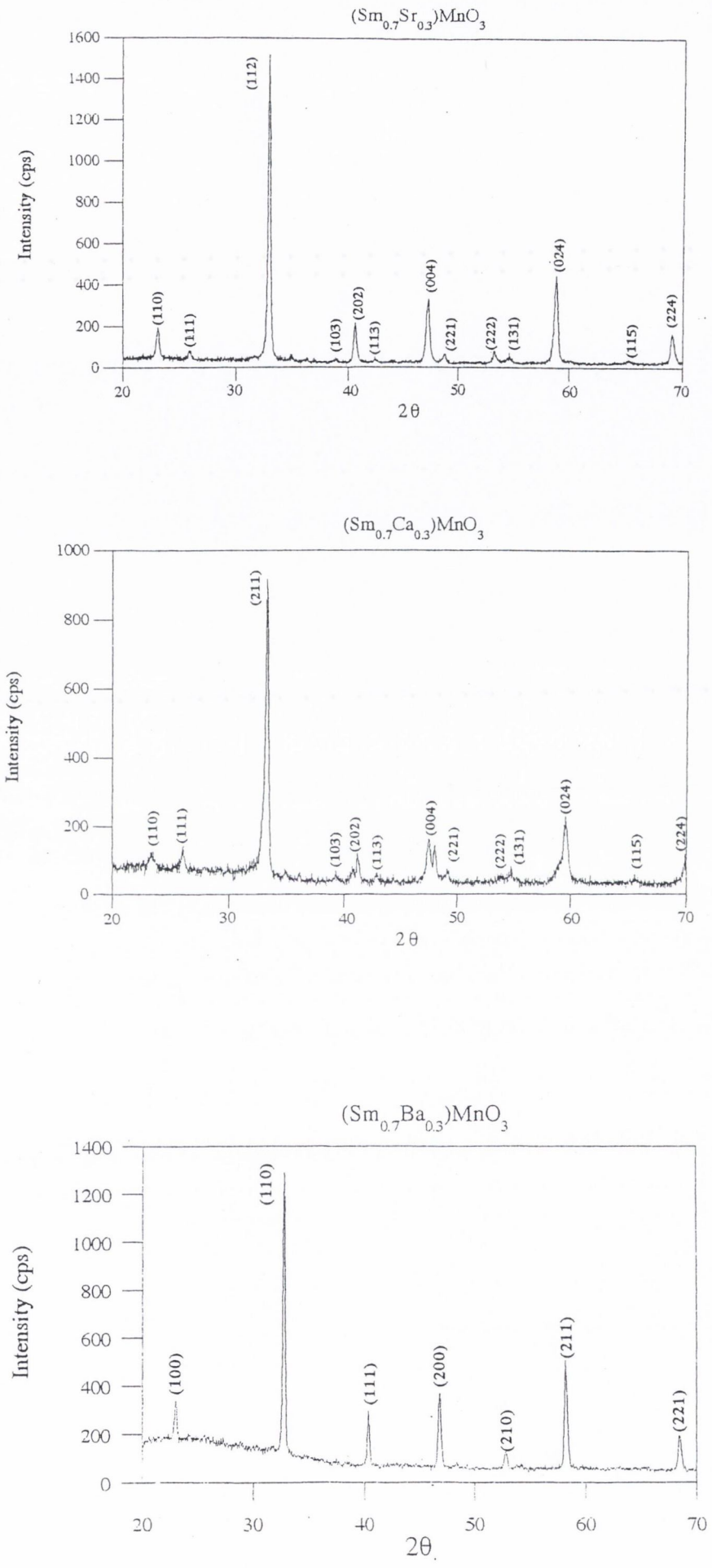

Figure 2.10 The X-ray diffraction spectra of $(Sm_{0.7}A_{0.3})MnO_3$, A = Sr, Ca, Ba.

Besides the ideal cubic perovskite structure introduced in Figure 1.1 (space group $Fm3m$), rhombohedral ($R\bar{3}c$) and orthorhombic($Pbnm$) distorted perovskites were also identified, isomorphous with $LaAlO_3$ [23] and $GdFeO_3$ [24] respectively. Table 2.2 summarizes the crystal structures and lattice parameters deduced for all sixteen samples.

Compound	Space group	Lattice parameters/Å
$(La_{0.7}Sr_{0.3})MnO_3$	R$\bar{3}$c	a = 5.490; $\gamma = 60.43°$
$(La_{0.7}Ca_{0.3})MnO_3$	Pbnm	a = 5.453, b = 5.499, c = 7.705
$(La_{0.7}Ba_{0.3})MnO_3$	R$\bar{3}$c	a = 5.537; $\gamma = 60.43°$
$(Pr_{0.7}Sr_{0.3})MnO_3$	Pbnm	a = 5.486, b = 5.467, c = 7.713
$(Pr_{0.7}Ca_{0.3})MnO_3$	Pbnm	a = 5.426, b = 5.478, c = 7.680
$(Pr_{0.7}Ba_{0.3})MnO_3$	Fm3m	a = 3.888
$(Nd_{0.7}Sr_{0.3})MnO_3$	Pbnm	a = 5.458, b = 5.430, c = 7.701
$(Nd_{0.7}Ca_{0.3})MnO_3$	Pbnm	a = 5.395, b = 5.431, c = 7.660
$(Nd_{0.7}Ba_{0.3})MnO_3$	Fm3m	a = 3.894
$(Nd_{0.7}Pb_{0.3})MnO_3$	Fm3m	a = 3.873
$(Sm_{0.7}Sr_{0.3})MnO_3$	Pbnm	a = 5.427, b = 5.415, c = 7.659
$(Sm_{0.7}Ca_{0.3})MnO_3$	Pbnm	a = 5.767, b = 5.347, c = 7.562
$(Sm_{0.7}Ba_{0.3})MnO_3$	Fm3m	a = 3.886

Table 2.2 Crystal structures and lattice parameters

2.3.2 Crystal structure

As illustrated in table 2.2, the ideal cubic perovskite structure as typified by $CaTiO_3$ (Figure 1.1) is rarely attained by the manganites. The misfit of the ionic radii causes the displacement of the ions from their ideal positions which results in the distorted structures observed. The "pseudocubic" lattice parameters, a_C, given in table 2.3 below, correspond to the elementary cubic cell from which these rhombohedral and orthorhombic perovskite structures are derived.

The most common distortion in perovskite systems [25] is due to the slight rotation of the oxygen octahedron about the (111) axis of the elementary cube, resulting in rhombohedral symmetry (space group R$\bar{3}$c). The cubic unit cell (lattice parameter, a_0) is effectively doubled, the lattice parameter, $a \approx \sqrt{2}a_0$ and the rhombohedral angle, α, is close to the ideal value, 60°. The oxygen displacements from their face-centred positions are shown in figure 2.11 (a), in accordance with neutron scattering studies on a $(La_{0.7}Sr_{0.3})MnO_3$ single crystal [26].

The cubic cell accommodates even greater cation size misfit through the buckling of the oxygen octahedra, in an effective cooperative rotation about the 110 axis. The resulting orthorhombic cell (space group $Pbnm$), as typified by the strucure of $GdFeO_3$ in figure 2.11 (b) , contains four cubic unit cells and the Mn-O-Mn bond angle is reduced from 180° to 161°.

A schematic illustration of the relation between all the unit cells described, is given in figure 2.12.

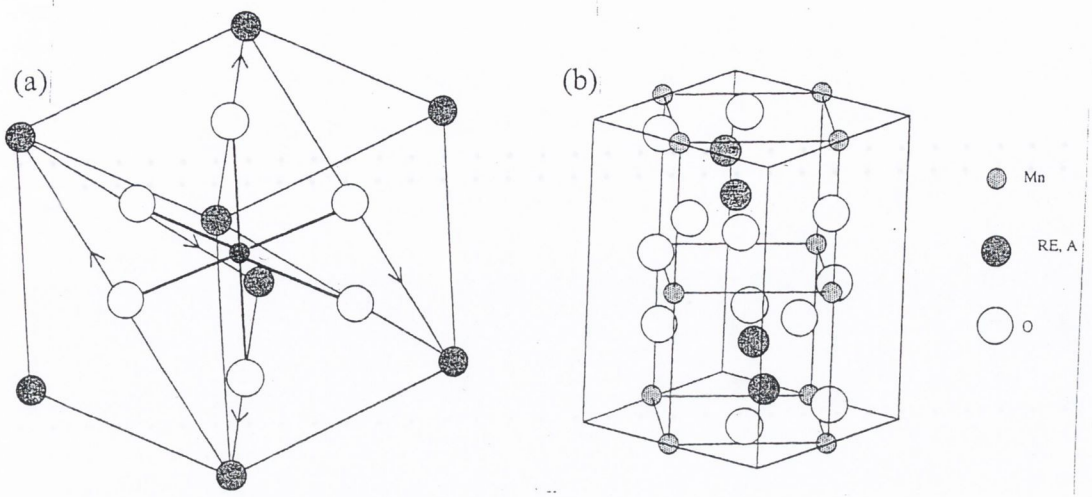

Figure 2.11 (a) A schematic illustration showing how the oxygen ions are displaced from their face-centred positions in the rhombohedral ($R\bar{3}c$) slightly distorted perovskite unit cell; (b) The orhorhombic ($Pbnm$) $GdFeO_3$ cell.

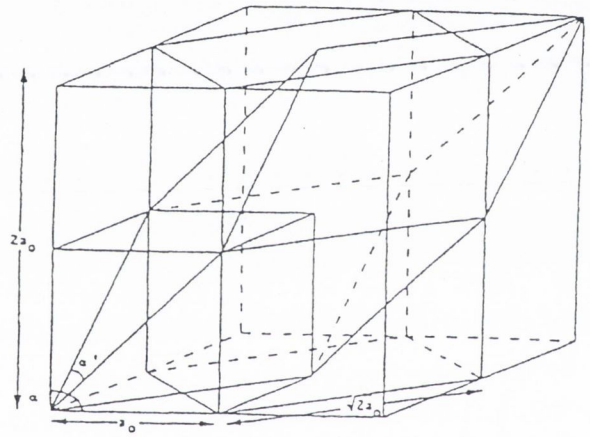

Figure 2.12 A schematic diagram of the relationship between the cubic, rhombohedral, hexagonal and orthorhombic unit cells characteristic of the twelve manganite samples studied.

Simple geometry gives the ideal A and B site cation radii - r_A and r_B - of the undistorted cubic perovskite cell, relative to the O^{2-} anion radius, r_O. Goldschmidt [27] first defined this relation as a *tolerance factor,*

$$t_o = \frac{(r_A + r_O)}{\sqrt{2}(r_B + r_O)} \tag{2}$$

which equals unity for the ideally sized ions of the perfect cubic structure. Deviation from this value, is thus a measure of the lattice distortion, and from a set of radii based on $r_O = 1.32$ Å, [27] Goldschmidt determined the limits for the stable formation of the perovskite structure in oxides as $0.8 < t_0 < 1$. These values differ slightly if different ionic radii conventions are adopted. In an apparent consensus reached in recent literature,[28], [29] [30] the effective ionic radii used are those given by Shannon [31], where the cationic radii are for ions in nine-fold coordination sites based on the O^{2-} radius, $r_O^{VI}(O^{2-}) = 1.40$ Å. In table 2.3, the values calculated in accordance with this convention are denoted as t'.

However, in numerous neutron diffraction studies on perovskites of formula $(A_{0.7}A'_{0.3})MnO_3$ [28],[32], [26], [33], the Mn-O bond length has been measured as 1.96 Å. This value is in perfect agreement with $(<r_B> + r_O)$ when the average weighted B-site radius is calculated using Shannon's effective ionic radii for $Mn^{3+/4+}$ in six-fold oxygen coordination sites and $r_O^{VI}(O^{2-}) = 1.40$ Å. In this basis, $r_A = 1.372$ Å; a value which may be obtained by using radii for A-site cations in twelve-fold oxygen coordination sites. Except in the case of extreme buckling of the MnO_6 octahedra [34], these coordination numbers are supported by the symmetry of the cubic perovskite structure and were used to calculate the tolerance factors, t_0 in table 2.3.

In figure 2.12 the pseudocubic lattice parameter a_C is plotted as a function of t_0. The linear relation shows the increasing deviation of the perovskite structure from the ideal cubic cell with $a_0 \approx 0.39$ Å, as t_0 varies from unity. The symmetry of the compounds is indicated in the figure by the use of different symbols.

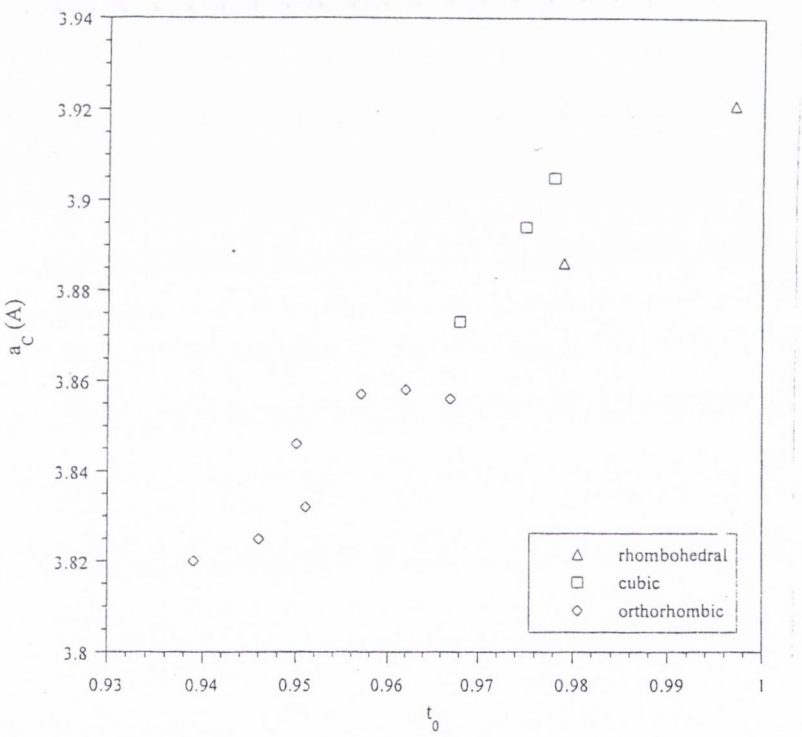

Figure 2.12 The "pseudocubic" lattice parameter, a_C plotted as a function of tolerance factor, t_0 for all twelve samples.

Listed in table 2.3 are the *weighted average ionic radii of the A-site cations* $<r_A>$ (calculated for ions in twelve-fold oxygen coordination sites), which are obviously proportional to t_0. Since these are both averaged values, no account is made of the random distribution of different sized A^{3+} and A'^{2+} cations throughout the lattice. A quantitative measure of this is provided by the *variance of the A site cation radius distribution,* σ^2. Defined as the average

of the squares of the differences from the mean of the ionic radii r_i about the mean $<r_A>$,

$$\sigma^2 = \sum y_i r_i^2 - < r_A > \tag{3}$$

where y_i is the fractional occupancy of the A site for two or more species. ($\sum y_i = 1$). The strong correlation of these structural parameters with the manganites' transport and magnetic properties is addressed in 4.1.4.

The last columns of table 2.3 compare the samples' theoretical X-ray density with that measured on fully sintered material. The densities were calculated using the lattice parameters listed in table 2.2, assuming that the orhorhombic unit cells equate to four cubic unit cells ($Z = 4$) and the rhombohedral cells correspond to the doubling of the primary cubic cell ($Z = 2$). The measured densities are seen to vary between 60% and 72% of the theoretical values.

Compound	Structure	a_C/Å	t_0	t'	$<r_A>$/Å	σ^2	$\rho_{theo}(kg/m^3)$	$\rho_{meas}(kg/m^3)$	$\frac{\rho_{meas}}{\rho_{theo}}(\%)$
$(La_{0.7}Ba_{0.3})MnO_3$	R	3.921	0.997	0.947	1.435	0.01313	6835.5	4648	68
$(La_{0.7}Sr_{0.3})MnO_3$	R	3.905	0.979	0.930	1.384	0.00134	6463	4605	72
$(Nd_{0.7}Ba_{0.3})MnO_3$	C	3.894	0.975	0.934	1.372	0.02428	6952.1	4518	65
$(Pr_{0.7}Ba_{0.3})MnO_3$	C	3.888	0.978	0.938	1.386	0.02150	6996	5041	72
$(Sm_{0.7}Ba_{0.3})MnO_3$	C	3.886	0.968	0.926	1.351	0.02875	7118.3	4301	60
$(Pr_{0.7}Sr_{0.3})MnO_3$	O	3.866	0.962	0.921	1.335	0.00473	6566.3	4500	68
$(La_{0.7}Ca_{0.3})MnO_3$	O	3.846	0.967	0.916	1.354	0.00008	6126.7	4305	70
$(Nd_{0.7}Sr_{0.3})MnO_3$	O	3.856	0.957	0.917	1.321	0.00607	6585	4525	69
$(Pr_{0.7}Ca_{0.3})MnO_3$	O	3.832	0.951	0.907	1.305	0.00053	6140	4500	68
$(Sm_{0.7}Sr_{0.3})MnO_3$	O	3.846	0.950	0.910	1.300	0.00840	6888.2	4615	67
$(Nd_{0.7}Ca_{0.3})MnO_3$	O	3.825	0.946	0.903	1.291	0.00103	6222.5	4233	68
$(Sm_{0.7}Ca_{0.3})MnO_3$	O	3.820	0.939	0.896	1.270	0.00210	6652	4375	66

Table 2.3 Structural parameters calculated for $(A_{0.7}A'_{0.3})MnO_3$; A = La^{3+}, Pr^{3+}, Nd^{3+}, Sm^{3+}, A' = Ca^{2+}, Sr^{2+}, Ba^{2+}.

[1] R. Valenzuela, *Magnetic Ceramics,* Cambridge University Press, London 1994.

[2] E. Barringer, N. Jubb, B. Fegley, R.L. Pober and H. K. Bowen, *Ultrastructure processing of Ceramics, Glasses and Composites,* eds. L. L. Hensch and D. R. Ulrich, 315, Wiley Publishers, New York, 1984.

[3] R. Roy, Journal of the American Ceramic Society, **39**, 145 (1956)

[4] *Sol-Gel Technology,* http://chemat.com/html/solgel.html

[5] C. J. Brinker and G.W. Scherrer, *Sol-Gel Science,* Academic Press Limited, London, 1990.

[6] G. Jonker and J. van Santen, Physica, **16**, 337 (1950)

[7] M.P. Pechini, U.S. Patent 3, **330**, 667 (July 11, 1967)

[8] H. Salze, P. Odier and B. Cales, Journal Non-Crystalline Solids **82**, 314 (1986)

[9] M. Ibarra, P. Algrabel, C. Marquina, J. Blasco and J. Garcia, Physical Review Letters, **75**, 3541, (1995).

[10] M. Hervieu, R. Mahesh and D. D. Sarma, Physical Review B, **47**, 15 397 (1993).

[11] B. C. Tofield and W. R. Scott, Journal of Solid State Chemistry, **10**, 183, (1974).

[12] J. H. Kuo, H. Andersen and D. Sparlin, Journal of Solid State Chemistry **83**, 52, (1989).

[13] J. A. Alonso, Philosophical Transactions of the Royal Society London A **356**, 1617, (1998).

[14] L. Ranno, M. Viret, A. Mari, R. M. Thomas and J. M. D. Coey, Journal of Physics: Condensed Matter **8**, L33 (1996).

[15] Oxides bibliography, http://www2.tcd.ie/Physics/People/Michael.Coey/oxsen

[16] J. A. M. Van Roosmalen and E. H. P. Cordfunke, Journal of Solid State Chemistry, **110**, 106 (1994).

[17] J. A. M. Van Roosmalen, E. H. P. Cordfunke, R. B. Zandbergen and H. W. Zandbergen, Journal of Solid State Chemistry, **110**, 100 (1994).

[18] R. M. Thomas, V. Skumryev, J. M. D. Coey and S. Wirth, Journal of Applied Physics, **85**, 5384, (1999).

[19] H. Y. Hwang, S. W. Cheong, N. P. Ong and B. Batlogg, Physical Review Letters **77**, 2042, (1996).

[20] G. J. Snyder, R. Hiskes, S. DiCarolis, M. R. Beasley, T. H. Geballe, Physical Review B, **53**, 1 (1996).

[21] H. Friedman and L. S. Birks, Review of Scientific Instruments, **19**, 323, (1948).

[22] R. Tertian and F. Claisse, *Principles of Quantitative X-ray Fluorescence Analysis*, Heyden and Son Limited, 1982.

[23] S. Geller and V. B. Bala, Acta crystallographica **9**, 1019, (1956).

[24] S. Geller and E. A. Wood, Acta crystallographica **9**, 563, (1956).

[25] A. M. Glazer, Acta Crystallographica B **28**, 3384 (1972).

[26] M. C. Martin, G. Shirane, Y. Endoh, K. Hirota, Y. Moritomo, Y. Tokura. Physical Review B **53**, 14 285, (1996).

[27] V. Goldschmidt, *Geochemistry*, Oxford University Press, (1958).

[28] H. Y. Hwang, S-W. Cheong, P. G. Radaelli, M. Marezio and B. Batlogg, Physical Review Letters, **75**, 914, (1995).

[29] A. Maignan, F. Damay, A. Barnabe, C. Martin, M. Herview and B. Raveau, Philosophical Transactions of the Royal Society London A **356**, 1635, (1998).

[30] R. Mahesh, Mahendiran et al. Journal of Solid State Chemistry, **120**, 204, 1996.

[31] R. D. Shannon and C. T. Prewitt, Acta Crystallographica A, **32**, 785, (1976).

[32] L. M. Rodriguez-Martinez and J. P. Attfield, Physical Review B **54**, R15 622, (1996).

[33] A. Lanzara, N. L. Saini, M. Brunelli, F. Natali, A. Bianconi, P. G. Radaelli and S.-W. Cheong, Physical Review Letters, **81**, 878, (1998).

[34] K. R. Poeppelmeier, M. E. Leonowicz, J. C. Scanlon, J. M. Longo and W. B. Yelon, Journal of Solid State Chemistry **45**, 71, (1982).

[35] A. P. Ramirez, Journal of Physics: Condensed Matter, **9**, 8171, (1997)

[36] P.J. Goodhew and F. J. Humphries, *Electron Microscopy and Analysis,* 2nd edition, Taylor and Francis publishers, London , 1988.

Chapter 3
Transport properties

3.1 Introduction

Historically, transport measurements have been the favoured characterisation and study method for the manganese perovskites. The pioneers, Jonker and van Santen, presented resistivity measurements of polycrystalline ceramics $(La_{1-x}A_x)MnO_3$ (A = Sr, Ca , Ba) as a function of both temperture and doping fraction, x, in the early fifties [1] [2], demonstrating the simultaneous occurrence of metallicity with ferromagnetism within the doping range, x = 0.2 - 0.4. Soon after, Volger discovered a negative magnetoresistance $\frac{\Delta R}{R(0)} \approx 8\%$ for polycrystalline $(La_{0.8}Sr_{0.2})MnO_3$ in an applied field 0.3 T near T_C and published the first measurements of Hall effect, thermopower and specific heat in 1954 [3]. Fifteen years elapsed before Searle and Wang [4] reported a substantial 20% decrease in resistivity near T_C (310K) in 1T for $(La_{0.69}Pb_{0.31})MnO_3$ as part of their extensive study of $(La_{1-x}Pb_x)MnO_3$, $0.2 < x < 0.44$, flux-grown single crystals [5] [6] [7]. This negative magnetoresistance, when rediscovered in high-quality thin films of $(La_{0.67}Ba_{0.33})MnO_3$ [8], $(La_{0.75}Ca_{0.25})MnO_3$ [9] and $(La_{0.67}Ca_{0.33})MnO_3$ [10] in the early nineties, was of an unprecedented, "colossal" magnitude $(R(0)/R(6T) = 127\ 000\%$ at 77 K- figure 3.1) prompting a rigorous re-examination of the manganites' transport properties, both experimentally and from a theoretical perspective [3.2].

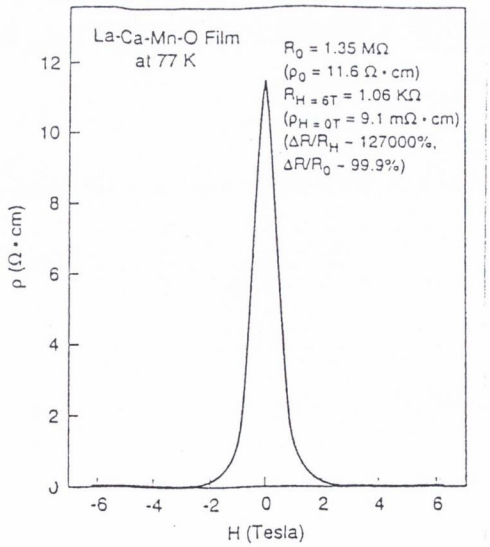

Figure 3.1 Colossal magnetoresistance displayed by a $(La_{0.67}Ca_{0.33})MnO_3$ thin film [10].

The resulting research frenzy was largely driven by the continually increasing demand for magnetic information storage and retrieval, based on magnetoresistive read-head technology. During the preceeding decade, "giant

magnetoresistance" (GMR) exhibited by heterogenous structures such as thin-film multilayers of alternating ferromagnetic metals and normal metals [11], had been developed to reproducibly achieve room temperature effects of order $\frac{\Delta R}{R(0)} \approx 10\%$ under in-plane fields around 5mT. With prototype disk drives employing GMR read-heads already presenting a challenge to conventional inductive or permalloy read-head technology, the "colossal magnetoresistance" (CMR) of the mixed-valence manganites presented the prospect of creating devices whose performance exceeded that of GMR structures, enabling even higher storage densities provided that a large magnetoresistive reponse could be achieved in a small field.

Attempts at optimising the manganites magnetoresistance response have proceeded via many different routes. The compositional dependence of the MR effect in bulk polycrystalline materials has been investigated through extensive chemical substitution [12] [13] [14]. For the compositions of interest, with doping ratio x = 0.3, chemical systematics have demonstrated that the magnetic ordering temperature, T_C correlates with e_g conduction bandwidth, as governed by the size of the A-site cations, $< r_A >$, via the Mn-O-Mn bond angle [section 4.2.4]. The alignment in an applied field of the increasingly disordered ground states of the lower T_C compounds results in greater resistivity change; the magnitude of the CMR effect increases with decreasing T_C [15] as the resistivity of the semiconducting state increases inherently with decreasing temperature. However, the largest magnetoresistance effects are associated with the transformation of an insulating charge-ordered material [figure 1.5] to a ferromagnetic, metallic phase, as typified by the $\frac{\Delta R}{R(0)} \approx 10^{13}$ % measured for a $(Pr_{0.7}Ca_{0.3})MnO_3$ single crystal in 4T at 4.2 K [16]. The irreversible nature of these first-order "charge-melting" transitions are of limited technological use, as the initial state is not recovered upon removal of the applied field unless the temperature is raised.

As a direct consequence of the reports in [8] [9] [10], thin film transport properties have been examined with particular attention paid to the influence of deposition conditions and post-annealing treatments. Most notably, Xiong *et al.* [17] [18] demonstrated that by increasing the deposition temperature from $600°C$ to $800°C$ the temperatures of the resistivity peaks, T_p, of $(La_{0.67}Ba_{0.33})MnO_3$ and $(Nd_{0.7}Sr_{0.3})MnO_3$ thin films were reduced by half from measured bulk values, whilst simultaneously increasing the heights of the resistivity maxima, leading to greater MR values. Additionally, annealing deposited films in oxygen atmospheres was shown to increase T_p, but lower the maximum value of resistivity as a function of increasing annealing temperature and duration. The influence of increasing substrate-induced lattice strain was extensively studied, through the use of different substrates [19] [20], and shown to correlate with the magnitude of the magnetoresistance effect. Jin [21] demonstrated that MR is maximum for epitaxial (as opposed to polycrystalline) films; presumably the absence of grain boundaries enables the most effective propagation of stress throughout the film, the optimum thickness of which for a $LaAlO_3$ substrate was determined as $\approx 100nm$.

Grain boundaries have assumed an important role in the discussion of magnetoresistance in these materials. In a study carried out by Hwang *et al.* [22], the transport properties of bulk polycrystalline $(La_{0.67}Sr_{0.33})MnO_3$ samples with different grain sizes were compared with those of a single-crystal of the same composition. The aforementioned colossal magnetoresistance effect, exhibited by all samples, was thus shown to be independent of grain size; an *intrinsic* property. However, the polycrystalline materials displayed an additional low-field magnetoresistance at all temperatures below T_C, which was notably absent in the grain-boundary-free single-crystal. The initial decrease in resistivity was shown to vary with temperature as $\rho(H) \sim \frac{a+b}{T+c}$, characteristic of spin-polarised tunneling across intergrain barriers in granular ferromagnets [23] [24]. The low-field MR reponse has been subsequently reported in other polycrystalline compounds [25] [26], and thin-film manganites [27] [28] [29] [30], and Gupta *et al* [31] have correlated the effect in films of $La_{0.67}A'_{0.33}MnO_{3-\delta}$ (A' = Sr, Ca , or vacancies introduced into lattice) with grain size, as determined using transmission electron microscopy .

An ingenious experiment by Mathur *et al.* [32] probed the grain boundary scattering mechanism of the low field MR through isolating the intergrain transport across a single grain boundary of $(La_{0.7}Ca_{0.3})MnO_3$. The peak in the resistivity just below T_C was associated with a MR effect measured in 0.18 T, which decreased almost linearly to zero at T_C. Similarly, the group in Jena, [33] investigated the field dependence of the grain boundary resistance and magnetoresistance through patterning a $(La_{0.8}Sr_{0.2})MnO_3$ thin film grown on a bicrystal substrate.

The concept of an *extrinsic,* microstructure-dependent magnetoresistance has been extended further with the development of powder magnetoresistance (PMR) [34] The magnetoresistance of cold pressed compacts of fine-grained $(La_{0.7}Ca_{0.3})MnO_3$ powder was measured as $\frac{\Delta R}{R(0)} \approx 20\%$ in 0.5T at 77K. The effect has been ascribed to spin-polarised electron transport across non-exchange coupled ferromagnetic grains, the relative orientation of which is modified by the applied field.

The drive to exploit the manganites' CMR response for possible technological application has been complemented by attempts at explaining the origin of the effect. In this chapter, the milestones which have marked the development of current theory, are noted and reference is subsequently made to supporting experimental evidence. The transport data collected on the twelve polycrystalline samples are presented and discussed with respect to both previously proposed ideas and more recent thinking.

3.2 Background

3.2.1 General theory

The double-exchange mechanism remains the principal tenet for understanding the physical properties of the manganese perovskites. The essential physics of the interaction are contained within the double-exchange Hamiltonian derived by Kubo and Ohata from the Kondo-lattice Hamiltonian in the limit where $J_H \gg t_{ij}$ [35]:

$$\mathcal{H} = -\sum_{<ij>} t_{ij} c_i^{\dagger} c_j - J_H \sum_i \mathbf{S}_i.\mathbf{s}_i \qquad (1)$$

where J_H is the on-site Hund rule coupling between a localised ion core spin, $S=\frac{3}{2}$ and that of a mobile electron $s = \frac{1}{2}$;the operators c_i and $c_i^{\dagger}$ respectively create and annihilate an electron on site i with spin parallel to the ionic core. t_{ij} is the transfer (hopping) integral determined from the original generalisation of the double-exchange mechanism by Anderson and Hasegawa [36] to include the interaction between two adjacent ions with an angle θ_{ij} between their spin directions,

$$t_{ij} = b_{\sigma} \cos(\frac{\theta_{ij}}{2}) \qquad (2)$$

where b_{σ} is the normal transfer matrix element dependent on the spatial wavefunctions of the e_g and t_{2g} orbitals, and is directly related to the e_g bandwidth W [4.2.4]. The mean-field treatment of [35], principally predicted a leading $T^{\frac{9}{2}}$ dependence of resistivity at low temperatures due to electron-magnon scattering within the double-exchange system [3.2.2], a fully spin-polarised ground state, with the minority spin subband reappering as the system disorders and an essentially temperature-independent resistivity above T_C. Furukawa [37], extending this treatement through a many-body approach, demonstrated that both majority and minority bands are split by Hund's rule exchange in the paramagnetic state. As the system orders magnetically, the majority spin subband gains spectral weight at the expense of the minority spin subband, ultimately resulting in a fully spin-polarised ground state (figure 4.1).

However, the validity of a mean-field approach for a system in which $J_H \gg t_{ij}$ was called into question by Millis, Littlewood and Shraiman [38]. Adopting a "dynamical mean field approximation" [39], their rigorous, quantitative consideration of the double-exchange Hamiltonian demonstrated that this mechanism alone could not explain the most obvious feature of the manganites, namely the magnitude of the change in resistivity at the ferromagnetic transition or the large resistivity of the $T > T_C$ phase. Furthermore, through using the dopant concentrations, x, as a measure of carrier concentration, the magnetic ordering temperatures predicted by the double-exchange model were more than an order of magnitude too large. If charge carriers in the paramagnetic regime were trapped through lattice distortion, T_C would be lowered. Millis *et al.* therefore included a strong electron-phonon coupling due to the dynamic Jahn-Teller effect within the double-exchange framework, which served to lo-

calise the conduction band electrons as so-called, *Jahn-Teller polarons* (figure 3.2(b)), and obtained results in qualitative agreement with experiment. In an alternative approach, Röder [40] introduced dynamic Jahn-Teller coupling into the original mean-field formalism of Kubo and Ohata [35], giving solutions for $T>T_C$ in which the electrons become "self-trapped" by the lattice distortion, and the composite particle - the "*small magnetopolaron*"- appears as a localised charge surrounded by a spin cloud on nearest neighbours (figure 3.2(c)). In both theories, for $T<T_C$ a large polaronic state is predicted in which polarons extending over several lattice sites overlap and form bands [section 3.2.2(2)].

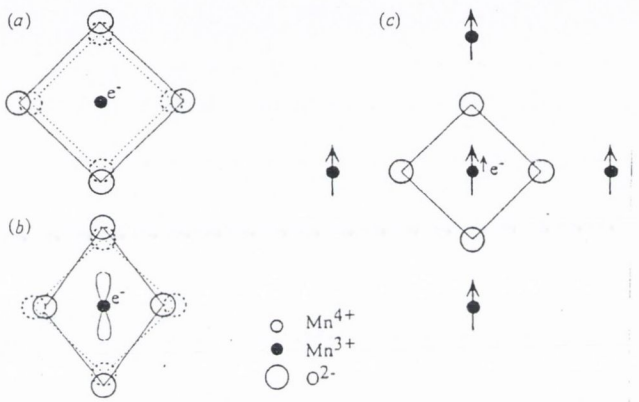

Figure 3.2 Schematic illustration of (a) a small dielectric polaron (b) a Jahn-Teller polaron and (c) a small magnetopolaron.

However, all these models neglect carrier localisation due to charge fluctuations or random fluctuations in the magnetic potential due to inherent cationic disorder. Since the principal energies which determine the electronic structure of the manganites - conduction bandwidth, W; Hund's rule coupling, J_H; interatomic Coulomb potential, V crystal-field interaction, Δ_{cf} and Jahn-Teller stabilization energy, δ_{JT} - are all of the order of 1eV (figures 1.3 and 3.3), the influence of localisation effects have merited investigation. Varma [41] has attributed the high resistivity of the $T>T_C$.phase to Anderson localisation of the carriers in the Mn e_g band arising from variations in the Coulomb potential due to the random distribution of A^{3+} and A'^{2+} cations. The localisation of carriers promotes spin polaron formation; the localisation length of which increases with increasing magnetic order, thus reducing resistivity with the onset of ferromagnetic order.

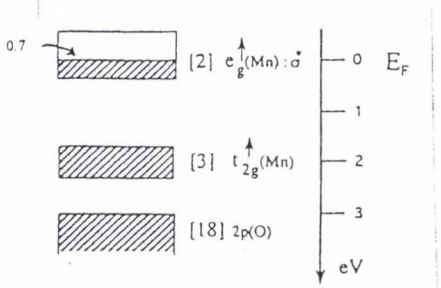

Figure 3.3 A schematic representation of the energy band structure of $(A_{0.7}A'_{0.3})MnO_3$.

Alternatively, potential fluctuation may be magnetic rather than Coulombic in origin. Localisation and scattering from an exchange potential which is attributed to the difference in local magnetisation at varying distances from a divalent impurity are the key components of a theory developed by Nagaev to account for the measured peak in resistivity and magnetoresistance effect [42]. A theory of magnetic localisation proposed by Viret [43] ascribes carrier localisation above T_C to fluctuations in the on-site Hund's rule coupling - J_Hs.S within the framework of Mott's variable range hopping theory [44] [section 3.2.2 (3)].

The following discussion develops these various models with reference to the corroborating experimental evidence in the high and low temperature limts. In the immediate vicinity of T_C, behaviour is best described by thermodynamic measurements which couple directly to the magnetic correlation length. Due to the lack of such published data, the manganites' behaviour in the critical region is not addressed in detail here.

3.2.2 High temperature transport

In the high temperature limit, the physics of double exchange is insufficient to account for the transport properties of the manganites. Most notably, the values of resistivity measured for $T>T_C$ are significantly greater than the modest electron scattering rate implied by double-exchange for disordered spins, requiring a complementary interaction to be invoked. Currently, three different models which incorporate the additional physics outlined above have been shown to agree qualitatively with the measured data: a simple Arrhenius law used to describe activated behaviour due to a band gap or mobility edge; the nearest neighbour hopping of small polarons, and Mott's variable-range hopping expression for carriers localised by random potential fluctuations. Each model is discussed.

(1) An Arrhenius Law

$$\rho = \rho_\infty \exp\left[\frac{E_g}{2kT}\right] \tag{3}$$

was first used to model the data for the x= 0.3 compounds, indicating a purely activated conductivity with a band gap E_g of typically 0.1 eV [45] [46] [47]. The interpretation of E_g poses some difficulty. Band transport, where E_g represents a real gap in the density of states at the Fermi level above T_C is supported by photoemission data measured for $(La_{0.7}Ca_{0.3})MnO_3$ [48] [49], but the surface-dependent nature of this technique means it is unrepresentative of the bulk sample. Furthermore, a valid small bandgap interpretation would require a distinct structural variation for the relevant doping range, $0.2 < x < 0.4$, which is not observed.

Alternatively, this simple activation law could indicate the formation of a mobility edge E_μ to which carriers are excited at high temperatures from the Fermi energy, E_F. However, the interpretation of E_g as $E\mu$-E_F is not supported by the complementary Hall resistivity measurement of [46], where a

small carrier mobility, 10^{-5} $m^2V^{-1}s^{-1}$ and corresponding mean free path (<0.1 nm) are incompatible with a picture of carrier excitation to extended states.

(2) A polaron model A charge carrier accompanied by a lattice distortion which is comparable in size to the lattice parameter of its crystalline host, is called a *small, or Holstein polaron* [50]. With reference to the manganites, the small polaron of figure 3.2 (a) first proposed by [51] [52] [45], is an electron, carrying with it a dilated MnO_6 octahedron. Nearest-neighbour hopping of small lattice polarons results in a thermally activated conductivity. In the "non-adiabatic limit" the motion of the charge carriers is slow compared to the lattice vibrations and the drift mobility is given by

$$\mu = \frac{3ea^2}{2\hbar}\frac{t^2}{kT}\left(\frac{\pi}{4W_pkT}\right)^{\frac{1}{2}}\exp\left[-\frac{W_p}{kT}\right] \tag{4}$$

where a is the hopping distance, e the electronic charge, ω_0 the longitudinal optical-phonon (or "attempt") frequency and W_p is one-half of the polaron formation energy, E_p. The magnitude of the mobility prefactor indicates whether the carrier motion is non-adiabatic, where the limiting condition for non-adiabatic behaviour is

$$t \ll t_{\max} = \left(\frac{2WpkT}{\pi}\right)^{\frac{1}{4}}\left(\frac{\hbar\omega 0}{\pi}\right)^{\frac{1}{2}} \tag{5}$$

where t is the electronic transfer integral. In the adiabatic regime, where the charge-carrier motion is faster than the vibration of the lattice, the drift mobility.is given by

$$\mu = \frac{3ea^2}{2}\frac{\omega_0}{2\pi kT}\exp\left[-\frac{W_p}{kT}\right] \tag{6}$$

where $W_p = \frac{E_p}{2-t}$. The resistivity is given by $\rho = \frac{1}{ne\mu}$ where n is the carrier density.

The resistvity data for a $(La_{0.67}Ca_{0.33})MnO_3$ crystal for $T>T_C$ [53], is well described by the adiabatic small polaron hopping law, $\rho = AT\exp\left[\frac{W_p}{kT}\right]$, up to the structural transition temperature, 750 K, above which the temperature-independent scattering of carriers becomes the dominant mechanism. They therefore ascribe the localisation of the charge carriers to energetically favourable lattice distortions. This elastic contribution to the polaron formation energy, E_p has been attributed to the A-site cation size mismatch which introduces elastic stress into the lattice [54] [55]. A mounting body of experimental evidence suggests that small polaron formation in the paramagnetic regime is due to Jahn-Teller lattice distortion.

The static Jahn-Teller effect has previously been introduced with reference to $La^{3+}Mn^{3+}O_3$ (Chapter 1), where the lattice distortion attributable to the d^4 electrons of the Jahn-Teller Mn^{3+} ion results in the insulating band structure of this end-member. In the compounds of interest, $(A_{0.7}A'_{0.3})MnO_3$, the hopping of charge carriers between Mn^{3+}/Mn^{4+} B-site cations leads to a dynamic Jahn-Teller effect. The dynamically-fluctuating local distortions provide a Jahn-Teller stabilization energy, δ_{JT} which, when comparable to the conduction

bandwidth, W, can result in the formation of small polarons called *Jahn-Teller polarons*. As illustrated in figure 3.2 (b), the Jahn-Teller polaron carries with it an axial distortion of the MnO_6 octaheron which removes the degeneracy of the e_g band in the electronic ground state.

This picture, theoretically described by Millis and co-workers [38], is evidenced by diverse and extensive experimental data which include: the anomalous temperature dependence of the lattice parameters [56] [57] [58] [59] and the optical conductivity, [60]; the infrared spectra [61]; the isotope effect where the T_C of $(La_{0.8}Ca_{0.2})MnO_3$ is increased by 21 K upon substitution of ^{16}O by ^{18}O [69] [70] [71]; and muon spin relaxation [72] The reduced value of the activation energy derived from thermopower data as compared to that estimated from the thermally activated behaviour of the electrical conductivity is also characteristic of small polarons, [64] [65] [66] [67] [68].

In addition to this overwhelming evidence in favour of strong coupling to Jahn-Teller distortions, the influence of an applied field on both the resistivity [73] [74] and volume thermal expansion [75] above T_C implies that these polarons have some magnetic character . These observations are further evidenced by small-angle neutron scattering studies which have confirmed the presence of nanometre-scale magnetic clusters in the vicinity of T_C which persist up to $\sim 1.3T_C$ [75] [76] [77]. Spin correlations on a similar scale have also been directly evidenced by nuclear magnetic resonance above T_C [76] [78].

Thus a picture emerges of a small lattice polaron with an accompanying magnetic polarization resulting from short-range ferromagnetic interactions. - an effective hybrid of Holstein's small polaron and the *bound magnetic polaron* first introduced by Kasuya and Yanase [79], to account for the large magnetoresistive effects observed in europium chalcogenide alloys [80] and further applied to magnetic semiconductors by von Molnár *et al.* [81]. The original magnetic polaron, also called a magnetic impurity state, was conceptually viewed as an island of local ferromagnetic order in a paramagnetic or antiferromagnetic host, and was unaccompanied by lattice distortion. Therefore, the quasiparticles doubtless present in the manganites, should be referred to as *small magnetopolarons* due to their elastic and magnetic character, to discriminate from other polaron concepts.

Small magnetopolarons are the predicted outcome of Röder *et al.*'s theoretical consideration of the manganites.[40]. They were also invoked by Emin *et al.* [82] to explain the large magnetoresistance exhibited by europium-rich EuO near the Curie temperature, T_C, and the thermally activated resistivity for $T > T_C$ [83]. Emin attributed the MR effect to the abrupt collapse of delocalised carriers into small polarons "self-localised by lattice distortions but also dressed with a magnetic cloud" as the ferromagnet disordered. Due to the degeneracy of a number of sites within the crystal lattice, a band of localised states could form. These energy bands would be extremely narrow, and the carrier mobility associated with them would only predominate at low temperatures. However, they were not regarded as extended states, even at the highest temperatures, where the dominant counduction mechanism was

thermally activated hopping [84] [85].

A similar scenario may hold for the manganites. If the electron transfer energy and the electron-phonon coupling energy are nearly equal, the severe localisation or extended state of the carriers is determined by spin disorder. Thus, the onset of ferromagnetic order at T_C leads to an abrupt expansion of the polaron radius, leading to the formation of large polarons with an itinerant character due to their small effective mass, and consequent metallic conductivity. Recent extended x-ray absorption fine structure spectra on $(La_{0.75}Ca_{0.25})MnO_3$ [86], provide compelling evidence for "large Jahn-Teller polarons" in the low temperature, metallic phase, characterised by an anomalous extended Mn-O bond ($\Delta R = 0.09$ Å). The appearance of small Jahn-Teller polarons at high temperatures, is characterised by the further elongation of the Mn-O bond ($\Delta R = 0.21$ Å) . These results also suggest the coexistence of large and small polarons immediately above the metal-insulator transition. This observation supports theoretical conjecture of a microscopic phase segregation into domains of large polarons and localised small polarons in this intermediate temperature region [87].

(3) Variable range hopping (VRH) Besides the elastic stress introduced into the lattice by the Jahn-Teller effect (or cation size mismatch), contributions to the polaron formation energy, E_p, can also be Coulombic or magnetic in origin. Many groups [88] [89] [90] have successfully fitted their resistivity data according to Mott's expression for the variable range hopping of electrons localised by random potential fluctuations in the absence of electron-electron interactions,

$$\rho = \rho_\infty \exp\left[\left(\frac{T_0}{T}^{\frac{1}{4}}\right)\right] \tag{7}$$

Mott's theory was originally developed to explain electron transport in doped semiconducters where the ratio of random Coulomb potential variation, ΔV to occupied σ^* bandwidth W was sufficient to produce "diagonal" or Anderson localisation of electrons with a localisation length $\frac{1}{\alpha}$. The wavefunctions of the occupied hydrogenic orbitals, with a "fall-off" rate, α, are written

$$\Psi = \Psi_0 e^{-\alpha r} \tag{8}$$

There is a competition between the potential energy difference and the distance the electrons can hop. This is reflected in the expression of the hopping rate, γ, to a site at a distance R where the energy of the carrier is ΔE higher than at the origin,

$$\gamma = \gamma_0 e^{-(2\alpha R + \frac{\Delta E}{kT})} \tag{9}$$

A sphere of radius R contains $\frac{4}{3}\pi\frac{R^3}{v}$ sites to which an electron can hop, where v is the volume per manganese ion. Thus, the smallest value of ΔE, is given by

$$\Delta E = \left[\frac{4}{3}\pi\frac{R^3}{v}N(E_m)\right]^{-1} \tag{10}$$

where $N(E_m)$ is the density of available states per m^3. To minimise the hopping rate,

$$\gamma = \gamma_0 e^{-(2\alpha R - \frac{3}{4\pi} R^{-3} \frac{1}{N(E_m)kT})} \tag{11}$$

let

$$x = e^{-(2\alpha R - \frac{3}{4\pi} R^{-3} \frac{1}{N(E_m)kT})} \tag{12}$$

then

$$\frac{dx}{dR} = (-2\alpha + \frac{9}{4\pi} R^{-4} \frac{1}{N(E_m)kT}) e^{-(2\alpha R - \frac{3}{4\pi} R^{-3} \frac{1}{N(E_m)kT})} = 0 \tag{13}$$

$$R = (\frac{9}{8\pi\alpha N(E_m)kT})^{\frac{1}{4}} \tag{14}$$

substituting this value into eq. 1.11 above and letting $\frac{1}{\rho}=\gamma$ gives

$$\rho = \rho_\infty e^{(2.06 \frac{\alpha^3}{N(E_m)kT})^{\frac{1}{4}}} \tag{15}$$

which, through comparison with Mott's original expression, gives

$$kT_0 = \frac{18\alpha^3}{N(E_m)} \tag{16}$$

Other derivations in the literature yield slightly different prefactors [91] [92] [93]. To interpret the data for $T>T_C$ in terms of this model, the electronic density of states, $N(E_F)$ is taken from heat capacity measurements at low temperature, $N(E_F) \sim 3 \times 10^{28}$ $m^{-3}eV^{-1}$ [section 3.5]. An estimate of the number of conduction electrons is $0.7/v \sim 1.2 \times 10^{28}$ m^{-3}corresponding to an occupied e_g bandwidth ~0.3 eV. The value of $kT_0 = 220$ eV evaluated for $La_{0.7}Sr_{0.3})MnO_3$ gives a localisation length, $\frac{1}{\alpha} = 0.14$ nm, corresponding to a room temperature average hopping distance, R = 0.50 nm and $\Delta E = 0.06$ eV. In order for this result to comply with VRH associated with Anderson localisation, the localisation length due to random potential fluctuations should exceed the interatomic distance, and the hopping distance should be several times greater. Since the average Mn-Mn distance for this compound is 0.38 nm (table 2.3), these criteria are not met.

The unphysical nature of this result prompted Viret to develop a theory of *magnetic localisation*, based on the results presented in section 3.4. He proposed that the random potential responsible for carrier localisation above T_C is of magnetic origin, and can be ascribed to the on-site Hund's rule interaction $-J_H \mathbf{s}.\mathbf{S}$, between the localised Mn t_{2g} cores ($\mathbf{S}=\frac{3}{2}$) and the spins, s, of the e_g electrons in the σ^* conduction band. Expressing this potential, E_m, in terms of θ_{ij}, the angle subtended by two Mn core spins between which an e_g electron hops,

$$E_m = \frac{1}{2} U_m (1 - \cos\theta_{ij}) \tag{17}$$

where $U_m = \frac{3}{2} J_H$ is the splitting between spin-up and spin-down e_g bands. For uncorrelated spins, $P(\theta_{ij}) = \frac{1}{2}\sin(\theta_{ij})$ is the probability of a subtending

angle θ_{ij},therefore the probability of a potential barrier, E_m is written

$$P(E_m) = P(\theta_{ij})\frac{d\theta_{ij}}{dE_m} = \frac{1}{U_m} \tag{18}$$

This probability is incorporated into the calculated density of states, by multiplying $P(E_m)$ by the number of available states per m^3, to give

$$N(E_m) = P(E_m)(1-x)\frac{\phi g}{v} \tag{19}$$

where (1-x)=0.7 is the probability of an unoccupied e_g orbital at the Mn destination, $\phi \sim 0.5$ is a geometric factor which accounts for the d_{z^2} state of the hopping electron (as opposed to a s-state [88]). g is the probability that an unoccupied manganese orbital can accept an electron; the dynamic Jahn-Teller effect imposes the condition that a hop may only take place if the receiveing site is free to distort or is already suitably distorted, therefore $g \neq 1$.

Taking $g \sim 0.7$ for x = 0.3, results in a reduced value of the electronic density of states results, $N(E_m)$=9 x 10^{26} $m^{-3}eV^{-1}$. Substitution into eq. 1.16 above, gives

$$kT_0 = 73\alpha^3 U_m v \tag{20}$$

where v is the lattice volume per manganese ion, 60 x 10^{-30} m^3, $U_m \sim 2$ eV, resulting in a localisation length 0.45 nm for $(La_{0.7}Sr_{0.3})MnO_3$. Average hopping distances at room temperature are then 1.24 nm and $\Delta E \approx 0.06$ eV. These values appear physically plausible since localisation is on the scale of the Mn 3d orbital and the hopping distances are 3-4 times the Mn-Mn separation.

Consensus has yet to be reached as to the precise nature of the high-temperature phase of the manganites. However, a recent study by Ziese [94] of the high-temperature resistivity of $(La_{0.7}Ca_{0.3})MnO_3$ and $(La_{0.7}Ba_{0.3})MnO_3$ thin films grown on various substrates, goes some way towards clarifying the respective roles of lattice effects, and intrinsic Coulombic and magnetic disorder. The principal conclusions are that epitaxial films exhibit thermally activated resistivity in accordance with the small polaron model in the adiabatic limit, whereas the data on polycrystalline films are best fitted by a variable-range hopping law. Thus, the VRH model is believed to describe *extrinisic* behaviour ,related to tunneling processes across grain boundaries or between regions of nonstoichiometry, and therefore dominating the measured resistivity behaviour of polycrystalline materials.

3.2.3 Low temperature transport ($T<T_p$)

As derived for the high temperature regime, the low temperature transport of the manganites is most likely dominated by intergrain processes and grain boundary scattering, resulting in the characteristically high values of residual resistivity, ρ_0,measured [3.4]. Indeed, of the x = 0.3 doped manganites only $(La_{0.7}Sr_{0.3})MnO_3$ meets the criterion that the mean free path of a metal should exceed the interatomic spacing, which implies that, $\rho_0 < 1.5$ x $10^{-6}\Omega m$ [44]. Nevertheless, several studies have addressed the intrinsic scattering mecha-

nisms, with the utmost attention paid to the original prediction by Kubo and Ohata [35] for electron-magnon scattering within the double-exchange system; $\rho(T)\ \alpha\ T^{\frac{9}{2}}$. Most notably, Schiffer *et al.* [95] found for $(La_{1-x}Ca_x)MnO_3$; x = 0.20, 0.33, 0.45, that the resistivity for $T < 0.5T_C$ is well fitted by the expression

$$\rho(T) = \rho_0 + \rho_1 T^p \tag{21}$$

where p=$\frac{5}{2}$, in contrast to the poor fit given by p=$\frac{9}{2}$. However, with the introduction of an additional T^2 term into the above expression the data is well-fitted using p=$\frac{9}{2}$. The T^2 term, which could represent electron-electron scattering was also invoked by Snyder *et al.* [53] to accurately fit data measured on high-quality thin films of $(La_{0.67}A'_{0.33})MnO_3$; A' = Ca, Sr, and also gave good agreement with the single crystal data of Urushibara *et al.* [96].

However, Jaime and Salamon [97], who recently studied the resistivity of a $La_{0.66}(Pb_{0.67}Ca_{0.33})MnO_3$ single crystal in the low temperature regime, invoke an electron-phonon term, T^5 and note that the dependence on the T^2 dependence disappears at the lowest temperatures, suggesting that electron-electron scattering is an unlikely explanation for this ubiquitously observed quadratic temperature dependence. They return to the standard perturbation calculations carried out on the double-exchange model by Mannari [98], which formed the basis for the original work of Kubo and Ohata, and extend the calculation to allow for split minority and majority spin sub-bands. The calculated $\rho(T)$, based on the calculation of one-magnon resistivity to describe spin-split bands gives a qualitative account of the measured data.

3.2.4 Thermal properties - specific heat capacity measurements

Defined as the ratio of the heat supplied to an object to its consequent rise in temperature, the *molar heat capacity, C,* is measured in $Jmol^{-1}K^{-1}$. At low temperatures (1<T<10 K), the temperature dependence of the heat capacity of a metal is expressed as the sum of a linear electronic term and a cubic lattice term:

$$C = \gamma T + \beta T^3 \tag{22}$$

In magnetic materials, a further term arising from spin-wave excitations varies as $T^{\frac{n}{2}}$ where n derives from the general dispersion relation $\omega = Dq^n$. For ferromagnets, $n = 2$, resulting in an additional term, $\delta T^{\frac{3}{2}}$. The determination of the coefficient, γ, provides an estimate of the electronic density of states at the Fermi level for both spin projections, $N(E_F)$, since

$$\gamma = \frac{(\pi k_B)^2 N(E_F)}{3} \tag{23}$$

In addition to the results presented [3.3], the low temperature specific heat capacity, *C(T)* of the manganites has been measured by several groups [99] [100] [101]. Most notably, the studies by Woodfield *et al.* [101] of $(La_{1-x}Sr_x)MnO_3$ for $0 \leq x \leq 0.3$ from T = 0.5 to 10 K showed that in addition to the electronic and lattice terms, an additional $T^{\frac{3}{2}}$spin wave term and a T^{-2} hyperfine term improved the fit to the *C(T)* data. The latter term, due to nuclear moments,

was deemed especially important due to the large internal fields in the materials. Significantly, the electronic γ coefficient, found to be approximately 3.2 $mJmol^{-1}K^{-1}$ for x = 0.2, 0.3 was absent for x = 0, 0.1 - a reflection of the metal-insulator transition already evidenced by the resistance measurements.

3.3 Experimental arrangements

3.3.1 Specific heat

Measurements of the specific heat capacity were carried out at the IPCMS, Strasbourg using a home-built pseudo-adiabatic calorimeter. Samples of width 5mm, smeared with thermally conducting Apiezon grease, were wrapped in aluminium foil, mounted on a resistor (Cr/Ti on saphire) and placed within a bath cryostat. Through recording the current supplied to the resistance, the heat delivered to the sample was determined, whilst the resulting temperature increase was measured using germanium thermometry.

3.3.2 Resistivity

Measurements of the variation of resistivity with temperature were carried out on ceramic bars of typical dimensions, 8mm x 2mm x 2mm, using a conventional four point probe method. Four silver wires fixed to the sample surface using $\sim 1mm$ diameter silver paint blobs (Electrodag), constituted the electrical contacts. As illustrated schematically in figure 3.4, the samples were affixed to the copper block attached to the head of a closed-cycle helium refrigerator (APD Cryogenics). A high thermal conductivity grease used as an adhesive, ensured that thermal contact was maintained with the sample throughout. The temperature range of the fridge extended from room temperature to $\sim 13K$. A chromal-gold (iron 0.03%) thermocouple controlled the temperature of the fridge and the resultant temperature was measured by a silicon diode (Southhampton diode) mounted beside the sample. DC currents in the range 50 nA to 1 mA were supplied by a Keithley 224 constant current source and the potential difference measured across the voltage contacts by a Keithley 195A voltmeter. The system was fully PC controlled using an IEEE interface.

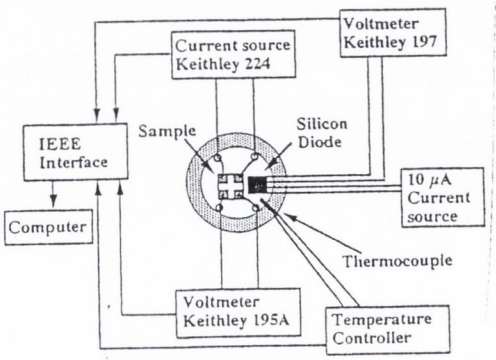

Figure 3.4 Schematic diagram of the set-up used to measure resistivity as a function of temperature for all twelve samples.

3.4 Results

In figure 3.5(a)-(d), the specific heat capacity measured as a function of temperature in the range 1.5 K to 20 K is presented for four samples: $(La_{0.7}Sr_{0.3})MnO_3$, $(La_{0.7}Ca_{0.3})MnO_3$, $(La_{0.7}Ba_{0.3})MnO_3$ and $(Nd_{0.7}Ba_{0.3})MnO_3$ respectively. Through plotting the data as C/T vs T^2, the y-axis intercept corresponds to the coefficient, γ, defined in equation (1.22) above, and listed for the three La samples in Table 3.1 below.

Figure 3.6 presents the variation of resistivity measured from room temperature to the lowest measurable temperature for all twelve polycrystalline ceramics. Table 3.1 summarises the parameters extracted from the data. In addition to the γ coefficient values deduced, other values include: the temperature of the metal-insulator transition (where applicable), T_p, and the resistivity at this peak, ρ_p; the resistivity measured in the vicinity of room temperature ρ_{RT} and the resistivity at the lowest measurable temperature, ρ_0.

The data in the thermally activated regime - this corresponds to $T > T_p$ for those samples which show a metal-insulator transition - were fitted according to three different localisation models: an Arrhenius law, $\ln(\rho)$ vs T^{-1}; adiabatic small polaron hopping, $\ln(\frac{\rho}{T})$ vs T^{-1}; variable range hopping $\ln(\rho)$ vs $T^{-\frac{1}{4}}$ and additionally, $\ln(\frac{\rho}{T})$ vs $T^{-\frac{1}{4}}$ which accounts for the T-dependence of the ρ_∞ prefactor in the variable range hopping expression of equation 11. Linear fits were obtained by a method of least squares. The resulting correlation coeffcient, R [3] is quoted for each data set in Table 3.2 as an indication of the fitting accuracy, where $R = 1$ for the perfect superposition of fitted points with the data.

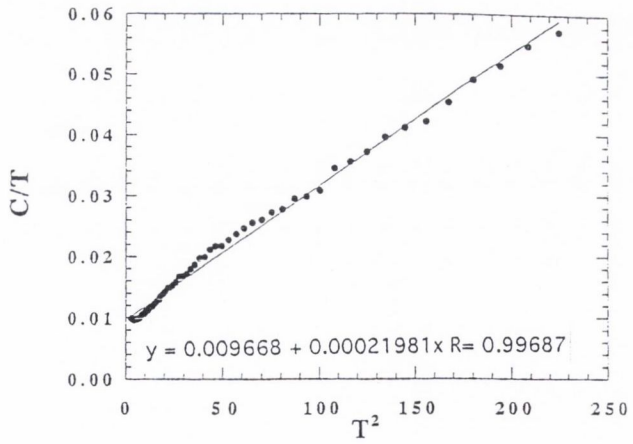

Figure 3.5 Temperature dependence of the specific heat capacity measured for (a) $(La_{0.7}Sr_{0.3})MnO_3$.

[3] The definition of the correlation coefficient, R, for a sample of n pair of x, y, values is

$$R = \frac{\Sigma xy}{\sqrt{(\Sigma x^2)(\Sigma y^2)}}$$

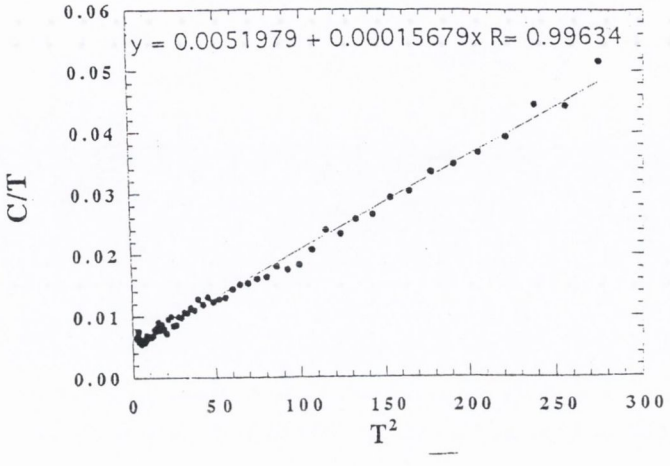

(b) $(La_{0.7}Ca_{0.3})MnO_3$.

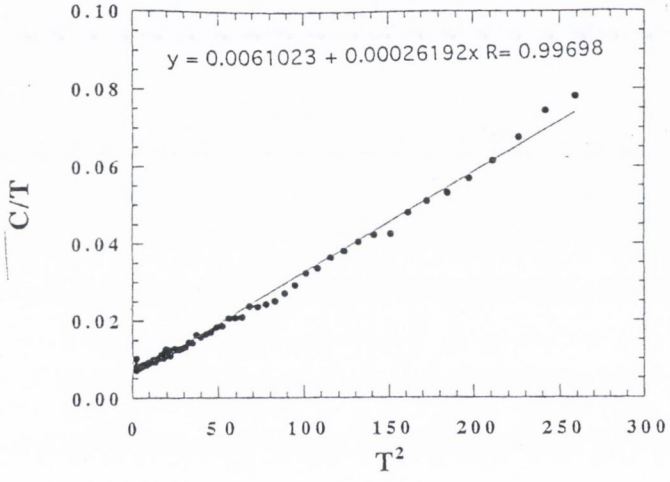

(c) $(La_{0.7}Ba_{0.3})MnO_3$.

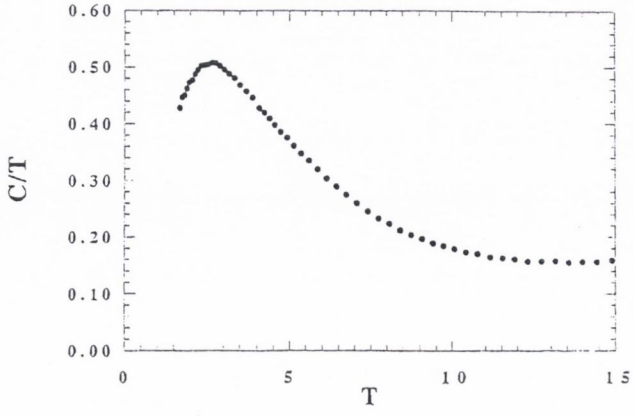

Figure 3.5 Temperature dependence of the specific heat capacity measured for (d) $(Nd_{0.7}Ba_{0.3})MnO_3$.

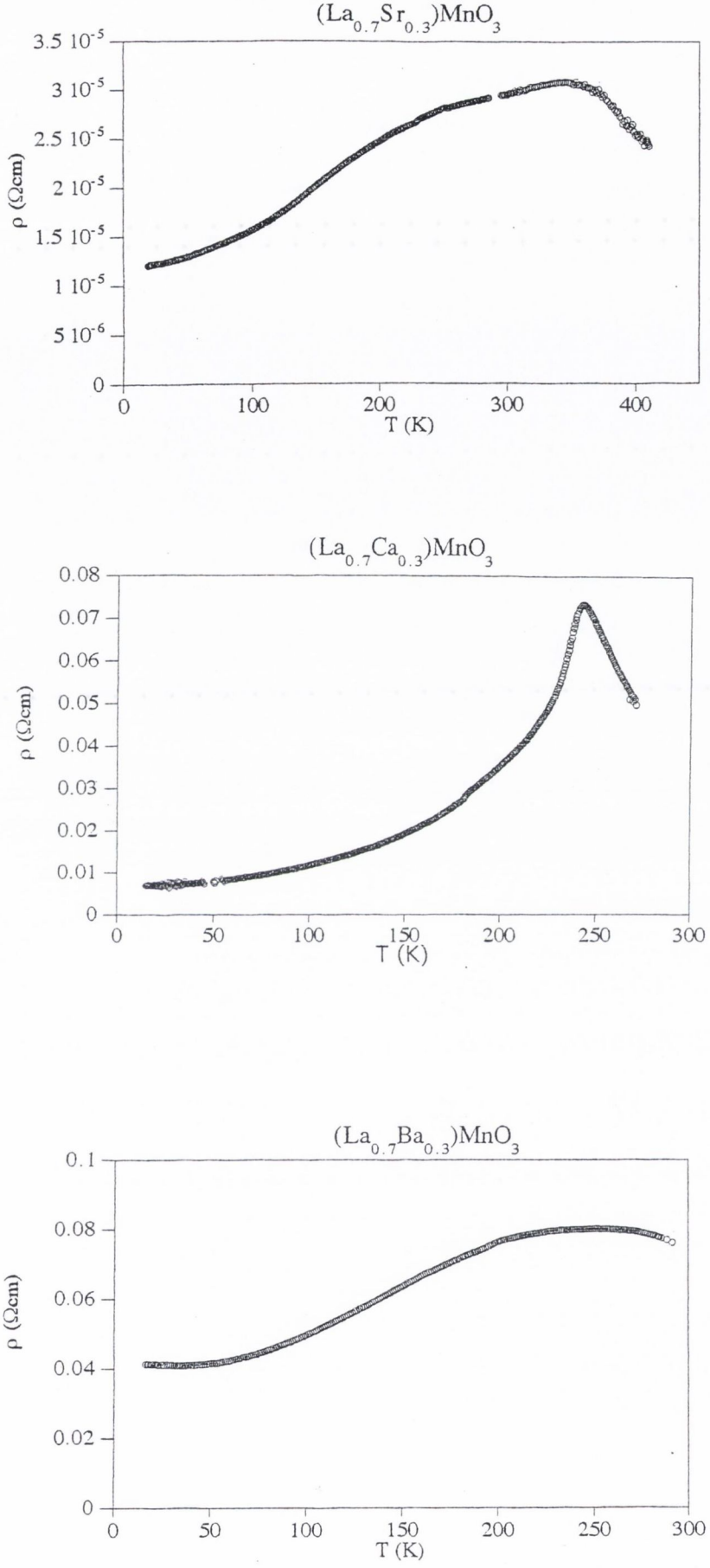

Figure 3.6 (a) Temperature dependence of resistivity for $(La_{0.7}A'_{0.3})MnO_3$; A' = Sr, Ca, Ba.

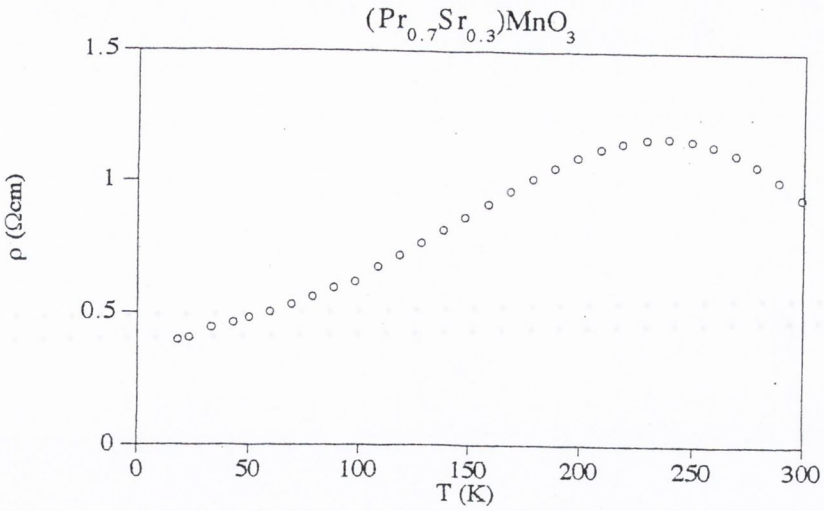

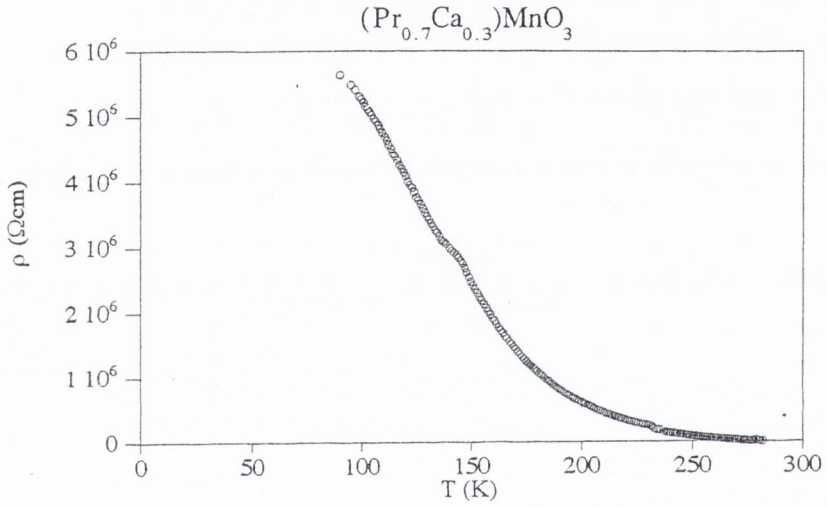

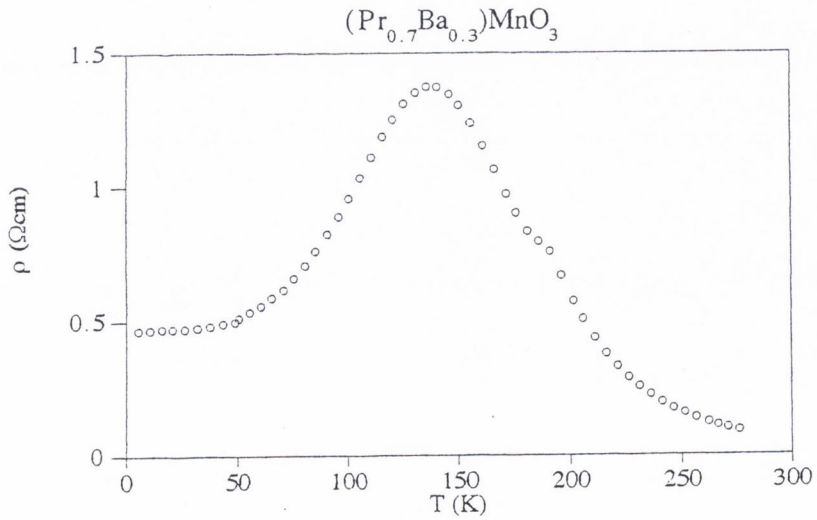

Figure 3.6 (b) Temperature dependence of resistivity for $(Pr_{0.7}A'_{0.3})MnO_3$; A' = Sr, Ca, Ba.

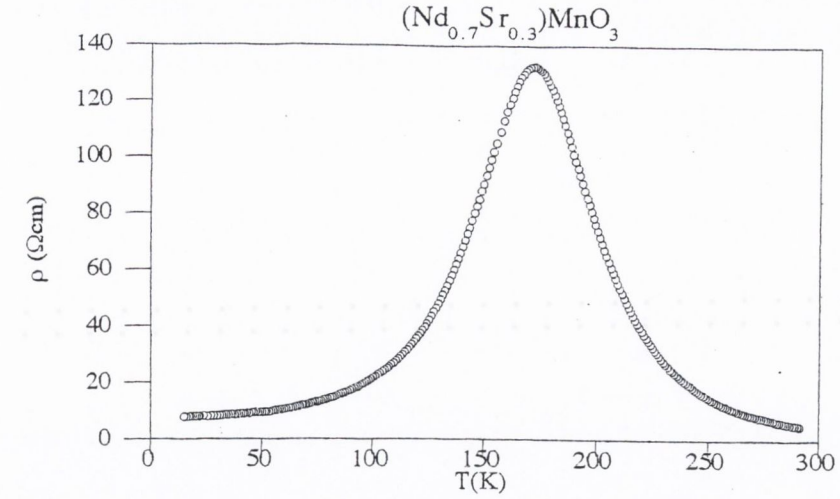

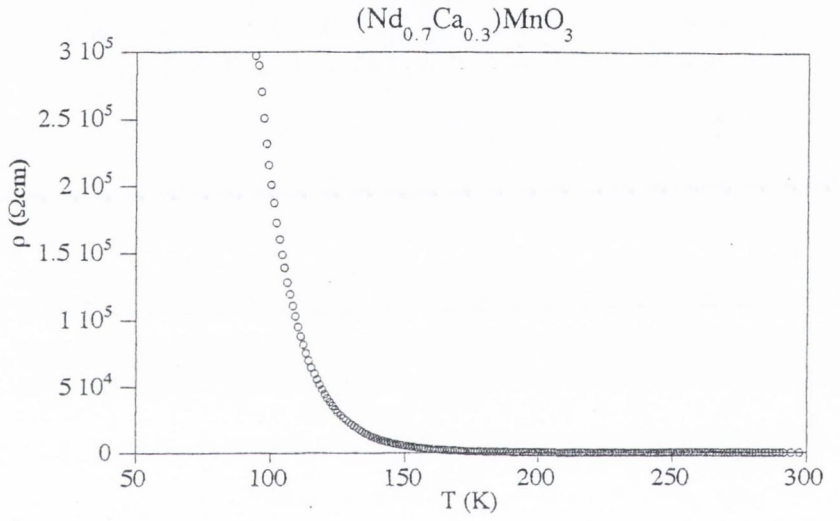

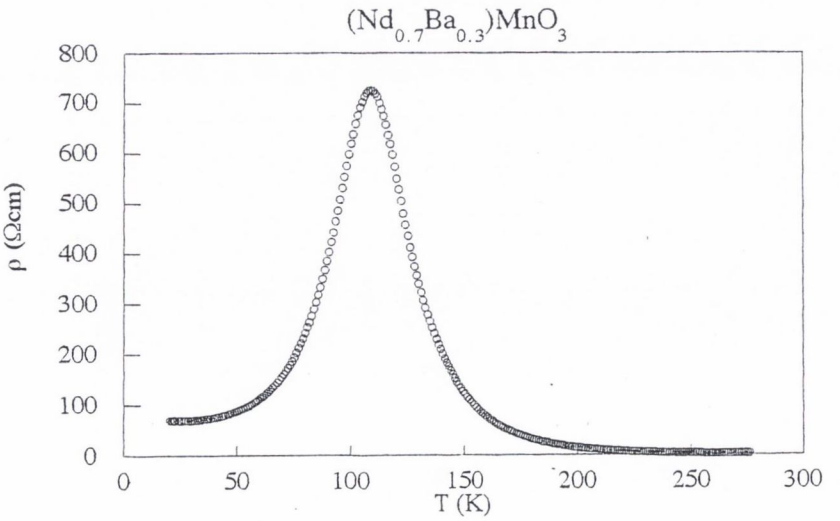

Figure 3.6 (c) Temperature dependence of resistivity for $(Nd_{0.7}A'_{0.3})MnO_3$; A' = Sr, Ca, Ba.

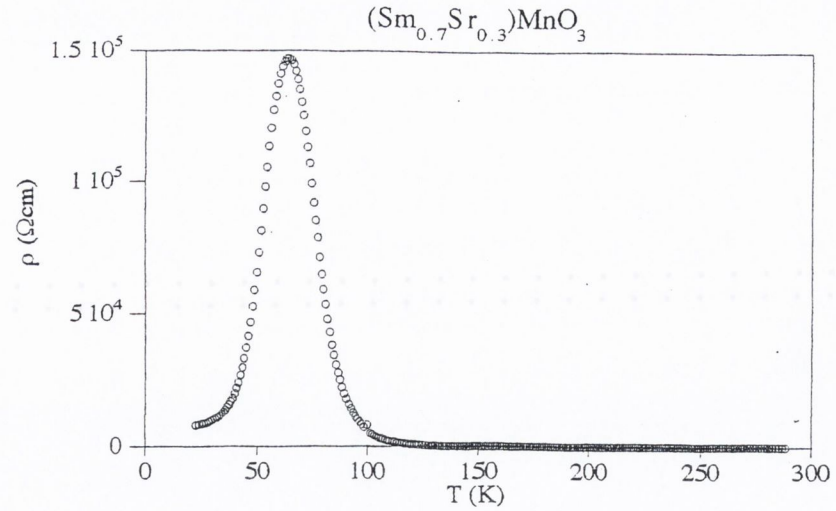

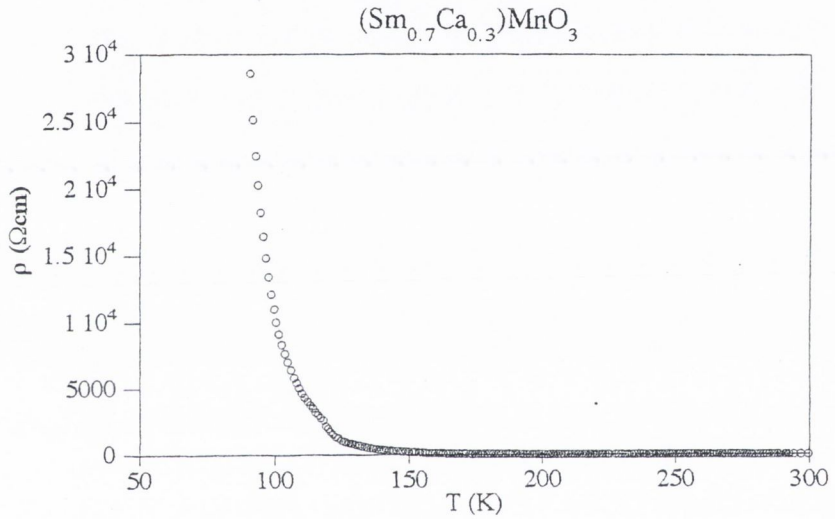

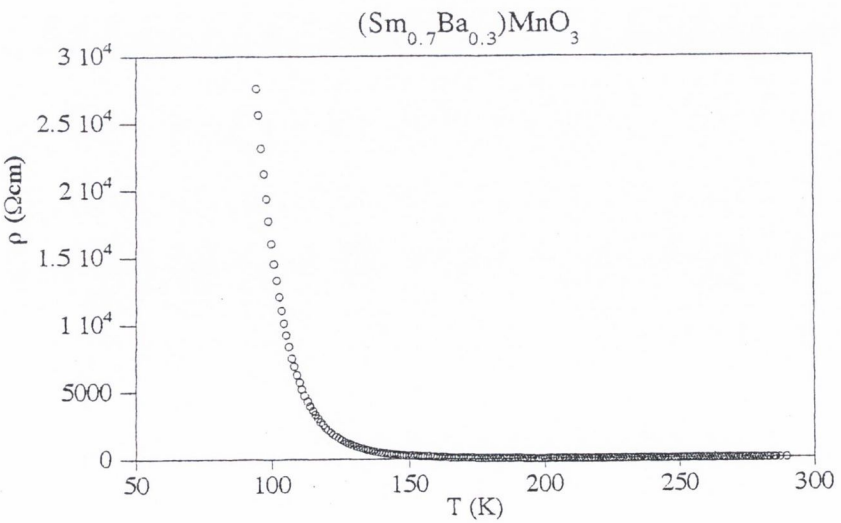

Figure 3.6 (d) Temperature dependence of resistivity for $(Sm_{0.7}A'_{0.3})MnO_3$; A' = Sr, Ca, Ba.

Compound	$T_C(K)$	$T_p(K)$	$\rho_p(\Omega cm)$	ρ_{RT} (Ωcm)	$\rho_0(\Omega cm)$	γ
				$T(K)$	$T(K)$	$(mJmol^{-1}K^{-2})$
$(La_{0.7}Sr_{0.3})MnO_3$	368	344	3.5 x 10^{-5}	2.98 x 10^{-5} (292)	1.64 x 10^{-5}	6.0
$(La_{0.7}Ca_{0.3})MnO_3$	250	235	7.3 x 10^{-2}	5 x 10^{-2} (290)	7.0 x 10^{-3} (17)	5.2
$(La_{0.7}Ba_{0.3})MnO_3$	350	250	8.0 x 10^{-2}	7.6 x 10^{-2} (292)	4.1 x 10^{-2} (17)	6.1
$(Pr_{0.7}Sr_{0.3})MnO_3$	288	237	1.17	0.94 (298)	0.04(17)	
$(Pr_{0.7}Ca_{0.3})MnO_3$	220	-	-	1.62x10^2(300)	-	
$(Pr_{0.7}Ba_{0.3})MnO_3$	177	140	1.36	0.20 (300)	0.78 (20)	
$(Nd_{0.7}Sr_{0.3})MnO_3$	220	172	132.30	4.94 (290)	7.69 (14)	
$(Nd_{0.7}Ca_{0.3})MnO_3$	114	-	-	13.86 (297)	-	
$(Nd_{0.7}Ba_{0.3})MnO_3$	143	107	724.12	1.62 (276)	57.88 (20)	
$(Sm_{0.7}Sr_{0.3})MnO_3$	88	65	1.47 x 10^5	0.72 (288)	7.18 x 10^3	
$(Sm_{0.7}Ca_{0.3})MnO_3$	85	-	-	0.78 (300)	-	
$(Sm_{0.7}Ba_{0.3})MnO_3$	91	-	-	1.16 (290)	-	

Table 3.1 A summary of parameters determined from the measured temperature dependence of resistivity.

Compound	T range (K)	$T^{-1}.\ln(\rho)$	$T^{-1}.\ln(\frac{\rho}{T})$	$T^{-\frac{1}{4}}.\ln(\rho)$	$T^{-\frac{1}{4}}.\ln(\frac{\rho}{T})$
$(La_{0.7}Sr_{0.3})MnO_3$					
$(La_{0.7}Ba_{0.3})MnO_3$	250 → 292	0.91449	0.99393	0.92016	0.99865
$(La_{0.7}Ca_{0.3})MnO_3$	240 → 290	0.99927	0.99969	0.99953	0.99969
$(Pr_{0.7}Sr_{0.3})MnO_3$	250 → 288	0.96330	0.96329	0.99571	0.99888
$(Pr_{0.7}Ba_{0.3})MnO_3$	160 → 276	0.95557	0.96619	0.97326	0.98138
$(Pr_{0.7}Ca_{0.3})MnO_3$	90→ 282	0.84701	0.87702	0.89184	0.96395
$(Nd_{0.7}Sr_{0.3})MnO_3$	180 → 292	0.99471	0.99525	0.99821	0.99854
$(Nd_{0.7}Ba_{0.3})MnO_3$	114 → 276	0.99309	0.99939	0.99940	0.99944
$(Nd_{0.7}Ca_{0.3})MnO_3$	94 → 297	0.98812	0.98831	0.99831	0.99851
$(Sm_{0.7}Sr_{0.3})MnO_3$	67 → 288	0.99053	0.98005	0.99725	0.99812
$(Sm_{0.7}Ba_{0.3})MnO_3$	94 → 290	0.99690	0.99636	0.99935	0.99958
$(Sm_{0.7}Ca_{0.3})MnO_3$	71 → 300	0.98972	0.98908	0.99983	0.99985

Table 3.2 The correlation coefficient evaluated from fitting the data in the thermally activated regime to the models given in section 3.2.2.

3.5 Discussion

Heat capacity measurements in the range 1.5 to 20 K for four samples, $(La_{0.7}Sr_{0.3})MnO_3$, $(La_{0.7}Ca_{0.3})MnO_3$, $(La_{0.7}Ba_{0.3})MnO_3$ and $(Nd_{0.7}Ba_{0.3})MnO_3$ are presented in figure 3.5. The data for the La compounds can all be fitted using the relation for the usual temperature dependence of a metal, equation 21. Thus, through plotting $\frac{C}{T}$ versus T^2, the y-axis intercept gives the value of the γ coefficients which are listed in Table 3.1. (However, the large excess heat capacity displayed by the neodymium perovskites below 40 K, prevent the quanititative separation of the γT term. This Schottky anomaly most likely originates from the crystal field of the Nd^{3+} ion which orders magnetically at $\sim 1K$ [section 4.4]).

Using relation (23) and $\gamma \sim 6$ $mJmol^{-1}K^{-2}$, density = 4605 kg/m^3 and molar mass = 226 x 10^{-3} kg/mol, experimentally determined for $(La_{0.7}Sr_{0.3})MnO_3$, yields a value of carrier density at the Fermi level of $N(E_F) \sim 3 \times 10^{28}$ $m^{-3}eV^{-1}$.

As previously discussed [section 3.2.2(3)], inserting this value into a VRH model based on Anderson localisation, yielded implausible localisation and hopping lengths; thus inspiring an additional localisation mechanism of magnetic origin to be invoked and the consequent formulation of the magnetic localisation theory.

As illustrated in Table 3.1, the transport behaviour of the twelve manganites studied may be divided into two distinct categories: compounds which show an activated conduction down to the lowest temperatures and those which exhibit a transition from an activated conduction mechanism to a metallic regime as the temperature is lowered. For all twelve samples, without exception, the data corresponding to activated conduction are best fitted to a variable range hopping law, $T^{-\frac{1}{4}}.\ln(\frac{\rho}{T})$ [table 3.2].

The latter result was originally explained in terms of spatial fluctuations in the Coulomb and spin-dependent potentials which localise the $e_g^{\uparrow}(\sigma^*$ band) electrons in large wave packets (with respect to the Mn-Mn separation) necessitating hops beyond nearest neighbours to sites with a smaller potential difference. A self-consistent theory of magnetic localisation was formulated, through incorporating random, spin-dependent potential fluctuations of magnetic origin into Mott's original variable-range hopping theory, as previously outlined in 3.2.2(3). Within this model, the observed metal–insulator transition is attributed to a narrowing of the random distribution of spin directions in the internal molecular field below T_C, leading to a decrease in the average magnetic potential fluctuations, ΔV.

The origin of the colossal magnetoresistance effect in an applied field is similarly explained. The notable absence of the metal-insulator transition in four of the compounds studied, namely, $(Pr_{0.7}Ca_{0.3})MnO_3$, $(Nd_{0.7}Ca_{0.3})MnO_3$, $(Sm_{0.7}Ca_{0.3})MnO_3$ and $(Sm_{0.7}Ba_{0.3})MnO_3$, is also broadly compatible with the rudiments of this theory. Viewed in terms of A-site cation radii [section 2.3.2], these Ca^{2+} containing manganites represent those samples with the smallest weighted average A-site radius, $< r_A >$, whereas $(Sm_{0.7}Ba_{0.3})MnO_3$ is the compound with the largest A-site ionic size mismatch as expressed by the variance σ^2, noted in table 2.3. The influence of $< r_A >$ and the corresponding Mn-O-Mn bond angle on the transfer integral t_{ij} [equation 3.2] and e_g conduction bandwidth, W, is derived in the following chapter [section 4.2.4]. Here, however, let it suffice to note that the narrower, occupied σ^* bandwidth, W, characteristic of compounds with a decreased Mn-O-Mn bond angle, may be sufficiently reduced so as to maintain the ratio $\Delta V/W$ above the critical value necessary for the weak localisation of e_g electrons on an extended length scale consistent with the ferromagnetic interaction. The influence of a large A-site cation size mismatch is consistent with this interpretation [102].

Despite the successful reproduction of the manganites' experimental behaviour by the magnetic localisation model [103], and the ubiquitous observation of a $T^{-\frac{1}{4}}$ resistivity variation [104], the extension of a theory initially proposed in the low temperature limit, to a higher temperature regime raises some concern. Mott's original theory was proposed in the low temeperature

limit where electron hopping is always of variable-range type since the thermal energy is insufficient to allow electrons to hop to their nearest neighbours. Thus, it is more favourable for the electrons to hop further to find a site with a smaller potential difference. An inherent difficulty in applying low temperature physics to higher temperature regimes, is that quantum coherent states extending across many atoms are disrupted by additional energy contributions, most notably, phonon interactions. It therefore becomes increasingly difficult to write good quantum mechanical wavefunctions, as required by the VRH theory. Thus, at higher temperatures, nearest-neighbour hopping ($\ln\rho \sim \frac{1}{T}$) is the more likely activated conduction mechanism.

As mentioned above [section 3.2.2(3)], Ziese's conclusion that VRH behaviour is an extrinsic transport mechanism, offers a plausible resolution of these conflicting observations. However, this statement implies that resistivity data originating from polycrystalline materials can merely provide qualitative analysis of the transport mechanisms in the manganites. Furthermore, the use of the intrinsic density of states in the calculation of a localisation length associated with an extrinsic mechanism is difficult to justify.

In the absence of a complimentary set of $\rho(T)$ data measured on single crystal samples - which through comparison with the data set presented could conclusively separate the intrinsic and extrinsic transport mechanisms - the observation of a ferromagnetic insulating state in four samples remains the most noteworthy result. Assuming, in accordance with Ziese's study, that the intrinsic resistivity of the manganites in the paramagnetic regime is best described by hopping of small polarons in the adiabatic limit, the absence of a metal-insulator transition in these compounds is re-addressed within the corresponding theoretical framework developed by Millis *et al.* [see section 3.2.1]. In this model, the dynamic Jahn-Teller effect leads to the localisation of conduction band electrons as small polarons in the high temperature regime. The competition between electron itinerancy and self-trapping is controlled by the dimensionless ratio, λ_{eff}, of the Jahn-Teller stabilisation energy, δ_{JT} (also referred to as the "self-trapping energy") to electron itinerancy energy, parametrised by an effective hopping matrix element t_{eff} (directly corresponding to the transfer integral, t_{ij} of equation 3.1). The reduction of λ_{eff} below a critical value, λ_C induces the expansion of small polarons into band electrons; double-exchange leads to an increase in t_{eff} as T is reduced through T_C . However, as outlined with respect to the analogous role of $\Delta V/W$ in the magnetic localisation model above, for those compounds with small $<r_A>$, t_{eff} is much reduced, thus off-setting the effect of lowering the temperature.

To summarise, the measured transport properties of these twelve polycrystalline manganites originally provided the foundation for a theory of electron localisation which influenced earlier discussion of the manganites transport properties. However, in light of recent results, the data are best interpreted in terms of a variable-range hopping mechanism which is attributed to extrinsic effects such as electron tunneling through grain boundaries. Theories of small magnetopolaron formation due to the dynamic Jahn-Teller effect may go some

way to describing the intrinsic properties of these materials; attributing the essential physics of the metal-insulator transition to strong-electron phonon coupling within the framework of double-exchange.

[1] G. H. Jonker and J. H. Van Santen, Physica **16**, 337, (1950).

[2] J. H. Van Santen and G. H. Jonker, Physica **16**, 599, (1950).

[3] J. Volger, Physica, **20**, 49, (1955).

[4] C. W. Searle and S. T. Wang, Canadian Journal of Physics, **48**, 2023, (1970).

[5] C. W. Searle and S. T. Wang, Canadian Journal of Physics, **47**, 2703, (1969).

[6] A. H. Morrish, B. J. Evans, J. A. Eaton, L. K. Leung, Canadian Journal of Physics, **47**, 2691, (1969).

[7] L. K. Leung, A. H. Morrish and C. W. Searle, Canadian Journal of Physics, **47**, 2697, (1969).

[8] R. vonHelmholt, J. Wecker, B. Holzapfel, L Schultz and K. Samwer, Physical Review Letters, **71**, 2331, (1993).

[9] K. Chahara, T. Ohno, M. Kasai and Y. Kozono, Applied Physics Letters, **62**, 1990, (1993).

[10] S. Jin, M. McCormack, T. H. Tiefel and R. Ramesh, Journal of Applied Physics, **76**, 6929, (1994).

[11] M. Baibich, J.-M. Broto, A. Fert, F. Nguyen Van Dau, F. Petroff, P. Etienne, G. Creuzet, A. Fredrich and J. Chazelas, Physical Review Letters, **61**, 2472, (1988).

[12] R. Mahendiran, R. Mahesh, A. K. Rauchauhuri and C. N. R. Rao, Physical Review B 53, 12160, (1996)

[13] Philosophical Transactions of the Royal Society London A, **356**, 1635, (1998).

[14] J. S. Fontcuberta, Philosophical Transactions of the Royal Society London A, **356**, 1577, (1998).

[15] K. Khazeni, Y. X. Jia, V. H Crespi, L. Lu, A. Zettl and M. L. Cohen, Journal of Physics: Condensed Matter, **8**, 7723, (1996).

[16] H. Yoshizawa, H. Kawano, Y. Tomioka and Y. Rokura, Journal of the Physical Society of Japan, **65**, 1043, (1996).

[17] G. C. Xiong, Q. Li, H. L. Ju, S. N. Mao, L. Senapati, S. S. Li, R. T. Greene and T. Venkatesan, Applied Physics Letters, 66, 1427, (1995).

[18] G. C. Xiong, Q. Li, H. L. Ju, R. L. Greene and T. Venkatesan, Applied Physics Letters, 66, 1689, (1995).

[19] N-C. Yeh, R. P. Vasquez, J. Y. T. Yeh and C. C. Fu, *Proceedings of Materials Research Society Meeting*, San Fransisco, California, (Pittsburgh Pennsylvania: Materials REsearch Society), 1997.

[20] N-C. Yeh, C. C.Fu, J. Y. T. Wei, R. P. Vasquez et al , Journal of Applied Physics, **81**, 97, (1997).

[21] S. Jin, T. H. Tiefel, M. McCormack, H. M. O'Bryen, L. H. Chen, R. Ramesh and D. Schurig, Applied Physics Letters, **67**, 557, (1995).

[22] H. Y. Hwang, S. W. Cheong, N. P. Ong and B. Batlogg, Physical Review Letters, **77**, 2041, (1996).

[23] J. S. Helman and B. Abeles, Physical Review Letters, **37**, 1429, (1976).

[24] A. E. Berkowitz, J. R. Mitchell, M. J. Carey, A. P. Young, S. Zhang, F. E. Spada, F. T. Parker, A. Hutten and G. Thomas, Physical Review Letters, **68**, 3745, (1992).

[25] H. L. Ju and H. Sohn, solid State Communications, **102**, 463, (1997).

[26] Ll. Balcells, J. Fontcuberta, B. Martinez and X. Obradors, Journal of Physics - condensed matter, **10**, 1883, (1998).

[27] G. J. Snyder, M. R. Beasley, T. H. Geballe, R. Kiskes, S. DiCarolis, Applied Physics Letters, **69**, 4254, (1996).

[28] R. Shreekala, M. Rajeshwari, K. Ghosh, A. Goyal, J. Y. Gu, C. Kwon, Z. Trajanovic, T. Boettcher, R. L. Green, R. Ramesh and T. Venkatesan, Applied Physics Letters, **71**, 282, (1997).

[29] X. W. Li, A. Gupta, G. Xiao and G. Q. Gong, Applied Physics Letters, **71**, 1124, (1997).

[30] J. Y. Gu, C. Kwon, M. C. Robson, Z. Trajanovic, K. Ghosh and R. P. Sharma, Applied Physics Letters, **70**, 1763, (1997).

[31] A. Gupta, G. Q. Gong, G. Xiao, P. R. Duncombe, P. Lecoeur, P. Trouillard, Y. Y. Wang, V. P. Dravid and J. Z. Sun, Applied Physics Letters, **69**, 3266, (1996).

[32] N. D. Mathur, G. Burnell, S. P. Isaac, T. J. Jackson, B-S. Teo, J. L. MacManus-Driscoll, L. F. Cohen, J. E. Evetts and M. G. Blamire, Nature, **387**, 266, (1997).

[33] K. Steenbeck, T. eick, K. Kirsch, K. O'Donnell and E. Steinbeiß, Applied Physics Letters, **71**, 968, (1997).

[34] J. M. D. Coey, Philosophical Transactions of the Royal Society London A, **356**, 1519, (1998).

[35] K. Kubo and N. Ohata, Journal of the Physical Society of Japan, **33**, 21, (1971).

[36] P. W. Anderson and H. Hasegawa, Physical Review **100**, 675, (1955).

[37] N. Furukawa, Journal of the Physical Society of Japan, **63**, 3214, (1994).

[38] A. J. Millis, P. B. Littlewood and B. I. Shraiman, Physical Review Letters, **74**, 5144, (1995).

[39] A. Georges and B. G. Kotliar, Physical Review B **45**, 6479, (1992).

[40] H. Röder, J. Zang and A. R. Bishop, Physical Review Letters, **76**, 1356, (1996).

[41] C.M. Varma, Physical Review B **54**, 7328, (1996).

[42] E. L. Nagaev, Physical Review B **54**, 16 608, (1996).

[43] M. Viret, L. Ranno and J .M. D. Coey, Physical Review B **55**. 8067, (1997).

[44] N. F. Mott, *Metal-Insulator Transitions* (2nd edition), (Taylor and Francis, 1990).

[45] R. M. Kusters, J. Singleton and D. A. Keen, Physica B **155**, 362, (1989).

[46] M. F. Hundley, M. Hawley, R. H. Heffner, Q. X Jia, J. J. Neumeier, J. Tesmer, J. D. Thompson and X. D. Wu, Applied Physics Letters, **67**, 860, (1995).

[47] G. C. Xiong, S. Bhagat, Q. Li, M. Dominguez,H. Ju, R. Greene and T. Venkatesan, Solid State Communications, **97**, 599, (1996).

[48] J.-H. Park, C. T. Chen, S. -W. Cheong, W. Bao, G. Meigs, V. Chakarian and Y.U. Idzerda, Physical Review Letters, **76**, 4215, (1996).

[49] J.-H. Park, C. T. Chen, S. -W. Cheong, W. Bao, G. Meigs, V. Chakarian and Y. U. Idzerda, Journal of Applied Physics, **79**, 4558, (1996).

[50] T. Holstein, Annalen Physik, 8, 343, (1959).

[51] P. Gerthsen and K. H. Härdtl, Zeitschrift Naturforschung (a), **17**, 514, (1962).

[52] R. R. Heikes, R. C. Miller and R. Mazelsky, Physica, **30**, 1600, (1962).

[53] G. J. Snyder, R. Hiskes, S. DiCarolis, M. R. Beasley and T. H. Geballe, Physical Review B **53**, 14434, (1996).

[54] M. Jaime, H. T. Hardner, M. B. Salamon, M. Ruinstein, P. Dorsey and D. Emin, Physical Review Letters, **78**, 951, (1997).

[55] M. Jaime, H. Hardner, M.B. Salamon , M. Rubinstein, P. Dorsey and D. Emin, Journal of Applied Physics, **81**, 4958, (1997).

[56] V. Caigneart, E. Suard, A. Maignan, C. Simon and B. Raveau, Jounral of Magnetism and Magnetic Materials, **153**, L260, (1996).

[57] J. L. Garcia-Munoz, J. Fontcuberta, M. Suuaidi and X. Obradors, Journal of Physics:

Condensed Matter, **8**, L787, (1996).

[58] P. G. Radaelli, M. Marezio, H. Y.Hwang, S-W. Cheong and B. Batlogg, Physical Review B **54**, 8992, (1996).

[59] D. N. Argyriou, J. F. Mitchell, C. D. Potter, D. G. Hinks, J. D. Jordensen, and S. D. Bader, Physical Review Letters, **76**, 3826, (1996).

[60] S. G. Kaplan, M. Quijada, H. D. Drew, D. B. Tanner, C. G. Xiong, R. Ramesh, C. Kwon and T. Venkatesan, Physical Review Letters, **76**, 2081, (1996).

[61] K. H. Kim, Physical Review Letters, **77**, 1877, (1996).

[62] C. H. Booth, F. Bridges, G. J. Snyder and G. T. Geballe, Physical Review B **54**, R15606, (1996).

[63] C. H. Booth, F. Bridges, G. H. Kwei, J.M. Lawrence, A. L. Cornelius and J. J. Neumeier, Physical Review B **57**, 10440, (1998).

[64] J. Tanaka, M. Umehara, S. Tamura, M. Tsukioka and S. Ehara, Journal of the Physical Society of Japan, **51**, 1236, (1982).

[65] V. H. Crespi, L. Lu, Y. X. Jia, K. Khazeni, A. Zettl and M.Cohen, Physical Review B **53**, 14303, (1996).

[66] J-S. Zhou, W. Archibald and J. B. Goodenough, Nature **381**, 770, (1996).

[67] T. T. Palstra, A. P. Ramirez, S-W. Cheong, B. R. Zegarski, P. Schiffer and J. Zaanen, Physical Review B **56**, 5104, (1997).

[68] M. F. Hundley and J. J. Neumeier, Physical Review B **55**, 11511, (1997).

[69] G. Zhao, K. Conder, H. Keller and K. A. Müller, Nature 381, 676, (1996).

[70] G. Zhao, M. B. Hunt and H. Keller, Physical Review Letters, 78, 955, (1997).

[71] I Isaac and J. P. Franck, Physical Review B 57, R5602, (1998).

[72] R. H. Heffner, L. P. Lee, M. F. Hundley, J. J. Neumeier, G. M. Luke, K. Kojima, B. Nachumi, Y. J. Uemura, D. E. MacLAughlin and S.-W. Cheong, Physical Review Letters, 77, 1869, (1996).

[73] M. Jaime, M. B. Salamon, K. Pettit, M. Rubinstein, R. E. Treece, J. S. Horowitz and D. E. Chrisey, Applied Physics Letters, **68**, 1576, (1996).

[74] J Fontcuberta, B. Martinez, A. Seffar, S. Piñol, J. L. Garcia-Munoz and X. Obradors, Europhysics Letters, **34**, 379, (1996).

[75] J M. De Teresa, M. R. Ibarra, P. A. Algrabel, C. Ritter, C, Marquina, J. Blasco, J. Garcia, A del Moral and Z. Arnold, Nature, **386**, 256, (1997).

[76] J. Lynn, R. Erwin, J. Borchers, Q. Huang and A. Santoro, Physical Review Letters, **76**, 4046, (1996).

[77] J. M. De Teresa, M. R. Ibarra, J. Blasco, J. Garcia, C. Marquina, P. Algrabel, Physical Review B **54**, 1187, (1996).

[78] C. Kapuzta, P. C. Reidel, G. J. Tomka, W. Kocemba, M. R. Ibarra, J. M. De Teresa, M. Vret and J. M. D. Coey, unpublished data.

[79] T. Kasuya and A.Yanase, Reviews of Modern Physics **40**, 684, (1968).

[80] L. Esaki, P. J. Stiles and S. von Molnár, Physical Review Letters, **19**, 852, (1967).

[81] S. Von Molnár, A. Briggs, J. Flouquet and G. REmenyi, Physical Review Letters, **51**, 706, (1983).

[82] D. Emin, M. S. Hillery and N. L. Liu, Physical Review B **35**, 641, (1987).

[83] T. Penney, M. W. Shafer and J. B. Torrance, Physical Review B **5**, 3669, (1972).

[84] D. Emin, contributed to *Electronic Properties of Amorphous Semiconductors*, edited by P. G. Le Comber and N. F. Mott, (Academic Press, New York, 1973).

[85] M. S. Hillery, D. Emin and N. H. Liu, Physical Review B **38**, 9771, (1988).

[86] A. Lanzara, N. L. Saini, M. Brunelli, F. Natali, A. Bianconi, P. G. Radaelli and S-W. Cheong, Physical Review Letters, **81**, 878, (1998).

[87] J. B. Goodenough and J. S. Zhou, Nature, **386**, 229, (1997).

[88] J. M. D. Coey, M. Viret, L. Ranno and K. Ounadjela, Physical Review Letters, **75**, 3910, (1995).

[89] Y. X. Jia, Li Lu, K. Khazeni, D. Yen, C. S. Lee and A. Zettl, Solid State Communications, **94**, 917, (1995).

[90] P. Wagner, V. Metlushko, L. Trappeniers, A. Vantomme, J. Vanacken, G. Kido, V. Moshchalkov and Y. Bruynserade, Physical Review B **55**, R14721, (1997).

[91] N. F. Mott and E. A. Davies, *Electronic processes in noncrystalline solids*, 2nd edition, (Oxford University Press, 1979).

[92] H. Boettger and V. Bryskin, Hopping conduction in solids, (Akademic-Verlag, Berlin, 1985).

[93] V. Ambegaokar, B. I. Halperin and J. S. Langer, Physical Review B **4**, 2612, (1971).

[94] M. Siese and C. Srinitiwarawong, Physical Review B **58**, 11519, (1998).

[95] P. Schiffer, A. P. Ramirez, W. Bao and S.-W. Cheong, Physical Review Letters, **75**, 3336, (1995).

[96] A. Urushibara, Y. Moritomo, T. Arima, A. Asamitsu, G. Kido and Y. Tokura, Physical Review B **51**, 14103, (1995).

[97] M. Jaime and M. B. Salamon, *Electronic Transport in La-Ca Manganites*, (Plenum Press, 1999).

[98] I. Mannari, Progress in Theoretical Physics, **22**, 325, (1959).

[99] J. J. Hamilton, E. L. Keatley, H. L. Ju, A. K. Raychaudhuri, V. N. Smolyaniova and R. L. Greene, Physical Review B 54, 14926, (1996).

[100] A. P. Ramirez, P. Schiffer, S-W. Cheong, W. Bao, T. T. M. Palstra, P. L. Gammel, D. J. Bishop and B. Zegarski, Physical Review Letters, **76**, 3188, (1996).

[101] B. F. Woodfield, M. L. Wilson and J. M. Byers, Physical Review Letters, **78**, 3201, (1997).

[102] L.M. Rodriguez-Martinez and J.P. Attfield, Physical Review B **54**, R15622, (1996).

[103] M. Viret, L. Ranno and J. M. D. Coey, Journal of Applied Physics, **81**, 4964, (1997).

[104] J. M. D. Coey, M. Viret and S. von Molnár, Advances in Physics, **48**, 167, (1999).

Chapter 4
Magnetic properties

4.1 Introduction

The first glimpse of the manganites' rich magnetic phase diagram was offered by Wollan and Koehler [1], courtesy of their extensive neutron and X-ray diffraction study of $(La_{1-x}Ca_x)MnO_3$, $0 \leq x \leq 1$. Amidst the variety of magnetic ground states [figure 1.4] the compound with x = 0.3 was established as the strongest ferromagnet -with a magnetic moment approaching the theoretical spin only value, 3.7 $\mu_B/formula\ unit-$ and the lowest resitivity, in accordance with the double-exchange model [chapter 1].

Despite its inadequacies at higher temperatures [3.2.2], double-exchange governs the manganites' low temperature physics and provides an accepted starting point for a microscopic description of their magnetic ground states; mobile electrons mediate the ferromagnetic double-exchange interaction through hopping between localised Mn sites with spin memory and the efficiency of the double-exchange mechanism is governed by the transfer integral, t_{ij} which describes the hopping of the itinerant-σ^* electrons between the adjacent Mn sites:

$$t_{ij} = b_\sigma cos(\frac{\theta ij}{2})$$

where θ_{ij} is the angle between the two spin directions and b_σ is the electron transfer matrix element which depends on the spatial wavefunctions. As derived later in this chapter [section 4.2.4], the structural distortion resulting from the reduced size of the A-site cations, relative to that of the oxygen anions, directly influences the σ^* bandwidth and consequently the transfer integral. Therefore, a collinear arrangement of Mn-O-Mn ions, characterised by a bond angle of 180° and global cubic symmetry, corresponds to maximum t_{ij} and optimised ferromagnetic exchange reflected in a high ordering temperature, T_C.

The ferromagnetic state resulting from double-exchange as the sole, dominant interaction, is expected to be 100% spin-polarised. Consideration of the Hund's rule on-site exchange interaction between the spin of an itinerant e_g electron (s $=\frac{1}{2}$) with that of a localised t_{2g} electron, (S $= \frac{3}{2}$) gives an exchange splitting, $U_{ex} = J_H(S+\frac{1}{2}) = 2J_H$. Optical conductivity data estimates U_{ex} = 2-3 eV [2], which exceeds the e_g electron bandwidth, W = 1eV, leading to a fully-spin polarised electronic density of states that is characteristic of *half-metallic ferromagnetism*. Defined by a semi-conductor-like energy gap for one of the spin projections at the Fermi level coexisting with the metallic behaviour of the other spin sub-band [figure 4.1], the half-metallic nature of the manganites has been widely discussed, [3] [4] [5]. A recent spin-resolved photoemission study of a $(La_{0.7}Sr_{0.3})MnO_3$ film determined an insulating gap

~0.6 eV on the occupied side of the minority-spin states and full polarisation of the majority spins at 40 K [6]. However, band structure calculations of $(La_{\frac{2}{3}}Ca_{\frac{1}{3}})MnO_3$ predicted a mere 36% spin-polarisation at the Fermi level [7] and other experimental techniques have yielded 54% [8] and 81% [9] for the conduction electrons of $(La_{\frac{2}{3}}Sr_{\frac{1}{3}})MnO_3$ tunnel junctions, as determined by previous spin-resolved tunneling measurements at 4.2K. Most recently, the spin polarization of $(La_{0.7}Sr_{0.3})MnO_3$ was estimated to be 78 $\pm$ 4% at 4.2 K, by a novel technique which measured the suppression of Andreev reflection at the interface of a superconding point contact and the material [10]. In short, conclusive evidence of half-metallic behaviour has yet to be demonstrated.

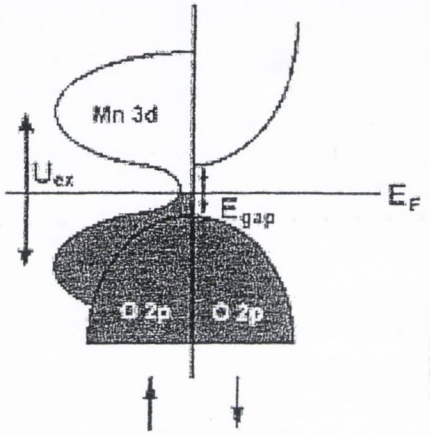

Figure 4.1 A schematic diagram showing the density of states for a postulated half-metallic ferromagnetic manganite.

Although the charge-ordering of Mn^{3+}/Mn^{4+} ions [11] is favoured by compounds with a typical doping ratio, x = $\frac{1}{8}$, $\frac{1}{2}$ or $\frac{3}{4}$, extensive neutron diffraction studies of $(Pr_{0.7}Ca_{0.3})MnO_3$ have shown both ferromagnetic and antiferromagnetic peaks below 220 K [12], suggesting local charge-order manifested as small domains of CE type antiferromagnetism [figure 1.4]. This compound may be regarded as an assembly of ferromagnetic and antiferromagnetic nanodomains, or as a ferromagnet with random spin canting so that the average angle between a manganese moment and the ferromagnetic z axis is about 60°. The transformation of this partly charge-ordered insulator into a ferromagnetic metal has been successfully achieved upon application of numerous external stimuli: a magnetic field [13]; pressure [14]; an electric current [15]; through irradiation with X-rays [16], infrared [17] and visible light [18]. This first-order magnetisation process, brought about at 4.2 K in an applied field of $\sim 6T$ is referred to as a "charge-melting" transition [4.3.4 (b)].

The preceeding chapter discussed the need to develop the double exchange mechanism in conjunction with other interactions so as to explain the most prominent feature of the manganites, namely the magnitude of the change in resistivity at the ferromagnetic transition [19]. As the temperature is raised, both double-exchange and polaronic distortions most likely due to the dynamic Jahn-Teller electron-lattice coupling of the Mn^{3+} ion are required to describe the magnetic structure of the x = 0.3 manganites. In 4.2.4 the paramagnetic

regime of the manganites under study is discussed with reference to the current, somewhat ambiguous picture of cluster formation above T_C.

Discussion of the manganites' magnetic structure has long neglected the direct contribution of the magnetic rare-earth ions of the A-site [20]. The detailed inelastic neutron scattering studies by Podlesnyak *et al.* represent conspicuous exceptions, in which the rare-earth energy levels of Pr^{3+} and Nd^{3+} in $PrGaO_3$ [21] and $NdGaO_3$ [22] were investigated. Likewise, through measuring the heat capacity of $NdGaO_3$, Bartolomé *et al.* [23] probed the magnetic interaction of the rare-earth ions; the non-magnetic Ga^{3+} ion facilitated the study of the isolated rare-earth in a perovskite environment. These gallates both crystallize in orthorhombically distorted variants of the ideal perovskite structure with characteristic space groups *Pbnm* and $Pbn2_1$ for $PrGaO_3$ and $NdGaO_3$ respectively. Their A-site point symmetry is significantly lowered from the ideal cubic, $m3m$ to a single mirror plane, m in the Pr compound and a C_2 two-fold axis in $NdGaO_3$. The crystal field resulting from this distorted environment serves to entirely lift the ninefold degeneracy of the ground state Pr^{3+} multiplet, $^3H_4$, leaving the rare-earth in a singlet ground state [figure 4.2(a)]. Moreover, the ground state $^4I_{\frac{9}{2}}$ multiplet of Nd^{3+} is split into the five Kramers doublets[4] of figure 4.2(b), with the 90 cm^{-1} energy gap between the ground and first excited doublet ensuring that at low temperatures, the ground doublet is the only occupied level.

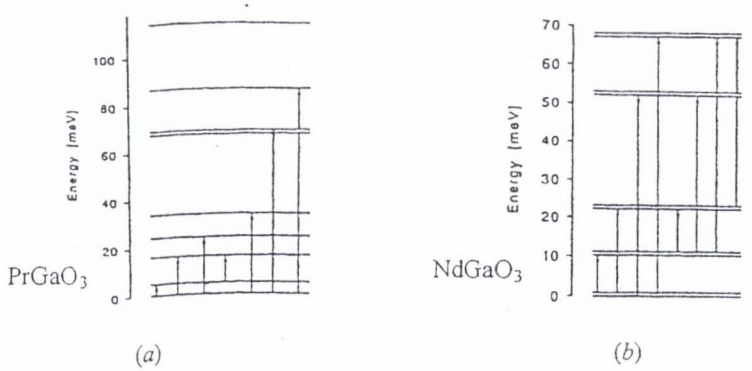

Figure 4.2 The energy-level scheme of (a) Pr^{3+} in $PrGaO_3$ and (b) Nd^{3+} in $NdGaO_3$ as determined by inelastic neutron scattering.

These results provided a basis for the calculation of the crystal field interaction at the rare-earth site of some of the Pr and Nd manganites. Theoretical calculation of these crystal field effects complement the experimental magnetisation data presented providing a more complete description of these compounds magnetic sublattice arrangements.

[4] If a system containing an odd number of electrons is placed in an external electric field (in this case the crystal field), at least a twofold degeneracy in the levels will remain. This theorem was expressed by Kramers [24] and the resulting twofold degenerate levels are thus named Kramers doublets.

With this aim in mind, this chapter concludes with a discussion of the inter- and intra-atomic coupling in the neodymium manganites, with reference to the dichroic spectra measured for these compounds using the powerful X-ray magnetic curcular dichroism technique described.

In conclusion, the magnetic structures of the manganese perovskites are described by double-exchange in conjunction with additional interactions. The antiferromagnetic superexchange interaction between the localised t_{2g} spins, the intersite Coulomb interaction betwen e_g electrons and the electron-lattice interaction occasionally compete with the ferromagnetism of double-exchange, to produce the complex but intriguing phase diagram characteristic of these materials.

4.2 AC-susceptibility measurements

The analysis of a sample's magnetic susceptibility provides qualititative information as to the strength of it's inherent magnetic interactions. Forty years ago, such investigations were carried out by Jonker [25] and Lotgering [26] to experimentally determine the contribution of the newly proposed "double-exchange" to the interactions in $La_{1-x}Ba_xMnO_3$ ($0 \leq x \leq 0.25$). Today, with the double-exchange mechanism generally accepted as providing a good description of the low temperature, ferromagnetic ground state of these materials, susceptibility analysis can contribute to the ongoing discussion regarding cluster or polaron formation in the managnites' high temperature phase, (see chapter 3), as an enhanced Curie-Weiss susceptibility would be a key signature of the magnetic polarons believed to exist above the ordering temperature T_C. The low field ac-susceptibility measurements presented provide a means of estimating these ordering temperatures, which are shown to correlate with the structural parameters introduced in chapter 2. Additionally, the measured data are discussed with reference to the postulated polarons of the paramagnetic regime.

4.2.1 Background

The magnetic susceptibility of a sample is the dimensionless quantity describing the response of the magnetization, M, of a material to a small change in the external field, H,

$$\chi = \frac{M}{H} \tag{1}$$

A rapid rise in the initial magnetic susceptibility of a sample with falling temperature marks the onset of magnetic order. By extrapolating the region of steepest descent on a plot of $1/\chi$ against T from its value at higher temperatures, the ordering temperature may be determined. This temperature dependence is expressed as the Curie-Weiss law,

$$\chi = \frac{C}{(T - \theta_p)} \tag{2}$$

where χ is the paramagnetic susceptibility, C the Curie constant and θ_p the

paramagnetic Curie temperature. The Curie constant for free ions, C, is given by

$$C = \frac{N\mu_0\mu_B^2 p_{eff}^2}{3k} \tag{3}$$

where N is the total number of paramagnetic entities per cubic metre; p_{eff}, the effective Bohr magneton number which is defined for 3d ions as $p_{eff} = g\sqrt{S(S+1)}$ where g is the Landé factor and S is the spin angular momentum quantum number.

It is customary to measure the initial susceptibility of a sample through applying a small, low-frequency alternating field. A suitable lock-in technique separates the induced in-phase and out-of-phase response of the induced signal, which corresponds to the real component χ' and imaginary (lossy) component, χ'' of the measured ac-susceptibility.

If the applied field is expressed as the sum of a static field, H and a sinusoidal ac-applied field of frequency $\omega = 2\pi f$ and amplitude H_1

$$H(t) = H + H_1 \cos\omega t \tag{4}$$

then the magnetization may be represented by

$$\begin{aligned} M(t) &= M_0 + M_1\cos(\omega t - \phi) \\ &= M_0 + M_1\cos\omega t\cos\phi + M_1\sin\omega t\sin\phi \end{aligned} \tag{4.5}$$

where M_0 is the equilibrium value of the magnetization in this static field and ϕ is the phase (or "loss") angle by which the magnetization lags behind the oscillating field. The static field is typically presumed parallel to the oscillating one, hence the equations may be written in scalar form. Then by analogy to equation 1.1 above,

$$\chi' = \frac{M_1\cos\phi}{H_1} \text{ and } \chi'' = \frac{M_1\sin\phi}{H_1}$$

so that $\chi'/\chi'' = \tan\phi$. Equation 1.4 then becomes

$$M(t) = \chi_0 H + \chi' H_1\cos\omega t + \chi'' H_1\sin\omega t \tag{6}$$

Thus, in complex notation

$$H(t) = H + H_1 e^{i\omega t} \tag{7}$$

and

$$M(t) = M_0 + \chi H_1 e^{i\omega t} \tag{8}$$

Thus,

$$\chi_{ac} = \chi' - i\chi'' = |\chi|\, e^{-i\phi} \tag{9}$$

χ' and χ'' show dependence on the magnitude of the static field H as well as the frequency of the ac-field. The variation of the real component, χ' with frequency ω is called the paramagnetic dispersion; χ'' the imaginary part of the ac-susceptibility is proportional to the energy absorbed by the substance from the oscillating field.

4.2.2 Experimental arrrangements

The mutual inductance method employed for measuring ac-susceptibility, involved applying an alternating magnetic field to the sample by means of a primary (magnetising) coil and detecting the induced emf with a system of two secondary (measuring and compensating) coils wound in opposite directions. The co-axial, concentric arrangement of these coils ensured that in the absence of a sample, no emf was induced in the sample space, whereas the emf induced in the secondary coil in the presence of a sample, was directly proportional to the magnetic susceptibility of that material,

$$U_{emf} = \frac{1}{\alpha} V \frac{\varpi}{2\pi} H_1 \chi_{ac} \tag{10}$$

where V is the volume of the sample, $\frac{\varpi}{2\pi}$ and H_1 the frequency of the alternating field and its amplitude respectively, whilst α is a calibration coefficient.

Measurements in the temperature range, 5 K - 295 K, and a 80A/m alternating applied field ($\frac{\varpi}{2\pi} = 1kHz$) were carrried out in a homemade co-axial susceptometer housed within an evacuated inner dewar which in turn was situated within a stainless steel chamber. Prior to the measurement, liquid nitrogen was poured into the outer chamber and liquid helium subsequently transferred to the inner dewar to reach the lowest temperatures. Data points were measured whilst heating the sample using a non-inductively wound manganin wire heater powered by an Isotherm power supply. A silicon diode was used as a temperature sensor, and the system was fully PC controlled. A second arrangement of concentric coils in conjunction with a non-inductively wound platinum coil heater was used to obtain data above room temperature under vacuum, for the samples, $(La_{0.7}Sr_{0.3})MnO_3$, $(La_{0.7}Ca_{0.3})MnO_3$,$(La_{0.7}Ba_{0.3})MnO_3$, $(Pr_{0.7}Sr_{0.3})MnO_3$ and $(Nd_{0.7}Sr_{0.3})MnO_3$.

The polycrystalline samples were prepared as narrow cuboids of typical dimensions 6mm x 2mm x 2mm so as to minimise demagnetising effects. [see 4.2.4]

4.2.3 Results

The real ac-susceptibility data, $\chi(T)$, measured for all twelve manganites, are presented in figure 4.3. The insert in each figure shows the $1/\chi(T)$ dependence for each sample, and the ordering temperatures evaluated from this data using equation 1.2 above, are summarised in the following Table 4.1.

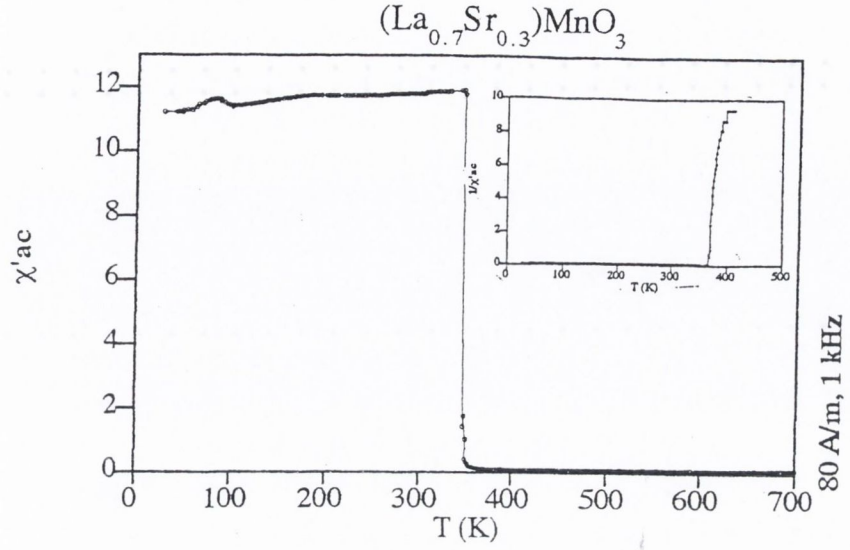
(La0.7Sr0.3)MnO3
χ'ac
T (K)
80 A/m, 1 kHz
1/χ'ac

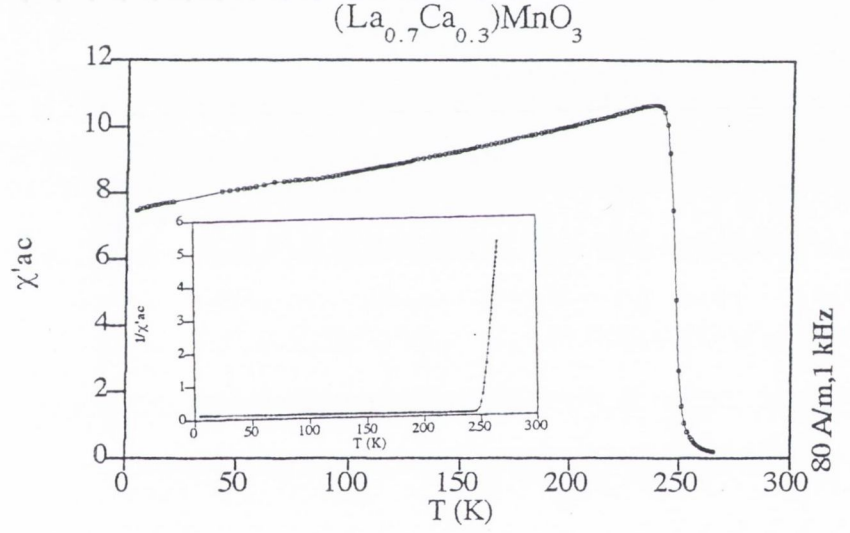
(La0.7Ca0.3)MnO3
χ'ac
T (K)
80 A/m,1 kHz
1/χ'ac

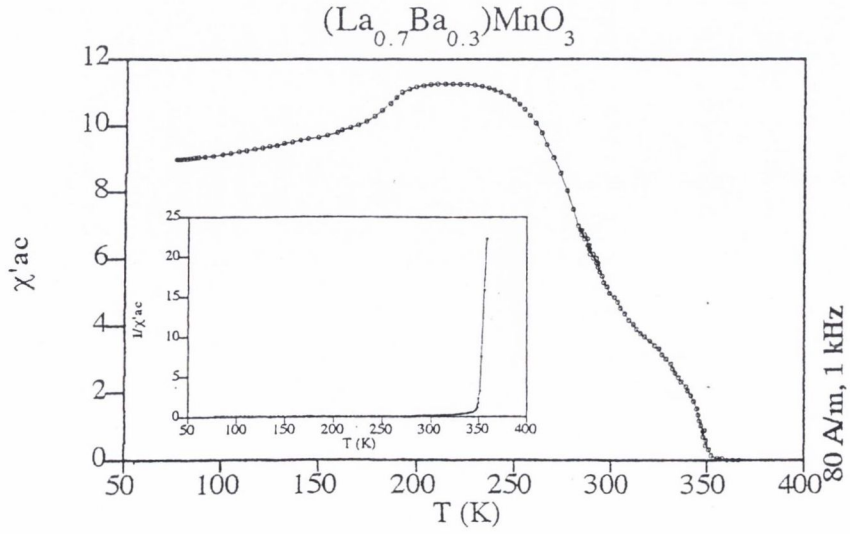
(La0.7Ba0.3)MnO3
χ'ac
T (K)
80 A/m, 1 kHz
1/χ'ac

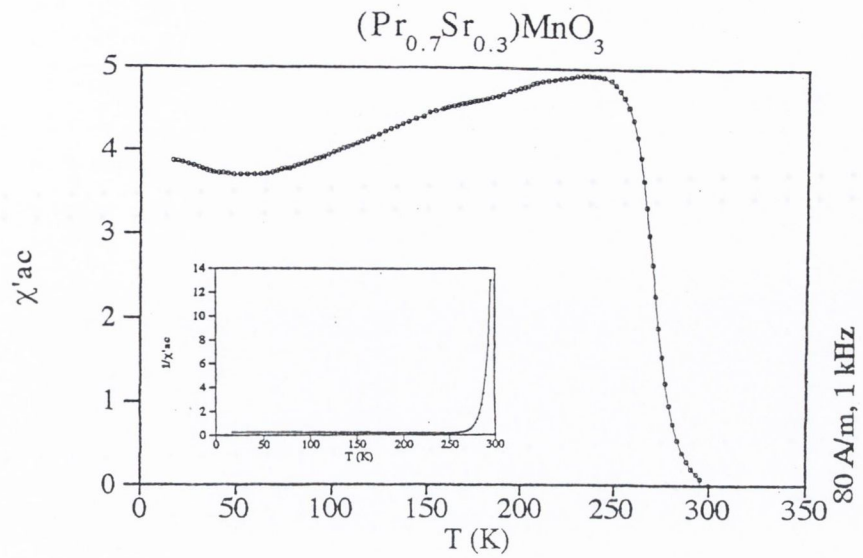
(Pr0.7Sr0.3)MnO3
χ'ac
T (K)
80 A/m, 1 kHz

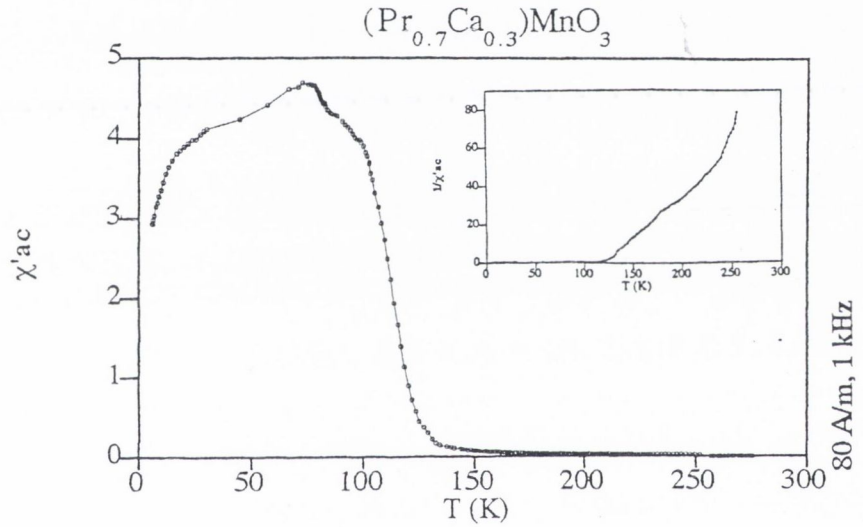
(Pr0.7Ca0.3)MnO3
χ'ac
T (K)
80 A/m, 1 kHz

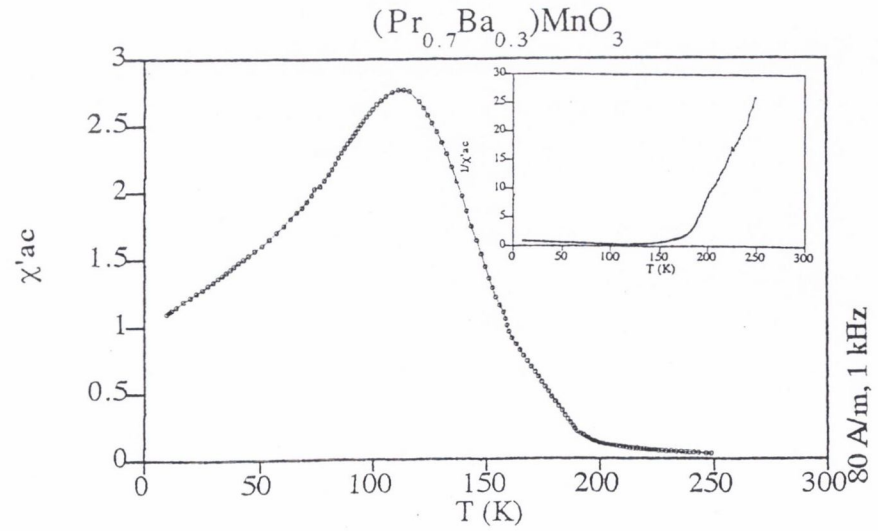
(Pr0.7Ba0.3)MnO3
χ'ac
T (K)
80 A/m, 1 kHz

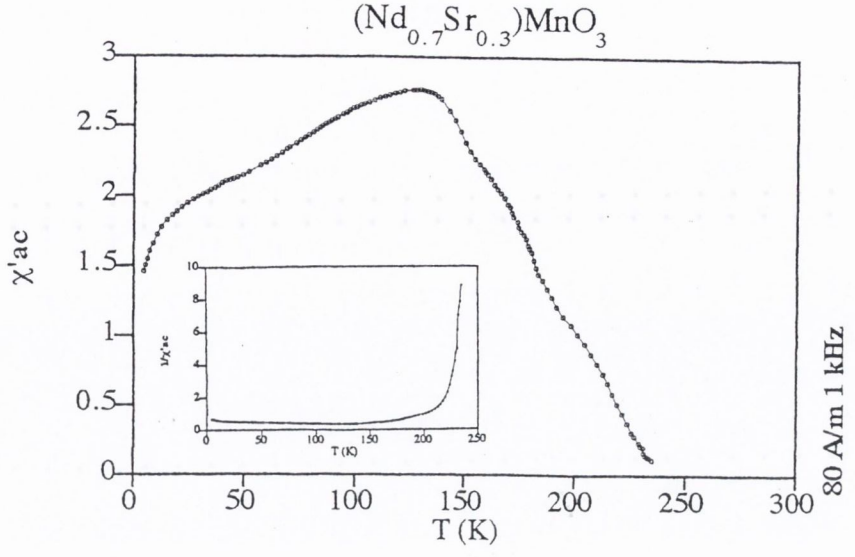
(Nd0.7Sr0.3)MnO3
χ'ac
T (K)
80 A/m 1 kHz

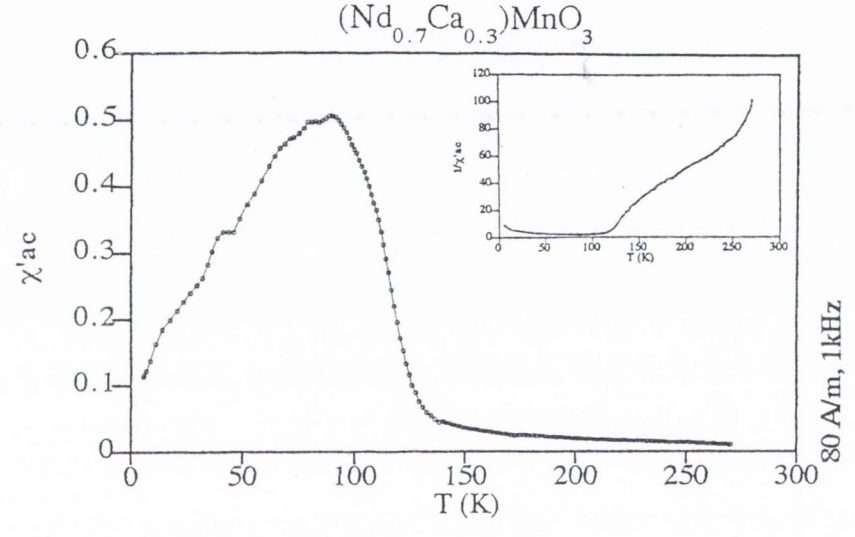
(Nd0.7Ca0.3)MnO3
χ'ac
T (K)
80 A/m, 1kHz

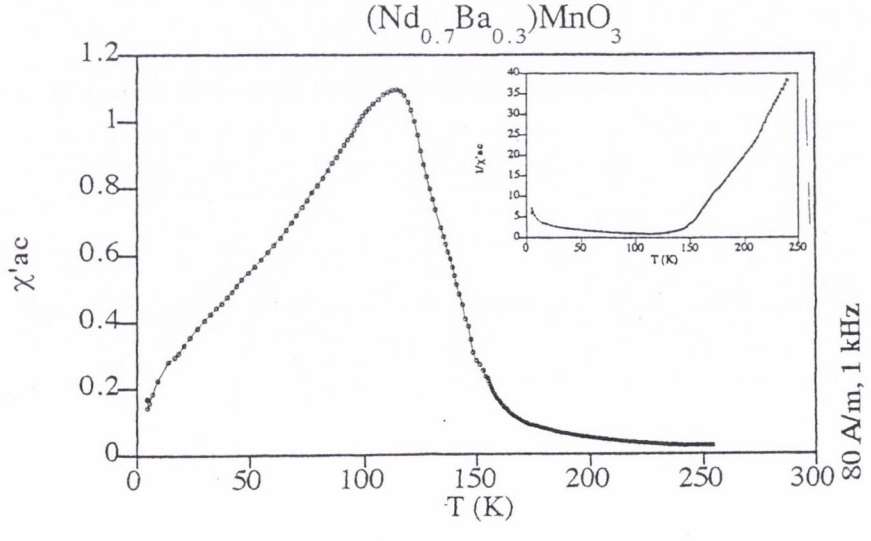
(Nd0.7Ba0.3)MnO3
χ'ac
T (K)
80 A/m, 1 kHz

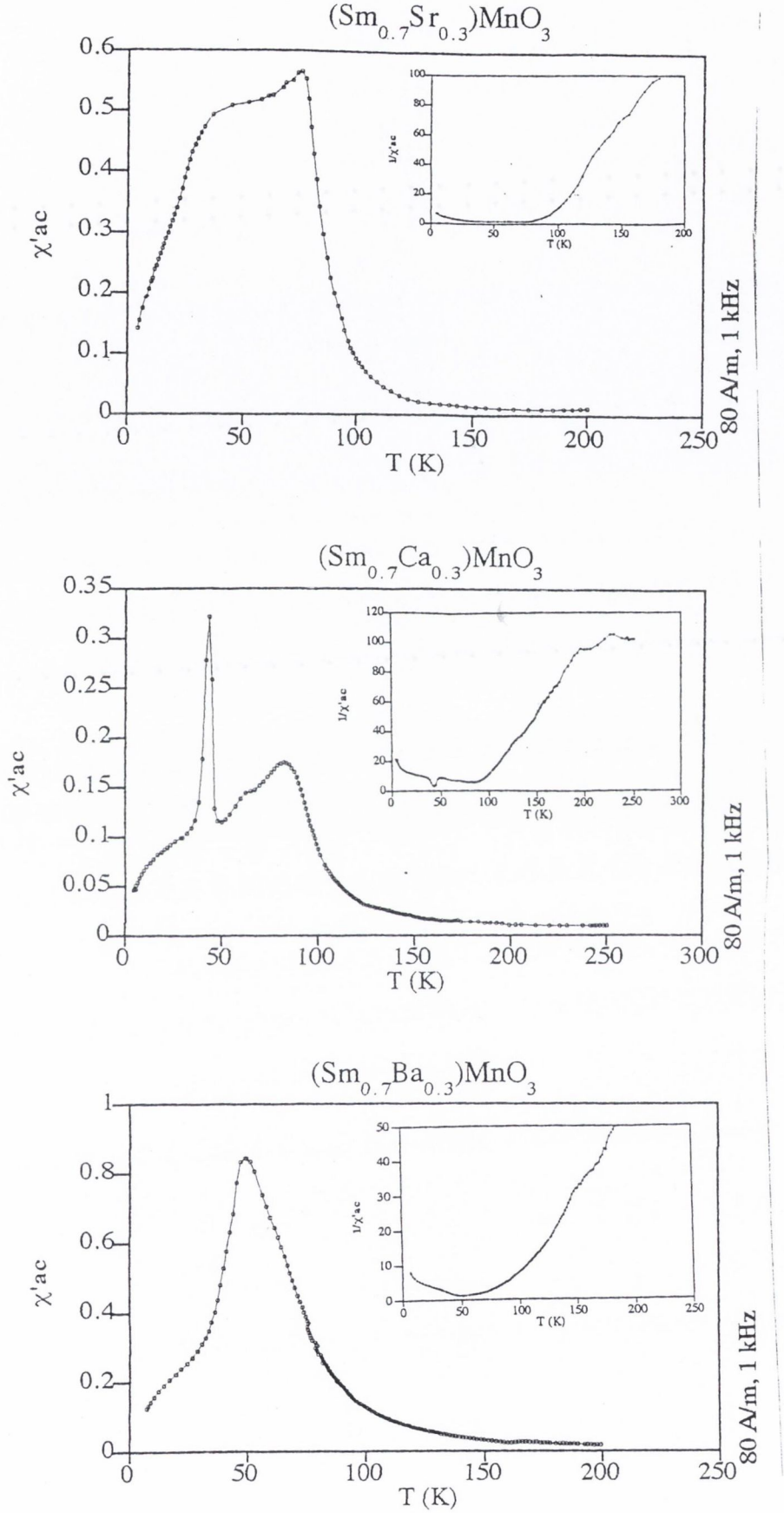

Figure 4.3 The real ac-susceptibility as a function of increasing temperature for the twelve manganites studied.

Compound	T_C (K)
$(La_{0.7}Sr_{0.3})MnO_3$	368
$(La_{0.7}Ca_{0.3})MnO_3$	250
$(La_{0.7}Ba_{0.3})MnO_3$	350
$(Pr_{0.7}Sr_{0.3})MnO_3$	288
$(Pr_{0.7}Ca_{0.3})MnO_3$	220
$(Pr_{0.7}Ba_{0.3})MnO_3$	177
$(Nd_{0.7}Sr_{0.3})MnO_3$	220
$(Nd_{0.7}Ca_{0.3})MnO_3$	114
$(Nd_{0.7}Ba_{0.3})MnO_3$	143
$(Sm_{0.7}Sr_{0.3})MnO_3$	88
$(Sm_{0.7}Ca_{0.3})MnO_3$	85
$(Sm_{0.7}Ba_{0.3})MnO_3$	91

Table 4.1 A summary of the ordering temperatures determined for all twelve manganites.

4.2.4 Discussion

The ac-susceptibility data are discussed with reference to the correlation of T_C with crystal structure, as represented by $< r_A >$ (the mean radius of the A-site cations) for the twelve manganites. A general discussion of the low temperature $\chi'(T)$ data is followed by a study of the$1/\chi'(T)$ behaviour above T_C in terms of both cluster formation and a possible distribution of T_C in a representative sample.

4.2.4.1 Correlation of T_C with crystal structure

It has long been established that the exchange interactions of the manganites are dependent on the interionic separation of the mangnese ions within the crystal lattice [25] [27] [28]. Moreover, the strength of these interactions correlate with the bond angle supported by two $Mn^{3+/4+}$ ions in octahedral sites. This was first demonstrated by Havinga [29] who calculated the Mn-O-Mn interbond angles of a series of distorted perovskites from their "pseudo-cubic" lattice parameters, assuming a model of stiff octahedra and a fixed Mn-O bond length. The validity of this model was brought into question following subsequent neutron powder diffraction studies [30], although the observed decrease in ordering temperature with decreasing Mn-O-Mn bond angle was evident. This relation was later quantitatively established by a neutron scattering study conducted by Hwang [31] on a series of ternary polycrystalline manganites, $(La_{0.7-x}Pr_x)Ca_{0.3}MnO_3$ and $(La_{0.7-y}Y_y)Ca_{0.3}MnO_3$. Through systematically varying the A site ionic radius, $< r_A >$, whilst maintaining the ratio Mn^{3+}/Mn^{4+}, the measured Mn-O-Mn bond angle could be decreased (from 180° for the ideal cubic perovskite) and so too, the ordering temperature, T_C.

Despite the unequivocal nature of this trend, a universal $< r_A > -T_C$ phase diagram [5] cannot be defined for the extensive data set studied here [32].

[5] Due to the proportionality that exists between $< r_A >$ and tolerance factor, t_0, these parameters may be used interchangeably during the following discussion.

This is illustrated in figure 4.4 (a). where the principal effect of reducing the lanthanide radius is to reduce T_C, *within a series in which the divalent cation is kept constant.* This apparent dependence on the nature of the A-site cation is also evident in figure 4.4 (b) in which T_C is shown to increase with decreasing A-site atomic mass.

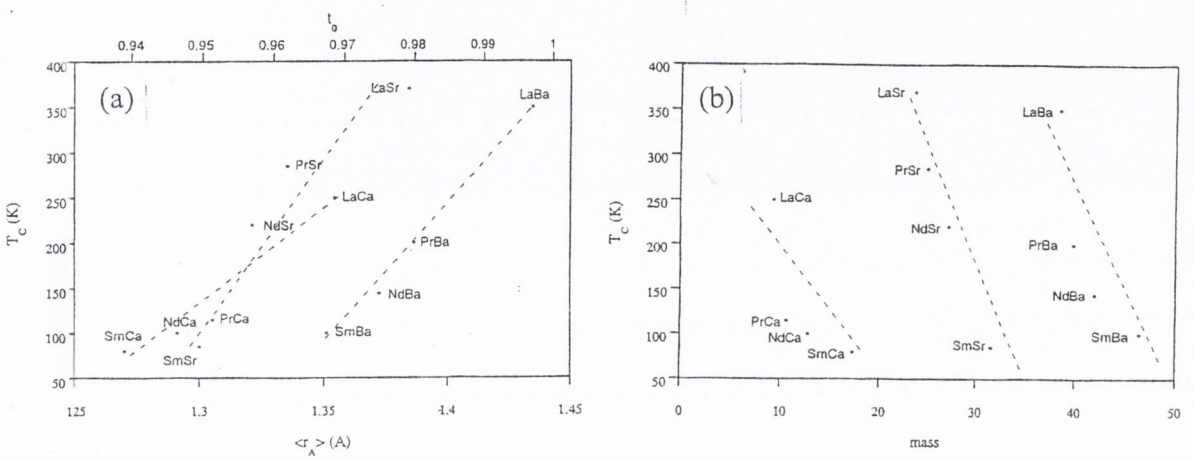

Figure 4.4(a) Ordering temperature, T_C versus average ionic radius of the A site $< r_A >$; (b) Ordering temperature, T_C, versus mass of the A site cations.

The influence of the divalent cation confuses the otherwise simple picture that relates the strength of the ferromagnetic exchange to the perovskites' bond angle and Mn-O bond length. The efficiency of the ferromagnetic double exchange mechanism is tuned by the transfer integral, t_{ij} which describes the hopping of itinerant-σ^* electrons between adjacent Mn sites:

$$t_{ij} = b_\sigma cos(\frac{\theta ij}{2}) \tag{11}$$

where θ_{ij} is the angle between the two spin directions and b_σ is the electron transfer matrix element which depends on the spatial wavefunctions. A reduction of $< r_A >$ results in the bending of the Mn-O-Mn bond angle from 180° to γ =$(180° - \phi)$ reducing b_σ

$$b_\sigma = \epsilon_s \lambda_s^2 + \epsilon_\sigma \lambda_\sigma^2 \cos\phi \tag{12}$$

which relates to the bandwidth

$$W \cong 2zb_\sigma \tag{13}$$

where ϵ_s, ϵ_σ are one-electron energies and λ_s, λ_σ are covalent-mixing parameters and z=6, the coordination number of Mn in the perovskite structure [33].

To summarize, decreasing the Mn-O-Mn bond angle through the substitution of A site cations, decreases the efficacy of the double exchange mechanism $[e_g(Mn) - 2p_\sigma(O) - e_g(Mn)]$ relative to the antiferromagnetic superexchange mechanism between the localised t_{2g} spins $[t_{2g}(Mn)\text{-}2p_\pi(O) - t_{2g}(Mn)]$ which results in a decreased T_C. This explanation also applies to the trends shown in figure 4.4(b) since the masses of the A-site cations are inversely proportional to their average radii, $< r_A >$.

That the data cannot be scaled to a universal $< r_A > -T_C$ curve does not detract from the plausibility of this idea. Rather, it reflects the inadequacy of $< r_A >$ to accurately represent the distortion of the perovskite structure over this wide range. In figure 4.5, the variance, σ^2, (defined as the average of the squares of the differences from the mean of the ionic radii r_i about the mean $<r_A>$) is plotted versus $<r_A>$. This is an indication of the "applicability" of $<r_A>$ for the compounds concerned, and as such is a further measure of lattice distortion As expected, for a fixed $< r_A >$, T_C has been shown to decrease with increasing σ^2 [34].

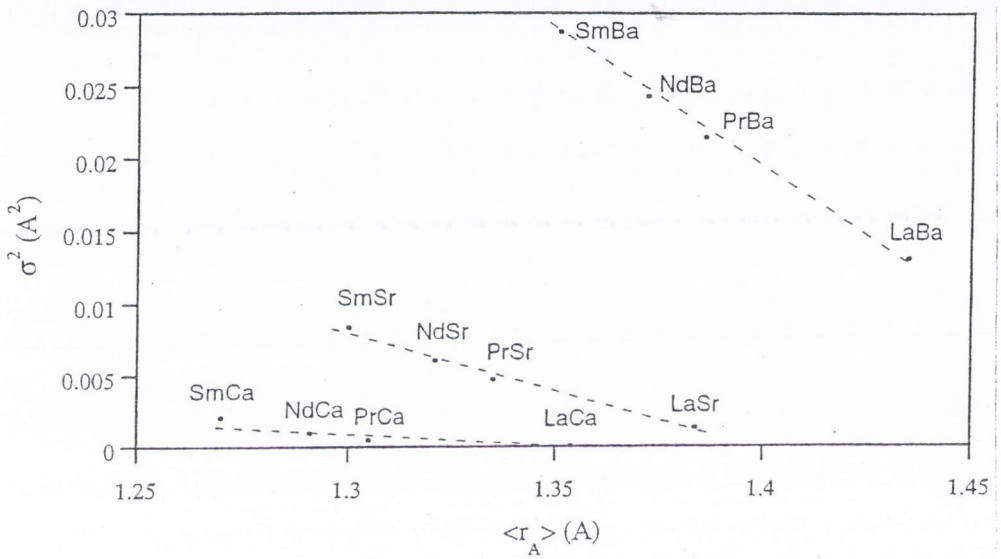

Figure 4.5 Variance, σ^2, plotted versus mean radius of the A-site cations, $< r_A >$

A universal curve remains elusive despite the introduction of this additional "distortion parameter". However, the argument remains that the influence of the divalent cations on T_C is purely steric. With reference to the ideal cubic perovskite cell, simple geometry gives the ideal A-site cationic radius for a doping ratio $x = 0.3$ as $< r_A > = 1.4433$Å based on an oxygen radius $r_O = 1.40$ Å. The applicable radii [35] indicate that the rare-earth ions are between 5.8% (La^{3+}) and 14.1% (Sm^{3+}) smaller than the ideal; likewise Sr^{2+} and Ca^{2+} are 0.22% and 7.2% too small respectively. However, the radius of Ba^{2+} is 11.6% *larger* than the ideal A-site cation in this case. It is this disparity that is reflected in the apparent dependence of T_C on the nature of the divalent cation and not some additional physical property, for example, their electronegativity as previously speculated [36].

The widely differing deviations of the divalent cationic radii from the ideal also explain the successful scaling on to a single $< r_A > -T_C$ curve of the series, $Ln_{2/3}(Ca_{1-x}Sr_x)_{1/3}MnO_3$ [37]. For this limited data set, the lattice distortion induced is incremental and directly comparable. Therefore, $< r_A >$ is an accurate representation of the influence of A-site substitution on the magnetic properties of the manganites.

4.2.4.2 Low temperature $\chi'(T)$ behaviour

The ac-susceptibility behaviour of the twelve samples in the low temperature regime are quantified through the parameters tabulated in Table 4.2 below. The values listed include the temperature at which the susceptibility reaches a maximum, $T(\chi'_{\max})$ and the measured value of this peak, $\chi'_{\max}$.

The demagnetising limits listed for each compound, χ'_d, were calculated using the demagnetising factors, D, for cylindrical samples, given by Chen [38], in accordance with the equation,

$$H_{internal} = H_{applied} - DM \tag{14}$$

Since $\chi = \frac{M}{H_{app}}$ it can be shown that when $\frac{M}{H_{int}} \to \infty$, $\frac{M}{H_{app}} \to \frac{1}{D}$. Thus,

$$\chi'_d = \frac{1}{D} \tag{15}$$

The "effective demagnetising limits", χ'_{eff} also listed account for the porosity of the samples measured. These values were calculated through invoking an "effective demagnetising factor" for randomly distributed spherical magnetic particles,

$$D_{eff} = \frac{1}{3} + f_m(D - \frac{1}{3})$$

where f_m is the volume fraction of the magnetic particles. This value was taken to equal the density of the compounds expressed as a percentage of the theoretical "X-ray" density, as listed in table 2.3.

The values shown in the final column, $\frac{d\chi'}{dT}$, represent the slope of the $\chi' - T$ data measured from the lowest temperatures to $\chi'_{\max}$.

Compound	$T(\chi'_{\max})$	$\chi'_{\max}$	χ'_d	χ'_{eff}	$\frac{d\chi'}{dT}$
$(La_{0.7}Sr_{0.3})MnO_3$	306	11.77	17.83	8.02	0.0017
$(La_{0.7}Ca_{0.3})MnO_3$	240	10.6	25.88	8.94	0.0136
$(La_{0.7}Ba_{0.3})MnO_3$	220	11	13.86	6.89	0.0111
$(Pr_{0.7}Sr_{0.3})MnO_3$	240	3.4	9.41	5.94	0.0050
$(Pr_{0.7}Ca_{0.3})MnO_3$	73	4.7	9.41	5.94	0.0140
$(Pr_{0.7}Ba_{0.3})MnO_3$	113	2.8	9.41	6.23	0.0153
$(Nd_{0.7}Sr_{0.3})MnO_3$	130	2.8	12.55	6.76	0.08629
$(Nd_{0.7}Ca_{0.3})MnO_3$	90	0.5	14.13	6.94	0.0049
$(Nd_{0.7}Ba_{0.3})MnO_3$	114	1.1	5.97	4.68	0.0087
$(Sm_{0.7}Sr_{0.3})MnO_3$	75	0.6	11.15	6.29	0.0119
$(Sm_{0.7}Ca_{0.3})MnO_3$	84	0.175	10.62	6.09	0.0015
$(Sm_{0.7}Ba_{0.3})MnO_3$	54	0.83	10.62	5.67	0.0073

Table 4.2 A summary of parameters evaluated for the twelve samples from measurements of $\chi' ac$ at low temperatures.

It can be seen from the table above, that with the exception of the La containing samples, the maximum susceptibility values of the samples do not exceed the demagnetising limits imposed by their geometrical dimensions and porosity. The measured values of $\chi'_{\max}$ are limited by these factors for $(La_{0.7}Ca_{0.3})MnO_3$, $(La_{0.7}Sr_{0.3})MnO_3$ and $(La_{0.7}Ba_{0.3})MnO_3$. Nevertheless, $\chi'_{\max}$ can be seen in figure 4.6, to approximately increase with T_C. This trend is an obvious re-

flection of the stronger ferromagnetism exhibited by those samples with the highest ordering temperatures.

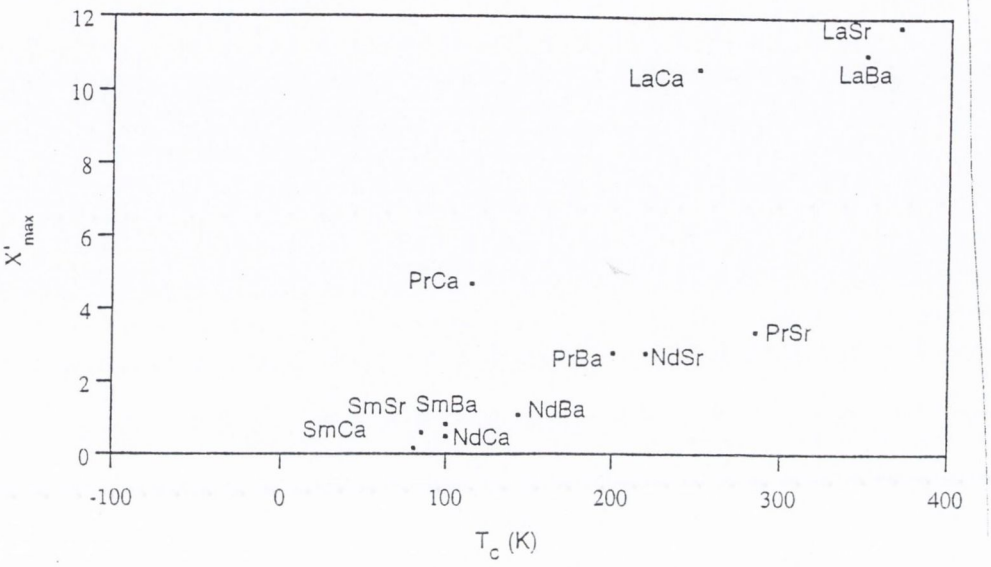

Figure 4.6 χ_{max} plotted versus T_C for the twelve mangnites studied.

As the temperature is decreased below $T(\chi'_{max})$, all the samples, without exception, show a decrease in susceptibility. This feature could be ascribed to the development of coercivity in these soft ferromagnetic materials[39]; typical values of the manganites' coercive fields are 0.05 T and 0.04 T for $(La_{0.7}Sr_{0.3})MnO_3$ and $(La_{0.7}Ca_{0.3})MnO_3$ respectively [4.3.3(i)]. However, a plot of $\frac{d\chi'}{dT}$ as a function of T_C (figure 4.7) suggests that a sharper decline of susceptibility broadly correlates with lower ordering temperatures, indicative of greater competition between the antiferromagnetic superexchange and ferromagnetic double-exchange interactions.

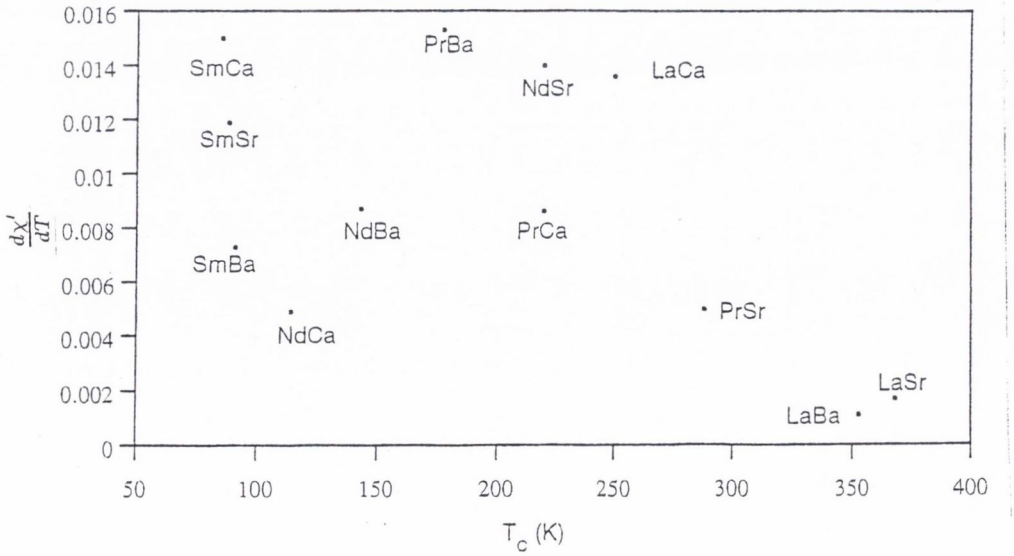

Figure 4.7 $\frac{d\chi'}{dT}$ evaluated at temperatures below $T(\chi'_{max})$, plotted versus T_C.

4.2.4.3 The Curie-Weiss susceptibility and magnetic clusters.

The values listed in table 4.3 relate to the paramagnetic regime of the samples. Tabulated values include: the theoretical spin-only Curie-Weiss constant, and expected slope of $1/\chi'(T)$, $1/C_{th(Mn^{3+}/Mn^{4+})}$, calculated for free Mn^{3+} and Mn^{4+} ions and the experimentally obtained values for the Curie-Weiss constant, C_{exp} measured just above the Curie temperature, T_C;

As previously stated, the Curie constant for free ions, C, is given by

$$C = \frac{N\mu_0\mu_B^2 p_{eff}^2}{3k}$$

where N is the total number of paramagnetic entities per cubic metre; p_{eff}, the effective Bohr magneton number which is defined for 3d ions as $p_{eff} = g\sqrt{S(S+1)}$ where g is the Landé factor and S is the spin angular momentum quantum number. For Mn^{3+} and Mn^{4+}, spin only moments are given by g = 2 and S = $\frac{3}{2}$ or S = 2. Values of p_{eff}^2 are equal to 24 and 15, giving a $< p_{eff}^2 >= 21.3$, from which the values of $C_{th(Mn^{3+}/Mn^{4+})}$ and $1/C_{th(Mn^{3+}/Mn^{4+})}$ were calculated.

Similarly, for free Pr^{3+}, Nd^{3+} and Sm^{3+} ions, $< p_{eff}^2 >$ equals 12.8, 13.1 and 0.7 respectively. However, since the magnetic ordering temperatures of Pr^{3+} and Nd^{3+} in perovskite compounds are of order 1 K [23], their contribution to the total Curie constant determined in the temperature range directly above T_C ($\sim$ 150K) for the $(Pr_{0.7}A'_{0.3})MnO_3$ and $(Nd_{0.7}A'_{0.3})MnO_3$, A' = Ca^{2+}, Sr^{2+}, Ba^{2+}. Likewise, the contribution of the Sm^{3+} ion to C represents at most, 2% of the total and can be neglected. Due to its empty 4f sub-shell, the La^{3+} ion has no moment to contribute to the Curie constant.

Compound	T_C (K)	C_{exp}	$\frac{1}{C_{\text{exp}}}$	$C_{th(Mn^{3+}/Mn^{4+})}$	$\frac{1}{C_{th(Mn^{3+}/Mn^{4+})}}$
$(La_{0.7}Sr_{0.3})MnO_3$	368	2.7724	0.3607	0.9495	1.0532
$(La_{0.7}Ca_{0.3})MnO_3$	250	2.9516	0.3388	0.9256	1.0396
$(La_{0.7}Ba_{0.3})MnO_3$	350	2.7113	0.3688	0.9256	1.0804
$(Pr_{0.7}Sr_{0.3})MnO_3$	288	1.6455	0.6077	0.9607	1.0409
$(Pr_{0.7}Ca_{0.3})MnO_3$	220	2.0920	0.4780	0.9735	1.0272
$(Pr_{0.7}Ba_{0.3})MnO_3$	177	3.106	0.3321	0.9453	1.0578
$(Nd_{0.7}Sr_{0.3})MnO_3$	220	2.604	0.3840	0.9737	1.0271
$(Nd_{0.7}Ca_{0.3})MnO_3$	114	2.1600	0.4630	0.9900	1.0101
$(Nd_{0.7}Ba_{0.3})MnO_3$	143	2.6309	0.3801	0.9406	1.0631
$(Sm_{0.7}Sr_{0.3})MnO_3$	88	2.1862	0.4574	0.9874	1.013
$(Sm_{0.7}Ca_{0.3})MnO_3$	85	2.1492	0.4653	0.9967	1.0033
$(Sm_{0.7}Ba_{0.3})MnO_3$	91	2.1631	0.4623	0.9468	1.0560

Table 4.3 A summary of the parameters evaluated from χ'_{ac} $-T$ measured for the paramagnetic region of the manganites.

Without exception, the Curie constant evaluated for each compound directly above T_C is larger than that expected from calculating the paramagnetic susceptibility of the free manganese ions. Such enhanced Curie-Weiss susceptibilities measured in low field are the key signatures of short range ferromagnetic correlations - possible evidence of magnetic clusters in the manganites' paramagnetic regime.

In an attempt to quantify this observation, the effective moment and Curie constants of some possible clusters of Mn^{3+} and Mn^{4+} are tabulated in Table 4.4 for the twelve compounds. The slight differences in the calculated values of C originate from the distinct values of N - the number of magnetic entities per cubic metre- measured for each sample.It can be seen that for the La containing compounds, a four ion cluster $(Mn_3^{3+}Mn_1^{4+})$ with $p_{eff}^2 = 255$ comes closest to the measured value, C_{exp}. A four cluster arrangement, albeit $(Mn_2^{3+}Mn_2^{4+})$ also fits the values of C_{exp} for $(Nd_{0.7}Sr_{0.3})MnO_3$ and $(Nd_{0.7}Ba_{0.3})MnO_3$, whereas the Ca containing compound is best fitted by a three ion cluster. The C_{exp} values for both $(Pr_{0.7}Ca_{0.3})MnO_3$ and $(Pr_{0.7}Sr_{0.3})MnO_3$ are comparable to those calculated for three ion clusters, $(Mn_1^{3+}Mn_2^{4+})$. However, the higher value of C_{exp} for $(Pr_{0.7}Ba_{0.3})MnO_3$ corresponds to a five cluster arrangement, $(Mn_2^{3+}Mn_3^{4+})$. A triple cluster arrangement comes closest to the values of C_{exp} for the Sm compounds, although a distribution of cluster size and composition would be expected in order to satisfy the electron stoichiometry for all twelve samples.

This crude model clearly highlights the effect of cluster formation on the susceptibility measured in the paramagnetic ground state of these materials. Since a small region of short-range ferromagnetic correlations in a paramagnetic background is essentially indistinguishable from a"magnetic" or "magnetoelastic" polaron [40] picture [section 3.2.2(2)], the two concepts may be analogous. This idea is supported by the work of De Teresa *et al.* [41] in which a measured deviation from the Curie-Weiss susceptibility of $(La_{2/3}Ca_{1/3})MnO_3$ up to 500 K - attributed to small ferromagnetic clusters - is accompanied by a lattice distortion detected through volume expansion measurements, characteristic of small polarons, most likely originating from the Jahn-Teller effect. Their additional small-angle neutron scattering experiments determine the size of these clusters immediately above T_C as $\sim$ 12 Å. This value is of the order of three unit cells; a congruous result with respect to the data presented above.

The origins and mechanisms of cluster formation above T_C are unclear; possible sources of clustering include: Anderson localisation of the carriers in the Mn e_g band due to the inhomogeneous distribution of the divalent cations or random potential fluctuations of magnetic origin. However, an overwhelming body of evidence suggests that carriers are localised through the introduction of elastic stress into the lattice by the dynamic Jahn-Teller distortion of the Mn^{3+} ions in an octahedral environment [see 3.2.2(2)].

In conclusion, this data set represents the first systematic observation of an enhanced effective moment above T_C in the manganites. As such it further contributes to the mounting experimental evidence of cluster formation in the paramagnetic regime of the x=0.3 doped manganese perovskites.

Mn	Mn^{3+}/Mn^{4+}	S	p^2_{eff}	C_{th} for $(A_{0.7}A'_{0.3})MnO_3$											
cluster size				LaSr	LaCa	LaBa	PrSr	PrCa	PrBa	NdSr	NdCa	NdBa	SmSr	SmCa	SmBa
1	1/0	$\frac{3}{2}$	24	1.07	1.06	1.04	1.08	1.10	1.07	1.10	1.12	1.06	1.11	1.12	1.12
1	0/1	2	15	0.67	0.66	0.65	0.68	0.69	0.67	0.69	0.70	0.66	0.70	0.70	0.70
3	2/1	$\frac{11}{2}$	143	2.13	2.11	2.06	2.15	2.18	2.13	2.18	**2.22**	2.11	**2.20**	**2.22**	**2.22**
3	1/2	5	120	1.78	1.77	1.73	**1.80**	**1.83**	1.78	1.83	1.87	1.77	1.85	1.87	1.87
4	3/1	$\frac{15}{2}$	255	**2.84**	**2.80**	**2.77**	2.87	2.91	2.83	2.91	2.96	2.81	2.91	2.98	2.96
4	2/2	7	224	2.50	2.47	2.44	2.53	2.56	2.56	**2.56**	2.61	**2.48**	2.60	2.62	2.61
5	3/2	9	360	3.21	3.17	3.13	3.25	3.29	3.29	3.29	3.35	3.18	3.34	3.37	3.35
5	2/3	$\frac{17}{2}$	322	2.87	2.83	2.80	2.90	2.94	**2.94**	2.94	2.99	2.84	2.98	3.01	2.99
6	3/3	$\frac{21}{2}$	483	3.59	3.54	3.50	3.63	3.68	3.68	3.68	3.74	3.56	3.73	3.77	3.74
6	4/2	11	528	3.92	3.87	3.82	3.97	4.02	4.02	4.02	4.09	3.88	4.08	4.11	4.09
C_{exp}				2.772	2.952	2.711	1.646	2.092	3.106	2.604	2.160	2.631	2.186	2.186	2.163

Table 4.4 Possible Mn^{3+}/M^{4+} cluster arrangements and their resultant spin-only moments, S, effective Bohr magneton numbers, p^2_{eff} and Curie constants, C.

A distribution of ordering temperatures - the effect on $1/\chi'(T)$ In the previous discussion, the enhanced Curie-Weiss susceptibility measured for the manganite samples was attributed to short-range ferromagnetic correlations in the paramagnetic phase. An alternate interpretation ascribes this observation to the effect of a wide distribution of ordering temperatures on the inverse susceptibility. To further investigate this possibility, $1/\chi'(T)$ was modelled by assuming a normal distribution of T_C,where the probability density function for a mean T_C and standard deviation, σ is given by

$$p(i; T_C, \sigma) = \frac{1}{\sigma\sqrt{2\pi}} e^{-\frac{(i-T_C)^2}{2\sigma^2}} \tag{16}$$

The measured data was accurately reproduced, as shown in figure 4.8. However, achieving this required a mean ordering temperature $T_C = 50K$ and a standard devation, $\sigma = 20K$.

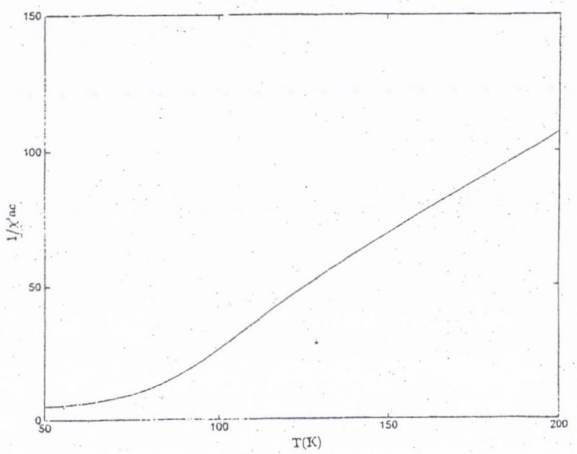

Figure 4.8 The inverse ac-susceptibility modelled from a normal distribution of ordering temperatures for $(Sm_{0.7}Sr_{0.3})MnO_3$.

The values of T_C measured for the series $(Sm_{1-x}Sr_x)MnO_3$ shown in figure 4.9 illustrate that the conditions predicted above are physically implausible. Thus, the form of the $1/\chi'(T)$ data cannot be ascribed to a distribution of T_C in this compound.

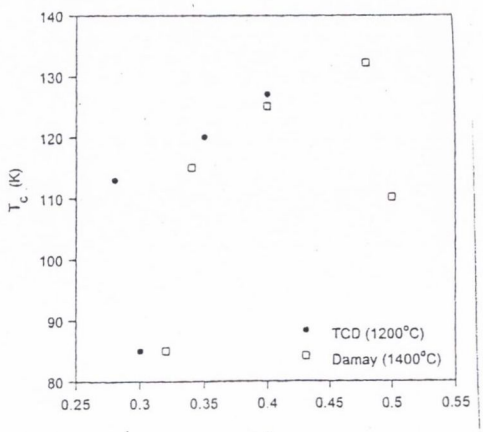

Figure 4.9 Values of T_C determined for the series $(Sm_{1-x}Sr_x)MnO_3$, $0.25 \leq x \leq 0.5$ from ac-susceptibility measurements and from [42].

4.3 High-field measurements

4.3.1 Background

Despite reports of high spin-polarisation at the Fermi level, the postulated fully-spin polarised, half-metallic nature of the manganites has yet to be conclusively demonstrated. The measurement of high-field susceptibility, $\frac{\partial M}{\partial H}$ can provide an indication of the spin polarisation at the Fermi level created by the application of a magnetic field. The Pauli susceptibiliy gives the relation

$$\chi_p = \frac{\partial M}{\partial H} = \frac{2\mu_0\mu_B^2\mathcal{D}(E_F)}{V} \tag{17}$$

where $\mathcal{D}(E_F)$ represents the density of states at the Fermi level, and V the sample volume.

The presence of both 3d spin projections at the Fermi level, characteristic of weak ferromagnetism, results in typical high-field slopes in the range 0.1 -10 x 10^{-3} μ_B/T [43], whereas a strong ferromagnet displays no high field slope at low temperature.

4.3.2 Experimental arrangements

4.3.2.1 (i) Steady field measurements

The field dependence of the magnetisation at 4.2 K of the twelve manganites were investigated at the high magnetic field laboratories at two different institutes. At both NHFML, Tallahassee and SNCI Grenoble, continuous fields up to 25 T were produced by Bitter magnets. These constitute an arrangement of perforated copper plates, densely stacked in an helical coil with $\sim$ 10^3 turns per metre, about the sample space. The power dissipated in such densely packed metallic segments whilst generating such high fields can exceed 15 MW, therefore necessitating continual cooling through the flow of water under high pressure.

However, the methods adopted for determining the magnetisation of the samples as a function of these applied fields were different. At the French institute, an *extraction method* was employed, where the sample positioned at the centre of a pick-up coil in the applied field is rapidly removed beyond the coil. Through integrating the emf consequently induced, the change of flux threading the coils was obtained, which was directly proportional to the magnetic moment of the sample. Oppositely wound, concentric pick-up coil segments cancelled changes in the applied field.

The ac equivalent of this extraction method is in place at the US laboratory, in the form of a *vibrating-sample magnetometer*. The sample was mounted on a vertical rod and vibrated vertically in the vicinity of similarly arranged pick-up coils at a vibration frequency in the range 10 - 100 Hz and a typical vibration amplitude of 10^{-4} m.

4.3.32 (ii) Pulsed field measurements

Measurements in pulsed fields up to 25 T were carried out at Trinity College and SNCMP, Toulouse. The experimental set-up at both facilities is similar [44]; the field is generated at the centre of a coil through which the charge stored in a bank of capacitors is discharged. At TCD, sixteen capacitors of $750\mu F$ are arranged in parallel and the coil is immersed in liquid nitrogen to dissipate the heat generated by the Joule heating effect. The magnetic field generated within the coil is directly proportional to the current passing through it, and is thus measured through monitoring the current passing through a shunt resistance connected in parallel with the coil. The pulse produced at TCD is of 0.75s duration, with a rise time 0.05 s. Similarly, at Toulouse the rise time of the pulse is 0.1s and the fall time 1.6s.

4.3.3 Results

4.3.31 (i) Steady-field measurements

Figure 4.10 presents the variation of the twelve samples' magnetisation in a steady applied field at 4.2 K. The saturation magnetization and high field slope evaluated from this data for each compound, are tabulated in the following table4.5.

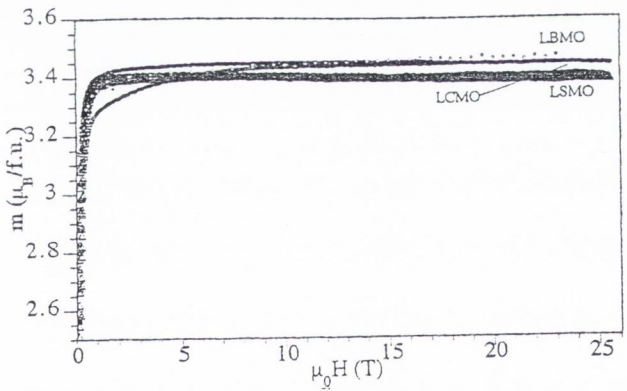

Figure 4.10(a) Magnetisation at 4.2 K for $(La_{0.7}A_{0.3})MnO_3$ (A = Sr^{2+}, Ca^{2+}, Ba^{2+})

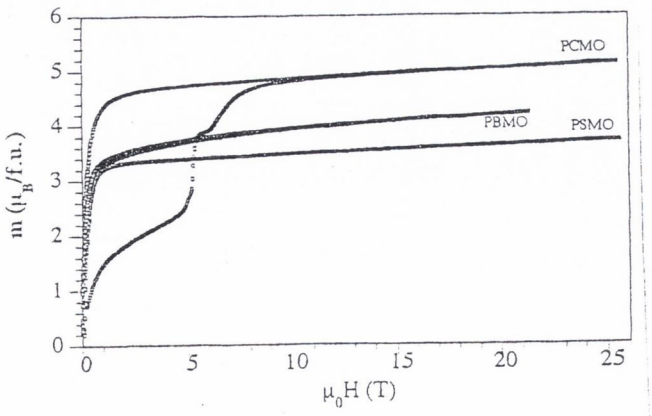

a

Figure 4.10(b) Magnetisation at 4.2 K for $(Pr_{0.7}A_{0.3})MnO_3$ (A = Sr^{2+}, Ca^{2+}, Ba^{2+})

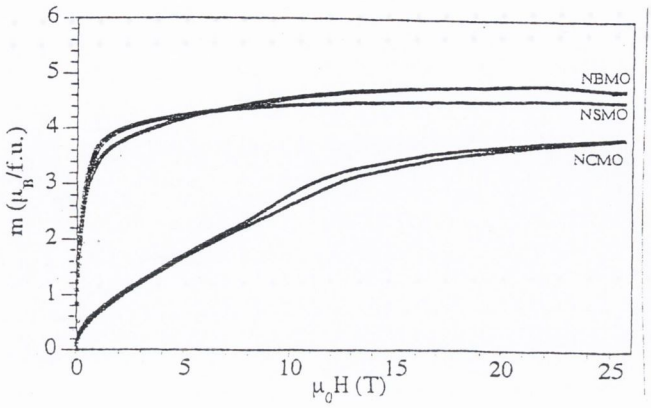

Figure 4.10(d) Magnetisation at 4.2 K for $(Sm_{0.7}A_{0.3})MnO_3$ (A = Sr^{2+}, Ca^{2+}, Ba^{2+})

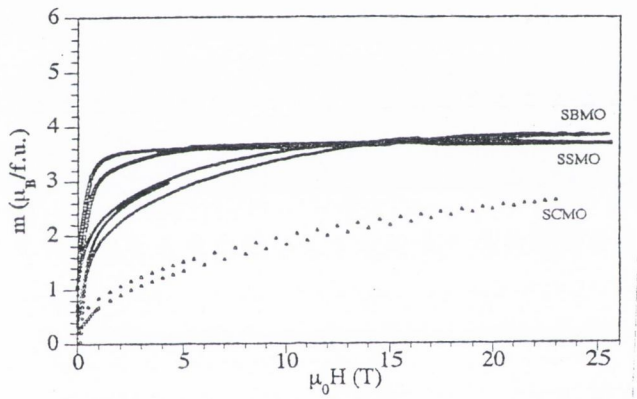

Figure 4.10(d) Magnetisation at 4.2 K for $(Sm_{0.7}A_{0.3})MnO_3$ (A = Sr^{2+}, Ca^{2+}, Ba^{2+})

Compound	Saturation moment (μ_B/formula unit)	High-field slope (μ_B/T)
$(La_{0.7}Sr_{0.3})MnO_3$	3.43	6×10^{-5}
$(La_{0.7}Ca_{0.3})MnO_3$	3.41	4×10^{-4}
$(La_{0.7}Ba_{0.3})MnO_3$	3.61	2.5×10^{-3}
$(Pr_{0.7}Sr_{0.3})MnO_3$	3.34	1.44×10^{-2}
$(Pr_{0.7}Ca_{0.3})MnO_3$	4.68	1.79×10^{-2}
$(Pr_{0.7}Ba_{0.3})MnO_3$	3.70	2.3×10^{-2}
$(Nd_{0.7}Sr_{0.3})MnO_3$	4.43	4.9×10^{-3}
$(Nd_{0.7}Ca_{0.3})MnO_3$	3.07	3.09×10^{-2}
$(Nd_{0.7}Ba_{0.3})MnO_3$	4.52	1.17×10^{-2}
$(Sm_{0.7}Sr_{0.3})MnO_3$	3.58	2.7×10^{-3}
$(Sm_{0.7}Ca_{0.3})MnO_3$	1.60	4.5×10^{-2}
$(Sm_{0.7}Ba_{0.3})MnO_3$	3.60	2.0×10^{-2}

Table 4.5 Summary of the saturation moment, extrapolated to zero field and high field slope of the polycrystalline $(R_{0.7}A_{0.3})MnO_3$; R = La^{3+}, Pr^{3+}, Nd^{3+}, Sm^{3+}, A = Sr^{2+}, Ca^{2+}, Ba^{2+}).

4.3.3.2 (ii) Pulsed field measurements

The variation of magnetisation of $(Pr_{0.7}Ca_{0.3})MnO_3$ and $(Nd_{0.7}Ca_{0.3})MnO_3$ with applied pulsed field at 4.2 K and 77 K is presented in figures 4.11 and 4.12 respectively.

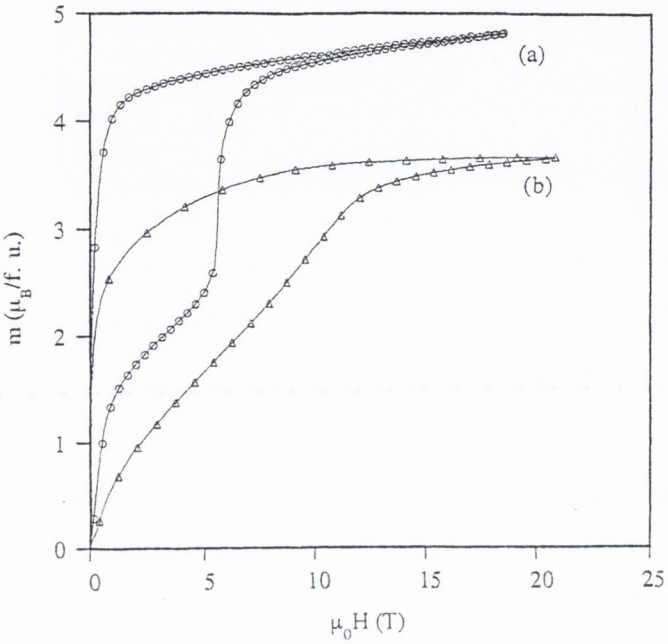

Figure 4.11(a) The magnetisation of $(Pr_{0.7}Ca_{0.3})MnO_3$ and (b) $(Nd_{0.7}Ca_{0.3})MnO_3$ measured at 4.2 K in pulsed field.

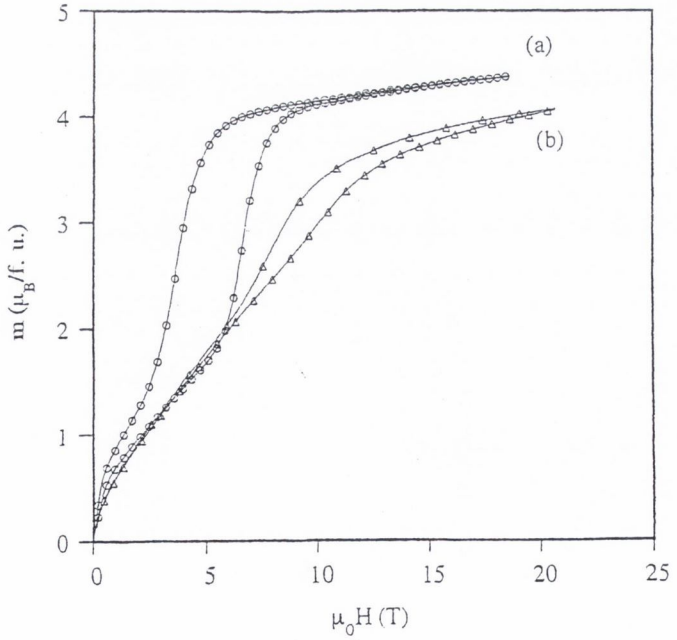

Figure 4.12(a) The magnetisation of $(Pr_{0.7}Ca_{0.3})MnO_3$ and (b) $(Nd_{0.7}Ca_{0.3})MnO_3$ measured at 77 K in pulsed field.

4.3.4 Discussion

4.3.4.1 (i) Steady field measurements

(a) $(La_{0.7}A_{0.3})MnO_3$; A = Sr^{2+}, Ca^{2+}, Ba^{2+} As summarised in table 4.5, the high-field slopes of the lanthanum containing compounds are less than those of the other manganites studied and their values of saturation magnetisation extrapolated to zero field approach the theoretical spin-only moment of 3.7 $\mu_B/formula\ unit$ expected for the full alignment of their constituent manganese ions. $(La_{0.7}Sr_{0.3})MnO_3$ shows essentially no high-field slope, indicative of a collinear ferromagnetic state as previously indicated by its high Curie temperature ($\sim$ 370 K) and the essentially constant value of its susceptibility measured in low fields below T_C [table 4.2]. Although the high-field slope for $(La_{0.7}Ca_{0.3})MnO_3$ is also small, 4 x 10^{-4} μ_B/T, the slight hysteresis observed between the virgin curve and saturation suggests that the ground state of this compound may not be a fully-aligned ferromagnet. $(La_{0.7}Ba_{0.3})MnO_3$, by contrast, remains unsaturated in a field of 23 T, showing a slope of 2.5 x 10^{-3} μ_B/T, characteristic of either a non-collinear state or weak ferromagnetism.

The negligible value of $\frac{\partial M}{\partial H}$ = 6 x $10^{-5}\mu_B/T$ measured, confirms the strong ferromagnetic nature of $(La_{0.7}Sr_{0.3})MnO_3$, in agreement with recent reports its high spin-polarisation [4.1]. The discrepant value of the saturation magnetisation in this sample is most likely attributable to oxygen non-stoichiometry, resulting in cation vacancies [2.1.4]. Assuming an even distribution of vacancies, the measured value of $M_{sat} = 3.43\ \mu_B/f.u.$suggests a formula, $[(La_{0.7}Sr_{0.3})Mn]_{0.98}O_3$.

The canted spin structure of $(La_{0.7}Ca_{0.3})MnO_3$ suggested by the hysteresis and reduced saturation magnetisation measured, was first indicated by neutron diffraction measurements [1]. The ordering temperature, $T_C = 250K$ is notably low by comparison with the other La containing compounds [table 4.1] lending further support to the conjecture that the ground state comprises of competing antiferromagnetic and ferromagnetic interactions. Conversely, NMR studies have ascribed the characteristics of this compound to microscale phase segregation [45] .

By comparison, $(La_{0.7}Ba_{0.3})MnO_3$ exhibits a higher saturation magnetisation, but also a much greater high field susceptibility than the aforementioned samples. The value of $\frac{\partial M}{\partial H}$ =2.5 x 10^{-3} μ_B/T is within the range quoted for typical weak ferromagnets [43]. This latter observation may indicate the presence of both 3d spin projections at the Fermi level; a characteristic of weak ferromagnetism for which high-field slopes are typically 0.1 -10 x 10^{-3} μ_B/T [43]. This compound is further distinguished by the large size mismatch of its A-site cations, quantified by means of the variance of the radius distribution, as discussed in 2.3.2. The local disorder effects introduced, probably explain why $(La_{0.7}Ba_{0.3})MnO_3$ has a lower T_C than $(La_{0.7}Sr_{0.3})MnO_3$ despite having a higher tolerance factor. Moreover, it's possible that the localisation of Mn electrons at sites with the most distorted Mn-O-Mn bond angles will result in a high local density of states, consequently influencing the high field slope.

(b) $(Pr_{0.7}A_{0.3})MnO_3$; A = Sr^{2+}, Ca^{2+}, Ba^{2+} Figure 4.10 (b) shows the field dependence of the magnetisation at 4.2K of the praesodymium compounds. In contrast to the La^{3+} containing manganites, none of the samples are saturated at 23 T and all of them show pronounced high-field slopes of order 0.02 μ_B/T.

The measured values of saturation magnetisation for $(Pr_{0.7}Sr_{0.3})MnO_3$ and $(Pr_{0.7}Ba_{0.3})MnO_3$ are 3.34 and 3.70 $\mu_B/f.u.$ respectively. Thus, Pr^{3+} appears to make no contribution to the total moment in either of these samples; the degeneracy of the ground state Pr^{3+} J multiplet $^3H_4$ is understood to be lifted by the crystal field, leaving the rare-earth in a singlet ground state, as previously established by inelastic neutron scattering in $PrGaO_3$ [figure 4.2(a)]. The high-field slope is presumably due to the mixing of higher crystal field states of $Pr^{3+}$with $M_J > 0$. The incongruous value of saturation magnetisation for the Sr compound is most likely indicative of cation deficiency, resulting from a formula, $[(Pr_{0.7}Sr_{0.3})Mn]_{0.946}O_3$.

$(Pr_{0.7}Ca_{0.3})MnO_3$, by contrast, exhibits markedly different behaviour to the other two compounds. The ground state does not appear to be ferromagnetic and there are two first-order magnetisation processes, with transitions ocurring at 5T and 6T. The first transition, at 5T, is the widely reported transformation [12] [46] [47] from the insulating, canted antiferromagnetic ground state with a moment of 1.4 $\mu_B/f.u.$, to the metallic, ferromagnetic, charge-disordered state in which the moment, 3.6 $\mu_B/f.u.$ corresponds to an almost fully-aligned manganese sublattice. The second transition at 6 T, where the magnetisation increases by a further $\sim 0.8\mu_B/f.u.$ is attributed to a level crossing transition of the lowest lying Pr^{3+} crystal field levels, $\Gamma^{(2)}$ and $\Gamma^{(1)}$. The $\Gamma^{(1)}$ singlet state with J = 0 is the ground state whereas the $\Gamma^{(2)}$ excited state is the field-stabilised state where Pr has a moment of $0.8\mu_B$. This interpretation is supported by the crystal field calculation carried out in section 4.3.

(c) $(Nd_{0.7}A_{0.3})MnO_3$; A = Sr^{2+}, Ca^{2+}, Ba^{2+} The field dependence of the magnetisation at 4.2 K of the neodymium compounds is given in figure 4.10 (c). Except for the Ca compound, which is assumed to be charge-ordered, they have a magnetisation which is $\sim 1\mu_B$ than their La counterparts and high-field slopes, 5 x 10^{-3} μ_B/T (Sr) and 12 x 10^{-3} μ_B/T (Ba).

Although the free-ion moment of Nd^{3+} is 3.3 μ_B, in $(Nd_{0.7}Sr_{0.3})MnO_3$ and $(Nd_{0.7}Ba_{0.3})MnO_3$ this value is reduced by the crystal field, which splits the ground state $^4I_{9/2}$ multiplet into five Kramers doublets [22]. Therefore, the additional $\sim$ 1 μ_B is contributed to the total moment by the Nd^{3+} aligned parallel to the ordered Mn. This is further explored through crystal field calculations in the following section. By analogy with the Pr compounds, the high-field slopes of these compounds can be attributed to the mixing of higher crystal-field states.

As in the case of $(Pr_{0.7}Ca_{0.3})MnO_3$, the corresponding Nd compound, is also believed to be charge-ordered [48] which accounts for its much-reduced moment, 3.07 $\mu_B/f.u.$ The high-field characteristics of this compound are further discussed with reference to the data measured in pulsed field (figures 4.13 and 4.14) in the following 4.3.4(ii).

(d) $(Sm_{0.7}A_{0.3})MnO_3$; A = Sr^{2+}, Ca^{2+}, Ba^{2+} The high-field characteristics of the Sm containing manganites are presented in figure 4.10(d). The moments measured for both the Sr and Ba compounds - 3.6 $\mu_B/f.u.$- roughly correspond to the theoretical value expected. However, the Ba compound shows a pronounced high-field slope 0.02 μ_B/T, which is an order of magnitude greater than that of $(Sm_{0.7}Sr_{0.3})MnO_3$ ($2.7 \times 10^{-3}\mu_B/T$). On the other hand, the magnetisation of the Ca sample is much-reduced, 1.6 $\mu_B/f.u.$, suggesting that this compound, like the aforementioned $(Pr_{0.7}Ca_{0.3})MnO_3$ and $(Nd_{0.7}Ca_{0.3})MnO_3$ has a charge-ordered ground state. The Sm^{3+} moment in all samples is expected to be <0.5 $\mu_B/f.u.$

Although $(Sm_{0.7}Sr_{0.3})MnO_3$ approaches the behaviour of a collinear ferromagnet, the distinct hysteresis between the virgin magnetisation curve and the saturation magnetisation measured upon decreasing field, suggests imperfect ferromagnetic order. This is further evidenced by the low susceptibility value measured for this compound, $\chi'_{max} = 0.6$ relative to the other Sr containing compounds (La, $\chi'_{max} = 11.8$;Pr, $\chi'_{max} = 3.4$; Nd, $\chi'_{max} = 2.8$) [table 4.2].

The field dependence of both the Ba and Ca compounds indicate a non-collinear ferromagnetic ground state. Although both show a progressive alignment of spins with increasing field, neither sample is saturated and both have comparable high-field slopes. However, whereas $(Sm_{0.7}Ba_{0.3})MnO_3$ approximates the behaviour of its La counterpart, the Ca containing sample is most certainly charge-ordered. This is supported by the exceptionally low value of susceptibility measured, $\chi'_{max} = 0.17$ and the characteristic sharp peak measured in its susceptibility.

4.3.4.2 (ii) Pulsed field measurements

The variation of magnetisation measured in pulsed fields for $(Pr_{0.7}Ca_{0.3})MnO_3$ and $(Nd_{0.7}Ca_{0.3})MnO_3$ shown in figure 4.11 is markedly different to the steady field magnetisation curves shown in figure 4.10 (b) and (c) for the same samples at 4.2 K. For the pulsed field data, only one transition is observed for the Pr compound at 6T, from the charge-ordered insulator to the high Pr moment ferromagnetic state. The Nd compound displays a broad hysteresis loop extending to 25T and the sample remains in the ferromagnetic state throughout the demagnetizing process. This data enables the relaxation time τ for the reverse transition from the metastable ferromagnetic state to the stable canted state at 4.2K to be deduced as lying between 1.6s (the rise time of the pulsed magnet) and 300s (the time for the scan from maximum to zero field in the VSM). An intermediate value $\tau = 30s$ is assumed in subsequent calculations.

The pulsed field data measured for $(Nd_{0.7}Ca_{0.3})MnO_3$ at 77 K show much less hysteresis [figure 4.14(a), (b)]. They resemble the steady field data at 4.2 K, with hysteresis only present at the top of the curve when $\mu_0 H > 10T$. The data indicate that the reverse transition in $(Nd_{0.7}Ca_{0.3})MnO_3$ is strongly time and temperature dependent since the rise time for this pulsed field measurement was only 0.05s Unlike normal magnetic hysteresis, which has a micromagnetic origin associated with the nucleation and propagation of reverse

domains, the hysteresis here is probably associated with melting/ freezing of the charge-ordered state. By considering the Nd compound, and assuming a thermally activated process with an energy barrier E_a so that the relaxation time τ for the reverse transition is given by

$$\tau = \tau_0 e^{\frac{E_a}{kT}} \tag{18}$$

Taking $\tau_0 = 10^{-12}s$, which is a typical attempt frequency for relaxation processes in solids, and using the value of τ measured at 4.2 K, $E_a = 130$ K.

In the Pr compound, τ is clearly much longer. A recent study [49] of the dynamics of the "charge-melting" transition at temperatures 40-50K shows an abrupt percolative transition in conductivity as a function of time in a regime where magnetization is relaxing smoothly. Interpreted in terms of a two state model, this data estimates an activation energy of 1380K.

Further analysis of the data invokes local regions of charge-order within a ferromagnetic matrix, analogous to the picture of nucleation and growth from an activation volume often drawn to explain magnetic hysteresis. The effect of the field is i) to change the relative energies of the charge-ordered and ferromagnetic states, and ii) to reduce the height of the activation barrier between them. The stabilization energy per manganese ion of the ferromagnetic phase is $\Delta\mu.B$ where $\Delta\mu$ is the difference in moment between the two magnetic structures as deduced from the magnetization curve. This has a maximum value $2.4\mu_B.10.5T$ or 17 K/Mn for the Nd compound. A rough estimate of the number of Mn ions involved in the charge-ordered cluster is thus N_{Mn}=130/17 $\approx$ 8. The same estimate for the Pr compound, where $(\Delta\mu.B)\,\mathrm{max} = 4.0K$, gives $N_{Mn} \approx 350$.

To summarise, the dynamic high-field hysteresis in $(Nd_{0.7}Ca_{0.3})MnO_3$ observed on a timescale of 0.1s at 4.2 K is related to magnetically induced melting of short-range charge order. The regions involved are clusters of CE type order comprising about 8 Mn ions, whereas a similar consideration of nucleation volume for $(Pr_{0.7}Ca_{0.3})MnO_3$ gives an estimated cluster size of roughly 350.

4.4 Rare-earth magnetism -"A-site" magnetic interactions

Echoing the prevalent situation in the published literature, this discussion of the manganites' magnetic properties has hitherto focussed solely on the role of the manganese sublattice. However, as evidenced by the high-field magnetisation data presented [figure 4.10 (b),(c)], a complete description of the manganites'magnetization curves requires a consideration of the roles of the constituent rare-earth ions.

This omission is partly addressed by the following theoretical calculation of the crystal field interaction at the rare-earth site in $(Pr_{0.7}Ca_{0.3})MnO_3$ and $(Nd_{0.7}A'_{0.3})MnO_3$, A = Sr, Ba. As previously noted [figure 4.2], the crystal field in these compounds results in a singlet ground state for the Pr^{3+} ion. Similarly, only the lowest doublet in Nd^{3+} is occupied at low temperature.

These conditions permit the significant simplification of the rare-earth Hamiltonian, which forms the basis of the subsequent calculations. However, the low-lying excited multiplets of Sm^{3+} invalidate this simplification. Therefore, the theoretical consideration of the Sm containing compounds is beyond the realms of the straightforward analysis presented.

4.4.1 Calculating the crystal field interaction

The principal motivation is provided by the steady field magnetisation behaviour of $(Pr_{0.7}Ca_{0.3})MnO_3$. As previously discussed, [4.3.4(i)(c)], the two distinct transitions shown by this compound in applied fields of 5T and 6T are most likely ascribed to a transformation from a charge-ordered to ferromagnetic state, and a subsequent level crossing of the lowest field-stabilised Pr^{3+} crystal field levels. The verification of this assumption and the further extension of the derived result to account for the additional $\sim 1\ \mu B/f.u.$ contributed to the total moment of $(Nd_{0.7}A'_{0.3})MnO_3$, A = Sr^{2+}, Ba^{2+} form the basis for the following analysis.

4.4.1.1 Background

The Hamiltonian for a single rare-earth ion includes the intra-atomic Coulomb and spin-orbit interactions, crystal-field and exchange interactions and a Zeeman magnetostatic energy term in an external field:

$$\mathcal{H}_{RE} = \mathcal{H}_C + \mathcal{H}_{SO} + \mathcal{H}_{cef} + \mathcal{H}_{ex} + \mathcal{H}_Z \qquad (19)$$

where $\mathcal{H}_C$ includes the intra-atomic Coulomb interactions that result in states with well defined angular momentum quantum numbers, L and S. Since the intra-atomic Coulomb and spin-orbit interaction are considerably stronger than the remaining terms, it is usually sufficient to confine further calculations to the ground-state multiplet only[6]. Hence, $\mathcal{H}_{SO}$ couples L and S to form J, the total angular momentum of the ground state, according to Hund's third rule. The exchange interaction, $\mathcal{H}_{ex} = g\mu_B \mathbf{S}.\mathbf{B}_R^{ex}$ where $\mathbf{B}_R^{ex}$ is the exchange field arising from the Mn sublattice, is normally larger in magnitude than the crystal field interaction term $\mathcal{H}_{cef}$ in rare-earth - transition metal compounds. Therefore, in the following discussion, the M_J states are taken as the basis set for considering the electrostatic crystal-field interaction, which is treated as a perturbation on the set of equally spaced Zeeman levels of the ground state R^{3+} multiplet. The Zeeman term $\mathcal{H}_Z = -\mu_B(\mathbf{L} + 2\mathbf{S}).\mathbf{B}_z$ represents the coupling of the rare-earth moment to an external field applied along the z-direction.

Consequently, the Hamiltonian for a rare-earth ion having a localized moment and a well defined total angular momentum quantum number, J, can be written explicitly:

[6] In the case of the heavier rare earth ions, such as Sm^{3+} and Eu^{3+}, the low-lying excited multiplets require consideration as there is significant J-mixing

$$\mathcal{H}_{RE} = -\lambda \mathbf{L}.\mathbf{S} + \mathcal{H}_{cef} + g_s \mu_B \mathbf{S}.\mathbf{B}_R^{ex} - \mu_B(\mathbf{L} + 2\mathbf{S}).\mathbf{B}_z \quad (20)$$

where λ denotes the spin-orbit coupling parameter and g_s the g-value of an ion's spin,

The calculations are simplified through restricting considerations to the ground state multiplet only, enabling the rare-earth Hamiltonian to be written as the sum of the exchange and crystal-field interactions [51].

$$\mathcal{H}_{RE} = \mathcal{H}_{cef} + g_J \mu_B \mathbf{J_z}.(\mathbf{B}_R^{mol} + \mathbf{B}_z) \quad (21)$$

where the molecular field, $\mathbf{B}_R^{mol}$, represents the intersublattice coupling between the rare-earth and 3d magnetic moments. The crystal-field Hamiltonian, $\mathcal{H}_{cef}$,is conventionally stated in terms of Stevens operators,

$$\mathcal{H}_{cef} = B_n^{m\alpha} \hat{O}_n^m \quad (22)$$

This expression is derived in the following subsection.

4.4.1.2 (i) Introduction to crystal field theory

The crystal field is an electrostatic field created by the charged ions within a crystal lattice. Crystal field effects arise when the spatial degeneracy of the angular momentum, J, of an ion with electron orbitals containing unpaired electrons is removed by an asymmetric potential resulting from the crystal field. Through assuming a simple point-charge ionic model of the crystal lattice, the crystal field effects are taken as a perturbation of the appropriate free-ion wave functions and energy levels of the 'magnetic ion'. The quantitative problem becomes that of evaluating the electrostatic potential $V_c(\mathbf{r}_i)$ at the location $\mathbf{r}_i$ of the magnetic ion in question. The perturbing crystal field Hamiltonian, $\mathcal{H}_{cef}$ and its matrix elements are subsequently determined.

If the magnetic ion has charge e at a position $\mathbf{r}_i$, then the perturbing crystalline potential due to a purely external surrounding charge density $\rho(\mathbf{R})$ is of the form

$$V_c(\mathbf{r}_i) = \frac{-|e|}{4\pi\varepsilon 0} \int \frac{\rho(\mathbf{R})}{|\mathbf{r}_i - \mathbf{R}|} d\mathbf{R} \quad (23)$$

As a solution of Laplace's equation, this expression may be expanded in either spherical harmonics, or more conveniently, in terms of tesseral harmonics, $Z_n^{m\alpha}(\theta, \phi)$ where $\alpha = c, s$ (corresponding to real and imaginary parameters respectively) with the electron position $\mathbf{r}_i$ given in spherical polar coordinates (r, θ, ϕ). These tesseral harmonics are real and the potential is written in terms of the position of the i^{th} electron $(\theta i, \phi i)$

$$V_c(\mathbf{r}_i) = \sum_{n=0}^{\infty} \sum_{m \geq 0}^{n} \sum_{\alpha} \gamma_n^{m\alpha} r_i^n Z_n^{m\alpha}(\theta i, \phi i) \quad (24)$$

The lattice coefficients, $\gamma_n^{m\alpha}$, are electric field components which reflect the point symmetry of the environment of the electron, They are written as

$$\gamma_n^{m\alpha} = \frac{1}{4\pi\varepsilon 0}\left[\frac{4\pi}{2n+1}\right]\int \frac{\rho(\mathbf{R})}{R^{n+1}} Z_n^{m\alpha}(\Theta,\Phi)dR \tag{25}$$

where $\mathbf{R} = (\mathrm{R}, \Theta, \Phi)$.

In the case of a rare-earth $4f$ ion, the $r_i^n Z_n^{m\alpha}(\theta i, \phi i)$ represent the various multipoles of the $4f$ electron distribution. Since f-electron configurations with angular momentum $l_{4f} = 3$ cannot have multipole distributions with n > 6, as higher order multipoles cannot excite transitions between $l_{4f} = 3$ states, only terms up to the sixth degree need to be considered. The resulting, limited crystal field Hamiltonian is thus written

$$\mathcal{H}_{cef} = -|e|\sum_{n=0}^{6}\sum_{m\geq 0}^{n}\sum_{\alpha}\gamma_n^{m\alpha}\sum_i r_i^n Z_n^{m\alpha}(\theta i, \phi i) \tag{26}$$

where the additional summation, i, is over the total number of $4f$ electrons. Thus, the modifications to the energy-levels of the $4f$ electrons through interaction with the crystal field may be deduced through calculating the matrix elements of $\mathcal{H}_{cef}$ between the free-ion states of the given manifold of angular momentum J, using first order perturbation theory [52]. The matrix thus formed can then be diagonalized to find the energy levels and eigenfunctions of the ion in the crystalline field.

Alternatively, a simpler calculation can be carried out through invoking an *operator equivalent* method, as developed by Stevens [53]. In this seminal work, the Wigner-Eckart theorem [54] was first applied to the matrix elements of $\mathcal{H}_{cef}$, yielding angular momentum operators which act on the angular part of the wave functions $|J, J_z\rangle$. By expressing the tesseral harmonics, $\sum_i r_i^n Z_n^{m\alpha}(\theta i, \phi i)$ in Cartesion coordinates, $\sum_i K_n^m f_n^{\alpha m}(x_i, y_i, z_i)$[7] and replacing the x, y, z combinations with appropriate combinations of J_x, J_y and J_z, "Stevens" operators, $\hat{O}_n^m$,were formed which transformed under rotation in the same manner as the potential. Therefore, the general equivalence relation which simplifies $\mathcal{H}_{cef}$ is written

$$\sum_i f_n^{m\alpha}(x_i, y_i, z_i) \equiv \theta_n \langle r^n \rangle \hat{O}_n^m \tag{27}$$

where the multiplicative factor θ_n is a reduced matrix element known as the Stevens coefficient for the given rare-earth ion. Its value dependson l (the orbital quantum number of the electrons in the unfilled shell), and J, and is represented by $\alpha_J, \beta_J, \gamma_J$ for $n = 2, 4, 6$ respectively. $\langle r^n \rangle$ is the radius of the $4f$ electron shell averaged over the wavefunction, which is listed for the R^{3+} rare-earth ions [55]. The $\hat{O}_n^m$ were originally tabulated by Stevens[53] and Hutchings [56] and the detailed work of Rudowicz [57] discusses the various notations which have subsequently been developed. Some simple examples, as listed in Hutchings [56], are

[7] Some of the more commonly occurring tesseral harmonics expressed in cartesian coordinates are listed by Hutchings [56]

$$\sum_i (3z_i^2 - r_i^2) \equiv \alpha_J \langle r^2 \rangle \left[3J_z^2 - J(J+1)\right] = \alpha_J \langle r^2 \rangle \hat{O}_2^0 \tag{28}$$

$$\sum_i (x_i^2 - y_i^2) \equiv \alpha_J \langle r^2 \rangle [3J_x^2 - J_y^2] = \alpha_J \langle r^2 \rangle \hat{O}_2^2 \tag{29}$$

$$\sum_i x_i y_i \equiv \alpha_J \langle r^2 \rangle [(J_x J_y + J_y J_x)/2] \tag{30}$$

where $J_\pm = J_x \pm i J_y$

Thus, expressing $\mathcal{H}_{cef}$ in operator equivalent form,

$$\mathcal{H}_{cef} = \sum_{n=0}^{6} \sum_{m \geq 0}^{n} \sum_{\alpha} \theta_n A_n^{m\alpha} \langle r^n \rangle \hat{O}_n^m \tag{31}$$

where the crystal field intensity coefficients, $A_n^{m\alpha} = -|e| K_n^{m\alpha} \gamma_n^{m\alpha}$. Alternatively, and more commonly,

$$\mathcal{H}_{cef} = \sum_{n=0}^{6} \sum_{m \geq 0}^{n} \sum_{\alpha} B_n^{m\alpha} \hat{O}_n^m \tag{32}$$

where the coefficients $B_n^{m\alpha} = \theta_n A_n^{m\alpha} \langle r^n \rangle$ are called the crystal field parameters which determine the scale of the crystal field splittings. Since they are very difficult to calculate quantitatively, it is customary to regard these coefficients as parameters to be determined empirically.

This simple point-charge formalism used to calculate the Hamiltonian has several weaknesses. It neglects the finite extent of charges of the ions, the overlap of the magnetic ions' wave functions with those of neighbouring ions, and the complex effects of screening of the magnetic electrons by the outer shells of the magnetic ion. However, it serves as a first approximation to illustrate the principles involved, and through the incorporation of the Stevens operator equivalent method is the most convenient way of calculating the effect of the crystal field on the energy levels of the R^{3+} ion.

4.4.1.3 (ii) Determination of the Hamiltonian, $\mathcal{H}_{RE}$,for the rare-earth site and deduction of the crystal field parameters.

The Hamiltonian for a rare-earth ion having a localized moment and a well defined total angular momentum quantum number, J was previously introduced (eq. 1.21 above) as

$$\mathcal{H}_{RE} = \mathcal{H}_{cef} + g_J \mu_B \mathbf{J_z}.(\mathbf{B}_R^{mol} + \mathbf{B}_z) \tag{33}$$

where $\mathbf{B}_z$ represents an external field applied along the z-direction, and g_J, the total angular momentum g-factor, equals $\frac{4}{5}$ and $\frac{8}{11}$ for Pr^{3+} and Nd^{3+} respectively. In applied fields, $\mathbf{B}_z > 1T$,the exchange field is negligible and can be effectively omitted from the calculations. To apply this expression to the manganites studied, requires the assumption that these materials are magnetically oriented parallel to the direction of the applied field, i.e. along the z-axis.

Although a gross simplification of the situation for a polycrystalline material with randomly oriented particles, this assumption serves as a first approximation. This topic is re-addressed in section 4.4.1.3(iii). The general expression for the perturbing crystal field Hamiltonian, $\mathcal{H}_{cef}$ in terms of Stevens operator equivaents was derived earlier (eq. 1.22 above) and shown to be

$$\mathcal{H}_{cef} = \sum_{n=0}^{6} \sum_{m \geq 0}^{n} \sum_{\alpha} B_n^{m\alpha} \hat{O}_n^m$$

The number of terms in the expansion is determined by the point symmetry of the rare-earth site. Both $(Pr_{0.7}Ca_{0.3})MnO_3$ and $(Nd_{0.7}Ca_{0.3})MnO_3$ crystallize as orthorhombic variants of the cubic perovskite cell, with space group Pbnm. The Pr^{3+} and Nd^{3+} ions occupy the 4c sites, the point symmetry of which is characterised by a single mirror plane, m. This low symmetry at the rare-earth site gives rise to a large number of independent crystal field parameters, $B_n^{m\alpha}$ - the crystal field potential of m symmetry at the Pr^{3+} site in $PrGaO_3$ is seemingly characterised by fifteen independent crystal field parameters [21]! The initial determination of so many parameters without recourse to experiment was an unrealistic task, therefore, by way of a simple approximation, only the leading second, fourth and sixth degree terms were considered, hence neglecting M_J-mixing by off-diagonal terms.

Consequently,

$$\mathcal{H}_{RE} = B_2^0 \hat{O}_2^0 + B_4^0 \hat{O}_4^0 + B_6^0 \hat{O}_6^0 - g\mu_B \mathbf{J}_z.\mathbf{B}_0$$

where

$$\hat{O}_2^0 = \left[3J_z^2 - J(J+1)\right]$$

$$\hat{O}_4^0 = 35J_z^4 - [30J(J+1) - 25]J_z^2 - 6J(J+1) + 3J^2(J+1)^2$$

$$\hat{O}_6^0 = 231J_z^6 - 105[3J(J+1) - 7]J_z^4 + [105J^2(J+1)^2 - 525J(J+1) + 294]J_z^2 - 5J^3(J+1)^3 + 40J^2(J+1)^2 - 60J(J+1)$$

(a) $(Pr_{0.7}Ca_{0.3})MnO_3$ For Pr^{3+}, $M_J = 4$, thus the non-vanishing matrix elements of the diagonal matrix, $\mathbf{J}_z$ could be written down;

$$\mathbf{J}_z = \begin{bmatrix} 4 & 0 & 0 & 0 & 0 & 0 & 0 & 0 & 0 \\ 0 & 3 & 0 & 0 & 0 & 0 & 0 & 0 & 0 \\ 0 & 0 & 2 & 0 & 0 & 0 & 0 & 0 & 0 \\ 0 & 0 & 0 & 1 & 0 & 0 & 0 & 0 & 0 \\ 0 & 0 & 0 & 0 & 0 & 0 & 0 & 0 & 0 \\ 0 & 0 & 0 & 0 & 0 & -1 & 0 & 0 & 0 \\ 0 & 0 & 0 & 0 & 0 & 0 & -2 & 0 & 0 \\ 0 & 0 & 0 & 0 & 0 & 0 & 0 & -3 & 0 \\ 0 & 0 & 0 & 0 & 0 & 0 & 0 & 0 & -4 \end{bmatrix}$$

Taking $J = 4$, the operators $\hat{O}_2^0, \hat{O}_4^0$ and $\hat{O}_6^0$ were subsequently constructed. The splitting of the ground-state multiplet of Pr^{3+} due to the combined perturbing effect of the individual operators and an effective applied field, $\mathbf{h}_z$ was evaluated. Three Hamiltonians were constructed:

$$\mathcal{H}_2^0 = \sum_{\mathbf{h}_z=0}^{25} \hat{O}_2^0 - \mathbf{h}_z.\mathbf{J}_z \qquad \{4.34\}$$

$$\mathcal{H}_4^0 = \sum_{\mathbf{h}_z=0}^{25} \hat{O}_4^0 - \mathbf{h}_z.\mathbf{J}_z \qquad \{4.35\}$$

$$\mathcal{H}_4^0 = \sum_{\mathbf{h}_z=0}^{25} \hat{O}_6^0 - \mathbf{h}_z.\mathbf{J}_z \qquad \{4.36\}$$

Evaluation

~~Diagonalization~~ of these simplified Hamiltonians yielded the energy eigenvalues (and corresponding eigenfunctions) which are plotted as a function of $\mathbf{h}_z$ for each operator in figures 4.15 (i)-(iii).

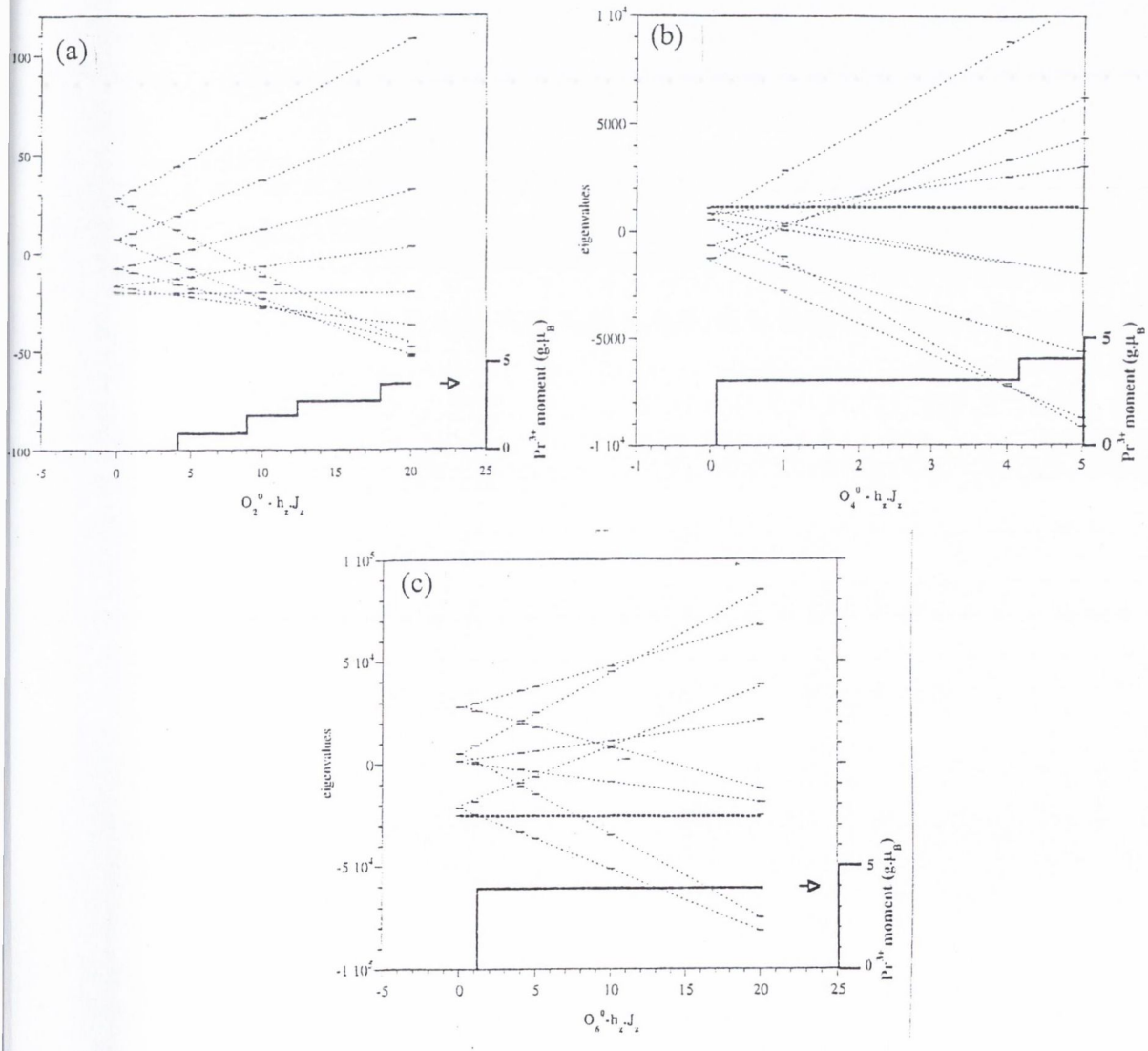

Figure 4.15 Energy-level schemes for the ground-state multiplet of the Pr^{3+} ion due to the combined effect of an applied field and Stevens operators, (i) $\hat{O}_2^0$,(ii) $\hat{O}_4^0$ and (iii) $\hat{O}_6^0$.

Despite the arbitary values of these calculated eigenenergies, the comparative ratios obtained from the three operators provided an indication of the order of magnitude of the crystal field parameters, B_2^0, B_4^0 and B_6^0. These initial values were refined through extensive trial and error, resulting in values, $B_2^0 = 10^5$and $B_6^0 = 2.3\text{x}10^3$ (the negligible effect of the $\hat{O}_4^0$ operator warranted its omission). The diagonalization of the resultant Hamiltonian,

$$\mathcal{H}_{RE}^{Pr} = \sum_{h_z=0}^{25} 10^5 \hat{O}_2^0 + 2.3x10^3 \hat{O}_6^0 - \frac{4}{5} \cdot \frac{10^7}{4\pi} \mu_B \mathbf{h}_z . \mathbf{J}_z \qquad (37)$$

yielded the energy eigenvalues plotted versus $\mathbf{h}_z$ in figure 4.13 below. The expectation value of the rare-earth magnetic moment, μ_R associated with each corresponding eigenstate, Γ_z was calculated according to the expression

$$\mu_R = g\mu_B \langle \Gamma_z | \mathbf{J}_z | \Gamma_z \rangle \qquad (38)$$

and appears as the inset in figure 4.16.

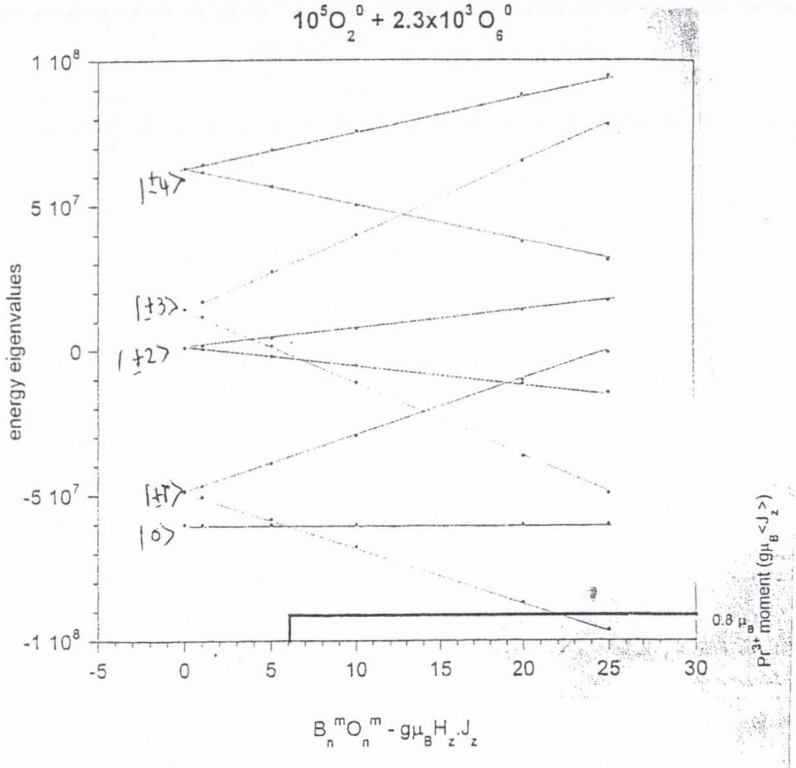

Figure 4.16 The calculated energy eigenvalues of $(Pr_{0.7}Ca_{0.3})MnO_3$ plotted versus applied field. The inset shows the variation of the corresponding Pr^{3+} moment as a function of applied field.

In conclusion, the ninefold degeneracy of the Pr^{3+} ground state, $^3H_4$ is entirely lifted by the combined crystal and applied fields resulting in the level crossing of the $|+1\rangle$ and $|-0\rangle$ states in an applied field of 6T, with no further level crossing up to 25 T. This corresponds to a contribution of 0.8 $\mu_B/formula\ unit$ from the rare-earth to the total magnetization of $(Pr_{0.7}Ca_{0.3})MnO_3$, *in accordance with measured data* [figure 4.12(b)]

(b) $(Nd_{0.7}A_{0.3})MnO_3$; **A** = Sr^{2+}, Ba^{2+}. As in the case of Pr^{3+}, the matrix elements of J_z could be written down, where M_J for Nd^{3+} is $\frac{9}{2}$,

$$J_z = \begin{bmatrix} \frac{9}{2} & 0 & 0 & 0 & 0 & 0 & 0 & 0 & 0 & 0 \\ 0 & \frac{7}{2} & 0 & 0 & 0 & 0 & 0 & 0 & 0 & 0 \\ 0 & 0 & \frac{5}{2} & 0 & 0 & 0 & 0 & 0 & 0 & 0 \\ 0 & 0 & 0 & \frac{3}{2} & 0 & 0 & 0 & 0 & 0 & 0 \\ 0 & 0 & 0 & 0 & \frac{1}{2} & 0 & 0 & 0 & 0 & 0 \\ 0 & 0 & 0 & 0 & 0 & \frac{-1}{2} & 0 & 0 & 0 & 0 \\ 0 & 0 & 0 & 0 & 0 & 0 & \frac{-3}{2} & 0 & 0 & 0 \\ 0 & 0 & 0 & 0 & 0 & 0 & 0 & \frac{-5}{2} & 0 & 0 \\ 0 & 0 & 0 & 0 & 0 & 0 & 0 & 0 & \frac{-7}{2} & 0 \\ 0 & 0 & 0 & 0 & 0 & 0 & 0 & 0 & 0 & \frac{-9}{2} \end{bmatrix}$$

In order to evaluate the splitting of the ten-fold degenerate Nd^{3+} ground-state J multiplet, $^4I_{\frac{9}{2}}$ due to the crystal-field at the rare-earth site and an external applied field, the crystal-field parameters, B_2^0 and B_6^0 needed to be determined and the eigenenergies of the following Hamiltonian calculated:

$$\mathcal{H}_{RE}^{Nd} = \sum_{h_z=0}^{25} B_2^0 \hat{O}_2^0 + B_6^0 \hat{O}_6^0 - \frac{8}{11}\frac{10^7}{4\pi}\mu_B \mathbf{h}_z.\mathbf{J}_z \qquad (39)$$

As noted previously [4.2.2 (i)], the crystal-field parameters included in this Hamiltonian can be written as

$$B_2^0 = \theta_2 A_2^0 \langle r^2 \rangle \text{ and } B_6^0 = \theta_6 A_6^0 \langle r^6 \rangle \qquad (40)$$

Since A_2^0 and A_6^0 are empirical coefficients, characteristic of the crystallographic structure under consideration, and $\langle r^2 \rangle$, $\langle r^6 \rangle$ are the average values of the 4f shell radius of the relevant rare-earth ion, simple substitution yields the values of B_2^0 and B_6^0 for Nd^{3+} from those previously determined for Pr^{3+}.

	B_2^0	A_2^0	θ_2	$\langle r^2 \rangle$
Pr^{3+}	10^5	-4.385x10^6	-2.1x10^{-2}	1.086
Nd^{3+}	2.82x10^4	-4.385x10^6	-6.4x10^{-3}	1.001
	B_6^0	A_6^0	θ_6	$\langle r^6 \rangle$
Pr^{3+}	2.3x10^3	2.398x10^6	6.1x10^{-5}	15.726
Nd^{3+}	-1.13x10^3	2.398x10^6	-3.8x10^{-5}	12.396

Substitution of these crystal-field parameters into $\mathcal{H}_{RE}^{Nd}$ above and subsequent diagonalization of the resulting Hamiltonian produced the eigenenergies which are plotted against $\mathbf{h_z}$ in figure 4.14. The inset shows the contribution of the Nd^{3+} moment to the total magnetization of the compound. This was calculated, as in the previous case, through evaluating the expectation value of the rare-earth magnetic moment, μ_R associated with each corresponding eigenstate, Γ_z ,according to the expression

$$\mu_R = g\mu_B \langle \Gamma_z | \mathbf{J}_z | \Gamma_z \rangle \qquad (41)$$

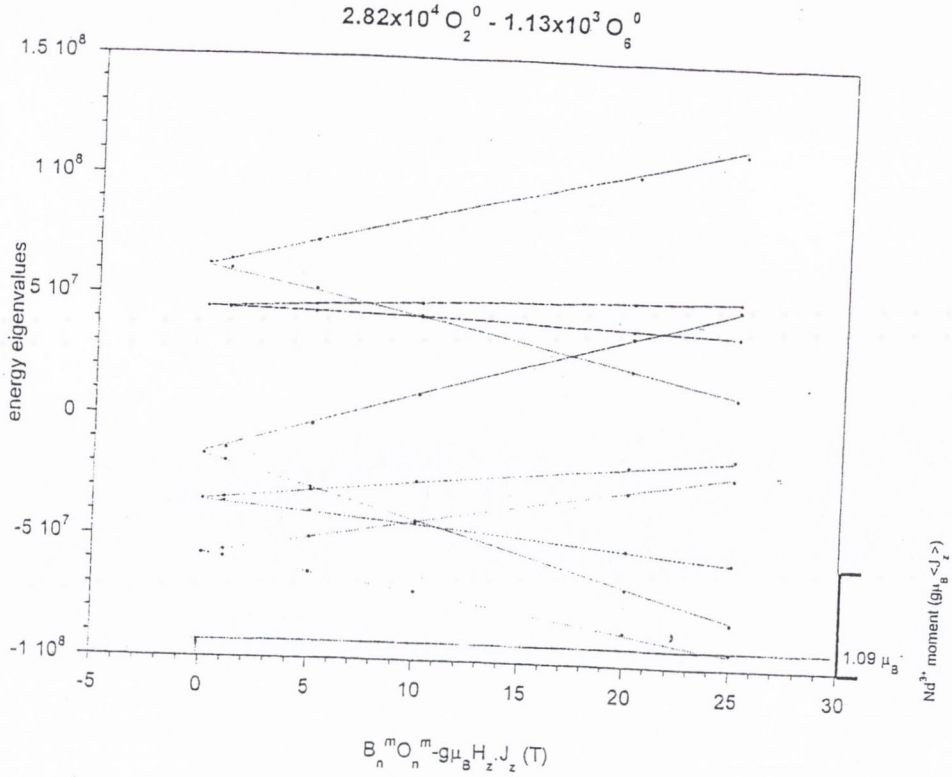

Figure 4.17 The calculated energy eigenvalues of $(Nd_{0.7}Ca_{0.3})MnO_3$ plotted versus applied field. The inset shows the variation of the corresponding Nd^{3+} moment as a function of applied field.

With the notable exception of the Ca containing compound, the total magnetization of the Nd^{3+} containing manganites were experimentally shown to exceed the theoretical spin-only moment expected for a fully aligned $Mn^{3+/4+}$ sub-lattice [table 4.5] . However, no abrupt transitions characteristic of an energy-level crossing were measured experimentally. Both these obsevations are consistent with the results of the crystal-field calculations presented.

4.4.1.4 (iii) Consideration of randomly oriented particles.

As previously noted, the calculation above is based on the assumption that these compounds are magnetically oriented along the crystallographic z-axis, parallel to the direction of the applied field, $\mathbf{B}_z$. As a direct consequence of this bold simplification, the rare-earth moment, as calculated for the Pr compound, increases in a step-like manner at 6T. However, closer inspection of the measured data of figure 4.10(b), indicates that the transition to the 4.4 μ_B high moment state is a gradual process, occuring between 6 T and 10 T [figure 4.18 (a)]. Adjacent to this figure is the result of a calculation which considers the effect of a field applied in the z direction on a system of particles whose individual magnetic orientation is described by a Gaussian distribution centred along the z-direction with a standard distribution, σ=1.4.. Hence, the magnetisation of the majority of particles is aligned parallel to $\mathbf{B}_z$, (i.e. at θ = 0°), whilst the number of particles oriented at an angle θ to $\mathbf{B}_z$ decreases as the angle deviates from 0° to 90°. Based on the preceeding calculations, it is presumed that an energy-level crossing occurs when a minimum field of 6T is applied parallel to the particle's magnetisation direction. Although this model successfully reproduces the experimental data, there appears no obvious physical explanation as to why the magnetic orientation of the particles within the polycrystalline sample should obey this distribution.

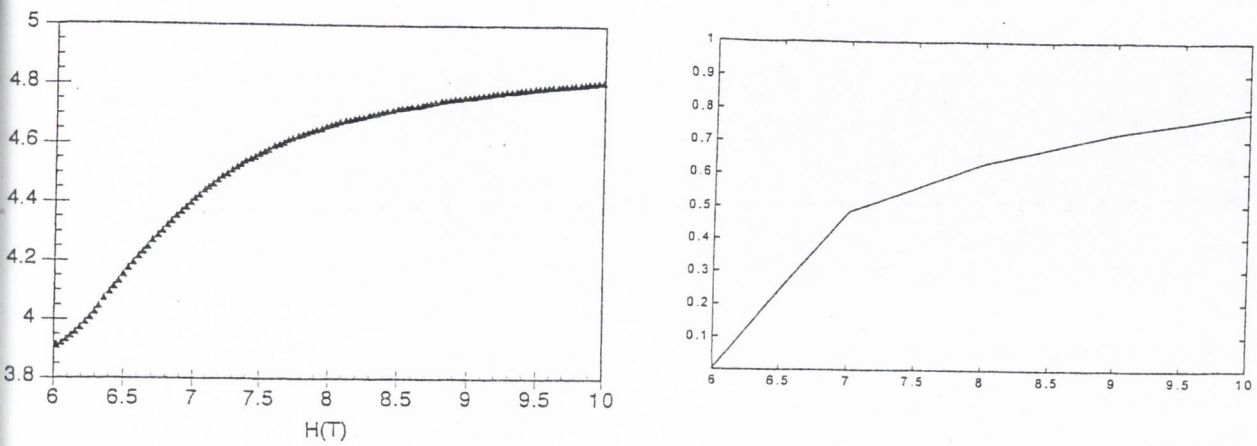

Figure 4.18 The gradual increase of the $(Pr_{0.7}Ca_{0.3})MnO_3$ moment with increasing field, (a) obtained experimentally and (b) modelled using a Gaussian distribution of particles' magnetic orientation.

4.4.2 X-ray magnetic circular dichroism (XMCD)

In high fields, the Nd^{3+} moments in $(Nd_{0.7}A'_{0.3})MnO_3$, A=Sr^{2+}, Ba^{2+}, are aligned parallel to those of Mn, resulting in the enhanced magnetic moments measured [figure 4.12 (c)]. Further support for this observation is lent by recent X-ray magnetic circular dichroism (XMCD) experiments carried out by Toulemonde *et al.* [58]. This powerful, spectroscopic technique is capable of providing quantitative, element-specific information about the spin character of electronic states, and consequently, the local spin and orbital moments of the constituent magnetic ions. Through comparing the dichroism spectra from both Mn and Nd ions, the French group have established the relative orientation of these ions' moments in $(Nd_{0.72}Ba_{0.28})MnO_3$; at 20 K the rare-earth and Mn sublattices are antiferromagnetically orderered. However, an applied field of 1.5 T switches the relative orientation of the Nd moment, and ferromagnetic alignment prevails in higher fields. The antiferromagnetic sublattice ordering at low temperature has also been confirmed for $(Nd_{0.7}Ba_{0.3})MnO_3$ by recent neutron diffraction measurements in zero field [59]. Moreover, similar measurements of the Ca and Sr substituted compounds have failed to identify a comparable transition, and the sublattices of these compounds remain ferromagnetically ordered, even in zero applied field [60] [61].

In response to these findings, further XMCD experiments were carried out on the Nd containing compounds in order to investigate the possible coupling mechanisms for the Nd and Mn sublattices.

4.4.2.1 Background

XMCD absorption spectroscopy, proposed by Erskine and Stern [62] and pioneered by Schütz *et al.* [63] elicits the quantitative determination of element-specific spin and orbital magnetic moments in ferromagnetic and ferrimagnetic materials. For a magnetised material, dipole selection rules together with the Pauli exclusion principle give different absorption probabilities for left and right circularly polarised X-rays. The XMCD signal is defined as the absorption difference,

$$I_{XMCD} = \mu^+ - \mu^- \tag{42}$$

where μ^+ and μ^- are the absorption cross-sections of a sample with a fixed magnetisation direction, for X-rays with left and right helicities respectively [8]. The resulting experimentally obtained spectra correlate to the electronic and magnetic ground state properties through powerful "sum rules" [65] [66] [67].

Historically, the predominant application of XMCD has been to the study of 3d transition metal elements [68], where the properties of the 3d-electrons are probed by *L-edge* excitation of 2p core electrons to unfilled 3d states. The relevant physics is best described in a two-stage, one-electron model, as illustrated in figure 4.19. Firstly, circularly polarised X-rays, in which the photon helicity is defined relative to the X-ray propagation direction as right or left, impinge on the sample, exciting a photoelectron from the spin-orbit split 2p core shell to empty 3d conduction band states above the Fermi level. Transference of the right and left polarised photons' angular momenta, h and -h respectively to the electron spin courtesy of the spin-orbit coupling, creates excited photoelectrons with opposite spins. Furthermore, since the $p_{\frac{1}{2}}$ (L_2) and $p_{\frac{3}{2}}$ (L_3) have opposite spin-orbit coupling ($l - s$ and $l + s$ respectively), the spin polarisation will be opposite at the two edges. During the second part of the mechanism, the spin-split valence shell acts as an effective detector for the spin of the excited photoelectron. The quantization axis of the detector is defined by the magnetization direction of the sample, which, when aligned with the photon spin direction, maximises the dichroic effect. The XMCD white line intensities, L_2 and L_3, recorded with right and left circular polarisation are of opposite sign, reflecting the opposite spin-orbit coupling of the $p_{\frac{1}{2}}$ and $p_{\frac{3}{2}}$ levels. The spin sum rule correlates the measured intensites, L_3 - $2L_2$ to the spin moment. Likewise, if the valence shell possesses an orbital moment, it will act as an orbital momentum detector for the excited photoelectron. Through simply summing over the L_2 ($l - s$) and L_3 ($l + s$) intensities the spin s is evidently eliminated, and the orbital moment of the valence shell is deduced. An orbital sum rule expresses the relation between the integrated intensities and the orbital moment of the valence shell.

[8] The following description is based on the premise of a fixed sample magnetisation direction and the dichroic signal consequently equals the difference between the intensities obtained for the two X-ray helicities. Although conceptually simpler, in practise, the spectra are measured using fixed circular polarisation while switching the magnetisation direction parallel and anti-parallel to the incoming photons. The equivalence of both arrangements is easily shown [64].

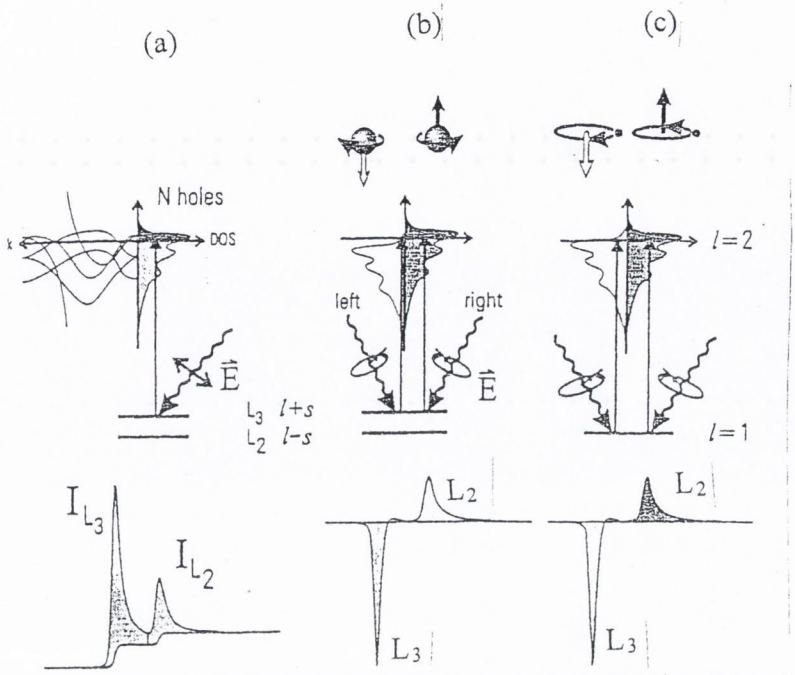

Figure 4.19 L-edge X-ray magnetic circular dichroism illustrated in a one-electron model. The transitions occur from the spin-orbit split 2p core shell to empty conduction band states above the Fermi level, E_F. In conventional L-edge X-ray absorption (a), the transition intensity measured, $I_{L_3} + I_{L_2}$ is proportional to the number of unoccupied states in the d band. By use of circularly polarised X-rays, the spin moment (b) and orbital moment (c) can be determined from the difference in dichroic intensities, using sum rules.

The straightforward picture described is directly applicable to transition metal elements such as manganese. Indeed, previous XMCD measurements have been successfully carried out at the Mn $L_{2,3}$-edge of the optimally doped manganites [58] [69] yielding crude estimates of the average orbital contribution to the Mn magnetic moment of - 2.1 x 10^{-2} μ_B to - 5.1 x 10^{-2} μ_B at low temperature.

Here, attention is drawn to the strong hybridisation of the Mn 3d and O 2p orbitals in the manganites - a prerequisite of the double exchange mechanism. Since the manganites' electronic structure cannot be accurately described in terms of a purely ionic model, the precise, quantitative interpretation of transitions to orbitals of mixed character is a somewhat ambiguous affair.

Quantitative analysis of the L edge dichroic spectra is also difficult for the rare-earth ions due to the presence of the localised 4f electronic states. Here, the transitions at the L_2 and L_3-edges correspond to electron excitation from $2p_{\frac{1}{2}} \rightarrow 5d_{\frac{3}{2}}$ and $2p_{\frac{3}{2}} \rightarrow 5d_{\frac{5}{2}}$ respectively. The partial occupancy of the 4f level, and the strong intra-atomic coupling which aligns the 4f and 5d electron spins, destroys the symmetry of the L_2 and L_3 dichroic intensities, thus compromising the sum rules [70]. Thus, for the manganite samples studied, a quantitative determination of the Nd^{3+} spin moment (electronic configuration, $[Xe]4f^3 6s^2$), is beyond the scope of any rudimentary analysis.

However, qualitative information regarding the nature of the inter and intra-atomic coupling of the Nd and Mn ions may be obtained through comparing the relative orientation of the dichroic signals with reference to the aforementioned results [58]. In this previous work, the reversal of the Nd moments' orientation relative to that of the Mn ions, was determined through comparing the relative directions of the L_3 edge and Nd $M_{4,5}$-edge dichrosim peaks. Earlier discussion has established that the former peak originates from the $2p_{\frac{3}{2}} \rightarrow 3d_{\frac{5}{2}}$ transition in Mn, providing a direct probe of the "magnetic" hybridised 3d orbitals. Similarly, the M-edges of Nd probe the "magnetic" 4f shell of the rare-earth ion, as the dichroic signal is ascribed to 3d $\rightarrow$ 4f transitions in this ion.

Therefore, through comparing the results of both experiments, conclusions may be drawn as to whether the applied field serves to break the intra-atomic Nd (5d) - Nd (4f) coupling or the inter-atomic coupling Nd (5d) - Mn (3d) as mediated by the Nd (5d) conduction electrons.

During the course of this experiment, XMCD spectra were obtained at both the Nd L_3 edge and Mn K edge. The K-edge absorption in manganese corresponds to a transition from the 1s to the empty 4p band states, with the dichroism originating from the polarisation of the final states, as opposed to the core shell as previously discussed for the L-edges. The polarisation of the Mn 4p states, previously attributed to the on-site Coulomb interaction between Mn 3d and 4p electrons [71], and more recently assumed to originate from the hybridisation of the 4p with the 3d orbitals on neighbouring Mn ions (either directly or via the intervening O 2p orbitals) [72]. The fortuitous proximity of the Mn K-edge (at 6540 eV) to the L_3-edge of Nd^{3+} (at 6208 eV) enabled both edges to be probed simultaneously, using the dispersive optics arrangement described in the following subsection.

4.4.2.2 Experimental arrangement

Although a theoretically straightforward technique, the experimental implementation of XMCD is not a trivial task, requiring highly collimated, circularly polarised X-rays and precise detection optics. The generation of hard X-rays (5 - 20 keV) at the Dispositif de Collision dans l'Igloo (DCI) synchrotron installation at the Laboratoire pour l'Utilisation du Rayonnement Electromagnétique (LURE), and the dispersive optics of the D11 beamline at that facility are described below.

(i) The generation of synchrotron radiation and circularly polarised photons

Synchrotron radiation is the intense, highly collimated electromagnetic field emitted by charged particles moving at relatavistic speeds in circular orbits in a magnetic field. At the DCI storage ring, a tungsten converter produces positrons from the electron beam that emerges from a linear accelerator with energies of a few hyndred MeV. Bending magnets apply state magnetic fields,

B, perpendicular to the horizontal orbital plane of the positron beam, accelerating the particles along a circular path, in accordance with the Lorentz force, $\underline{F} = e\underline{v} \times \underline{B}$. The resulting radius of curvature is

$$\rho = \frac{m\gamma v^2}{F} \approx \frac{m\gamma c}{eB} \approx \frac{3.32E}{B} \; (GeV) \tag{43}$$

for relatavistic particles of energy, $E = \gamma mc^2$, where $\gamma \gg 1$ and m is the particles' rest mass. At the DCI facility, the circumference of the positrons' orbit is 96 m, the particle energy, E = 1.85 GeV and the applied, accelerating field, B = 1.6 T. The synchrotron radiation is emitted tangentially along the particles' circular trajectory with a spectral bandwidth ranging from the infra-red up to a critical wavelength, $\lambda_c = 3.4$ Å ($E_c = 3.62$ keV), defined such as half the total power is radiated at energies greater than E_c.

The D11 beamline is situated at the exit of the D1 bending magnet light source at DCI. The beam emitted is linearly (plane) polarised both within the plane of the particles' rotation and perpendicular to this plane. These orthogonal linear polarisation states, denoted as σ and π respectively, are phase shifted by $\frac{\pi}{2}$ since one is real and the other imaginary. Consequently, although the beam is fully horizontally polarised when the direction of observation lies in the midplane of emission, (i.e. at $\psi = 0°$), above and below this plane the light is circularly polarised with right-handed and left-handed helicity respectively;.the degree of circular polarisation increasing with increasing ψ. However, the total flux, defined as the number of photons emitted per second within a defined spectral bandwidth, decreases as ψ deviates from 0°.

The selection window of width 1mm for the incident circularly polarised beam used during the XMCD measurements presented, was situated 15 m from the bending magnet source, at 5 mm below the midplane of emission, corresponding to $\psi = 0.3$ mrad. This position represents the optimal compromise between total flux and degree of circular polarisation, yielding light with a left-handed helicity, 60% circular polarisation and a total flux of 3 x 10^{11} photons/s.

(ii) *Dispersive optics at D11*

Illustrated in figure 4.20 is the arrangement of monochromator and detector which constitutes the energy dispersive optics situated 15 m from the point source at beamline D11. The triangularly-shaped silicon single crystal "monochromator" is curved so that the continuous variation of incident angle produces a polychromatic beam with a defined energy-reflection angle correlation, in accordance with Bragg's law

$$2d_n \sin\theta = n\lambda \tag{44}$$

The relation betwen the X-ray energy and the direction of propagation translates into an energy-position correlation at the position-sesitive detector, which comprises 1024 photodiodes of width 25 μm. This arrangement enables precise and simultaneous energy measurement over a broad energy spectrum.

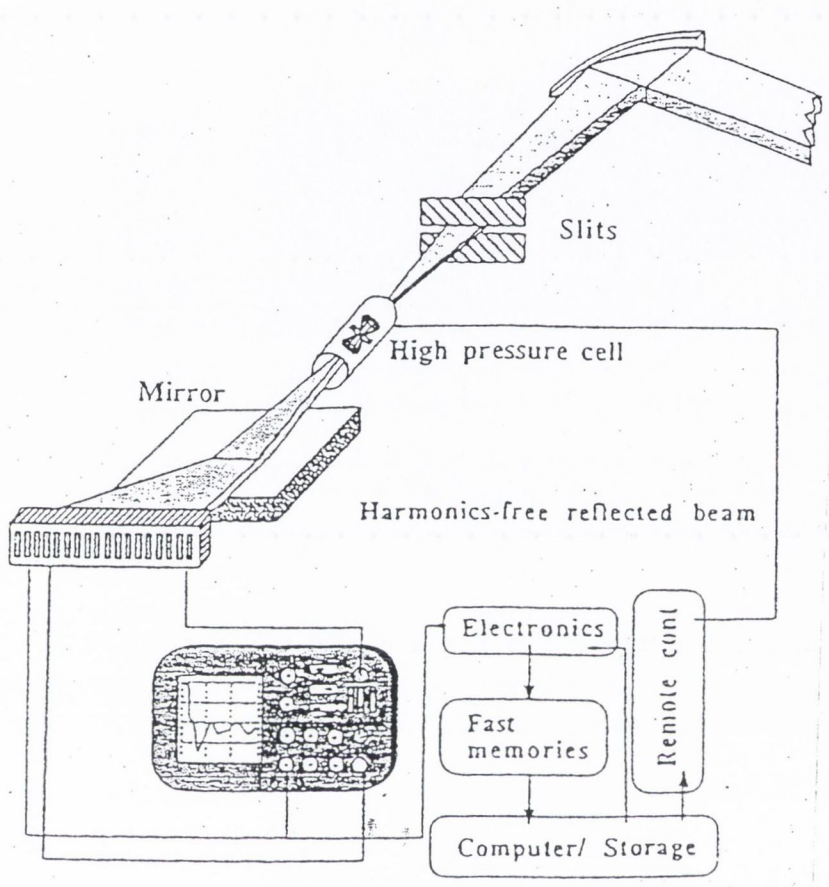

Figure 4.20 Schematic illustration of the dispersive optics arrangement which allows simultaneous collection of a full spectrum.

(iii) Data aquisition

To achieve dichroism, the dispersive optics are tuned to the energy of the probed edge, and the direction of the sample's bulk magnetisation interchanged through the alternate application of a magnetic field parallel and anti-parallel to the direction of propagation of the X-rays. An applied field up to 4T was produced by a helium-cooled superconducting magnet, whilst a cryostat enabled the measurement to be carried out at 4.2 K.

The measurement was carried out in a transmission geometry; the intensity of the signal measured by the bank of photodiodes, I, depends on the absorption coefficient, μ, of the sample and its thickness, l,

$$I = I_0 e^{-\mu.l} \tag{45}$$

giving

$$\mu = \frac{l}{t} \ln \left[\frac{I_0}{I} \right] \tag{46}$$

During XMCD, the signal measured with the field parallel and antiparallel to the X-rays, gives successively,

$$\mu^{+} = \frac{l}{t} \ln \left[\frac{I_0}{I^{+}} \right] \tag{47}$$

and

$$\mu^{-} = \frac{l}{t} \ln \left[\frac{I_0}{I^{-}} \right] \tag{48}$$

which gives,

$$\mu^{+} - \mu^{-} = \frac{l}{t} \ln \left[\frac{I^{-}}{I^{+}} \right] \tag{49}$$

The small amplitude of the effect necessitates the repeated aquisition of the signal; each Nd^{3+} L-edge absorption measurement was repeated 85 times. The rapid rate of aquisition and stability offered by the dispersive optics set-up enabled the signal to noise ratio to exceed 10.

(iv) Sample preparation

Samples for transmission spectroscopy are required to be transparent to x-rays. Therefore, a solution of ground manganite powder in cyclohexane was filtered through an adhesive 0.8 μm micropore membrane, yielding a 10 μm thick layer of homogenously distributed manganite particles. The membrane was subsequently secured to the sample holder using Kapton tape.

4.4.2.3 Results

Figure 4.21 show the XMCD signals measured for (a) $(Nd_{0.7}Sr_{0.3})MnO_3$, (b) $(Nd_{0.7}Ca_{0.3})MnO_3$ and (c) $(Nd_{0.7}Ba_{0.3})MnO_3$ at 4.2 K in applied fields in the range 0.1 T to 4 T as noted.

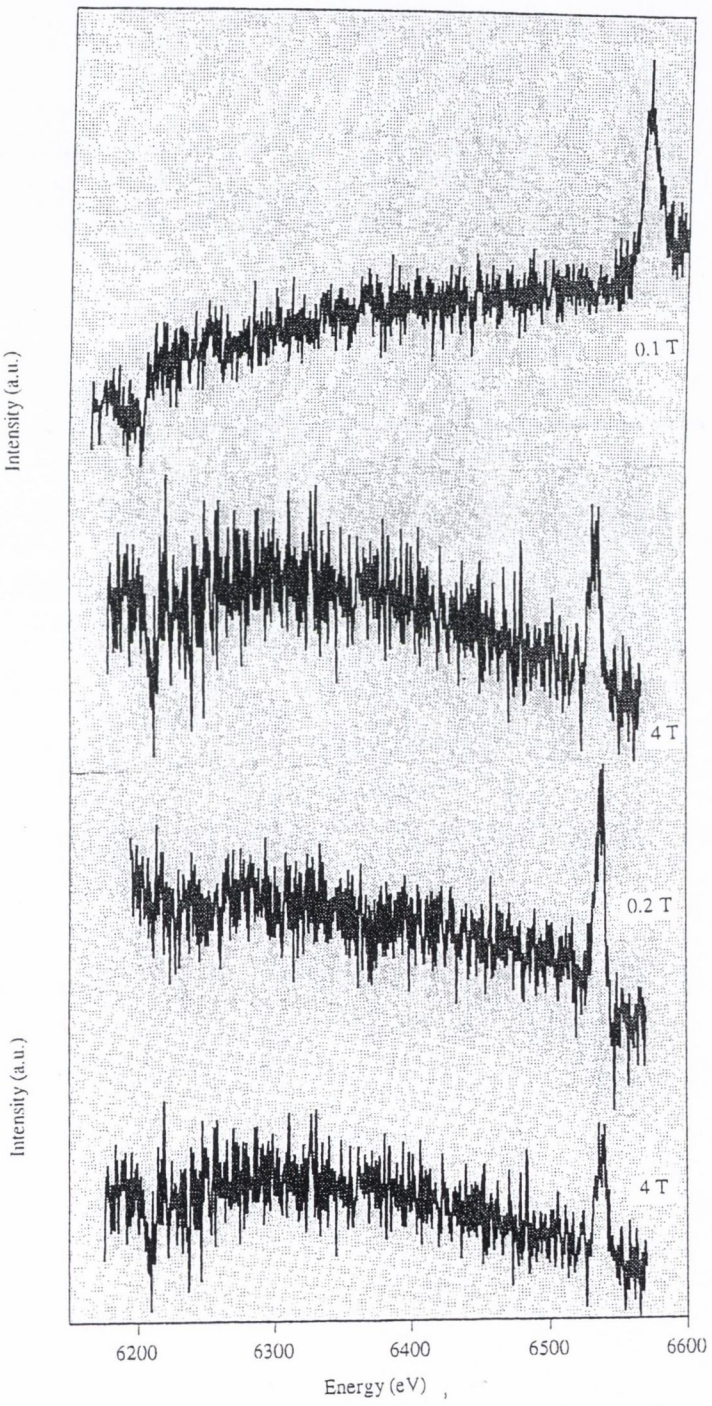

Figure 4.21 X-ray magnetic circular dichroism spectra measured for (a) $(Nd_{0.7}Sr_{0.3})MnO_3$ in applied fields 0.1 T and 4 T; (b) $(Nd_{0.7}Ca_{0.3})MnO_3$ in applied fields 0.2 T and 4 T.

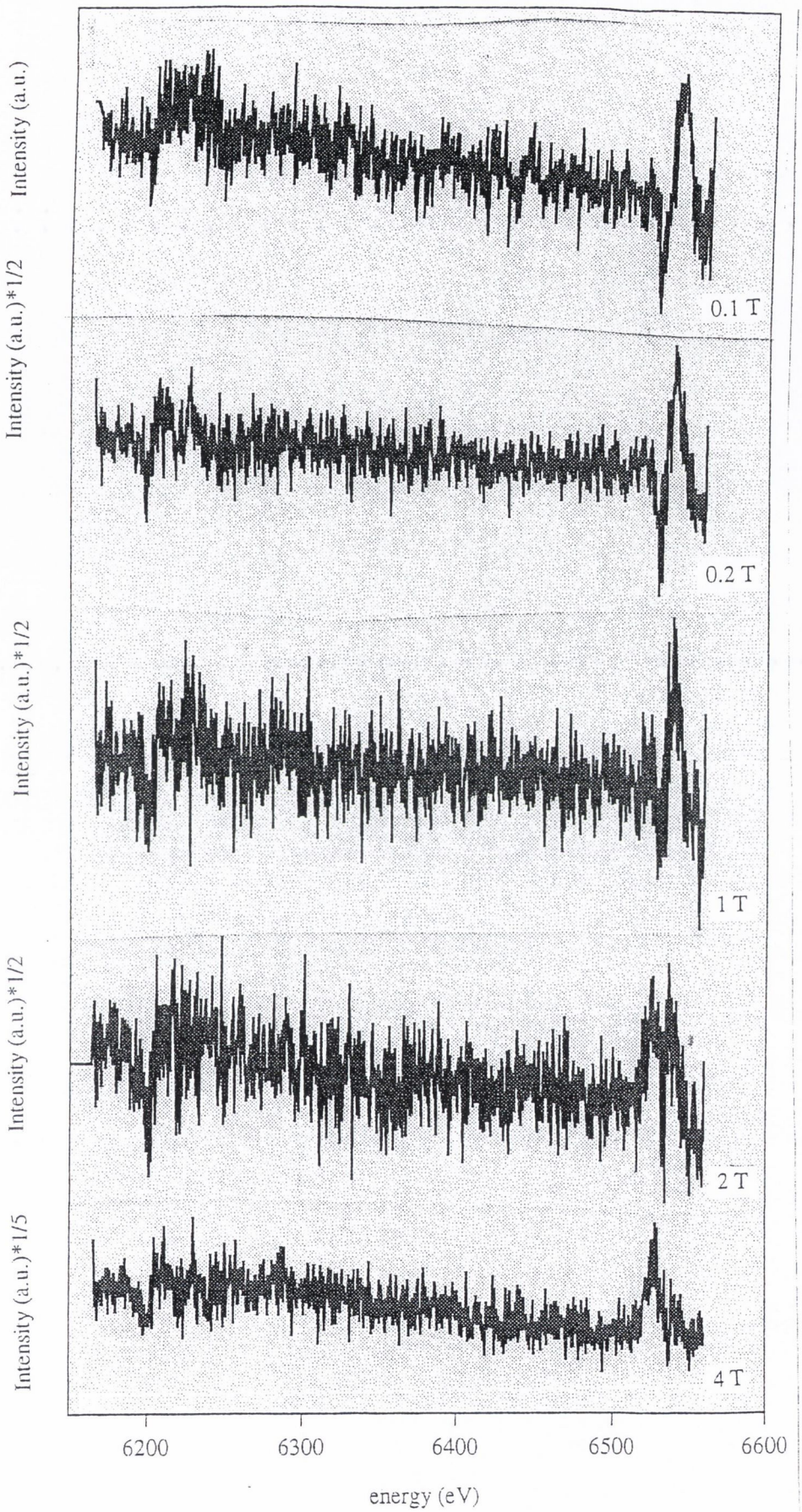

Figure 4.21(c) X-ray magnetic circular dichroism spectra measured for $(Nd_{0.7}Ba_{0.3})MnO_3$ in applied fields 0.1 T, 0.2 T, 1 T, 2 T and 4 T as noted.

4.4.2.4 Discussion

Although the dispersive optics employed during the XMCD measurements were specifically designed to minimise the inherent noise, the poor signal to noise ratio of the XMCD data presented in figure 4.21 provokes comment. The most obvious origin of this unwanted signal is the inhomogeneous dispersion of the manganite particles on the membrane - an inevitable difficulty when preparing polycrystalline samples. A further possible cause of noise is the shifting of a magnetised sample in a rotating applied field.

Nevertheless, a strong positive peak at 6540 eV is clearly discernible in each data set, corresponding to the K-edge transition of Mn. With the exception of the Ca containing sample, the height of this peak, which is proportional to the manganese moment, increases with increasing field, whilst its orientation with respect to the applied field remains constant. That this is not observed in $(Nd_{0.7}Ca_{0.3})MnO_3$ is attributed to the charge-ordering of this material, evidenced by the hysteretic M(H) loops measured in pulsed field at 4.2 K [figure 4.11].

Due to the small magnetic moment on the Nd cation, the peak corresponding to the L_2 edge at 6208 eV is barely distinguishable from the noisy background signal. However, it may be observed that for the Ca and Sr compounds, the relation between the Nd and Mn peak directions is unchanged in the lowest applied fields - 0.1 T and 0.2 T- respectively. The width of the Nd L_3 peak of $(Nd_{0.7}Ba_{0.3})MnO_3$ and a signal to noise ratio which approaches unity, makes the interpretation of the data measured in 0.1 T and 0. 2 T less obvious for this compoud. However, the conclusion is drawn that the peak direction is *not* reversed.

The exchange coupling of the Nd and Mn sublattices most likely proceeds via the 5d conduction electrons. The defined transition from the 2p to the empty 5d band characterising the Nd^{3+} L_2 edge supports this mechanism. Additionally, the 4f-4f interaction of the localised 4f (Nd^{3+}) orbitals is negligible above 0.97 K (the antiferromagnetic ordering temperature established for the Nd sublattice in $NdGaO_3$ [23]). Thus, the most plausible mechanism for this indirect interaction is one where the 4f electron spin creates a positive local 5d moment through intra-atomic 4f-5d exchange with subsequent 5d-3d exchange, as proposed by Campbell for rare-earth - transition metal intermetallic compounds [73].

It has been previously shown that the Nd M-edge peak (3d $\rightarrow$4f transition) of $(Nd_{0.7}Ba_{0.3})MnO_3$ changes sign in an applied field. Since no reversal of the Nd L-edge peak (2p $\rightarrow$5d transition) is observed, it is concluded that the applied field breaks the Nd (5d) - Nd (4f) coupling whilst the Nd (5d) - Mn (3d) coupling is preserved [figure 4.22].

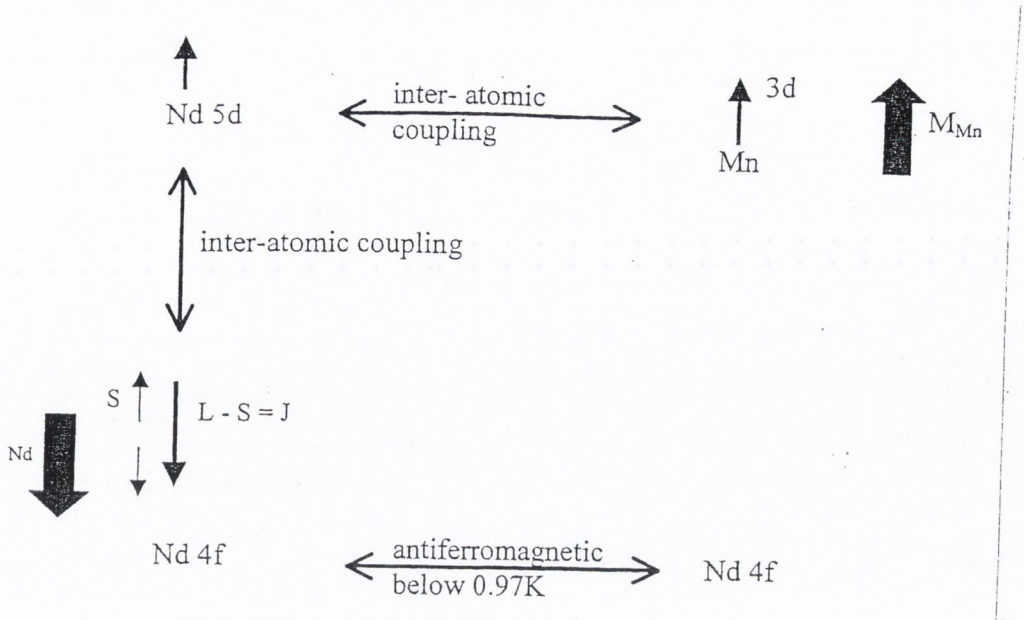

Figure 4.22 Schematic diagram illustrating the spin and moment coupling between antiferromagnetically aligned Nd and Mn elements as evidenced by XMCD measurements.

[1] E. O. Wollan and W. C. Koehler, Physical Review, **100**, 545, (1955).

[2] M. Quijada, J. Cerne, J. R. Simpson, H. D. Dresm K. H. Ahn, A. J. Millis, G. C Xiong, R. Ramesh, C. Kwon, M. Rajeswari, and T. Venkatesan, Physical Review Letters, **58**, 16093, (1998).

[3] Y. Okimoto, T. Katsufuji, T. Ishikawa, A. Urushibara, Physical Review Letters, **75**, 109, (1995).

[4] H. Y. Hwang, S.-W. Cheong, N. B. Ong, and B. Batlogg, Physical Review Letters, **75**, 109, (1995).

[5] P. K. de Boer, H. van Leuken, R. A. de Groot, T. Rojo and O. B. Barberis, Solid State Communications, **102**, 621, (1997).

[6] J-H. Park, E. Vescoveo, H-J. Kim, C. Kwon, R. Ramesh and T. Venkatesan, Nature **392**, 794, (1998).

[7] W. B. Pickett and D. J. Singh, Physical Review B **53**, 1146, (1996).

[8] Y. Lu, X. W. Li, G. Q. Gong, G. Xiao, A. Gupta, P. Lecoeur, J. Z. Sun, Y. Y. Wang and V. P. Dravid, Physical Review B, **54**, R8357, (1996).

[9] J. Z. Sun, L. Krusin-Elbaum, P. R. Duncombe, A. Gupta and R. B. Laibowwitz, Applied Physics Letters, **70**, 1769, (1997).

[10] R. J. Soulen Jr, J. M. Byers, M. S. Osofsky, B. Nadgorny, T. Ambrose, S. F. Cheong, P.R. Broussard, C. T. Tanaka, A. Barry and J. M. D. Coey, Science, **282**, 85, (1998).

[11] J. R. Cullen and E. Callan, Physical Review, **100**, 545, (1955).

[12] Z. Jirák, S. Krupicka, Z. Simša, M. Dlouhá and S. Vrastislaj, Journal of Magnetism and Magnetic Materials, **53**, 153, (1985).

[13] M. R. Lees, J. Barratt, G. Balakrishnan and D. M. Paul, Physical Review B **52**, 14303, (1995).

[14] Y. Moritomo, H. Kuwahara, Y. Tomioka and Y. Tokura, Physical Review B 55, 7549, (1997).

[15] A. Asamitsu, Y. Tomioka and Y. Tokura, Nature, 388, 50 (1997).

[16] V. Kiryukhin, D. Casa, J. P. Hill, B. Keimer, A. Bigilante, Y. Tomioka and Y. Tokura, Nature, 386, 813, (1997).

[17] K. Miyano, T. Tanaka, Y. Tomioka and Y. Tokura, Physical Review Letters, 78, 4257, (1997).

[18] M. Fiebig, K. Miyano, Y. Tomioka and Y. Tokura, Science, 280, 1925, (1998).

[19] A. J. Millis, P.B. Littlewood and B. I. Shraiman, Physical Review Letters, **74**, 5144, (1995).

[20] J. M. D. Coey, M. Viret and S. von Molnár, Advances in Physics, **48**, 167, (1999).

[21] A. Podlesnyak, S. Rosenkranz, F. Fauth, H.J. Scheel and A. Furrer, Journal of Physics of Condensed Matter, **6,** 4066, (1994).

[22] A . Podlesnyak, S. Rosenkranz, F. Fauth, W. Marti, A. Furrer, A. Mirmelstein and H.J. Scheel, Journal of Physics of Condensed Matter, **5,** 8973, (1993).

[23] F. Bartolome, M. D. Kuzmin, R. Merino and J. Bartolome, IEEE Transactions on Magnetics, **30**, 960, (1994).

[24] H. A. Kramers, Proceeding of the Academy of Sciences, Amsterdam, **33**, 959, (1930).

[25] G.H. Jonker, Physica, **22**, 707 (1956).

[26] F. Lotgering, Philips Research Reports, **25**, 8, (1970).

[27] J. B. Goodenough, Physical Review, **100**, 564, (1955).

[28] H. Watanabe, Journal of the Physical Society of Japan, **16,** 433 (1961).

[29] E.E. Havinga, Philips Research Reports, **21**, 432 (1966).

[30] J.B.A.A. Elemans, B. van Laar, K.R. van der Veen and B. O. Loopstra, Journal of Solid State Chemistry, **3,** 238 (1971).

[31] H.Y. Hwang, S-W. Cheong, P.G. Radaelli, M. Marezio and B. Batlogg, Physical Review Letters, **75**, 914 (1995).

[32] R. M. Thomas, L. Ranno and J.M.D. Coey, Journal of Applied Physics, **81**, 5763, (1997).

[33] W. Archibald, J-S. Zhou and J. B. Goodenough, Physical Review B 53, 14445, (1996).

[34] L.M. Rodriguez-Martinez and J.P. Attfield, Physical Review B **54**, R15622, (1996).

[35] R. D. Shannon and C. T. Prewitt, Acta Crystallographica A, **32**, 785, (1976).

[36] J.L. Garcia-Munoz, B. Nartinez, A Seffar, S. Pinol and X. Obradors, Physical Review B, **55** R668 (1995).

[37] J. Fontcuberta, Physics World,12, **33** (1999).

[38] D.X. Chen, *Demagnetising factors for cylinders,* IEEE Transaction on Magnetics, Volume 24, No. 4, (1991).

[39] A. H. Morrish, *The Physical Principles of Magnetism*, (John Wiley and Sons, New York), 383, (1965).

[40] M. Jaime and M. B. Salamon, *Electronic Transport in La-Ca manganites*, (Plenum Press,1999).

[41] J. M. De Teresa, M. R. Ibarra, P. A. Algrabel. C. Ritter, C. Marquina, J. Blasco, J. Garcia, A. del Moral and Z. Arnold, Nature, **386**, 256, (1997).

[42] F. Damay, N. Nguyen, A. Maignan, M. Hervieu and B. Raveau, Solid State Communications, **98**, 997, (1996).

[43] J. J. M. Franse and R. J. Radwanski, *Handbook of Magnetic Materials Volume 7*, editor K. H. J. Buschow, (Elsevier, Amsterdam), p.340, (1993).

[44] F. Valentin, Research report, Department of Physics, Trinity College Dublin, (1995).

[45] G. Allodi, R. D. Renzi, G. Guidi, F. Licci and M. Pieper, Physical Review B, **56**, 6036, (1997).

[46] Y. Tomioka, A. Asamitsu, Y. Moritomo, Y. Tokura, Journal of the Physical Society of Japan, **64**, 3626, (1995).

[47] J. Barratt, M. Lees, G. Balakrishnan, D. McK. Paul, Applied Physics Letters, **68**, 424, (1996).

[48] R-M. Thomas, V. Skumryev, J. M. D. Coey and S. Wirth, Journal of Applied Physics, **85**, 5384, (1999).

[49] A. Anane, J-P. Renard, L. Reversat, C. Dupas, P. Veillet, M. Viret, L. Pinsard, a. Revcolevschi, Physical Review B **59**, 77, (1999).

[50] K. N. R. Taylor, M. I. Darby, *Physics of Rare Earth Solids*, (Chapman and Hall, 1972).

[51] J. M. D. Coey, *Rare-Earth Permanent Magnets*, (Clarendon Press, Oxford, 1996).

[52] H. Bethe, Annalen Physikalische Leipzig 3, 133, (1929).

[53] K.W.H. Stevens, Procedings of the Physical Society A, **65**, 209, (1952).

[54] A.R. Edmonds, *Angular Momentum in Quantum Mechanics*, (Princeton University Press, Princeton, New Jersey), (1957).

[55]. A.J. Freeman and R.E. Watson, Physical Review, **139**, A1606, (1965).

[56] M.T. Hutchings, *Solid State Physics* volume 16, ed. F. Seitz and D. Turnbull, (New York:Academic), 227, (1964).

[57] C. Rudowicz, Journal of Physics C: Solid State Physics, **18,** 1415, (1985).

[58] O. Toulemonde, F. Studer, A. Llobet, L. Ranno, A. Maignan, E. Pollert, M. Nevriva, E. Pellegrin, N. B. Brooks and J. Goedkoop, Journal of Magnetism and Magnetic Materials,

190, 307, (1998).

[59] F. Fauth, E. Suard, C. Martin and F. Millange, Physica B **241**, 427, (1998).

[60] F. Millange, V. Caigneart, G. Mather, E. Suard and B. Raveau, Journal of Solid State Chemistry, **127**, 131, (1996).

[61] V. Caigneart, preprint.

[62] J. L. Erskine and E. A. Stern, Physical Review B **12**, 5016, (1975).

[63] G. Schütz, W. Wagner, W. Wilhelm, P. Kienle, R. Zeller, R. Frahm and G. Materlik, Physical Review Letters, 58, 737, (1987).

[64] J. Stöhr and Y. Wu, "*New Directions in Research with Third-Generation Soft X-ray Synchrotron Radiation Sources*", Editors A. S. Schlachter and F. J. Wuilleumeier, pp.241, (Kluwer Academic Publishers, Netherlands, 1994).

[65] B. T. Thole, P. Carra, F. Sette and G. van der Laan, Physical Review Letters, **68**, 1943, (1992).

[66] P. Carra, B. T. Thole, M. Altarelli and X. Wang, Physical Review Letters, **70**, 694, (1993).

[67] J. Stöhr and H. König, Physical Review Letters, **75**, 3748, (1995).

[68] J. Stöhr and R. Nakajima, Journal de Physicque IV, **7**, 47, (1997).

[69] E. Pellegrin, L. H. Tjeng, F. M. F. deGroot, R. Hesper, C. F. J. O'Mahony, J. D. Moritomo, Y. Tokura, C. T. Chen and G. A. Sawatzky, Journal Electron Spectron., **86**, 115, (1997).

[70] C. Giorgetti, Ph. D. Thesis, Université Paris Sud, (1994).

[71] S. Ishihara and S. Maekawa, Physical Review Letters **80**, 3799, (1998).

[72] I. S. Elfimov, V. I. Anisimov and G. A. Sawatzky, Physical Review Letters, **82**, 4264, (1999).

[73] I. A. Campbell, Journal of Physics F : Metal Physics, **2**, L47, (1972).

Chapter 5
The role of oxygen stoichiometry - $LaMnO_3$

5.1 Introduction

As the end-member of an exciting series of compounds, $LaMnO_3$ is regularly described as the "parent compound" from which the prototype CMR materials, $(La_{0.7}Sr_{0.3})MnO_3$ and $(La_{0.7}Ca_{0.3})MnO_3$ are derived through cation substitution. Whilst correct, such a description fails to emphasize that $LaMnO_3$ is a worthy research topic in itself.

As previously outlined, [section 2.1.4] preparation of the sample using the standard ceramic method, yields over-oxygenated samples in which deviations from the nominal stoichiometry are accommodated as cation vacancies, resulting in a Mn^{3+}-Mn^{4+} mixed valence state. Therefore, assuming that O^{2-} remains divalent, and vacancies (denoted by $\square$) are equally distributed over both La and Mn sites, the formula for the end-member may be written:

$$(La^{3+}_{1-\delta'}\square_{\delta'})(Mn^{3+}_{1-7\delta'}Mn^{4+}_{6\delta'}\square_{\delta'})O_3 \qquad (1)$$

which corresponds to

$$(LaMn)_{1-\delta'}O_3 \qquad (2)$$

However, convention dictates that the formula unit of these "oxygen-rich" samples be written $(LaMn)O_{3+\delta}$, where $\delta \approx 3\delta'$ and the fraction of Mn present as Mn^{4+} as expressed by these different notations is related by $6\delta'/(1-\delta') = 6\delta/(3-\delta)$. Although pure $LaMnO_3$ is an A-type antiferromagnet [chapter1], for sufficiently high Mn^{4+} content, the non-stoichiometric end-member should show ferromagnetic behaviour, as in the case of the mixed valence compounds produced through divalent cation substition. In the Ca^{2+} doped series, $(La^{3+}_{1-x}Ca^{2+}_x)(Mn^{3+}_{1-x}Mn^{4+}_x)O_3$, ferromagnetism is exhibited for $0.14 \leq x \leq 0.38$, with ordering temperatures, T_C 182 K to 278 K respectively [1]. The relevant non-stoichiometric compounds with equivalent Mn^{4+} content are thus in the range, $(LaMn)_{0.977}O_3$ to $(LaMn)_{0.937}O_3$.

Therefore, in order to draw a comparison between the physical properties of the optimally doped, x= 0.3 substituted lanthanides and their corresponding non-stoichiometric end-member, a polycrystalline ceramic sample of $(LaMn)_{0.95}O_3$ was prepared and characterised. The properties of the end-member were futher investigated through reducing the sample to produce a stoichiometric oxide, $LaMnO_3$, which was duly characterised.

5.2 Experimental procedure

5.2.1 Sample preparation

Using the standard ceramic method detailed in chapter 2, lanthanum oxalate, $La_2(C_2O_4)_3.9H_2O$ and manganese carbonate, $MnCO_3$, precursors were sintered at $900°C$ and subsequently ground and annealed repeatedly at $1200°C$ in air. X-ray diffraction [section 2.3.1] established that the polycrystalline ceramic produced was a single phase, with lattice parameters corresponding to those expected for the oxygen-deficient end-member with formal composition, $(LaMn)_{0.95}O_3$ [section 5.2.2].

The near-stoichiometric sample, $LaMnO_3$ was prepared through the thermal reduction of finely ground $(LaMn)_{0.95}O_3$ powder under hydrogen, using a *thermopiezic analyser* (TPA) [2]. Through measuring the change in pressure exerted by the sample within a fixed volume as a function of temperature, this instrument can provide a quantitative measurement of the gas desorbed by the compound. A schematic illustration of the apparatus is given in figure 5.1. The powdered sample is contained within a narrow quartz tube, the dimensions of which constrict the active volume to 2.64 cm^3. The furnace consists of a length of Kanthal wire wound around an Inconel bobbin and set in refractory cement. Thermal insulation is ensured by Kaowool; a fibre with a suitably high melting point. A computer interfaced power supply delivers current to the heater and a chromel-alumel thermocouple is used to measure the resulting temperature.

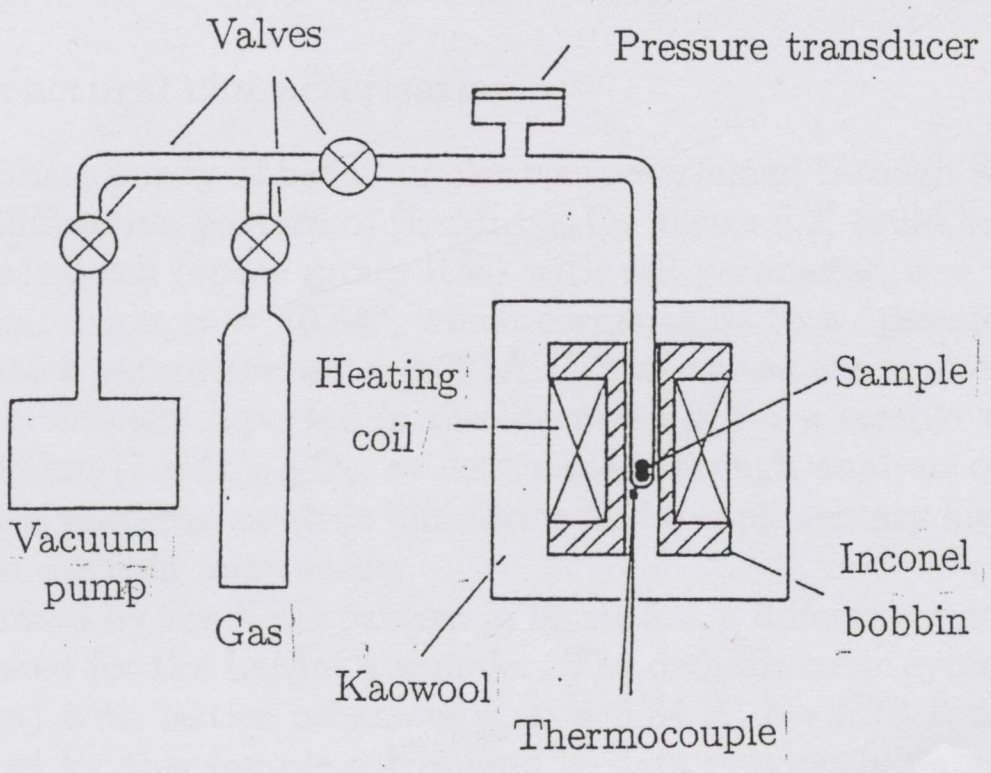

Figure 5.1 Schematic representation of the thermopiezic analyser (TPA).

Figure 5.2 below shows a typical temperature-pressure scan measured for 44.9 mg of $(LaMn)_{0.95}O_3$, heated at 20 $°C$/min to 700°C under 1 bar of hydrogen. The sample is seen to react at $\sim 400°C$, where the measured change in pressure, $\Delta P \approx 73$ mbar. The mass of the end-product was 44.5 mg; a decrease, which if solely attributed to oxygen desorption from the compound, is consistent with the formation of $LaMnO_3$. Although the possible additional incorporation of some hydrogen into the lattice as OH^- cannot be excluded on the basis of this result, the lattice parameters deduced for this compound (see below) are in good agreement with those reported for stoichiometric $LaMnO_3$ prepared using alternative methods; firing in a reduced pressure (10^{-3} Pa) of oxygen [3], or in nitrogen [4] or argon [5] atmospheres.

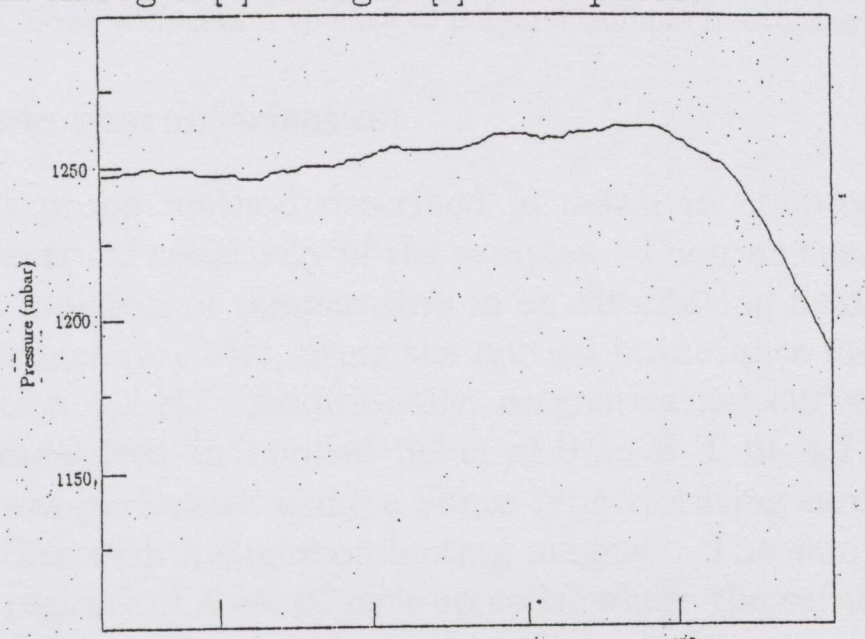

Figure 5.2 The variation of pressure with increasing temperature during the thermal reduction of $(LaMn)_{0.95}O_3$.

5.2.2 Structural characterisation

The single-phase purity of both samples was determined through X-ray diffraction. The diffraction pattern of $(LaMn)_{0.95}O_3$ [figure 5.2] could be indexed on a rhombohedral cell (space group $R\bar{3}c$) with cell parameter, a = 5.524 Å and rhombohedral angle, $\gamma = 60.64°$, which corresponds to a "pseudocubic" unit cell with lattice parameter, $a_C = 0.391$Å. These values are in close agreement with those previously reported in the literature [6] for a sample with the formal composition $(LaMn)_{0.95}O_3$, as determined through analysis of powder X-ray diffraction patterns, neutron diffraction and complimentary high-resolution transmission electron microscopy.

As illustrated by the XRD pattern in figure 5.2, a different crystal structure was established for the $LaMnO_3$ sample. The orthorhombic symmetry (space group *Pbnm*) with lattice parameters: a = 5.54 Å, b= 5.73 Å and c = 7.73 Å determined for this sample correspond to data previously published for the near-stoichiometric end-member [10] [4].

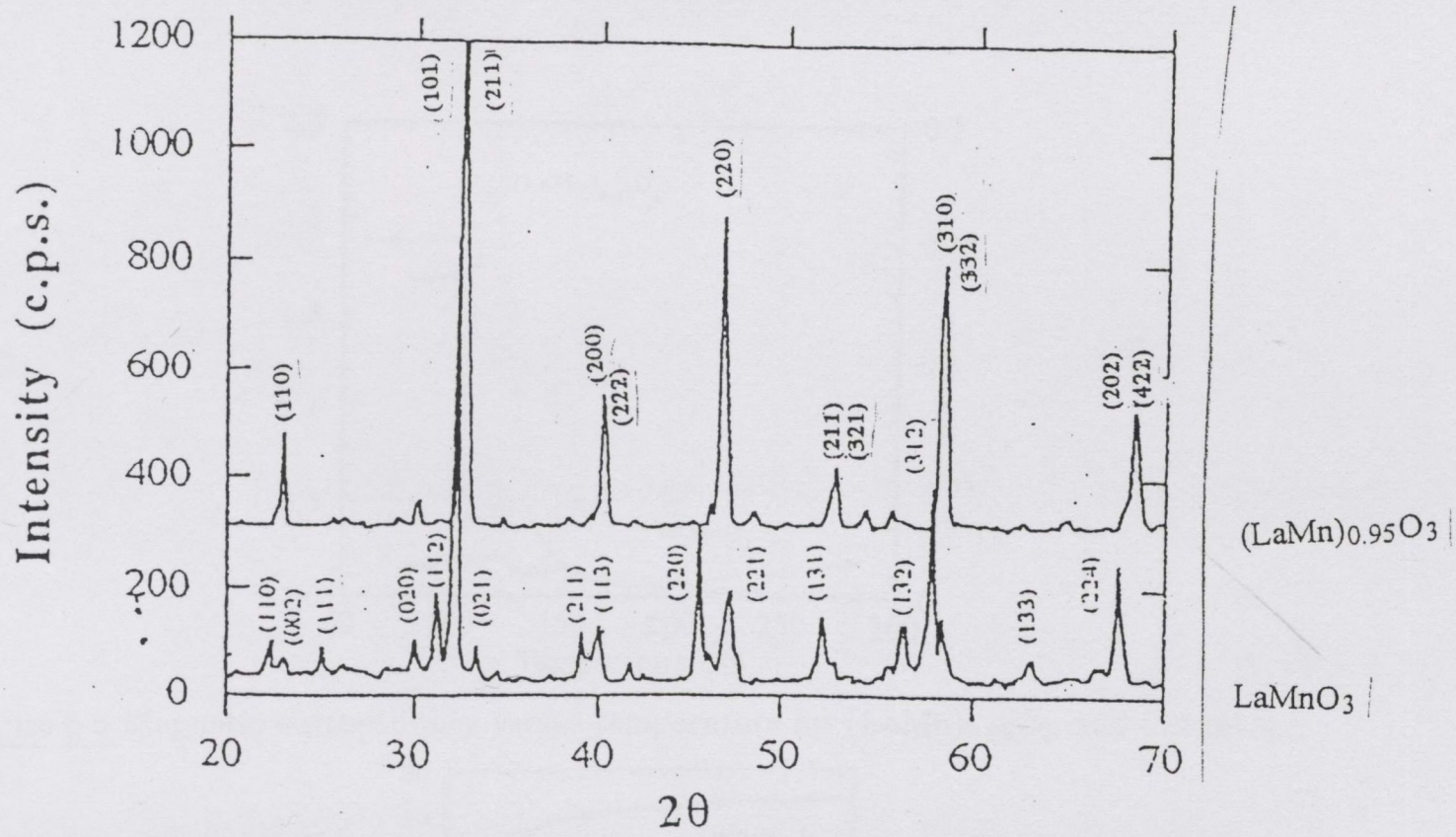

Figure 5.3 The X-ray diffraction spectra of polycrystalline $(LaMn)_{0.95}O_3$ and $LaMnO_3$.

5.2.3 Sample characterisation

The four-point probe method described in detail in chapter 3 was used to measure the electrical resistivity of the samples. Their ac-susceptibilities were measured as a function of temperature in an alternating field with amplitude 80 A/m and frequency 1 kHz, using the mutual inductance method previously described [section 4.2.2]. Additionally, magnetisation curves for both compounds were measured in applied fields of 0 to 6 T at 4.2 K. This latter measurement was performed using a Foner-type vibrating sample magnetometer in conjunction with a superconducting magnet. The sample was vibrated in the "active region" of a set of pick-up coils, where the sensitivity of the coil system varies slowly with position, making it insensitive to the exact location of the sample. A standard nickel sample was used for calibrate the detected signal with the bulk magnetisation. A liquid-helium cooled superconducting solenoid was used to generate the applied field, up to a maximum of 6T.

5.3 Results

Figures 5.4 through 5.6 present, respectively: the temperature dependence of the resistivity of $(LaMn)_{0.95}O_3$; the magnetic susceptibility of $(LaMn)_{0.95}O_3$ and $LaMnO_3$; the low temperat[illegible]s of both samples as a function of applied field.

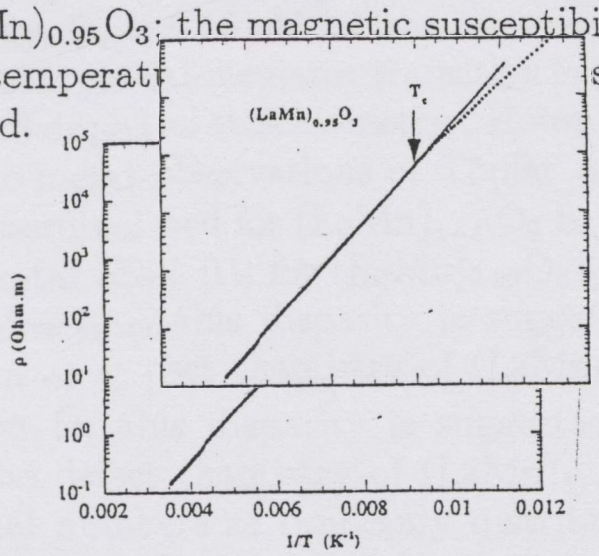

Figure 5.4 The resistivity of $(LaMn)_{0.95}O_3$ as a function of temperature. (The Curie temperature is denoted by the arrow).

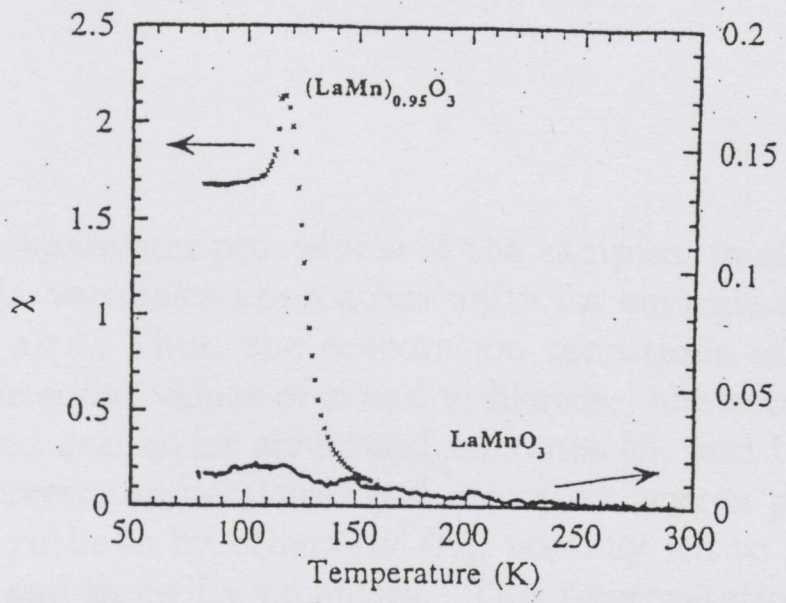

Figure 5.5 Magnetic susceptibility versus temperature for $(LaMn)_{0.95}O_3$ and $LaMnO_3$.

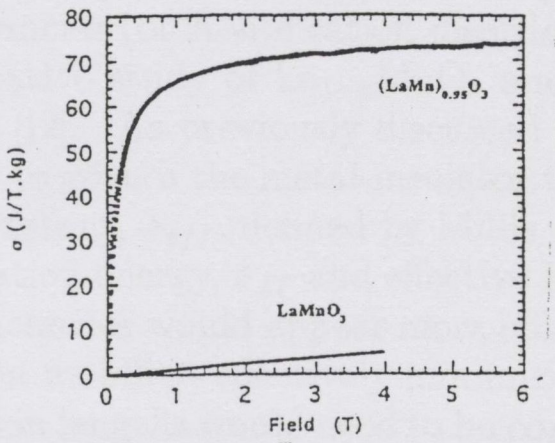

Figure 5.6 Magnetisation curves at 4.2 K for $(LaMn)_{0.95}O_3$ and $LaMnO_3$.

5.4 Discussion

The structural and physical properties of these two compounds are strikingly different. $LaMnO_3$ is typically insulating [8] whereas $(LaMn)_{0.95}O_3$ is a semiconductor, characterised by a room temperature resistivity of $10^{-1}\Omega m$ and a thermally activated conduction mechanism above the ordering temperature, T_C. As shown in figure 5.4, a convincing straight line fit is obtained for the data in the paramagnetic regime when plotted according to a simple activation law,

$$\ln \rho = \frac{E_a}{kT}$$

giving an activation energy, $E_a = 0.16$ eV. Although there is a change of activation regime at T_C, the sample does not exhibit the metal-insulator transition characteristic of the x= 0.3 doped lanthanum manganites. Activated, semiconducting behaviour with no metal-insulator transition is also observed by Alonso [9] for a sample with this nominal stoichiometry. However, this result curiously contradicts the experimental observations of Töpfer *et al.* [10], where metal-insulator transitions are described for $(LaMn)_{1-\delta'}O_3$ for $\delta' > 0.04$; a result also supported by Mahendiran *et al.* [11] for $(LaMn)_{0.96}O_3$ and $(LaMn)_{0.94}O_3$.

A possible explanation for this disparity is suggested by recent work [9] which determines that the defect chemistry of $(LaMn)_{1-\delta'}O_3$ does not necessarily correspond to equal numbers of randomly distributed La and Mn vacancies. Therefore, the non-stoichiometry of the sample cannot be accurately denoted by a single parameter, δ', but requries the specification of two parameters, x and y, as in $La_{1-x}Mn_{1-y}O_3$. The relative values of x and y

depend on the preparation procedures of the samples, in such a way that the ratio of La to Mn vacancies approaches unity for ceramic synthesis at higher temperatures in air. Thus, the preparation conditions of the sample under study here favour equal values of x and y; likewise, the conditions adopted in the studies quoted earlier for structural reference [6], and those of Alonso [9]. Conversely, the lower temperatures and increased oxygen pressures employed during ceramic synthesis by others [10] [11], possibly led to samples with relatively fewer Mn and more La vacancies. This interpretation implies that the localisation of conduction electrons is more efficiently achieved by B-site vacancies than A-site vacancies (or A-site cation disorder) - a conclusion that is supported by a comparative study of $La_{1-x}MnO_3$ and $LaMn_{1-x}O_3$ for $0 \leq x \leq 0.2$ by Arulraj *et al.* [12]. As previously discussed in section 3.5, the most likely crucial parameter to govern the metal-insulator transition is the effective Jahn-Teller coupling constant, λ_{eff}, defined by Millis *et al.* [13] as the ratio of the Jahn-Teller stabilisation energy, δ_{JT} and effective hopping matrix element, t_{eff}. Intuitively, Mn vacancies would appear more efficient than A-site vacancies at impeding electron mobility, effectively minimising t_{eff} and maximising λ_{eff}; although localisation lengths would need to be compatible with the provision of the double-exchange ferromagnetic interaction. Although more recent systematic studies have shown that increasing the vacancy concentration, δ leads to more open Mn-O-Mn bond angles [4], - which were previously shown to favour carrier mobility in substituted manganites [section 3.5] - the perturbation of transport due to missing Mn ions appears the more influential factor with respect to the cation deficient end-member.

The magnetic properties of both samples are also markedly dissimilar. The ac-susceptibility of the non-stoichiometric compound [figure 5.5] is characteristic of a ferromagnet with an ordering temperature, $T_C = 125K$. This value is much reduced from the ordering temperatures of the substituted lanthanum manganites, In contrast, the small peak shown in the data for near-stoichiometric $LaMnO_3$ is characterstic of an antiferromagnet centred at a Neél temperature, $T_N \approx 120$ K. The latter result concurs with early neutron diffraction studies [8] which established the A_y-type antiferromagnetic structure of the stoichiometric end-member; the a-b plane is ferromagnetic with Mn^{3+} spins parallel to the orthorhombic b axis in the *Pbnm* space group, whereas successive planes are coupled antiferromagnetically.

These observations are further confirmed by the M(H) curves measured at 4.2 K [figure 5.6] where the saturation magnetisation of the ferromagnetic material was measured as $\sigma = 75\ JT^{-1}kg^{-1}$; corresponding to an average manganese moment of 3.3 μ_B. Assuming the perfect collinear alignment of the Mn lattice, and an equal number of A and B site vacancies, this value is slightly reduced from the expected theoretical spin-only moment of 3.52 μ_B per unit $(LaMn)_{0.95}O_3$ and corresponds to the spin-only moment expected of ferromagnetically aligned Mn^{3+} / Mn^{4+} in a ratio 0.47:0.53. Alternatively, the reduced value may be attributed to a canted ferromagnetic structure with a canting angle of 20.4°. This latter interpretation is in broad agreement with recent

neutron diffraction measurements [9] which determine the magnetic structure of rhombohedral $(LaMn)_{0.95}O_3$ as a canted ferromagnet with a canting angle of 27°.

In conclusion, the insulating, antiferromagnetic character of $LaMnO_3$, can be dramatically altered through the introduction of a Mn^{3+}/Mn^{4+} mixed valence state, afforded through the divalent substitution of La^{3+} or changing the oxygen stoichiometry, $O_{3+\delta}$. The latter may be achieved through a judicious choice of preparation conditions during the ceramic synthesis process, which introduces La and Mn vacancies. Both methods result in an increased carrier mobility which in turn mediates the ferromagnetic double-exchange. However, as compared to the substituted lanthanum manganites with an equivalent $e_g^{\uparrow}$ band occupancy, the introduction of vacancies (most notably in the Mn sub-lattice) leads to strong carrier localisation effects and frustrated magnetic structures with low ferromagnetic ordering temperatures.

[1] C. N. R. Rao and A. K. Cheetham, Science, **272**, 369, (1996).

[2] D. H. Ryan and J. M. D. Coey, Journal of Physics E, **19**, 693, (1986).

[3] G. Matsumoto, Journal of the Physical Society of Japan, **29**, 606, (1970).

[4] Q. A. Huang, A. Santoro, J. W. Lynn, R. W. Erwin, J. A. Borchers, J. L. Peng and R. L. Greene, Physical Review B, **55**, 14 987, (1997).

[5] A. Urushibara, Y. Moritomo, T. Arima, A. Asamitsu, G. Kido and Y. Tokura, Physical Review B **51**, 14103, (1995).

[6] J. A. M. van Roosmalen, E. H. P. Cordfunke, R. B Helmholdt and H. W. Zandbergen, Journal of Solid State Chemistry, **110**, 100, (1994).

[7] M. Hervieu, R. Mahesh, N. Rangavittal and C. N. R. Rao, European Journal of Solid State Inorganic Chemistry, **32**, 79, (1995).

[8] E. O. Wollan and W. C. Koehler, Physical Review, **100**, 545, (1955).

[9] J. A. Alonso, Philosophical Transactions of the Roayl Society A, **356**, 1617, (1998).

[10] J. Töpfer, J. P. Doumerc and J. C. Grenier, Journal of Materials Chemistry, **6**, 1511, (1996).

[11] R. Mahendiran, S. K. Tiwary, A. K. Raychaudhuri, T. V. Ramakrishnan, R. Mahesh, N. Ragavittal and C. N. R. Rao, Physical Review B **53**, 3348, (1996).

[12] A. Arulraj, R. Mahesh, G. N. Subbanna, R. Mahendiran, A. K. Raychaudhuri and C. N. R. Rao, Journal of Solid State Chemistry, **127**, 87, (1996).

[13] A. J. Millis, P. B. Littlewood and B. I. Shraiman, Physical Review Letters, **74**, 5144, (1995).

Chapter 6
Double perovskites - the next generation

6.1 Introduction

The deluge of recently published work pertaining to the mixed-valence manganites attests both to their intriguing physical properties, and to a widespread optimism towards their possible potential for device applications. In addition to the possible direct application of the CMR effect in magnetic field sensors, position sensors and bolometers, [1], the high degree of spin polarisation in the e_g conduction band suggests the incorporation of the ferromagnetic metallic manganites as a potential source of spin-polarised electrons.in magnetoelectronic devices such as tunnel junctions [2].

To investigate their capability as spin injectors, *tunnel spin valves* have been fabricated, in which an insulating, metallic or superconducting spacer layer is sandwiched between two ferromagnetic (manganite) layers. In principle, if the decoupled ferromagnetic electrodes are fully spin polarised, electron tunneling between them is determined by the relative orientation of their magnetisations. Thus, tunneling occurs for a parallel magnetisation configuration and is classically prohibited for an antiparallel arrangement, which, in the absence of spin-flipping, delivers a magnetoresistance effect when an applied field switches the magnetisation of the two magnetic layers. The impressive 80% magnetoresistance measured for Lu *et al.*'s oft-cited $(La_{0.7}Sr_{0.3})MnO_3/SrTiO_3/(La_{0.7}Sr_{0.3})MnO_3$ trilayer structure at 4.2 K confirmed the high-degree of spin-polarisation in this particular manganite [3], as did the remarkable 410 % effect sunsequently measured by Viret *et al.* [4] in a similar structure. However, the decreasing magnitude of the effect with increasing temperature meant that the MR vanished at 200 K. The dramatic reduction has been ascribed to the appearance of a so-called "dead layer"; an oxygen-deficient layer at the $SrTiO_3$-$(La_{0.7}Sr_{0.3})MnO_3$ interface, where, on increasing the temperature, the spins become progressively more disordered than within the bulk, which promotes spin-flipping and thus decreases the MR effect. Since the practically-useful temperature range for operating devices centres around room temperature, these detrimental interface effects and a $\sim$ 400 K upper limit on the manganites' ordering temperature [section 4.2.3] have impelled the research community to consider other half-metallic ferromagnetic oxides, such as chromium dioxide [5] and most recently, the *double perovskites.*

In a manner reminiscent of the aforementioned manganites, these perovskites with the general formula, A'A"B'B"O_6 (where the primes indicate the possibility of different ions) were initially studied in the 50s [6], and are currently being re-examined in the context of future novel devices. However, in contrast to the experimental observations which rekindled interest in the manganites [discussed in section 3.1], the renewed interest in the double perovskites de-

to the experimental observations which rekindled interest in the manganites [discussed in section 3.1], the renewed interest in the double perovskites derives from recent band calculations [7] which suggest that Sr_2FeMoO_6 is a half-metallic ferrimagnet, with the possiblity of exhibiting a notable 60% spin polarisation at room temperature. The ordering temperature, at $410 - 450$ K [8], is already higher than the best manganite, but the characteristic malleability of perovskite chemistry offers the possibility of enhancing T_C and the prospect of uncovering intriguing physics. To this end, the preliminary results presented in this chapter represent an introduction to three double perovskites, Sr_2FeMoO_6, Ca_2FeMoO_6 and Ba_2FeMoO_6.

6.2 Background

The double perovskites, A'A"B'B"O_6, had been studied for thirty years prior to the advent of accessible high-flux neutron sources in the 1980s [6] [9] [10] [11] [12] [13], which enabled the crystallography of many known double perovskite compounds to be unambiguously determined [14] [15] [16]. Since the B cations generally dictate the physical properties of these materials, the double perovskites are classified according to three B-cation sublattice arrangements: random, layered and rock salt, illustrated in figure 6.1 [17]. Compounds that have a random sublattice show no evidence of B-cation order, whereas the latter two are ordered arrangements.

The rock salt sublattice is exemplified by the studied compounds, Ca_2FeMoO_6, Sr_2FeMoO_6 and Ba_2FeMoO_6, where the B-sites are alternately occupied by Fe^{3+} ($S=\frac{5}{2}$) and Mo^{5+} ($S=\frac{1}{2}$) cations; an arrangement analogous to the interpenetrating Na^+ and Cl^- face-centred cubic lattices of sodium chloride. An intervening oxygen ion bridges each Fe and Mo ion pair, forming alternating FeO_6 and MoO_6 octahedra, with the A-site cations sitting in the interstitial sites. The precise symmetries of the double perovskite compounds, as determined by X-ray diffraction, are discussed in detail in the following section, 6.3.2.

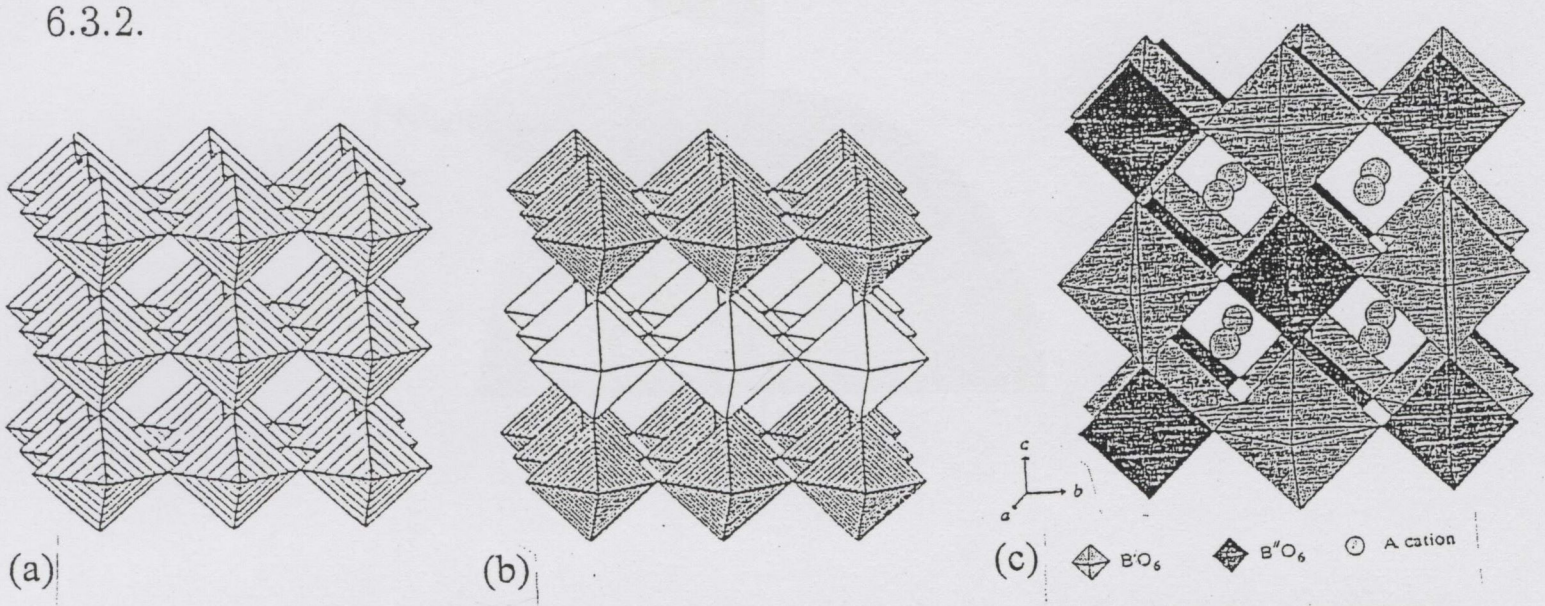

Figure 6.1 (a) Random, (b) Layered and (c) Rock salt arrangement of B cations in the absence of BO_6 octahedral tilts.

By contrast to the manganese perovskites of previous chapters, in which both the conduction electrons and localised spins originate from the Mn 3d electronic states, the original local spin model of the ordered A_2FeMoO_6 is based on a division of labour between the two B-site species. Whereas the $Fe^{3+}(3d^{5\uparrow})$ electrons constitute the localised spin states, the $Mo^{5+}(4d^{1\downarrow})$ electrons are delocalised. The antiferromagnetic superexchange interaction between the $S=\frac{5}{2}$ core spins and the itinerant $S=\frac{1}{2}$ spins indicates a ferrimagnetic structure below the ordering temperature, T_C, and a theoretical total saturation moment of (5-1) = 4 $\mu_B/formula\ unit$ for the ideal ferrimagnetic configuration.

This intuitive model finds support from the Sr_2FeMoO_6 electronic band structure calculations of Kobayashi *et al.*[7], the results of which are schematically illustrated in figure 6.2. From this diagrammatic representation of the density of states, the half metallic nature of this compound's ground state becomes immediately apparent; at the Fermi level, E_F, an energy gap in the up spin subband coexists with an occupied down spin band. In accordance with the aforementioned model, a hybridised $Fe(3d^{\uparrow})$-$O(2p^{\uparrow})$ state constitutes the occupied up spin band, with the $Mo(4d^{\uparrow})$ states at energies above E_F. Likewise, the down spin subband is predominantly composed of O $(2p^{\downarrow})$ states, with $Fe(t_{2g}^{\downarrow})$ and $Mo(t_{2g}^{\downarrow})$ electrons at the Fermi level. Furthermore, it is the overlap of the delocalised Mo electrons with the empty $Fe(t_{2g}^{\downarrow})$ orbitals, which produces the ferromagnetic Fe^{3+}-Fe^{3+} coupling. In the ideal rock salt structure there are no Fe-O-Fe superexchange bonds.

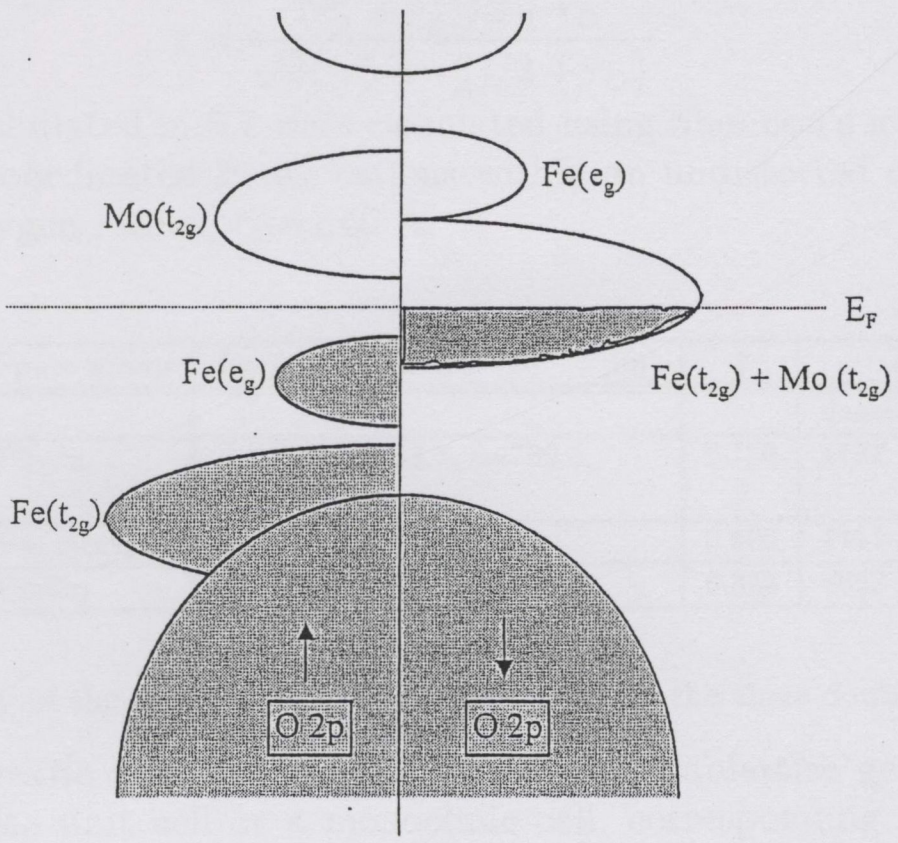

Figure 6.2 Schematic representation of the density of states for Sr_2FeMoO_6 as adapted from [7].

6.3 Experimental procedure

6.3.1 Sample preparation

Polycrystalline ceramic samples of A_2FeMoO_6; A = Ca^{2+}, Sr^{2+}, Ba^{2+} were prepared from stoichiometric mixtures of appropriate oxide and carbonate precursors using the standard ceramic method previously described [chapter 2]. The initial calcination was carried out at 980 °C in air. The resulting decomposed precursors were then repeatedly ground and sintered, culminating in a final, 8 hour firing at 1100 °C in a mixed atmosphere of 1% hydrogen in argon.

6.3.2 Structural characterisation

X-ray diffraction spectra [section 2.3.1], established that the samples were pure with no secondary phases present. Rietveld analysis of the patterns indicated that the compounds had crystallised in three different variants of the double perovskite crystal structure, exhibiting a series of superstructure reflections due to cation order of Fe and Mo on alternate B-sites. The lines could be indexed using a monoclinic ($P2_1/n$), tetragonal (P4/mmm) and cubic (Fm3m) space group for the Ca, Sr and Ba compound respectively. These are noted in table 6.1 alongside the corresponding lattice parameters and X-ray density determined for these samples. Additionally, the concept of Goldschmidt's tolerance factor, t, previously defined for the magnanese perovskites [equation 2.2] is extended to the double perovskites, and may be written

$$t = \frac{(r'_A + r''_A)/2 + r_O}{\sqrt{2}\{(r'_A + r''_A)/2 + r_O\}} \qquad (1)$$

The values tabulated in 6.1 were calculated using Shannon's ionic radii [18] for twelve-fold coordinated B-site cations within an undistorted cubic lattice, based on the oxygen radius, r_O=1.40 Å.

Compound	Space group	Lattice parameters (10^{-12} pm)	t	X-ray density (kg/m^3)
Ca_2FeMoO_6	$P2_1/n$	a=541.6, =552.7, c=769.8; $\beta = 90.04°$	0.780	4727
Sr_2FeMoO_6	P4/mmm	a=b=557.3, c=790.5	0.808	5714
Ba_2FeMoO_6	Fm3m	a =806.2	0.858	6623

Table 6.1 Summary of the structural parameters deduced for the three double perovskites.

Double perovskite compounds with a rock salt sublattice generally have either a cubic $2a_0$ unit cell or a monoclinic cell, corresponding to a slightly distorted $\sqrt{2}a_0$, $\sqrt{2}a_0$, $2a_0$ doubled perovskite supercell, where a_0 is the lattice parameter for an ideal cubic ABO_3 perovskite. The monoclinic cell is observed when the tolerance factor is notably less than unity and results from rotations of the BO_6 octahedra about the $[011]_{cubic}$ and the $[100]_{cubic}$ axes, as depicted in figure 6.3 below.

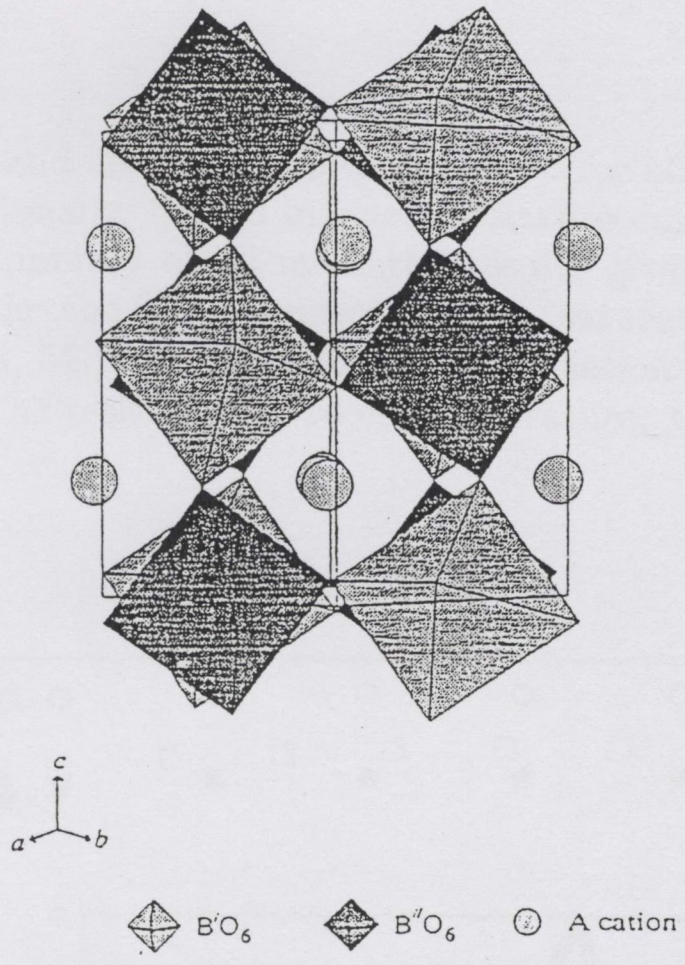

Figure 6.3. Rock salt sublattice with tilted BO_6 octahedra. The crystal structure is monoclinic, with space group $P2_1/n$, as determined for Ca_2FeMoO_6.

The tetragonal $\sqrt{2}a_0$, $\sqrt{2}a_0$, $2a_0$ unit cell determined for the Sr_2FeMoO_6 polycrystalline ceramic warrants further discussion. This cell is not one of those specified as being compatible with the allowed topological transformations of the perovskite structure and a rock salt arrangement of the B ion [19]. However, published reports of ordered double perovskites with rock salt sublattices and alternative crystal structures has prompted Anderson *et al.* [17] to speculate that "small monoclinic distortions, expansions to a larger unit cell size or perhaps incomplete order of the B cations are present [in these compounds]". The latter point is re–addressed in section 6.5.

6.3.3 Sample characterisation

The ac-susceptibility of each sample was measured using the mutual inductance method [section 4.2.2] in an 80 A/m, 1 kHz excitation field in both the high and low temperature concentric coil rigs. The samples were prepared as elongated cuboids, with typical dimensions, 9mm x 1 mm x 1mm.

Magnetisation as a function of applied field was measured at 5 K using a "Quantum Designs" superconducting quantum interference device (SQUID) magnetometer in fields up to 5 T.

Resistivity measurements were carried out as a function of temperature, in the range 12 - 300 K. The four point probe technique and experimental apparatus used are described in chapter 3.

6.4 Results

The magnetisation and ac-susceptibility measured for all three compounds are presented. Additionally, typical magnetoresistance curves are shown for Sr_2FeMoO_6, with a summary of all measured results given in the following table 6.2. These include: the Curie temperature, T_C; saturation magnetisation measured in 5 T at 5 K, M_0; the spontaneous magnetisation measured at room temperature, M_s and the resistivity at room temperature, ρ_{RT}.

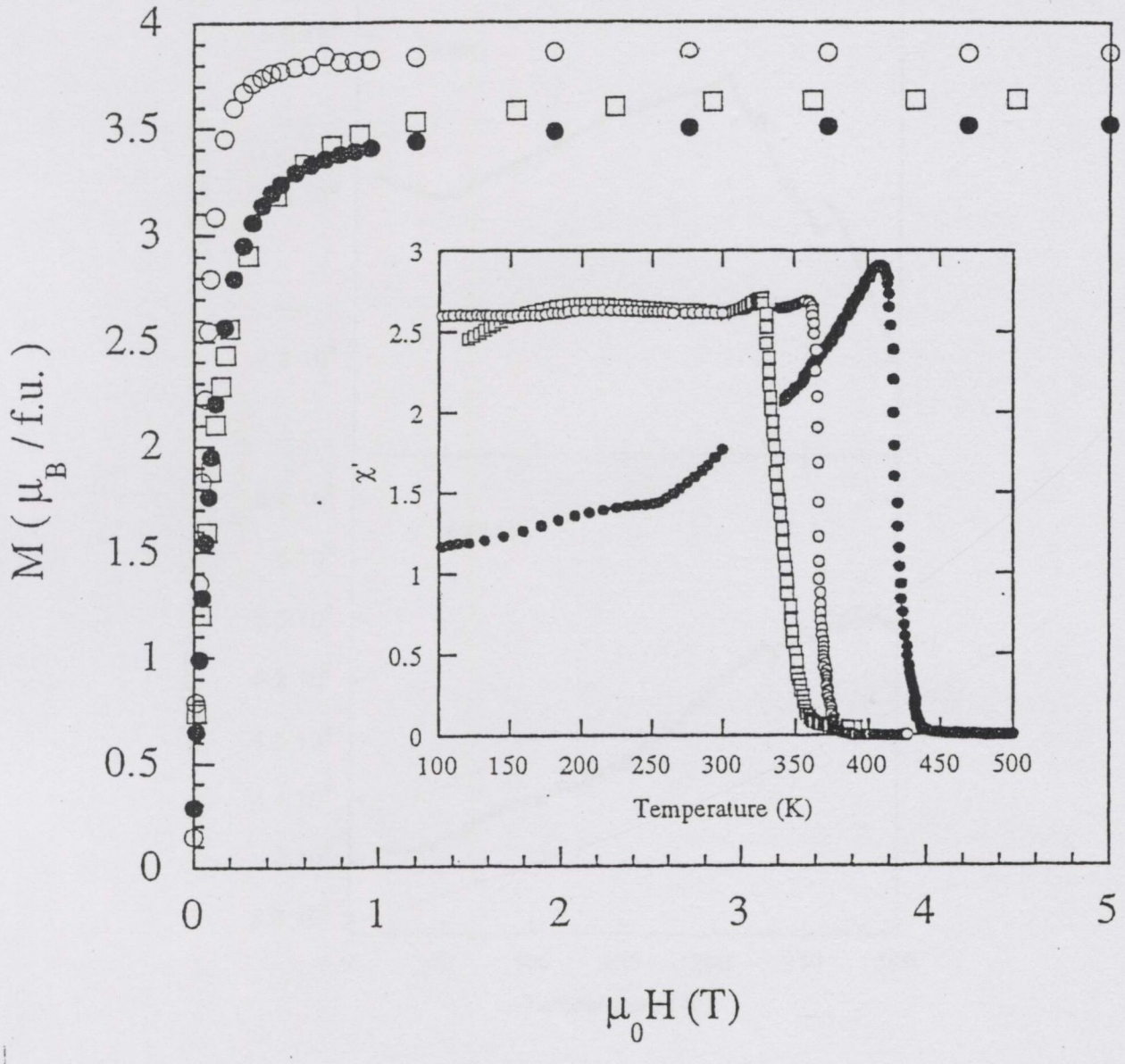

Figure 6.4 Variation of magnetisation with applied field for A_2FeMoO_6 at 5 K (A = Ca, □ ; Sr, • ; Ba, ○).

The insert shows the real part of the susceptibility measured in 80 A/m at 1 kHz.

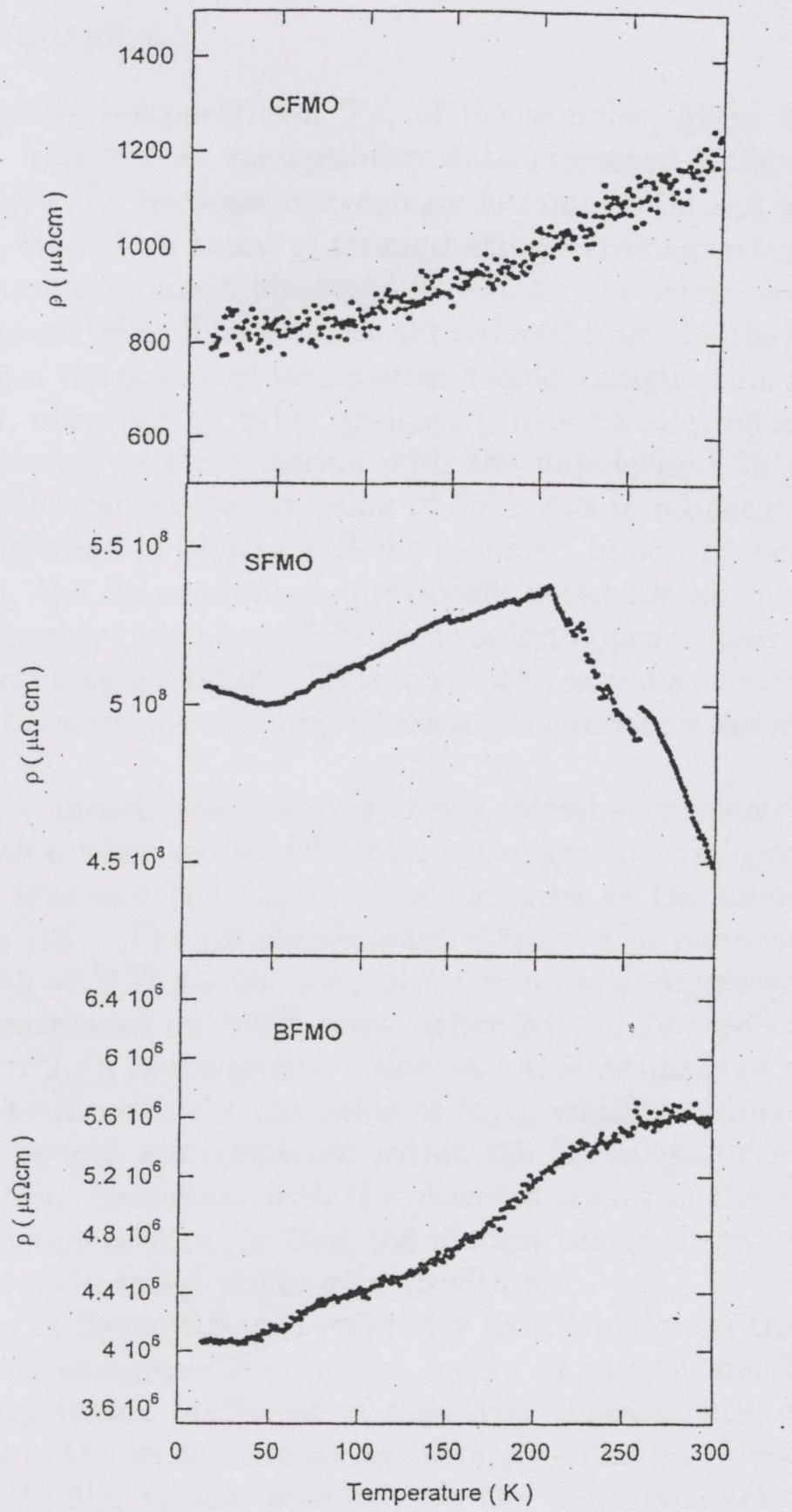

Figure 6.5 Resistivity of (a)Ca_2FeMoO_6, (b)Sr_2FeMoO_6 and (c) Ba_2FeMoO_6.

Compound	T_C (K)	M_0	M_s	ρ_{RT}
		$(\mu_B/f.u.)$	$(\mu_B/f.u.)$	$(\mu\Omega m)$
Ca_2FeMoO_6	345	3.63	1.58	10
Sr_2FeMoO_6	425	3.51	2.04	4.5×10^6
Ba_2FeMoO_6	367	3.85	1.56	5.5×10^4

Table 6.2 A summary of the measured physical properties for the three double perovskites studied.

6.5 Discussion

The ordering temperatures, T_C, of the samples, given in table 6.2, were determined from the ac-susceptibility data presented in figure 6.5. The χ'_{ac} response below T_C becomes increasingly ferromagnetic and step-like in the series Sr, Ca, Ba. This trend of strengthening ferromagnetism is also reflected in the increasing moment measured at 5 K for the series; 3.53, 3.63 and 3.85 $\mu_B/f.u.$ respectively. These values are reduced from the theoretical 4 $\mu_B/f.u.$ expected from the proposed ferrimagnetic ionic configuration Fe^{3+}/Mo^{5+}. This discrepancy, observed by other groups [7], may be attributed to a number of possible factors: covalent mixing with the unpolarised 2p(O) orbitals; spin canting; antiferromagnetic coupling of Fe^{3+} ions in adjacent B-sites or disordered arrangement of alternate B-site cations. In accordance with this latter explanation, the Sr compound, previously noted for an incongruous crystal structure possibly indicative of B-site disorder, appropriately displays the lowest saturation magnetisation. This hypothesis may also account for the lack of correlation between the calculated tolerance factors and the measured physical properties.

To further investigate this hypothesis, Mössbauer spectroscopy and neutron diffraction was used to determine the electronic configuration of the constituent Fe ions and the degree of cation order in the monoclinic rock salt, Ca_2FeMoO_6 [22]. The results obtained attributed a moment of 4.0(1) μ_B to the iron with -0.2(3) μ_B on the molybdenum, and suggested that 6% of the Fe^{3+} were misplaced on Mo^{5+} sites. (sites 2d and 2c respectively within the appropriate $P2_1/n$ space group). However, this estimate of cation disorder is insufficient to account for the value of M_{sat}, which requires that 24% of the constituent Fe ions are misplaced within the ferrimagnetic model. A plausible explanation, consistent with the observed trends in the susceptibility and saturation magnetisation, is that the modest cation disorder order gives rise to some non-collinearity in the spin structure.

As shown in figure 6.6, the resistivity as a function of temperature of the three ceramic samples differ by six orders of magnitude, but all have the positive temperature coefficient of resistivity characteristic of a metal. The Ca_2FeMoO_6 is the most conducting, with $\rho \sim 10\mu\Omega m$ at room temperature, comparable to the values measured for the more conducting ferromagnetic manganites [table 3.1]. However, a range of room temperature values, ρ_{RT}, from 1 - 1000 $m\Omega m$ measured for Sr_2FeMoO_6,attributable to differences in previous thermal treatment, suggests that like their manganite forebears, the transport properties of the polycrystalline double perovskites are dominated by extrinsic effects. The significant contribution of the grain boundaries to the resistivity is again suggested by the magnetoresistance effects measured [21], where the maximum effect is measured for the Sr compound with greatest ρ_{RT}. The Ca compound shows a negligible MR effect suggesting that the low resistivity measured for this particular sample is almost entirely intrinsic in origin.

In conclusion, through exhibiting higher ordering temperatures (with re-

spect to the manganites) and a high degree of spin polarisation, as borne out by the good preliminary room temperature magnetoresistance measured for Sr_2FeMoO_6 [22], the possible incorporation of the double perovskites in a future spin electronics based technology seems most auspicious.

[1] T. Venkatesan, M. Rajeswari, Z. W. Dong, S. B. Ogale and R. Ramesh, Philosophical Transactions of the Royal Society A, **356**, 1593, (1998).

[2] R. Meservey and P. M. Tedrow, Physics Reports, **238**, 173, (1994).

[3] Y. Lu, X. W. Li, G. Q. Gong, G. Xiao, A. Gupta, P. Lecoeur, J. Z. Sun, Y. Y. Wang and V. P. Dravid, Physical Review B **54**, R8357, (1996).

[4] M. Viret, M. Drouet, J. P. Contour, J. Nassar, C. Fermon and A. Fert, Europhysics Letters, **39**, 545, (1997).

[5] A. Barry, Ph.D. Thesis, University of Dublin , 1999.

[6] R. Roy, Journal of the American Ceramic Society, **37**(12), 581, (1954).

[7] K. I. Kobayashi, T. Kimura, H. Sawada, K. Terakura and Y. Tokura, Nature, **395**, 677, (1998).

[8] F. S. Galasso, *"Structure, properties and preparation of perovskite-type compounds"*, Pergamon Press, (1969).

[9] F. Galasso, L. Katz, R. Ward, Journal of the American Ceramic Society, **81**, 820, (1959).

[10] F. Galasso, L. Katz, C. W. Möller and R. Ward, Journal of Physical Chemistry, **66**, 131, (1962).

[11] F. K. Patterson, C. W. Möller and R. Ward, Inorganic Chemistry, **2**(1), 196, (1963).

[12] E. E. Havinga, Phillips Research Reports, **21**, 432, (1966).

[13] T. Nakamura and J-H. Choy, Journal of Solid State Chemistry, **20**, 233, (1977).

[14] P. D. Battle, J. B. Goodenough and R. Price, Journal of Solid State Chemistry, **46**, 234, (1983).

[15] P. D. Battle and W. J. Macklin, Journal of Solid State Chemistry, **52**, 138, (1984).

[16] P. D. Battle and W. J. Macklin, Journal of Solid State Chemistry, **54**, 245, (1984).

[17] M. T. Anderson, K. B. Greenwood, G. A. Taylor and K. R. Poeppelmeier, Progress in Solid State Chemistry, **22**, 197, (1993).

[18] R. D. Shannon and C. T. Prewitt, Acta Crystallographica A, **32**, 785, (1976).

[19] A. M. Glazer, Acta Crystallographica B, 28, 3384, (1972).

[20] Manufactured by Magnetic Solutions Limited, IDA Centre, Unit 13, Pearse St., Dublin, Ireland.

[21] R. P. Borges, R. M. Thomas, C. Cullinan, J. M. D. Coey, R. Suryanarayanan, L. Ben-Dor, L. Pinsard-Gaudart and A. Revcolevschi, Journal of Physics: Condensed Matter, in press.

[22] L. Pinsard-Guadart, R. Suryanarayanan, A. Revcolevschi, J. Rodriguez-Carvajal, J-M. Greneche, P. A. I. Smith, R. M. Thomas, R. P. Borges and J. M. D. Coey, submitted for publication.

[23] Private communications with R. Suryanarayanan.

Chapter 7
Conclusions

7.1 Conclusions

The malleability of perovskite chemistry has offered the opportunity to compare the structural, transport and magnetic properties of twelve manganites, $(A_{0.7}A'_{0.3})MnO_3$; A = La^{3+}, Pr^{3+}, Nd^{3+}, Sm^{3+}, A' = Ca^{2+}, Sr^{2+}, Ba^{2+}. Additional studies of $LaMnO_3$ and three double perovskites complement this central research theme, through exploring the role of oxygen content, and extending the upper limit of ordering temperatures exhibited by these oxides respectively.

A solid state reaction method efficiently produced the twelve principal perovskites studied. Their phase purity and bulk nominal stoichiometry were confirmed by X-ray diffraction (XRD) and X-ray fluorescence (XRF) respectively. However, as this preparation technique is based on the thermal decomposition and repeated sintering of component carbonates and oxides at $1200°C$, it proved an inappropriate synthesis method for $(A_{0.7}Pb_{0.3})MnO_3$ due to the volatility of the PbO precursor. The resulting Pb deficiency of the four compounds was identified by XRF. To a first approximation, their stoichiometry was determined as $(La_{0.7}Pb_{0.15})MnO_3$, $(Pr_{0.7}Pb_{0.07})MnO_3$, $(Nd_{0.7}Pb_{0.10})MnO_3$ and $(Sm_{0.7}Pb_{0.02})MnO_3$. A sol-gel synthesis route was also explored. However, the superior sample homogeneity expected from this method was not evidenced by the scanning electron micrographs taken of the single-phase $(Nd_{0.7}Sr_{0.3})MnO_3$ compound prepared.

Investigation of the manganites' transport properties was effectively confined to measuring their resistivity as a function of temperature, $\rho(T)$. However, through establishing the $T^{-\frac{1}{4}}$ dependence of the activated conduction regime, a contribution was made to the debate surrounding the compounds' possible conduction mechanism at high temperatures. The superior linear fit obtained for all twelve samples through plotting their resistivity as $\ln(\frac{\rho}{T})$ vs $T^{-\frac{1}{4}}$, suggested that their activated conduction is best described by a variable-range hopping (VRH) mechanism. The original interpretation of this result invoked spatial fluctuations in the Coulomb and spin-dependent potentials which localised the $e_g^{\uparrow}$ (σ^* band) electrons in large wave packets. Thus, current transport proceeded via hops beyond nearest neighbours to sites with a smaller potential difference. Development of this picture led to the formulation of a self-consistent theory of magnetic localisation. This model introduced random, spin-dependent potential fluctuations of magnetic origin into Mott's fundamental VRH theory. Deducing the resulting localisation and hopping lengths - 0.34 nm and 1.24 nm respectively for $(La_{0.7}Sr_{0.3})MnO_3$ - required values for the density of states, $N(E_F) \sim 3 \times 10^{28}$ $m^{-3}eV^{-1}$ for $(La_{0.7}Sr_{0.3})MnO_3$; these were provided by specific heat capacity measurements.

The theory attributed the metal-insulator transition exhibited by all but

four samples near T_C, to a narrowing of the random distribution of spin directions in the internal molecular field below T_C, leading to a decrease in the average magnetic potential fluctuations, ΔV. Similarly, within this model, the activated behaviour shown to lowest temperatures by $(Pr_{0.7}Ca_{0.3})MnO_3$, $(Nd_{0.7}Ca_{0.3})MnO_3$, $(Sm_{0.7}Ca_{0.3})MnO_3$ and $(Sm_{0.7}Ba_{0.3})MnO_3$ could be attributed to the narrowing of the $e_g^{\uparrow}$ conduction bandwidth due to a decreased Mn-O-Mn bond angle. VRH behaviour observed in polycrystalline samples may be extrinsic, being associated with grain boundaries. Recent experimental evidence suggests that the manganites' intrinsic conduction mechanism is activated, and related to small magnetopolarons, originating from the dynamic Jahn-Teller effect. Therefore, it appears that magnetically-controlled VRH in grain boundaries controls the resistivity of the ferromagnetic manganite ceramics.

The principal conclusions of this work pertain to the magnetic properties of the samples studied. Application of the Curie-Weiss law to the low-field susceptibility data measured for each sample from 4.2K to room temperature, gave the ferromagnetic ordering temperatures, T_C, of the sample matrix. In order to achieve the stated objective of this project, a detailed investigation of the correlation between T_C and the various physical properties of the manganites ensued. Athough a universal relation could not be determined, the T_C of the optimally doped ferromagnetic manganites was conclusively shown to correlate with the average size of the A-site cations. This result could be explained in terms of the double-exchange mechanism, decreasing the Mn-O-Mn bond angle from the ideal 180° through substitution of smaller A-site cations, decreases the efficacy of the double-exchange mechanism relative to the antiferromagnetic superexchange interaction between the localised t_{2g} spins. The inherent competition may also be reflected in the sharper decline of susceptibility at $T<T_C$, generally shown by those samples with the lowest ordering temperatures.

At $T>T_C$, the Curie constant evaluated for each compound was larger than that expected from calculating the paramagnetic susceptibility of the free manganese ions. These enhanced Curie-Weiss susceptibilites could be modelled in terms of ferromagnetic clusters containing an average of three Mn ions. Attempts to fit the data to a distribution of T_C within a representative sample were shown to be physically implausible.

Further insight into the manganites' magnetic structure was offered by the magnetisation measurements conducted at 4.2 K in a steady applied field ranging up to 23 T. The variety of structures suggested by these data for the different compounds, reflects the fine balance of interactions which govern the manganites' ground state. For $(La_{0.7}Sr_{0.3})MnO_3$, the negligible value of high field slope measured, $\partial M/\partial H \sim 6 \times 10^{-5} \mu_B/T$ confirms the strong ferromagnetic nature of this compound, in agreement with recent reports of its high spin-polarisation. In stark contrast, none of the Pr containing compounds are saturated in 23 T, showing pronounced high field slopes of order 0.02 μ_B/T. Furthermore, the M(H) behaviour of $(Pr_{0.7}Ca_{0.3})MnO_3$ is characterised by two

first-order magnetisation processes. The first of these, at 5 T, is the transformation from the charge-ordered ground state to the metallic, ferromagnetic, charge-disordered state, widely observed in pulsed field measurements. The moment, 3.6 $\mu_B/f.u.$ corresponds to an almost fully-aligned manganese sublattice. At 6 T, the magnetisation increases by a further $\sim 0.8\ \mu_B$. This hitherto unreported transition is attributed to a level crossing transition of the lowest lying Pr^{3+} crystal field levels; an argument buttressed by the calculation of the crystal field interaction at the rare-earth site. Extrapolation of this crystal field calculation to the Nd containing compounds supports the experimental observation that the Nd^{3+} sublattice contributes a further $\sim 1\mu_B$ to the total magnetic moment of $(Nd_{0.7}Sr_{0.3})MnO_3$ and $(Nd_{0.7}Ba_{0.3})MnO_3$.

For these compounds, the nature of the inter-sublattice coupling was investigated through conducting X-ray magnetic circular dichroism (XMCD) at the Nd L_3 and Mn K edges. This study concluded that the exchange coupling between the rare-earth and transition metal ions is mediated by the Nd (5d) and Mn (3d) conduction electrons. Moreover, the Nd and Mn sublattices of $(Nd_{0.7}Ba_{0.3})MnO_3$ have been previously shown to be antiferromagnetically aligned in zero applied field at low temperature. Application of a field ~ 1 T was shown by this study to break the Nd(5d)- Nd(4f) intra-atomic coupling, resulting in the ferromagnetic alignment which prevails up to the highest applied fields. The ferri- to ferromagnetic transition is irreversible.

Pulsed field measurements up to 25 T were carried out at 4.2 K and 77 K on the charge-ordered $(Pr_{0.7}Ca_{0.3})MnO_3$ and $(Nd_{0.7}Ca_{0.3})MnO_3$. The hysteresis measured for both samples, which was notably absent in the steady field measurements, was quantitatively attributed to the magnetically induced melting of short-range charge-order in these compounds.

In addition to the systematic study of the twelve perovskites presented, the physical properties of the end member, $LaMnO_3$ were investigated as a function of oxygen stoichiometry. Using an original method to prepare the stoichiometric sample - thermal reduction of $(LaMn)_{0.95}O_3$ powder under hydrogen in a thermopiezic analyser - the crystal structure, resistivity, susceptibility and magnetisation of both these samples were compared. Whereas the former is orthorhombic, insulating and antiferromagnetic, the latter is rhombohedral, semi-conducting and ferromagnetic. Through comparing the data obtained for $(LaMn)_{0.95}O_3$ with substitued lanthanum manganites with an equivalent $e_g^{\uparrow}$ band occupancy - $(La_{0.7}A'_{0.3})MnO_3$ - the principal conclusion is that vacancies introduced in the Mn sub-lattice lead to strong carrier localisation effects and frustrated magnetic structures with low ferromagnetic ordering temperatures.

Enhancing the T_C of the substituted manganites beyond 370 K through manipulation of composition or stoichiometry cannot be achieved. Therefore, those interested in device development have shifted their attention to the double perovskites, $A_2B'B''O_6$. These compounds, with ordering temperatures which already exceed the highest value exhibited by $(La_{0.7}Sr_{0.3})MnO_3$, (for Sr_2FeMoO_6 $T_C = 425$ K) may have a half-metallic ground state Thus the preliminary study of their physical properties, as presented in the final chap-

ter of this thesis, lays the groundwork for the continued investigation of these promising new generation of perovskite materials.

7.2 Suggestions for further work

Measuring the resistivity of single crystal samples as a function of temperature, would complement the transport data measured for the polycrystalline samples. Thus, the intrinsic transport mechanisms of the manganites could be distinguished from the extrinsic effects systematically investigated here.

The nature of the postulated ferromagnetic clusters should be explored. A suitable experimental avenue is offered by small angle neutron scattering for the non-Sm containing compounds. Further investigation of the Sm moment could proceed using X-ray synchrotron radiation experiments.

Additionally, the calculation of the crystal field interaction at the rare-earth site of the Pr and Nd compounds could be used as the basis for a more sophisticated model, incorporating further crystal field parameters.